GEOTECHNICAL SPECIAL PUBLICATION NO. 197

SLOPE STABILITY, RETAINING WALLS, AND FOUNDATIONS

SELECTED PAPERS FROM THE 2009 GEOHUNAN INTERNATIONAL CONFERENCE

August 3–6, 2009
Changsha, Hunan, China

HOSTED BY
Changsha University of Science and Technology, China

CO-SPONSORED BY
ASCE Geo-Institute, USA
Asphalt Institute, USA
Central South University, China
Chinese Society of Pavement Engineering, Taiwan
Chongqing Jiaotong University, China
Deep Foundation Institute, USA
Federal Highway Administration, USA
Hunan University, China
International Society for Asphalt Pavements, USA
Jiangsu Transportation Research Institute, China
Korea Institute of Construction Technology, Korea
Korean Society of Road Engineers, Korea
Texas Department of Transportation, USA
Texas Transportation Institute, USA
Transportation Research Board (TRB), USA

EDITED BY
Louis Ge, Ph.D. P.E.
Jinyuan Liu, Ph.D.
James –C. Ni, Ph.D. P.E.
Zhao Yi He, Ph.D.

Published by the American Society of Civil Engineers

Library of Congress Cataloging-in-Publication Data

Slope stability, retaining walls, and foundations : selected papers from the 2009 GeoHunan International Conference, August 3-6, 2009, Changsha, Hunan, China / hosted by Changsha University of Science and Technology, China ; co-sponsored by ASCE Geo-Institute, USA … [et al.] ; edited by Louis Ge … [et al.].
p. cm. -- (Geotechnical special publication ; no. 197)
Includes bibliographical references and indexes.
ISBN 978-0-7844-1049-3
1. Soil stabilization--Congresses. 2. Slopes (Soil mechanics)--Stability--Congresses. 3. Retaining walls--Design and construction--Congresses. 4. Foundations--Design and construction--Congresses. I. Ge, Louis. II. Changsha li gong da xue. III. American Society of Civil Engineers. Geo-Institute. IV. GeoHunan International Conference on Challenges and Recent Advances in Pavement Technologies and Transportation Geotechnics (2009 : Changsha, Hunan Sheng, China)

TE210.4.S56 2009
624.1'51363--dc22 2009022667

American Society of Civil Engineers
1801 Alexander Bell Drive
Reston, Virginia, 20191-4400

www.pubs.asce.org

Any statements expressed in these materials are those of the individual authors and do not necessarily represent the views of ASCE, which takes no responsibility for any statement made herein. No reference made in this publication to any specific method, product, process, or service constitutes or implies an endorsement, recommendation, or warranty thereof by ASCE. The materials are for general information only and do not represent a standard of ASCE, nor are they intended as a reference in purchase specifications, contracts, regulations, statutes, or any other legal document. ASCE makes no representation or warranty of any kind, whether express or implied, concerning the accuracy, completeness, suitability, or utility of any information, apparatus, product, or process discussed in this publication, and assumes no liability therefore. This information should not be used without first securing competent advice with respect to its suitability for any general or specific application. Anyone utilizing this information assumes all liability arising from such use, including but not limited to infringement of any patent or patents.

ASCE and American Society of Civil Engineers—Registered in U.S. Patent and Trademark Office.

Photocopies and reprints.
You can obtain instant permission to photocopy ASCE publications by using ASCE's online permission service (http://pubs.asce.org/permissions/requests/). Requests for 100 copies or more should be submitted to the Reprints Department, Publications Division, ASCE, (address above); email: permissions@asce.org. A reprint order form can be found at http://pubs.asce.org/support/reprints/.

Copyright © 2009 by the American Society of Civil Engineers. All Rights Reserved.
ISBN 978-0-7844-1049-3 Manufactured in the United States of America.

Preface

The papers in this Geotechnical Special Publication were presented in the session of Soil Stabilization, Dynamic Behavior of Soils and Foundations and in the session of Earth Retaining Walls and Slope Stability at GeoHunan International Conference: Challenges and Recent Advances in Pavement Technologies and Transportation Geotechnics. The conference was hosted by Changsha University of Science and Technology on August 3-6, 2009.

Contents

Soil Stabilization and Dynamic Behavior of Soils and Foundations

Earth Retaining Walls and Slope Stability

Indexes

Experimental Study on T-shaped Soil-cement Deep Mixing Column Composite Foundation

Yaolin Yi[1], Songyu Liu[2], M. ASCE, Dingwen Zhang[3] and Zhiduo Zhu[3]

[1]Ph.D candidate, Institute of Geotechnical Engineering, Southeast University, 2# Sipailou, Nanjing , China, 210096; yiyaolin@seu.edu.cn
[2]Professor, Institute of Geotechnical Engineering, Southeast University, 2# Sipailou, Nanjing, China, 210096; liusy@seu.edu.cn
[3]Doctor, Institute of Geotechnical Engineering, Southeast University, 2# Sipailou, Nanjing, China, 210096; zhangdw@seu.edu.cn
[4]Associate professor, Institute of Geotechnical Engineering, Southeast University, 2# Sipailou, Nanjing, China, 210096; zhuzhiduo63@sohu.com

ABSTRACT: Soil-cement deep mixing method is widely used in soft ground improvement for highway engineering application in China. However, there are some disadvantages of the conventional soil-cement deep mixing method in China, such as insufficient mixing, grouting spill and decrease of strength along column depth. In addition, small column spacing and cushion or geosynthestic reinforcement are often required, resulting in high cost. In order to conquer these disadvantages, a new deep mixing method named T-shaped deep mixing method is developed. The mechanism, construction issues, and pilot project monitoring results of T-shaped deep mixing column foundation are presented in the paper. The results indicate that the T-shaped deep mixing method makes the deep mixing much more reliable and economical.

INTRODUCTION

Deep mixing method is a soil improvement technique that delivers reagent (cement or lime or a combination), either slurry or powder, into the ground and mixes it with in situ soils to form a hardened column (DM column). The deep mixing method was introduced to China in the late 1970’s (Han et al., 2002). The technology spreads rapidly throughout China in the 1990’s, especially for highway engineering application. Many engineering practices of deep mixing method in China have demonstrated that it has many merits, such as easy and rapid installation and relatively small vibration. More important, it can effectively reduce the settlement and increase the stability of soft ground (Liu and Hryciw, 2003; Chai et al., 2002).

However, deep mixing method also encounters following problems in China: (1) Insufficient mixing, grouting spill, and decrease of column strength along column depth. (2) Small column spacing and cushion or geosynthestic reinforced layer are often required, which cause high cost. In order to conquer these disadvantages, a new deep mixing method called T-shaped deep mixing method and the relevant machine are developed (Liu et al., 2006). The mechanism, construction issues, and pilot project monitoring results of T-shaped deep mixing column composite foundation are presented below.

FUNDAMENTALS OF T-SHAPED DEEP MIXING MTHOLD

In highway or railway engineering, the differential settlement between DM columns and the surrounding soil is induced by embankments which are usually treated as flexible foundation, as a result of the different compressibility behavior between DM column and soil. The differential settlement is about 8%~20% of the average settlement (Bergado et al., 2005). The differential settlement at the surface of ground can transfer to the embankment, and even harm pavement if the differential settlement is large enough. As a result, small spacing (typically 1.1 m to 1.5 m in China) is adapted in DM column composite foundation in highway engineering. And cushion or geosynthestic reinforced layer is often set above columns to reduce the differential settlement, which cause high cost. The additional stress in upside of DM column composite foundation is larger than in underside. So a DM column with large upside column diameter and small underside column diameter can improve the soft ground better than conventional shaped column.

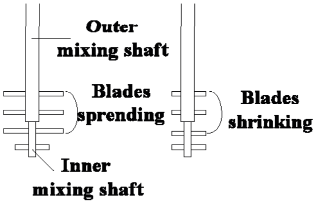

FIG. 1. Blades sketch of T-shaped deep mixing machine

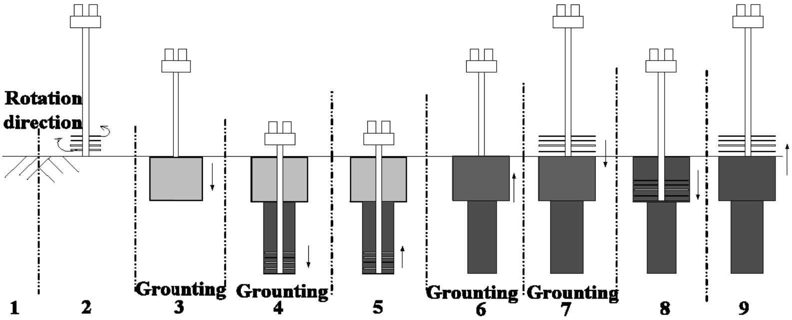

FIG. 2. Construction process of T-shaped deep mixing method

The blades of T-shaped deep mixing machine can spread outward and shrink inward at any position when they work underground (as shown in FIG. 1), and a column with two column diameters can be installed by this new deep mixing machine. So a deep mixing column which has large diameter upside and small diameter underside can be installed by this new deep mixing machine (as shown in FIG. 2). The shape of this new deep mixing column is similar to the shape of ‘T’, so it is called T-shaped deep mixing column (TDM column).

Before the usage of this new method, almost all of the soil-cement deep mixing columns in China are installed with single mixing method that the mixing blades run in one direction (Yi and Liu, 2008). The single mixing method results in insufficient mixing of soil-cement, grouting spill, and decrease in column strength along column depth. From this point of view, double mixing method (Shen et al., 2003, 2008; Chai et al., 2005; Liu et al., 2008) is adopted in TDM column installation to improve mixing efficiency and column uniformity(Yi and Liu, 2008). The construction process of T-shaped deep mixing method is shown in FIG. 2.

FIELD TESTS

Test Site and Column Composite Foundation Design

The pilot project was set in the construction field of Husuzhe highway. The test site was divided into four sections, and two sections were presented in this paper. One section was improved by TDM columns, and the other was improved by conventional DM columns. CPTU testing results indicated the engineering geological conditions in the two sections are similar (Yi and Liu, 2008). Laboratory tests were also conducted, and the main index properties of each layer are presented in Table 1.

Table 1. Index properties of soil layers in test site

Soil layers	Depth (m)	γ (kN•m^{-3})	W (%)	e_0	W_L (%)	W_p (%)	c (kPa)	φ (°)	$E_{s1\text{-}2}$ (MPa)
Clay	0~2	19	35	0.94	41.9	23.6	31.2	25	8.8
Mucky clay	2~14	17	50.9	1.43	53.6	24.1	12.6	16.3	1.9
Silty clay	14~16	20.3	23.9	0.67	46.7	21.7	40.3	23.5	7.5
Clay	16~	20.5	24.1	0.65	35.8	14.8	37.9	29.7	25.1

The arrangements of columns were quincunx in both sections. The cement content was 255 kg/m^3, and water cement ratio of was 0.55. The design parameters of TDM and conventional DM column composite foundation are shown in FIG. 3. It can be easily calculated with the design parameters in FIG. 3 that the replacement ratio of the upside TDM column composite foundation is 0.227, of the underside TDM column composite foundation is 0.057, and of conventional DM column composite foundation is 0.116. On one hand, the upside replacement ratio of TDM column composite foundation is almost twice that of conventional DM column composite foundation, which can reduced differential settlement between column and surrounding soil. On the other hand, the underside replacement of TDM column composite foundation is nearly half that of conventional DM column composite foundation, which can save much cement. The cement cost is 535 kg/m^2 in TDM column composite foundation, and 632 kg/m^2 in conventional DM column composite foundation, which means the former is 15.3 % less than the latter. The photos of T-shaped cement-soil deep mixing column are shown in FIG. 4.

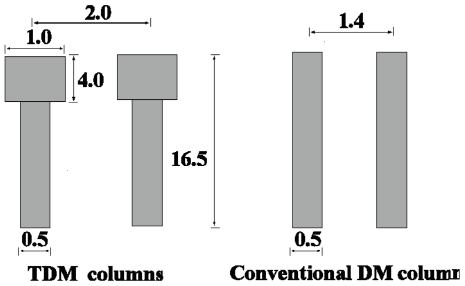

FIG. 3. Parameters of column composite foundation (not to scale, unit: m)

FIG. 4. Photo of T-shaped cement-soil deep mixing column

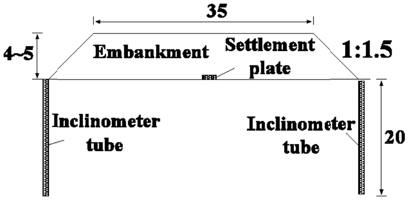

FIG. 5. Cross-section view of instrumentation (not to scale, unit: m)

Monitoring Results While Embankment Filling

Before embankment was filled, monitoring instruments, including settlement plates and inclinometers were installed in both section, and the cross-section view of instrumentation was shown in FIG. 5. The settlements plates were installed on top of the soil between the columns along the embankment centerline. The inclinometers were installed at the embankment toes to measure the lateral displacement of soil under embankment loads. Staged construction and surcharge techniques were used for the embankment filling.

The measured settlements with time are presented in FIG. 6. It is shown that the measured settlement increased with the embankment height. The embankment height in TDM column composite foundation is 0.6 m larger than in conventional DM column composite foundation, while the total settlement in the former is only 50% of that in the latter.

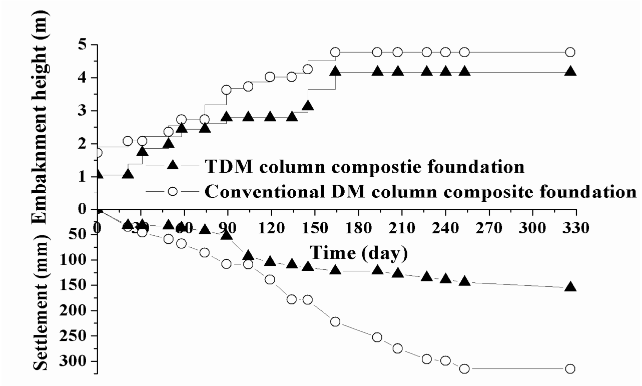

FIG. 6. Variation of ground settlement during embankment filling

The lateral displacement of the soil at the embankment toe was measured by an inclinometer (shown in FIG. 5). The measured results are shown in FIG. 7 (one of the inclinometer tubes was destroyed 3 months after installed). It was found that the embankment heights were similar in two sections, but the maximal lateral displacement in TDM column composite foundation is 20.84 mm while in conventional DM column composite foundation is 55.57 mm.

CONCLUSION

The filed tests indicate that when the embankment heights were almost the same, the ground surface settlement and maximal lateral displacement in TDM composite foundation are much less than in conventional DM column composite foundation while cost less cement. This means that the T-shaped deep mixing method makes the deep mixing much more reliable and economical than conventional deep mixing method.

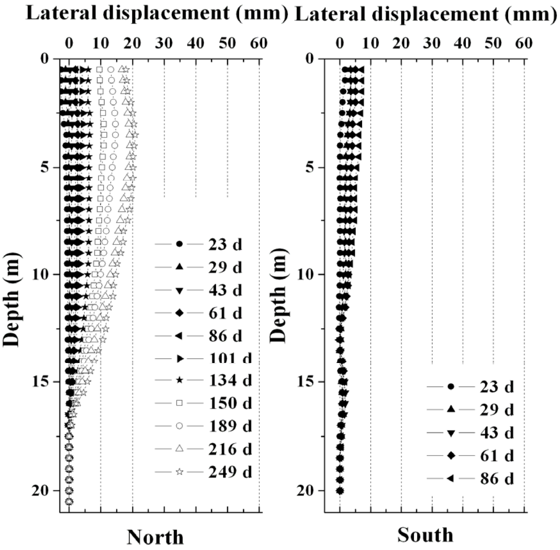

(a) TDM column composite foundation

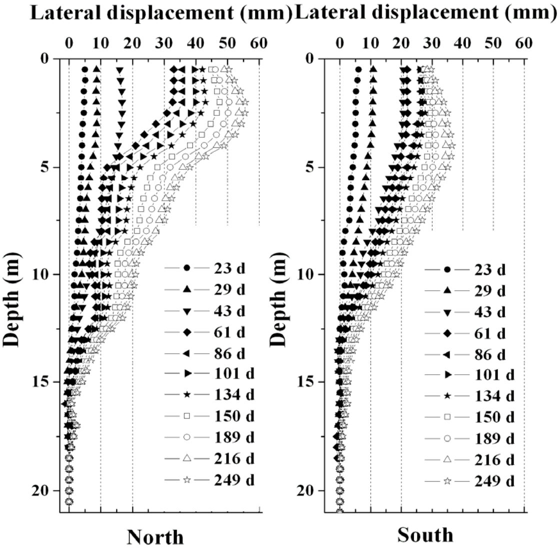

(b) Conventional DM column composite foundation

FIG. 7. Variation of lateral displacement during embankment filling

ACKNOWLEDGMENTS

The authors are very grateful to Mr. Peisheng, Xi, Mr. Bafang, Zhang and Mr. Zhihua, Zhu in the research group. This work is supported by National Natural Science Foundation of China (Grant No. 50879011) and Scientific Research Innovation Program for Graduate Students in Jiangsu Province (Grant No. CX08B_101Z).

REFERENCES

Bergado, D.T., Noppadol, P. and Lorenzo, G.A. (2005). “Bearing and Compression Mechanism of DMM Pile Supporting Rein-forced Bridge Approach Embankment on Soft and Subsiding Ground”. *16th International Conference on Soil Mechanics and Geotechnical Engineering*, Osaka, Japan: 1149-1153.

Chai, J.C., Liu, S.Y. and Du, Y.J. (2002). “Field Properties and Settlement Calculation of Soil Cement Improved Soft Ground-A Case Study”. *Lowland Technology International*, Vol.4(2): 51-58.

Chai, J. C., Miura, N. and Koga, H. (2005). Lateral displacement of ground caused by soil–cement column installation. *Journal of Geotechnical and Geoenvironmental Engineering*. Vol.131(5): 623-632.

Han, J., Zhou, H. T. and Ye, F. (2002). State of practice review of deep soil mixing techniques in China. *Journal of the Transportation Research Board.* No.1808:49-57.

Liu, S.Y. and Hryciw, R.D. (2003). “Evaluation and Quality Control of Dry-Jet-Mixed Clay Soil-Cement Columns by Standard Penetration Test”. *Journal of The Transportation Research Board*, No.1849: 47-52.

Liu, S. Y., Gong N. H., Feng, J. L. and Xi, P. S. (2007). Installation method of T-shaped soil-cement deep mixing column. *Chinese Patent*: ZL 2004 10065862.9. (in Chinese)

Liu, S.Y., Yi, Y. L. and Zhu, Z. D. (2008). Comparison tests on field bidirectional deep mixing column for soft ground improvement in expressway. *Chinese Journal of Rock Mechanics and Engineering*. Vol.27(11): 2272-2280. (in Chinese)

Shen, S. L., Miura, N., and Koga, H. (2003). Interaction mechanism between deep mixing column and surrounding clay during installation. *Canadian Geotechnical Journal*. Vol.40(2): 293-307.

Shen, S. L., Han, J. and Du, Y. J. (2008). Deep mixing induced property changes in surrounding sensitive marine clays. *Journal of Geotechnical and Geoenvironmental Engineering*. Vol.134(6):845-854.

Yi, Y. L. and Liu, S. Y. (2008). Bearing Behavior of single T-shaped cement-soil deep mixing column. *International Symposium on Lowland Technology 2008*. Busan, Korea: 261-265.

Effects of Core on Dynamic Responses of Earth Dam

Pei-Hsun Tsai[1], Sung-Chi Hsu[2], and Jiunnren Lai[3]

[1]Assistant Professor, Department of Construction Engineering, Chaoyang University of Technology, 168 Jifong E. Rd., Wufong Township Taichung County, 41349, Taiwan; phtsai@cyut.edu.tw
[2] Professor, Department of Construction Engineering, Chaoyang University of Technology, 168 Jifong E. Rd., Wufong Township Taichung County, 41349, Taiwan; schsu@cyut.edu.tw
[3]Assistant Professor, Department of Construction Engineering, Chaoyang University of Technology, 168 Jifong E. Rd., Wufong Township Taichung County, 41349, Taiwan; jrlai@cyut.edu.tw

ABSTRACT: This paper investigates the dynamic response of the Pao-Shan II Dam subjected to the Chi-Chi earthquake (M_L=7.3) in Taiwan by using FLAC^{3D}. The elastic modulus of the dam is considered to vary with mean stress in this study. Staged construction, seepage, static equilibrium and dynamic response are sequentially analyzed. Fourier power spectra are analyzed as the earth dams subjected to a sweep frequency dynamic loading. Influences of core dimensions on the dynamic responses of the earth dam are investigated. The influence of the core width-height ratio and length-height ratio of the dam on the first natural frequency is studied in this study. The results show that 3D effect could be neglected for $\imath > 4$ cases. The first natural frequency decreases with the increase of core width-height ratio or length-height ratio of an earth dam. The first natural frequency increases slightly after the seepage phase. The stiffness of the dam decreases at the end of an earthquake which causes the first natural frequency to decrease.

INTRODUCTION

The Pao-Shan II Dam, located in Hsinchu, Taiwan, is a roller compacted earth dam with 61 m high and 360 m long. The stage construction of the dam was simulated numerically using a three dimensional finite difference program, FLAC^{3D}. The dam materials were added up sequentially to the top of the dam by 10 different layers. Seepage analysis was performed considering a 56 m water level. The initial effective stress of the dam was obtained after the seepage analysis and static equilibrium has reached before applying acceleration caused by the earthquake. Since the Pao-Shan II Dam did not undergo any strong earthquake, the acceleration time history during the Chi-Chi earthquake is used as an input to the base of the dam for the dynamic analyses in order to estimate its dynamic response under strong earthquake. The numerical results of displacement time history were computed at the dam. In order to estimate the first natural frequency of vibration for the earth dam, 5 length-height ratios and 4 core width-height ratios are assumed, and a proposed procedure to find natural frequency is performed in this study. Moreover, they were estimated in construction, full water level, and the Chi-Chi earthquake phases in order to find out the variation of natural frequency on these phases.

NUMERICAL MODEL FOR THE STUDY

Earth Dam Configuration

A typical configuration and finite difference mesh for the dam was generated and discretized by FLAC^{3D}, as shown in Fig. 1. The dam with height H, length L and core width W is assumed to be situated above a hard rock formation. Therefore, the base of the dam is assumed to be impermeable and fixed, i.e. the deformability is constrained and sliding will be prevented at the base. In addition, the crests are placed at both sides of the core and the filter is presented between the core and below the downstream crest. The Pao-Shan II Dam with length L=360 m, height H=61 m, width of 352 m, and core width W=55 m was assumed for dynamic analysis. Since there are mountains located at both sides of the dam, the side boundaries are assumed to be fixed and impermeable at the both ends of the dam in z direction. Length of the dam is normalized with respect to height, thus, a length-height ratio $\eta$is used to estimate the 3D effect on dynamic response. In the same way, a core width-height ratio λ, i.e. core width W divides by dam height H, is used to estimate the influence of core width on natural frequency of an earth dam. In order to estimate the impacts of dimensions on natural frequency of an earth dam, a fixed dam width of 352 m and height of 61 m are used, five different length-height ratios (η=2, 3, 4, 5 and 6) and four core width-height ratios (λ=0.4, 0.6, 0.9 and 1.2) are used for analyses.

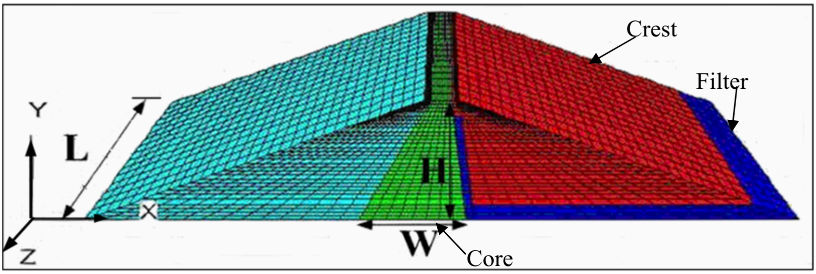

FIG. 1. A typical finite difference mesh of an earth dam by FLAC

Material Characteristics of the Earth Dam

For the numerical analysis, the crest and core of the earth dam are assumed to be satisfied to the Mohr-Coulomb model. The material properties of the dam were divided into the crest, core and filter. Material properties of the dam are estimated from the field and laboratory testing results during construction. The engineering properties for the simulation are listed in Table 1. Because the dam is huge, the stiffness could be different in any location. Therefore, the soil modulus will be considered to vary with the mean stress as

$$E = KP_a\left(\frac{p}{P_a}\right)^n \tag{1}$$

where K is the modulus constant, n is the modulus exponent and P_a is the atmospheric pressure. The material parameters, K and n, for the core and crest were found by using regression method with the triaxial compression test results by Central Region Water Resources Office in Taiwan. The parameters K= 592 and n=0.3 for the crest are used, while K= 888 and n=0.1 for the core. A FISH program is coded and used by FLAC^{3D} in order to perform the function of Eq. 1.

Table 1. The material parameters of the earth dam (Central Region Water Resources Office, 2006)

Zone	Density ρ (kg/m^3)	Young's Modulus E (MPa)	Poisson ratio ν	Cohesion c' (kPa)	Friction angle ϕ (°)	Permeability, K_h, (m/ sec)
Crest	2090	46	0.355	19	33.8	2.2×10^{-7}
Core	2120	15.5	0.36	-	31.3	8.5×10^{-8}
Filter	2110	31	0.412	-	36	3.2×10^{-4}

Procedures of the Simulation

The dam is formed by simulation of stage construction using 10 layers. The purpose of the construction simulation is to obtain a reasonable stress state for the dam during the construction phase before applying retaining water behind the dam. Thus, when a layer is added, a new static equilibrium for the dam is carried out. The steady state seepage calculation is performed after completion of the dam construction without interaction with mechanical equilibrium. Uncoupled with mechanical analysis, steady state seepage of the dam for a 56 m water level is then performed. The final state of static equilibrium, called initial stress state, of the dam was then computed again after the steady state seepage has reached. By using the same grid and the obtained initial stresses, the acceleration time history recorded during the Chi-Chi earthquake is applied to the base of the dam. The acceleration time histories are filtered under 5 Hz to reduce the chance of numerical instability before applying to the base. In addition, baseline corrections for the acceleration time histories are also made for zero velocity and displacement after integration.

In order to find the natural frequency of a dam, a harmonic acceleration with multiple frequencies is inputted to the base of the dam. From Fourier spectrum analysis, the natural frequency of a dam can be obtained as its response is amplified, i.e., resonant occurs. If the source is a harmonic loading with multiple exciting frequencies, it should be possessed the same amplitude in all forced vibration frequencies, that is the same energy in all exciting frequencies is fair subjected. Therefore, it could be rational as the vibration source with the same acceleration amplitude in all exciting frequencies. Because the first natural frequency is smaller than 10 Hz from the past research, the harmonic exciting frequency will be varied from 0.01 Hz to 10 Hz for the natural frequency analysis. The exciting acceleration of multiple frequencies can be expressed as the following:

$$a(t) = \sum_{i=1}^{1000} 10^{-6} \sin\left(\frac{i\pi t}{50}\right) \tag{2}$$

in which t is time, and the acceleration amplitude is limited to a small value of 10^{-6} to assure it is in elastic range. It is found that the stress field inside a dam and the following analyses are not influenced according to the acceleration level. A FISH program is also coded in FLAC in order to apply a multiple frequencies (0.01~10 Hz) harmonic acceleration to the base of the dam.

RESULTS OF THE NUMERICAL ANALYSIS

Dynamic Responses of the Pao-Shan II Dam

The calculated stress of σ_{xx} and σ_{yy} from the numerical analysis after the Chi-Chi earthquake are shown in Fig. 2, respectively. The computed maximum stress σ_{xx} and σ_{yy} occur at the center of the dam base.

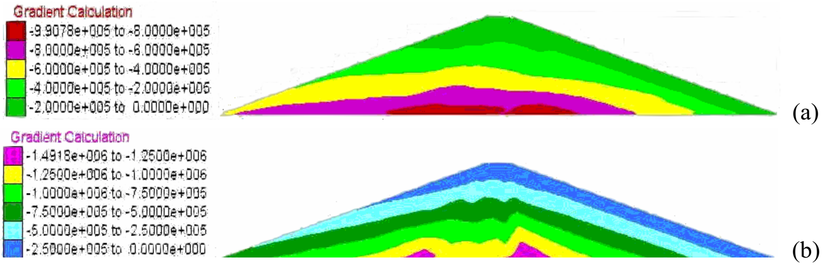

FIG. 2. Stress contours from the dynamic analysis : (a) σ_{xx}, and (b) σ_{yy}

Parametric Analysis on Natural Frequency

Influence of Length-Height Ratio of a Dam on the Natural Frequency

In order to study the influence of length-height ratio, length in z or axial direction divided by dam height, on natural frequency of an earth dam, the width-height ratio of the core will be fixed at λ=0.9. The impacts of length-height ratios of 2, 3, 4, 5 and 6 on the first natural frequency are studied, and the results can be observed from Fig.

3. As can be seen in Fig. 3, the first natural frequency of an earth dam decreases with increasing length-height ratio. The increase of the axial length of a dam may cause the dam to behave more flexible and to have lower natural frequency. The length-height ratio has less influence on natural frequency as $\eta > 4$. The first natural frequency is about 2.5 Hz as $\eta > 4$. For $\eta > 4$ cases, the result from 3D analysis is the same as that from plane strain case. Thus, the 3D effect could be neglected for $\eta > 4$ cases.

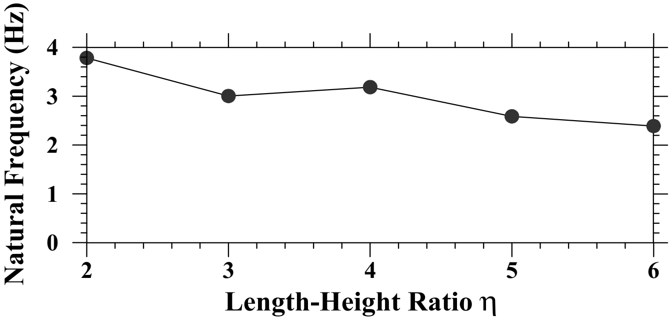

FIG. 3. The first natural frequency verse length-height ratio

Influence of Core Width-Height Ratio on Natural Frequency

To study the influence of core dimensions on the natural frequency of a dam, the length-height ratio, η is assumed to be fixed at 6, and core width-height ratio, λ is equal to 0.4, 0.6, 0.9 and 1.2. It can be seen from Fig. 4 that the natural frequency decreases with the increase of core width-height ratio. Since the core of a dam is made of soft materials like clay, a dam will become more flexible as the core width-height ratio increases. Thus, the first natural frequency decreases as the core width-height ratio increases. The results also indicate that the first natural frequency is close to 2.5 Hz for $\lambda > 0.9$ cases.

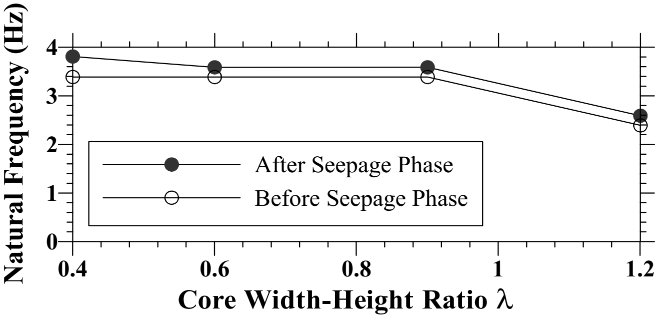

FIG. 4. The first natural frequency verse core width-height ratio

Influence of Phases on Natural Frequency

In order to study the influence of each phase, i.e. construction, seepage, and Chi-Chi earthquake phases, on natural frequency of a dam, the dimension of the earth dam will be fixed at η=6 and λ=0.4, the same dimension as the Pao-Shan II dam. In addition, a predominant frequency during the Chi-Chi earthquake is also estimated. The predominant frequency is 0.83 Hz in the Chi-Chi earthquake. The numerical results showed that the first natural frequency after stage construction, after seepage and after earthquake is 3.38 Hz, 3.58 Hz and 1.59 Hz, respectively. The first natural frequency of a dam increases after the seepage phase. The reason could be the water weight is placed on the upstream surface of the dam and to result in increasing stresses in the dam. The dam may then become stiffer, and the natural frequency is larger. However, for the phase during earthquake condition, the pore water pressure increases and effective stress decreases due to earthquake load. The stiffness of the dam decreases at the end of the earthquake. Therefore, the first natural frequency decreases at the end of the earthquake.

CONCLUSIONS

Based on the numerical analyses presented in this paper, the following conclusions may be made:

1. The 3D effect could be neglected for $\eta > 4$ cases. The first natural frequency is close to 2.5 Hz as $\eta > 4$.
2. The first natural frequency decreases with the increase of the core width-height ratio or length-height ratio of an earth dam.
3. The first natural frequency increases slightly after the seepage phase.
4. The first natural frequency decreases at the end of an earthquake due to the decrease of stiffness of the dam.

ACKNOWLEDGEMENTS

The authors are thankful to the “Sinotech Engineering Consultants, Inc.” for providing FLAC^{3D} software and helpful discussions.

REFERENCES

Chugh, A.K. (2007). ”Natural vibration characteristics of gravity structures,” *International Journal for Numerical and Analytical Methods in Geomechanics*, Vol. 31: 607-648.

Itasca Consulting Group, Inc. (2002). *FLAC^{3D}– Fast Lagrangian Analysis of Continua in 3 Dimensions,* Minneapolis, Itasca.

Central Region Water Resources Office. (2006). *Report on Experiment of filled material and safety evaluating of Pao-Shan II Dam* (in Chinese), Taichung, Taiwan, Central Region Water Resources Office.

Influence of Cement Kiln Dust on Strength and Stiffness Behavior of Subgrade Clays

Pranshoo Solanki[1] and Musharraf Zaman[2]

[1]Doctoral Candidate, School of Civil Engineering and Environmental Science, University of Oklahoma, 202 W. Boyd Street, Room 334, Norman, Oklahoma 73019, pranshoo@ou.edu
[2]David Ross Boyd Professor and Aaron Alexander Professor, Associate Dean for Research and Graduate Education, College of Engineering, University of Oklahoma, zaman@ou.edu

ABSTRACT: A comparative laboratory study was conducted to evaluate the suitability of different percentages of cement kiln dust (CKD) for stabilizing three different types of subgrade clays. Cylindrical specimens were compacted and cured for 28 days in a moist room having a constant temperature and controlled humidity. After curing specimens were tested for unconfined compressive strength (UCS), modulus of elasticity (M_E) and resilient modulus (M_r). These properties were compared with those of the raw clay specimens to determine the extent of enhancement. The study revealed that the addition of CKD substantially increased the UCS, M_E and M_r values of the clay specimens. In addition, these improvements increased with the increase in the amount of CKD. The extent of improvement, however, was found to be dependent upon the characteristics of the clay such as plasticity index (PI) and silica/sesquioxide ratio (SSR).

INTRODUCTION

A subgrade layer plays a vital role in a pavement structure. It provides a stable platform for layers above it. According to the new AASHTO 2002 mechanistic-empirical pavement design guide (MEPDG, AASHTO 2004), proper treatment and preparation of subgrade soil is extremely important for a long-lasting pavement structure. In order to prevent pavement damage, cementitious stabilization using different additives is widely used. Among the additives used for cementitious stabilization, lime is frequently used to treat clays since it chemically alters the plasticity-related soil properties. Although lime stabilization is quite effective, it is often limited by moderate strength and stiffness enhancements. On the other hand, because of the existence of major Portland cement manufacturing facilities in Oklahoma and movement toward industrial waste utilization, interest recently has turned to the potential of using cement kiln dust (CKD) in pavement construction projects (Miller and Zaman 2000).

In order to utilize CKD-stabilized clay as structural pavement component (stabilized subgrade), it is necessary to predict the pertinent properties affecting pavement performance with reliability. The new MEPDG recommends the evaluation of new material properties for critical performance prediction of stabilized subgrade layer (AASHTO 2004). These properties includes: unconfined compressive strength (UCS), elastic modulus ($M_{E,}$) and resilient modulus (M_r).

Consequently, this study was undertaken with the objective of exploring cement kiln dust (CKD) for stabilizing three subgrade clays commonly encountered in Oklahoma. Three different percentages of CKD, namely 5%, 10% and 15%, are used. The performance of 28-day cured stabilized clay samples was evaluated by conducting M_r, M_E, and UCS tests, consistent with the new MEPDG.

BACKGROUND

Cement kiln dust (CKD) is a fine material given off and carried out by the flow of hot gas within a cement kiln, generated during the cement making process. Due to its lime content and cementitious properties, CKD can be used for cementitious stabilization of subgrade soils.

The findings of previous researches in this area have shown that stabilizing soil with CKD can improve its properties. In a related study, Baghdadi (1990) determined the UCS of kaolinite clay stabilized with 16% CKD and compacted at near optimum moisture content (OMC) and maximum dry density (MDD). Results showed that the average 28-day UCS values increased to 1,115 kPa as compared to 210 kPa of raw soil specimens. Although relevant to the present study, Baghdadi (1990) study did not make any attempt to evaluate the M_E and M_r.

In another laboratory study, Miller and Azad (2000) studied engineering properties of three different soils (CH, CL, and ML) stabilized using CKD. These engineering properties included pH, UCS and Atterberg limits. Increases in UCS were found to be inversely proportional to the plasticity index (PI) of the raw soil. Significant PI reductions occurred with CKD stabilization, particularly for high PI soils. However, no attempt was made to evaluate the M_r, an important pavement design parameter (AASHTO 2004).

In a recent study, Peethamparan and Olek (2008) studied the feasibility of four different CKDs for stabilizing Na-montmorillonite clay. The improvement in engineering properties was evaluated by conducting UCS, Atterberg limits and moisture resistance test. The extent of the stabilized clay characteristics was found to be a function of the chemical composition of the particular CKD. But, this study was limited to only one type of soil and no attempt was made to compare results with other soils.

MATERIALS AND TEST PROCEDURE

In this study, three subgrade clays: (1) Port (P-soil), (2) Kingfisher (K-soil), and (3) Carnasaw (C-soil) were used. P-soil, K-soil and C-soil are CL-ML, CL and CH clays, respectively, in accordance with the Unified Soil Classification System (USCS). The P-soil is silty clay having an average liquid limit (LL) of approximately 25 and a plasticity index (PI) of approximately 5. The K-soil is a lean clay with a LL and PI of 39 and 21, respectively. On the other hand, C-soil is a fat clay with a high LL and PI of 58 and 29, respectively. The chemical properties of soil determined using X-ray Fluorescence analysis are given in Table 1.

As noted previously, CKD is used as the only stabilizing agent supplied by Lafarge North America located in Tulsa, Oklahoma. The physical and chemical properties of CKD were provided by the supplier and are presented in Table 1. Many properties of soil and stabilizing agents are related to the silica/sesquioxide ratio (SSR) (Fang 1997), as shown in Table 1.

Table 1. Chemical properties of soils and stabilizing agents used in this study

Chemical Compound	Percentage by weight, (%)			
	P-soil	K-soil	C-soil	CKD[d]
Silica (SiO_2)[a]	73.7	60.7	47.5	14.1
Alumina (Al_2O_3)[a]	7.0	11.9	16.1	3.1
Ferric oxide (Fe_2O_3)[a]	2.2	4.4	6.8	1.4
Silica/Sesquioxide ratio (SSR) $SiO_2/(Al_2O_3+Fe_2O_3)$	14.9	7.0	3.9	6.0
Calcium oxide (CaO)[a]	2.9	3.3	0.1	47.0
Magnesium oxide (MgO)[a]	1.8	3.2	0.9	1.7
Free lime[a]	…	…	…	8.5
Loss on Ignition[b]	5.1	7.8	25.1	25.8
Percentage passing No. 325[c]	54.0	88.8	87.2	94.2
pH[c]	8.91	8.82	4.17	12.44
28-day UCS[c] (MPa)	0.22	0.19	0.21	3.2

[a]X-ray Fluorescence analysis; [c]Determined independently
[b]ASTM C 575; [d]CKD: Cement Kiln Dust

Specimen Preparation and Tests

A total of 36 specimens were prepared. The mixture for each specimen consists of raw soils blended with a specific amount of CKD namely, 5%, 10%, or 15%. After the blending process, a desired amount of water was added based on the OMC as determined in accordance with the ASTM D 698-91 test method. Then, the mixture was compacted in a mold having a diameter of 101.6 mm (4.0 in) and a height of 203.2 mm (8.0 in) to reach a dry density of approximately between 95%-100% of the MDD. After 28 days of curing, specimens were tested for Modulus of Elasticity (M_E) and unconfined compression (UCS) in accordance with the ASTM D 1633 test method. The M_r tests were performed in accordance with the AASHTO T 307-99 test method. The detailed procedure has been discussed in Solanki et al. (2007).

PRESENTATION AND DISCUSSION OF RESULTS

Moisture-Density Relationship

The moisture-density test results (i.e., OMCs and MDDs) are presented in Table 2. In the present study, laboratory experiments showed an increase in OMC with increased percentage of CKD. On the other hand, a decrease in the MDDs with increasing percent of CKD is observed from Table 2. For example, the MDD of K-soil mixed with 15% CKD is 16.9 kN/m^3 compared to 17.4 kN/m^3 for raw K-soil.

Other researchers (e.g., Zaman et al. 1992; Miller and Azad 2000; Sreekrishnavilasam et al. 2007) also observed effects similar to those in the current study.

Table 2. Summary of OMC-MDD of CKD-soil mixtures

Percent of CKD / Type of Clay	OMC (%)				MDD (kN/m^3)			
	0%	5%	10%	15%	0%	5%	10%	15%
P-soil	13.1	14.8	15.2	15.3	17.8	17.4	17.2	17.1
K-soil	16.5	16.9	17.3	17.6	17.4	17.3	17.1	16.9
C-soil	20.3	21.6	21.7	21.9	16.3	16.1	16.0	15.9

Unconfined Compressive Strength

The variation of UCS values with the CKD content is illustrated in Figure 1. It is clear that UCS values of all the soils used in this study increase as the amount of CKD increases. For example, the UCS values increased by 6.2-, 6.1- and 2.6-folds for the P-, K-, and C-soil specimens, respectively, when stabilized with 15% CKD. This observation is consistent with that of Miller and Azad (2000), Sreekrishnavilasam et al. (2007), and Peethamparan and Olek (2008).

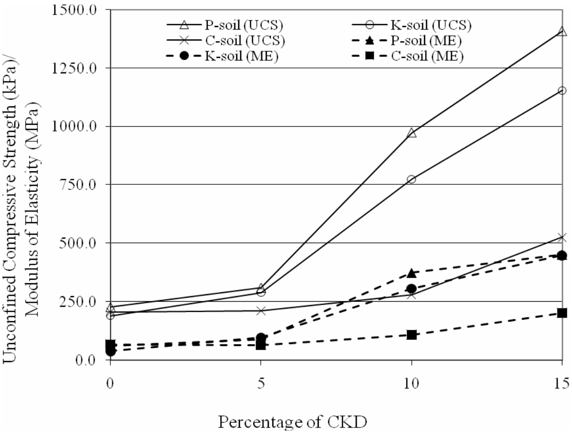

FIG. 1. Variation of unconfined compressive strength and modulus of elasticity with percent of CKD for different soil types.

A comparison of the behavior of three clays from Figure 1 shows that improvement in strength due to CKD stabilization is more enhanced for P-soil (PI = 5) than for the K-soil (PI =29) and C-soil (PI = 21). Similar observations were reported by other researchers, such as Miller and Azad (2000). It is believed that the differences in the UCS values of three stabilized subgrade clays are attributed to the differences in physical and chemical properties of the clays (Table 2) and various pozzolanic reactions. The pozzolanic reactivity of a soil-CKD mix depends on the amount of silica, alumina and ferric oxide available in the mix, which can be contributed by both soil and CKD (Bhatty and Todres 1996; Parsons et al. 2004; Khoury 2005). In this study, the highest UCS values of CKD-stabilized P-soil specimens can be attributed to the P-soil characteristics such as high SSR ratio (as shown in Table 1).

Modulus of Elasticity

It is evident that there is significant increase in the modulus of elasticity (M_E) with increasing amount of CKD content in the stabilized clays. As depicted from Figure 1, in P-soil specimens the maximum increase (about 638%) in M_E values was observed by adding 15% CKD. Similarly, 15% CKD-stabilized K- and C-soil specimens exhibited the maximum increase of approximately 1061% and 196%, respectively, compared to the raw soil. This trend in M_E values for different CKD-stabilized clays is similar to that observed for UCS values.

Stress-Strain Behavior

The stress-strain behaviors of the three raw clays and 10% CKD-stabilized specimens are presented in Figure 2. Generally, the addition of CKD increased the peak stress and reduced the peak strain considerably. Brittle failure was exhibited by the stabilized soil specimens at axial strains of approximately 0.5 – 1%, whereas raw soil specimens exhibited plastic behavior. This is consistent with the observations reported by Miller and Azad (2000) and Peethamparan and Olek (2008).

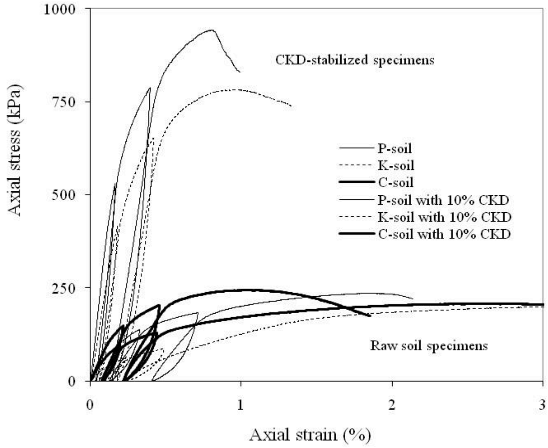

FIG. 2. Stress-strain response of different raw soil and 10% CKD-stabilized specimens.

Resilient Modulus

Figure 3, 4, 5 and 6 show typical results of (M_r) test on different soil samples stabilized with 0%, 5%, 10% and 15% CKD, respectively. It is clear that M_r values for each of the three raw clay specimens showed substantial improvements with increased confining stress as compared to CKD-stabilized specimens. For example, at a confining pressure (S_3) of 13.8 kPa and 41.4 kPa (deviatoric stress, S_d = 37 kPa), the average M_r values of raw P-soil specimens are approximately 105 MPa and 137 MPa (approximately 30% increase), respectively. On the other hand, for the same stress levels, the M_r values of 10% CKD-stabilized P-soil specimens increase by approximately 9%.

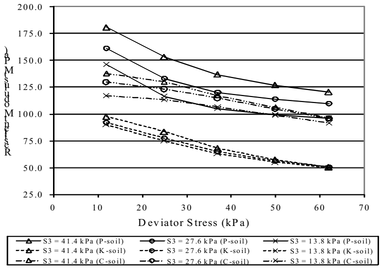

FIG. 3. Resilient modulus test result for specimens stabilized with 0% CKD.

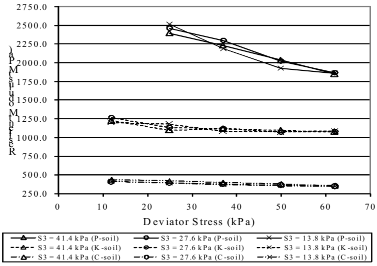

FIG. 4. Resilient modulus test result for specimens stabilized with 5% CKD.

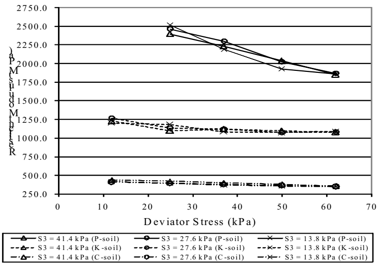

FIG. 5. Resilient modulus test result for specimens stabilized with 10% CKD.

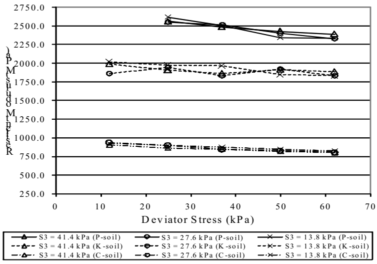

FIG. 6. Resilient modulus test result for specimens stabilized with 15% CKD.

As shown in Figures 3 to 6, the laboratory tests produce a set of curves that relate M_r to deviator stress and confining pressure. However, pavement design according to the AASHTO 2002 design guide requires a single input for the M_r. This is determined by calculating the in-situ stress using the computer program KENLAYER (Huang 1993), which is based on the multi-layer elastic model. The design load used in the computation is the allowable 80 kN (18 kips) Equivalent Single Axle Load (ESAL). For a 800 mm pavement section with 203 mm thick stabilized subgrade layer, the analysis results show that the S_d would be about 21 – 40 kPa. The S_3 at the top of the stabilized subgrade layer due to load are small compared with the stresses due to overburden (11 kPa) and can be neglected. These in-situ stresses are directly used in a semi-log model (Solanki et al. 2008) between M_r versus deviator and confining stresses to establish the design M_r.

$$M_r = k_1 \times k_2^{S_d} \times k_3^{S_3}$$

where, k_1, k_2 and k_3 are the regression constants, as shown in Table 3. It was noted from Table 3 that the design M_r values increased with the increased percentage of CKD. It is also clear that CKD stabilization produces maximum enhancement in M_r values of P-soil as compared to K-soil and C-soil. For example, 10% CKD increased the mean design M_r values of P-, K- and C-soils by 20-, 17- and 3.5-folds, respectively. Similar reasons, as mentioned in preceding section, can be used to rationalize this behavior.

Table 3. Summary of the regression constants of different raw and stabilized soil specimens

Type of soil	% of CKD	$M_r = k_1 x (k_2)^{S_d} x(k_3)^{S_3}$			R^2	Design M_r (MPa)
		k_1	k_2	k_3		
P-soil	0	133,520	0.991	1.009	0.941	112
	5	745,564	0.986	1.004	0.936	507
	10	2,807,022	0.993	1.000	0.936	2,266
	15	2,680,406	0.997	1.000	0.898	2,446
K-soil	0	102,468	0.986	1.002	0.990	68
	5	351,791	0.995	1.002	0.978	309
	10	1,242,050	0.997	1.000	0.728	1,133
	15	1,996,855	0.999	1.000	0.689	1,937
C-soil	0	127,709	0.993	1.004	0.960	108
	5	232,970	0.991	1.004	0.990	185
	10	415,595	0.996	1.002	0.975	376
	15	984,832	0.997	0.999	0.967	889

CONCLUDING REMARKS

The effect of different percentages of CKD on the strength and stiffness properties of three soils, namely, P-, K- and C-soil were examined. An increase in OMC and a decrease in MDD were observed with increasing amounts of CKD. Large increases in UCS, M_E, and M_r values were observed for the soil by CKD stabilization. The enhancements of these properties were more noticeable, in general, with the increase in the percentage of CKD. In addition, the improvement is more significant for soils with low PI and high silica/sesquioxide ratio. The CKD-stabilized soil exhibited brittle behavior with the addition of CKD due to decrease in the strain at failure.

ACKNOWLEDGMENTS

The authors are thankful to the Oklahoma Department of Transportation (ODOT) for providing funds for this project.

REFERENCES

AASHTO (2004). "Guide for Mechanistic-Empirical Design of new and rehabilitated pavement structures." *Final Report prepared for National Cooperative Highway Research Program (NCHRP),* Transportation Research Board, National Research Council, Washington D.C., http://www.trb.org/mepdg/guide.htm.

Baghdadi, Z.A. (1990). "Utilization of kiln dust in clay stabilization." *J. King Abdulaziz Univ.: Eng Sci*, 2, 53 – 163.

Bhatty, J.I., Todres, H.A. (1996). "Use of Cement Kiln Dust in Stabilizing Clay Soils.*" Portland Cement Association*, Skokie, Illinois.

Fang H. Y. (1997). *Introduction to Environmental Geotechnology,* CRC Press, New York.

Huang, Y. H. (1993). *Pavement Analysis and Design*, Prentice Hall, Englewood, New Jersey.

Khoury, N. N. (2005). "*Durability of Cementitiously Stabilized Aggregate Bases for Pavement Application.*" Ph.D. dissertation, University of Oklahoma, Norman, Oklahoma.

Miller, G.A. and Azad, S. (2000). "Influence of soil type on stabilization with cement kiln dust." *Construction and Building Materials*, 14, 89 – 97.

Miller, G.A. and Zaman, M. (2000). "Field and laboratory evaluation of cement kiln dust as a soil stabilizer." *Transportation Research Record*, TRB, National Research Council, Washington, D.C., 1714, 25 – 32.

Parsons, R.L., Kneebone, E., and Milburn, J.P. (2004). "Use of cement kiln dust for subgrade stabilization." *Final Report No. KS-04-03*, Kansas Department of Transportation, Topeka, Kansas (USA).

Peethamparan, S. and Olek, J. (2008). "Study of the effectiveness of cement kiln dusts in stabilizing N-montmorillonite clays." *Journal of Materials in Civil Engineering*, 20(2), 137-146.

Solanki, P. Khoury, N. and Zaman, M. M. (2008). "Experimental analyses and statistical modeling of cementitiously stabilized subgrade soils." *Proceedings of Transportation Research Board 2008 Annual Meeting (CD-ROM)*, Transportation Research Board, Washington D. C.

Solanki, P., Khoury, N. and Zaman, M. M. (2007). "Engineering Behavior and Microstructure of Soil Stabilized with Cement Kiln Dust." *Geotechnical Special Publication*, 172, 1-10.

Sreekrishnavilasam, A., Rahardja, S., Kmetz, R. and Santagata, M. (2007). "Soil treatment using fresh and landfilled cement kiln dust." *Construction and Building Materials*, 21, 318-327.

Zaman M., Laguros J.G. and Sayah A.I. (1992). "Soil stabilization using cement kiln dust." *Proceeding of the 7th International Conference on Expansive Soils*, Dallas, TX, 1 -5.

Bayesian Inference of Empirical Coefficient in Foundation Settlement

Zhen-Yu Li[1], Yong-He Wang[2], and Guo-Lin Yang[3]

[1]Doctoral candidate, College of Civil Architectural Engineering, Central South University, Changsha, China; hdlizhenyu@163.com
[2]Professor, College of Civil Architectural Engineering, Central South University, Changsha, China; yhwang45@163.com
[3]Professor, College of Civil Architectural Engineering, Central South University, Changsha, China; yangguolin6301@163.com

ABSTRACT: Baysian theory, a new approach is proposed to determine the empirical coefficient in calculating soil settlement. The choice of prior distribution and the inference of posterior distribution are two important components of this method. According to previous knowledge available, the empirical coefficient determined by compression module in the interval [0.2-1.4], prior distribution is assessed uniform distribution in this interval. Posterior density function is developed in the condition of prior distribution combined with observed samples information based on bayes principle. Taking four locations in a passenger dedicated line for example, the results show that the posterior distribution of the empirical coefficient obeys Guass distribution parameter μ and σ. The value of μ is decreased gradually with the load on ground increased. In addition, the observed samples information has great influence on the posterior distribution, and the size of samples is larger, the results are more reliable.

INTRODUCTION

In recent years, many methods of settlement calculation have been developed all over the world including elastic theory method, numerical method and so on. Among them, summation layered method is one of important approximate approaches and is widely used in design and practical engineering with simple principle. Due to the complication and inhomogeneity of the soil material, it is necessary to take many assumptions as premise conditions in calculations. Consequentially, it always leads to a greater difference between theoretical deformation value and actual value. To solve this problem, the concept of modification coefficient is introduced into summation layered method. But the accuracy of this calculation method depends on how to correctly choose the value of settlement empirical coefficient. In Foundation ground and foundation design standard, the value depends on the load on ground and ground compression module, and the range of settlement empirical coefficient is from 0.2 to1.4. Code for Foundation of Port Engineering indicates that the settlement empirical coefficient is chosen by specific region experience. Elsoufiev considers it dimensionless coefficient usually to be 0.8 in German. However, uncertainties can be found during the process of determination of the coefficient due to many factors. Therefore, a lot of calculation methods have been proposed in previous literature considering some kinds of effect on determination of the coefficients. Wang et al.have proposed 1-D calculation of embankment settlement method considering the height of embankment and soil lateral deformation. Sun et al. have studied on how the stress history to influence on settlement empirical coefficient. Due to the complication and anisotropy of soil material, the parameters of soil samples from the same zone, even the same layer, are different each other, which has been demonstrated by many laboratories. So it is difficult to use only a certain empirical coefficient to modify calculate value. Nevertheless, it is feasible to use a certain distribution to describe it. The empirical coefficient expressed as a distribution is more reasonable than as a fixed value. In this aspect, Bayes' theory is an excellent vehicle.

BAYESIAN APPROACH TO PARAMETER ESTIMATION

Prior Distribution

From a Bayesian point of view, a prior density of variable θ has to be defined initially. Frequently, a prior density of variable θ is described as $\pi(\theta)$. Prior distributions are essentially the basis in Bayesian analysis. Different types of prior distributions exist, namely information and non-information. Non-information prior distributions are distributions that have no bias and play a minimal role in the posterior distribution. The idea behind the use of non-informative prior distributions to make inferences is not greatly affected by external information or when external information is not available. The uniform distribution is frequently used as a non-informative prior distribution.

On the other hand, informative priors have a stronger influence on the posterior distribution. The influence of the prior distribution on the posterior is related to the sample size of the data and the form of the prior. Generally speaking, large sample sizes are required to modify strongly priors, where weak priors are overwhelmed by even relatively small sample sizes. Informative priors are typically obtained from previous knowledge.

Posterior Distribution

The prior knowledge about the parameter θ is expressed as $\pi(\theta)$, called the prior distribution. The posterior distribution of θ given the sample data, using Bayes rule, provides the updated information about the parameters θ. This is expressed with the following posterior probability density function:

$$f(\theta|x) = \frac{p(x|\theta)\pi(\theta)}{\int_{\zeta} p(x|\theta)\pi(\theta)d\theta} \tag{1}$$

where

θ is a vector of the parameters of the chosen distribution

ζ is the range of θ

$p(x|\theta)$ is the joint density function based on the samples

$f(\theta|x)$ is the posterior distribution

$\pi(\theta)$ is the prior distribution

When the samples $x_1, x_2, \ldots x_n$, which size is n, have been determined, $x_1, x_2, \ldots x_n$ in $p(x_1, x_2, \ldots, x_n|\theta)$ are constant, only θ is changed. Hence $p(x|\theta)$ may be considered as a function called likelihood function, regarding θ as a parameter. It can be express as $l(\theta|x_1, x_2, \ldots, x_n)$. Therefore, the posterior probability density function also can be described as following:

$$f(\theta|x_1, x_2, \ldots, x_n) \propto \pi(\theta) \cdot l(\theta|x_1, x_2, \ldots, x_n) \tag{2}$$

For empirical coefficients from results of field tests and laboratory tests, we can determine the observed sample of empirical coefficients to obey a certain distribution according to histogram. This distribution denoted as $Q(\theta)$.

$$p(x_1, x_2, \ldots, x_n|\theta) \sim Q(\theta) \tag{3}$$

Therefore, the likelihood function $l(\theta|x_1, x_2, \ldots, x_n)$ can be expressed as following formula:

$$l(\theta|x_1, x_2, \ldots, x_n) = \prod_{i=1}^{n} Q(\theta_i) \tag{4}$$

From above, the posterior distribution also can be described as:

$$f(\theta|x_1, x_2, \ldots, x_n) = \pi(\theta) \cdot \prod_{i=1}^{n} Q(\theta_i) \tag{5}$$

EMPIRICAL COEFFICIENT ANALYZED BY BAYESIAN

Random Variable

At present, settlement calculation method proposed in Foundation ground and foundation design standard is widely used in China. It is a simplified total layered method introducing conception of average addition stress. The empirical coefficient ψ_s is defined in the code as the ratio of observed value S and calculation value S'. The formula of empirical coefficient is expressed as:

$$\psi_s = S / S' \tag{6}$$

Where S is settlement observed value;

S' is settlement calculation value.

Because soil material is complicate and anisotropy, the soil parameters are not fixed values in different locations. So the settlements of observation and calculation are changed with different geological conditions. Therefore, it is variation of the empirical coefficient ψ_s which can be taken as a random variable.

Bayesian Analysis

The prior distribution may be derived from a single source, or from a collection of available sources. In geo-engineering, it is deserved attention of experts' experience. Based on the achievements of engineers, the choice of the settlement empirical coefficients is depended on the soil compression module.The settlement empirical coefficient can not be a constant with compression module changed. According to Code for design of building foundation, the settlement empirical coefficient of clay is chosen from 0.2 to 1.4. Hence, uniform distribution is suggested for the prior distribution of empirical coefficient noted $\theta \sim U(a,b)$. The probability density is expressed as following:

$$\pi(\theta)=\begin{cases}\dfrac{1}{b-a}, & a<\theta<b \\ 0 & \text{otherwise}\end{cases} \tag{7}$$

So the available information before measuring is expressed in the form of the prior density $U(a,b)$, in which the values of a and b equal to 0.2 and 1.4 respectively. An updated probability density function for empirical coefficient ψ_s can be obtained by combining prior information with parameter distribution treated with a small observed sample at the considered location. The distribution of sample can be assumed according to the histogram shape of the observed data.

CASE STUDY

In this paper, a typical red clay soil was taken from a new high-speed express line for an example to investigate the distribution of settlement empirical coefficient with limited small samples. From above, the prior distribution of empirical coefficient ψ_s was known uniform distribution. The focus of this case lied on getting information from observed sample in this region to set up Bayesian framework.

The settlement observed values and data samples came from four different locations (1#, 2#, 3#, 4#). A lot of undisturbed soil samples had been gotten nearby these sites to do some experiments. Many red clay physics and mechanic indexes had been obtained from laboratory. The results were showed as table 1.

Table 1 Physical and mechanical indexes of red clay

Site	**Water content** w **(%)**	**density** ρ **(**g/cm^3**)**	**Void ratio** e	**Plastic limit** w_P **(%)**	**Liquid limit** w_L **(%)**	**Compression module** E_s **(**MPa^{-1}**)**
$1^{\#}$	28.0	1.83	0.947	27.3	50.4	14.45
$2^{\#}$	36.2	1.80	1.075	29.5	47.0	11.82
$3^{\#}$	24.9	1.95	0.751	28.6	48.8	8.18
$4^{\#}$	25.5	1.93	0.761	28.1	43.5	19.4

The settlement observed value and calculation value were list in table 2.

Table 2 The settlements of field observation and theoretical calculation

Load σ **(** KPa **)**	$1^{\#}$		$2^{\#}$		$3^{\#}$		$4^{\#}$	
	s' (mm)	s (mm)	s' (mm)	s (mm)	s' (mm)	s (mm)	s' (mm)	s (mm)
40	4.03	4.69	1.55	1.78	2.84	3.02	1.05	1.23
80	4.66	5.14	3.53	2.56	3.24	3.44	3.78	3.14
120	7.34	5.58	5.56	3.34	5.11	3.86	5.87	4.60
160	10.03	6.03	7.59	4.13	6.97	4.29	8.01	4.90
200	12.71	6.48	9.63	4.91	8.84	4.71	10.16	5.21
240	13.54	6.93	10.54	5.30	9.87	5.14	12.18	6.14

From above, prior distribution $\pi(\theta)$ of empirical coefficient was considered of a uniform distribution in the given rang according to previous knowledge. The prior probability was taken as given in the figure 1.

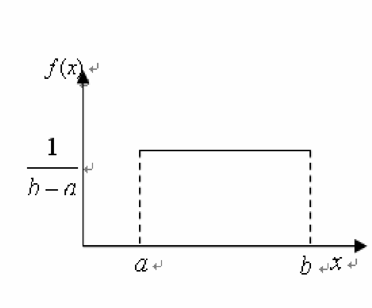

Fig. 1 Prior distribution of ψ_s

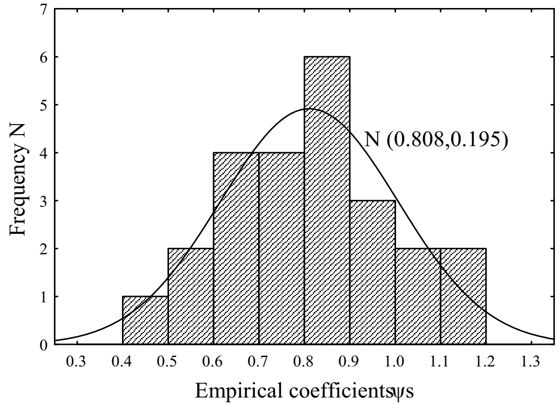

Fig. 2 Histogram of samples

The results indicated that the settlement empirical coefficients were changed with different loads on ground in table 2. Together with the settlement empirical coefficients of four locations analyzed, their histogram shapes can be gotten. It was found that the distribution of empirical coefficients obeyed Gaussian distribution (shown in figure 2). The probability density of it was expressed as following:

$$p\left(x|\theta\right)=\frac{1}{\sqrt{2\pi}}e^{-\frac{(x-\mu)}{2\sigma^2}}, \quad -\infty<x<\infty \tag{8}$$

According to Bayesian approach, the posterior distribution of empirical coefficient was obtained by combining the prior distribution with the update information. If Eq. (7) and Eq. (8) were inserted into Eq. (1), and if

$$m=\frac{\pi(\theta)}{\int_a^b p(x|\theta)\pi(\theta)d\theta} \tag{9}$$

Then

$$f\left(x\right)=m\cdot p\left(x|\theta\right)$$

(10)

Written $f\left(x\right)=\mathrm{Y}$ and $p\left(x|\theta\right)=\mathrm{X}$, then formula (12) was expressed as

$$\mathrm{Y} = m \cdot \mathrm{X}$$

(11)

Eventually, the probability density function of Y was obtained:

$$P_Y(y) = P_Y\left(f^{-1}(y)\right)\left|f^{-1}(y)'\right| = P_Y\left(f^{-1}(y)\right)\left|\frac{1}{m}\right|$$

$$= \frac{1}{\sqrt{2\pi}\sigma}\exp\left\{-\frac{(y/m-\mu)^2}{2\sigma^2}\right\}\left|\frac{1}{m}\right| = \frac{1}{\sqrt{2\pi}|m|\sigma}\exp\left\{-\frac{(y-m\mu)^2}{2m\sigma^2}\right\}$$

(12)

Denoted as $\mathrm{Y} \sim \mathrm{N}\left(m\mu, m^2\sigma^2\right)$

It can be seen from Eq. (12) that the posterior distribution was also a Gaussian distribution parameter $m\mu$ and $m^2\sigma^2$ .The posterior parameters of empirical coefficients analyzed under different loads in four locations were given as table 3.

Table 3 Posterior statistics of modification coefficients

	Load P **(** KPa **)**	μ	σ	$\mathrm{N}(\mu,\sigma^2)$
1	40	1.140	0.20	N1(1.140,0.040)
2	80	0.093	0.230	N2(0.093,0.057)
3	120	0.720	0.268	N3(0.720,0.072)
4	160	0.590	0.170	N4(0.590,0.029)
5	200	0.520	0.10	N5(0.520,0.010)
6	240	0.510	0.084	N6(0.510,0.007)

And the posterior distributions of the empirical coefficients were shown in figure 3.In figure 3(a), N_1,N_2,N_3 represented the posterior distribution of different loads 40 KPa , 80 KPa and 120 KPa , respectively. When loads on ground were 160 KPa , 200 KPa and 240 KPa , their poster distributions were N_4,N_5,N_6 in figure 3(b). Figure 4 showed that the posterior distributions under different loads were different each other, in spite of the same prior distribution. The results showed the empirical coefficients obeyed Gaussian distributions but not a certain value in traditional calculation method. With the loads on ground increased, the values μ of empirical coefficients were decreased gradually. However, there was no regularity of the values σ in analysis. The observed datum played very important role in posterior density function. Sometimes, the standard deviations can be reduced by larger observed sample size

CONCLUSION

The primary problem in term of applying Bayesian theory into geo-technology engineering is how to get the prior distribution and infer the posterior distribution. On the basis of pervious experience, the uniform distribution is assumed to be the prior in the interval $[a,b]$. The histogram of given samples shows that empirical coefficients observed sample obeys Gaussian distribution. According to Bayesian approach, the posterior is obtained also Gaussian distribution. Information of such an observed sample is used to estimate the mean value, variance of Gaussian distribution.

The results show that empirical coefficients are changed with loads on ground. With the loads on ground increased, the values μ of empirical coefficients are decreased gradually. But there is no regularity of the values σ in analysis. The posterior distributions are obtained by combining sample with prior information, which makes the sample information used in most extend. The sample information has a great effect on posterior distribution from the example analyzed. Furthermore, the size of sample is larger, the results are more reliable.

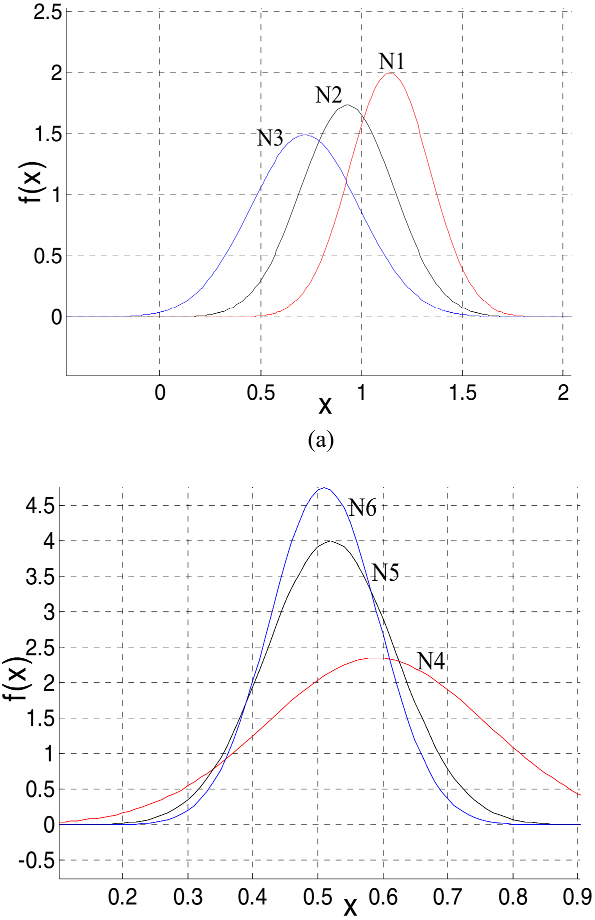

(a)

(b)

Fig. 3 Posterior distributions of empirical coefficients

.

ACKNOWLEDGEMENTS

The authors appreciate the support of the Natural Science Foundation of China(50808179).

REFERENCES

YOU Chang-Long, (2007). The Integration Concept on Observation and Evaluation of Ballastless Track . *Journal of railway engineering society*, 3 :25-29

TJSH [2005], Designed guide of Ballastless track for passenger dedicated railway. China Railway Press, Beijing

EM 11101-1-1902, Engineering and Design. Department of Army U.S.Army Corps of Engineers, Washington, DC

Hu Zhongxiong, (1997). Soil mechanic and Environment geotechnology. The Tongji University Publisher, Shanghai

GB 50007－2002, Code for design of building foundation. China Architecture and Building Press, Beijing

JTJ250-98, Code for soil foundations of port engineering. China Communications Press, Beijing

Serguey A.(2007). Strenth Analysis in Geomechanics. Springer Berlin Heidelberg, NewYork

WANG Zhi-liang,GAO Feng, YIN Zong-ze.(2005). Study on modified factors for 1-D calculation of embankment settlement considering soil lateral deformation. *Rock and Soil Mechanics*,26(5):763-769 (in Chinese)

WANG Zhi-liang, SUN Xi-jie.(2006). Discussion of settlement empirical considering stress history of soil mass. *Rock and Soil Mechanics*, 27(10): 1723-1726

Vojkan J., Matthew C., Brian S.(2006). Interpretation and modeling of deformation characteristics of a stiff North Sea clay. *Ganadian Geotechnical Journal*, 43: 341-354.

Berger J.(1985). Statistical decision theory and Bayesian analysis. Spring-Verlag, New York

Nicolas D., Mark R, Patrick B.(2007). Spatial analysis and modelling of land use distributions in Belgium. *Computers Environment and Urban Systems*, 31:188-205.

Ditlevsen O., Tarp-Johansen N.J, Denver H.(2000). Bayesian soil assessments combining prior with posterior censored samples. *Computers and Geotechnics*, 26: 187-198.

Harvey T.(2006). Introduction to Bayesian Statistics. Center for Computer Research in Music and Acoustics (CCRMA)Department of Music, Stanford University, California

A Andrew G.(2002). Prior distribution. Encyclopedia of Environmetrics, Chichester

Ka-Veng Y., Lambros S.K.(2001). Bayesian time-domain approach for modal updating using ambient data. *Probabilistic Enigeeing Mechanics*,16: 219-231.

YANG Yong, WEN Dan, LUO, An, (2006). Fuzzy sliding mode variable structure control based on multi-objective optimization and its application. *Journal of central south university*, 37(12)1149-1154

Rackwitz R.(2000). Reviewing probabilistic soils modeling. *Computers and Geotechnics*, 2:199-223.

MAO Shi-song, (1999). Bayes statistics. China Planning Press, Beijing

Elasto-plastic FEM Analyses of Large-Diameter Cylindrical Structure in Soft Ground Subjected to Wave Cyclic Loading

Qinglai Fan[1] and Maotian Luan[2]

[1]Lecturer, Ph.D., Key Laboratory of Geotechnical Engineering, Ludong University, Shandong, Yantai, 264025, People's Republic of China; PH (86-535)6656609; email: ldufanqinglai@163.com
[2]Professor, State Key Laboratory of Coastal and Offshore Engineering, Dalian University of Technology, Liaoning, Dalian, 116024, People's Republic of China; PH (86-411)84707609; email: mtluan@dlut.edu.cn

ABSTRACT: The large-diameter cylindrical structures have been increasingly applied recently in coastal and offshore engineering practice in China. This novel type of structure is composed of a steel or reinforced concrete cylindrical thin-wall shell which is embedded partially into the ground by special penetration procedure. The performance of such structures is obviously different from that of the traditional gravity-type foundations. Therefore, in this paper, the elasto-plastic finite element procedure based on effective stress method is developed for the cylindrical structure subjected to cyclic wave loading. To simulate the behavior of soft soil under cyclic loading, an improved dynamic Cam-clay constitutive model proposed by Carter et al (1982) is numerically implemented into the finite element package ABAQUS through implicit integration algorithm. In the analyses, the contact-pairs algorithm in ABAQUS is employed to simulate nonlinear interaction behavior of the contact between the structure and soil. By using the proposed numerical method, the failure mode of cylindrical structure is obtained and distribution of friction stress on the wall outside of cylindrical structure is evaluated.

INTRODUCTION

The large-diameter cylindrical structure is a novel type of coastal structure applicable for soft marine soil. This novel type of structure is composed of a steel or reinforced concrete cylindrical thin-wall shell which is embedded partially into the ground by special penetration procedure. In ocean environments, the cylindrical structure is subjected to wave-induced loading in addition to the self-weight. Although a certain efforts based on numerical analyses have been made to investigate the ultimate bearing capacity of cylindrical structure under monotonic loading, however, currently the attention is paid on the working mechanism of the type of structure in soft ground under cyclic loading. Wang et al. (2004) utilized discrete spring and dashpot system to simulate the reaction of the soft ground to the structure and the effect of cylinder diameter, embedment depth and soil property etc. on the dynamic response was investigated. A modified Hardin model was introduced by Liu and Wang (2002) in the equivalent linear method and the dynamic nonlinear analyses were conducted to investigate the mechanism of instability of cylindrical structure. Nonetheless, the effect of the permanent deformation and excess pore pressure accumulation on the response of such type of structure is not considered.

In the paper, an elasto-plastic effective stress FE model is proposed and in this model, the improved Cam-clay dynamic constitutive model proposed by Carter et al. (1982) is numerically implemented into the software ABAQUS through implicit integration algorithm. In addition, the interaction behavior between the soil and cylindrical structure is simulated rationally by contact pairs algorithm. According to the suggestion of Jeng et al. (2003), the dynamic effects for typical seabed problem can be neglected and the result of the quasi-static consolidation analysis is sufficient for engineering practice. Therefore the analysis model proposed in this paper is based on the simplified form of general Biot's consolidation theory neglecting inertia effect of soil skeleton and pore water.

INTEGRATION ALGORITHM FOR IMPROVED CAM-CLAY MODEL

An improved Cam-clay dynamic model was proposed by Carter et al. (1982) to take account of the behaviour of soft soil under cyclic loading. The initial yield surface formula is same as that of traditional modified Cam-clay model. In order to consider the effect of stress path under cyclic loading, a loading surface is assumed in the inner region of the initial yield surface. The model includes the following parameters: M, the slope of critical state line in p-q space; λ and κ the slope of the virgin compression line and isotropic recompression line in e-ln$p$ space respectively; v, Poisson's ratio; χ a model parameter considering OCR degradation of soil under cyclic loading (Carter et al. 1982).

To minimize the error and improve the convergence, the implicit integration algorithm of constitutive model is adopted in this paper. The integration strategy is based on backward Euler integration procedure and applies an elastic stress predictor and plastic stress corrector to determine the final stress point. When combined with Newton-Raphson iteration approach to solve the nonlinear system of equations on the global finite element level, the computation can attain better convergence and accuracy than traditional explicit integration algorithm.

FINITE ELEMENT MODEL

In practice, the breakwater is composed of some large-diameter cylindrical structures connected by special procedure. Therefore the complex problem of response of cylindrical breakwater under wave loading can be simplified to plane strain model. In the model, the cylinder is simulated by linear elastic model and discretized by eight-noded reduced integration element. The soft ground and backfills are simulated by improved Cam-clay model and linear elastic model respectively, both discretized by eight-four noded displacement-pore pressure hybrid element.

To deal with the contact problem between the soil and structure, the contact pairs technique in the software ABAQUS is adopted. Frictional contact pairs are set up between the outer wall, inner wall, bottom surface and their neighboring soil. Tangential contact is described by Coulomb friction law

$$\tau = \mu p_{int} \tag{1}$$

where p_{int} is the effective normal contact pressure, τ is the limiting friction on the interface, and the coefficient of friction is $\mu = \tan\phi_{\text{int}}$, ϕ_{int} is the friction angle on the interface. According to some experience, $\phi_{\text{int}} = 2/3\,\phi'$ is adopted in the paper, where ϕ' is the effective friction angle of soil.

The horizontal and vertical direction is fixed under the bottom of the model and the horizontal direction is constrained on the sides. Taking account that to accelerate the consolidation of the ground, the plastic drainpipes are embedded into the backfills in engineering practice, therefore the top boundary of backfills is fully drained in the consolidation period before the wave loading, however is assumed to be undrained in the wave loading period.

The computation method for wave force imposed on the large-diameter cylindrical structure is now being investigated. So the wave-induced pressure formulation for upright-walled dyke is utilized in the paper,

$$p_{\text{d}} = \gamma_{\text{w}} H \frac{\cosh k(d+z)}{\cosh kd} \sin \omega t \tag{2}$$

where H, L and T is the height, length and period of wave, d is the depth of water, the number of wave k=2πL and the circle frequency ω=2π/T.

Referring to the large-diameter cylindrical structure employed in the second-phase project of deep-water channel of the Yangtze estuary in China, the diameter and embedment of the cylinder are D=L_e=13.5m, the height above mudline is L_a=10.5m, the thickness of cylinder wall is b=20mm. The wave length L=83.77m, d=8m, and the period T=10s, wave height H is assumed to be 1m and 3m respectively to investigate effect of wave height on cyclic response of the structure in soft ground. The length and depth of the finite element model for soft ground is selected to be 100m and 50m. Because the effect of progressive wave on the response of seabed is neglected in this paper, such truncated boundary is sufficient for the problem studied.

The model parameters for cylinder are E=210GPa, v=0.3, and those for backfills are E=10MPa, v=0.3, the permeability coefficient is k_w=10^{-5}m/s. The model parameters for soft ground are $\lambda = 0.34$, $k = 0.07$, $M = 1.23$, $v = 0.3$, and $\chi = 0.01$, initial void ratio is $e_0 = 1.092$, k_w=10^{-8} m/s. According to the relation between internal friction angle of soil and the parameter M in the Cam-clay model, $M = \frac{6\sin\phi'}{3-\sin\phi'}$, the internal friction angle of soil can be obtained as ϕ= 30.69°, therefore in the interface friction model, the coefficient of friction μ= 0.37 is adopted.

RESULTS AND DISCUSSIONS

Shown in Fig. 1 are the failure modes of instability of structure-soil coupling system with wave height H=1m and H=3m. It is noted that under condition of wave height H=3m, the large-diameter cylindrical structure overturns shoreward, however under condition of *H*=1m, the structure overturns seaward. According to investigation of the model tests, Liu et al. (2002) concluded that under wave loading, the large-diameter cylindrical structure in soft ground may overturns seaward in a certain condition. In previous studies about the ultimate capacity of cylindrical structure on soft soil, the structure overturns shoreward in any case in total stress finite element analyses. This shows that the effective stress analysis must be utilized to explore the failure mechanism of cylindrical structure in soft ground.

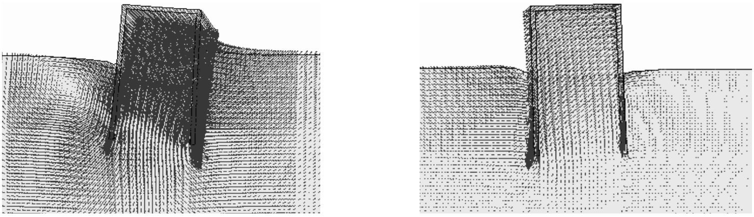

a) *H*=1m b) *H*=3m

FIG. 1. Failure mechanism of instability of cylindrical structure in soft soil

Shown in Fig. 2 is the distribution of excess porepressure ratio in soft soil when the state of instability of soil-structure coupled system is reached. From Fig. 2, it can be seen that under condition of wave height *H*=3m, the excess porepressure ratio $r_u=u_w/\sigma'_v$ is more larger on the shoreward side of soft ground, however under wave height *H*=1m, the excess porepressure ratio is more larger on the seaward side of seabed. Particularly on the interface between the structure and soil, the porepressure ratio already reaches 1.06. This maybe the main cause for the different failure mechanisms under condition of wave height *H*=3m and *H*=1m respectively.

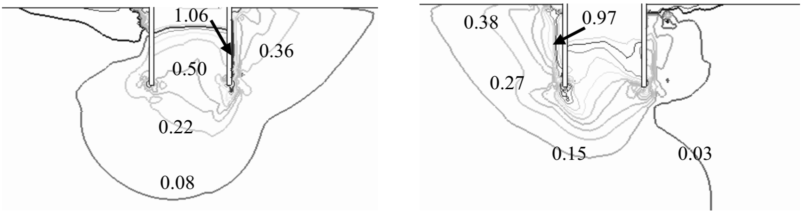

a) *H*=1m b) *H*=3m

FIG. 2. Distribution of excess porepressure ratio at failure

In the Fig. 3, the relationship between the lateral displacement of the point on the structure at the mudline and time of wave loading is shown. From Fig. 3, it can be seen more clearly that the permanent displacement of the structure accumulates along the direction seaward (The positive direction is seaward in the FE model in this paper), under condition of wave height *H*=1m. However under condition of wave height *H*=3m, the oscillatory component of the displacement is dominant although there is the residual component of the displacement along direction shoreward. This different tendency may show that the overturning of cylindrical structure is induced by large residual deformation in the soft marine ground when the wave induced load level is lower, but is induced by apparent oscillatory deformation when the wave loading level is higher.

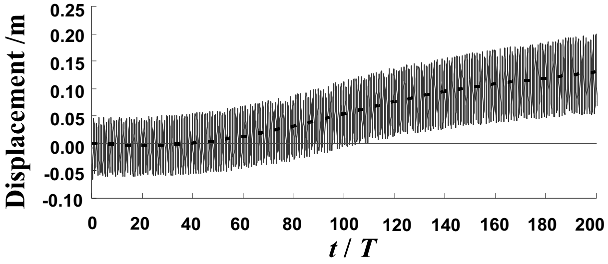

a) H=1m

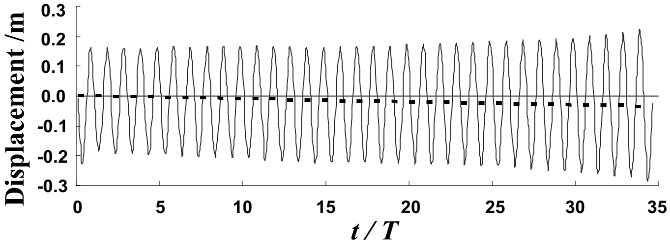

b) H=3m

FIG. 3. Variation of lateral displacement of structure with time of cyclic loading

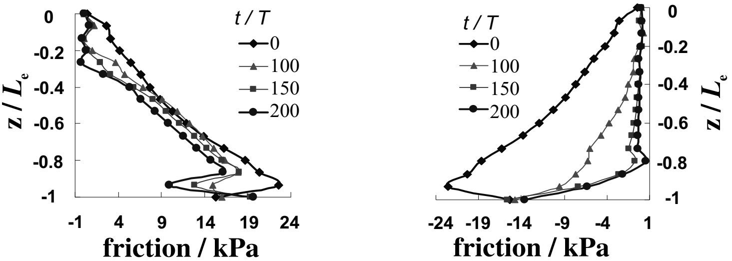

a) landward b) seaward

FIG. 4. Distribution of friction stress along the outer wall

Fig. 4 shows the distribution of friction stress along the outer wall at various time, for example, t/T=0, 100, 150, 200, under wave height H=1m. It can be found from these figures that the friction on the outer wall decreases with wave loading time, and the friction on the outer wall seaward decreases more obviously.

CONCLUSIONS

The improved dynamic Cam-clay model proposed by Carter et al. (1982) is numerically implemented into ABAQUS/Standard module through implicit integration algorithm. Then the effective stress elasto-plastic FE model for the large-diameter cylindrical structure in soft ground under wave loading is proposed and the interaction behavior between the soil and the wall of cylindrical structure is investigated. The results indicate that the larger the wave height, the larger cyclic displacement of soil-structure coupled system will be, but the residual displacement is smaller. When the wave height is smaller, the residual displacement will be larger and leads to the instability of cylindrical structure.

ACKNOWLEDGMENTS

The authors appreciate the support of the National Nature Science Foundation of China (Grant No. 50639010) and Talent Introduction Foundation of Ludong University (Grant No. LY20075602).

REFERENCES

Carter, J.P., Booker, J.R. and Wroth, C.P. (1982). "A critical state soil model for cyclic loading." In: Pande, G.N. and Zienkiewicz, O.C. (eds). *Soil Mechanics-Transient and Cyclic Loads*. London: John Wiley and Sons: 219-252.

Jeng, D.S., and Cha, D.H. (2003). "Effects of dynamic soil behavior and wave-nonlinearity on the wave-induced pore pressure and effective stresses in porous seabed." *Ocean Engineering*, (30): 2065-2089.

Liu, H.X., Wang, Z.J. and Tang, Y. (2002). "Dynamic earth pressures on deeply embedded large cylindrical structure under random waves and mechanism investigation on structural instability." *China Harbour Engineering*, (6): 21-25(in Chinese).

Wang, Y.Z., Zhu, Z. Y. and Zhou, Z.R. (2004). "Dynamic response analysis for embedded large-cylinder breakwaters under wave excitation." *China Ocean Engineering*, Vol. 18 (4): 585-594.

Combined Mode Decomposition and Precise Integration Method for Vibration Response of Beam on Viscoelastic Foundation

Youzhen Yang[1] and Xiurun Ge

[1]School of Naval Architecture, Ocean and Civil Engineering Shanghai Jiao Tong University, Room 2302 Haoran High Technique Building, 1954 HushanRoad, Shanghai, 200030, People's Republic of China yangyzh@sjtu.edu.cn;

ABSTRACT: In this research, an approach combining the precise time integration method (PTIM) and mode decomposition method is proposed to compute the response of beam structures resting on viscoelastic foundation. The PTIM has high precision, high efficiency, but it still suffers from the problem of large-size matrices when directly computing structure. And this problem can be overcome by mode superposition. Thus, the present paper integrates the PTIM and mode decomposition method together which holds the explicit recurrence form of precise algorithm. Comparing with the other numerical methods, it is found that the presented method is much more precisely and time-saving. The effect of the speed of moving load, the foundation stiffness and the length of the beam on the response of beam have also been studied. These numerical computation results show that the present method is effective and feasible.

INTRODUCTION

The dynamic analysis of beam resting on foundation as a dynamic soil-structure interaction problem is of great importance in structural and foundation engineering. It has been studied by many investigators such as Hetenyi, Andersen ,Thambiratnam and Sun who adopted the numerical methods such as the central difference, Newmark-β , and $Wilson-\theta$ method. Undoubtedly, these mainstream methods have played important role, but they still have some limitations(Wang2006).To improve the accuracy of time step integration, Zhong and Williams (1994)proposed the Precise Time Step Integration Method—PTSIM with arbitrary order of accuracy. This paper applies PTSIM to study the dynamic responses of beam on foundation. For a beam structure, without an elastic foundation, the authors(Zhu2001,Tang2007) have applied the integration method to calculate the dynamic response of Euler-Bernoulli beam under moving load.

In this research work, a procedure using the mode decomposition method together with the precise time integration method (MDPIM) is proposed to investigate the dynamic behavior of Euler-Bernoulli beam resting on viscoelastic foundation subjected to moving load. The mode decomposition method serves to transform the dynamic equations from geometric coordinates to normal coordinates and makes reduction of the degrees, and then the precise integration method serves to solve the transformed equations whose order has been reduced. Numerical examples are presented for moving load across the beam and the results show that this new coupling method can improve the computation efficiency significantly.

EQUATIONS OF MOTION

Let y(x, t) denote the vertical deformation of the beam with x being the traveling direction of the moving load and t being time. The well-known governing equation of a Bernoulli-Euler beam on a foundation(Kenny 1954) is:

$$EI\frac{\partial^4 y}{\partial^4 x}+ky+c\frac{\partial y}{\partial t}+m\frac{\partial^2 y}{\partial^2 t}=F(x,t) \tag{1}$$

Where *EI* is the rigidity of the beam; m is the unit mass of the beam, *k* is the modulus of sub-grade reaction, *c* is a dashpot of viscosity, and *F(x, t)* is applied external load. The deflection *y(x, t)* at position x can be expresses by

$$y(x,t)=\sum_{n=1}^{\infty}A_n(t)\Phi_n(x) \tag{2}$$

Where $A_n(t)$ the amplitude or the generalized coordinate; $\Phi_n(x)$ is the mode shape for the nth mode, respectively.

Applying Lagrange's equation and mode orthogonality, the normal equation for the nth mode could be obtained and given in the standard form as:

$$\ddot{A}_n+2\xi_n\omega_n\dot{A}_n(t)+\omega_n^2A_n(t)=F_n(t)/M_n \tag{3}$$

Where ω_n and ξ_n =natural frequency and the damping ratio; and M_n and $F_n(t)=$ generalized mass and force for the nth mode, respectively.

THE HIGH-PRECISION INTEGRATION SCHEME

Eq. (3) can be rewritten in matrix form:

$$\ddot{A}+2\xi\Omega\dot{A}+\Omega^2A=f(t) \tag{4}$$

Where

$2\xi\Omega=(\Phi^T M\Phi)^{-1}(\Phi^T C\Phi)$, $\Omega^2=(\Phi^T M\Phi)^{-1}(\Phi^T K\Phi)$, $f(t)=(\Phi^T M\Phi)^{-1}(\Phi^T F)$

M is a diagonal matrix of the generalized modal masses M_n, K is a diagonal matrix of the generalized modal stiffness K_n, C is a diagonal matrix of coefficients C_{nm}, and *f (t)* is a column vector of the generalized modal forces $F_n(t)$.

According to the precision time-step integration method[6], the equation of the motion of the beam on foundation in Eq. (4) can be written as

$$\dot{u}=Hu+P \tag{5}$$

Where u is the response vector of size $2n\times1$, H is a $2n\times2n$ matrix, and P is the force vector of size $2n\times1$, with:

$$u=\begin{Bmatrix} A \\ \dot{A} \end{Bmatrix}, H=\begin{bmatrix} 0 & I \\ -\Omega^2 & -2\xi\Omega \end{bmatrix}, P=\begin{Bmatrix} 0 \\ f(t) \end{Bmatrix} \tag{6}$$

Eq. (5) can be written into discrete equations using the exponential matrix representation. Integrating Eq. (5) and then can be expressed in the following discrete form:

$$\begin{aligned} u((j+1)h) &= e^{Hh}u(jh)+\int_{jh}^{(j+1)h} e^{H((j+1)h-\tau)}P(\tau)d\tau \\ &= e^{Hh}u(jh)+H^{-1}[e^{Hh}-I]P(jh) \qquad \text{(j=0,1,2...)} \end{aligned} \tag{7}$$

Where h is the time step of integration. The force $P(\tau)$ is assumed to be constant within the time interval from j h to (j+1) h. Thus, the basic recursive formula of MDPIM is :

$$\begin{Bmatrix} y \\ \cdot \\ y \end{Bmatrix}_{j+1} = \begin{bmatrix} \Phi & 0 \\ 0 & \Phi \end{bmatrix} \left(T \begin{Bmatrix} A \\ \cdot \\ A \end{Bmatrix}_j + H^{-1}[T-I]P_j \right) \tag{8}$$

The precision of integration depends on the accuracy of exp (Hh). The 2N algorithm is presented[6] to compute $T=\exp(Hh)$

According to Eq. (8), for a structure with N DOF, if only the first p modes are considered, the order of matrix T will be reduced from $2n\times2n$ to $2p\times2p$. Moreover, Eq. (8) indicates that the present method holds the explicit recurrence form of precise algorithm; therefore, the present method is highly efficient.

SIMULATION AND RESULTS

To examine the performance of the present method, the following computation examples are presented.

A Beam on Winkler Foundation Subjected to a Concentrated Moving Load

In this numerical analysis the beam is assumed to be a typical rail, which is subjected to a concentrated external force at the middle of the beam with the following properties (Andres 2006).

Table1. The parameters for the beam on foundation

L(m)	m(kg/m)	E(Nm^{-2})	I(m^4)	k(Nm^{-2})	v(ms^{-2})
50	43650.86	3.303e10	18.638	1.14e7	90

A load traveling with a velocity v takes $t_d = L/v$ to cross the beam. The theoretical formulation of this problem is presented by Chopra (2005).

The vertical response of the beam is calculated by the central difference, Houbolt, Wilson-θ, where θ is 1.4 and Newmark-β, where α is 0.5, δ is 0.25 for the time step $\Delta t = 0.01$. The comparison of the solutions of MDPIM and other numerical methods are shown in Table 2, Table 3. In Table 2 the current method is consistent with the theoretical solutions, better than other numerical methods. The example shows that MDPIM has a higher precise than other numerical methods and three times faster than Newmark-β.

Table. 2. The comparison of the mid-span dynamic response computed by several methods

t_k	$1\Delta t$	$5\Delta t$	$10\Delta t$	$15\Delta t$	$20\Delta t$	$25\Delta t$	$30\Delta t$	$35\Delta t$	$40\Delta t$
A	0.000731	-0.0109	-0.689	-1.641	-2.4000	-2.433	-1.880	-1.293	-1.1400
P	0.000735	-0.0923	-0.689	-1.549	-2.384	-2.450	-1.958	-1.336	-1.151
N	0.0013	-0.0366	-0.535	-1.487	-2.310	-2.470	-1.993	-1.421	-1.231
W	0.0000	-0.0575	-0.579	-1.522	-2.358	-2.476	-1.971	-1.372	-1.185
C	0.0000	-0.0723	-0.608	-1.542	-2.362	-2.462	-1.953	-1.333	-1.152

A: analytical, P: proposed method, N: Newark-β, W: Wilson-θ, C: central difference, H: Houbolt

Table 3. Computation time for time analysis comparing between two methods

Method	Proposed method	Newmark-β
Computation time(s)	4.06	11.49

The Effect of Traveling Speed

The same beam as above is also considered. But now let the beam resting on viscoelastic foundation with a stiffness k=1.14e7 N/m^2 and damping $\xi = 0.1$. The velocity of the moving load varies from 30m/s to 100m/s. The results for the dynamic normalized deflections in mid-span are shown in Fig.1 (a). It is interesting to note that the dynamic normalized deflections are reasonably constant for traveling speeds which are within the range of 60m/s, and only increase slightly as the traveling speed increasing for the velocity is beyond the value of 60m/s. When the stiffness reaches to 1.14e8 N/m^2, the peak of normalized deflections are constant. However, when the value of the foundation stiffness becomes smaller, this is not the case, shown in Fig.1 (a). When the foundation stiffness is lower than 1.14e7 N/m^2, the peak of normalized deflections increase distinctly with the traveling speed increasing, but remain constant for different foundation stiffness. Hence, when the foundation stiffness is relatively large, as in the case of foundation of railway tracks, the influence of the traveling speed, especially, within the range 60m/s, is negligible as the results in Fig.1 (a) demonstrates.

The Effect of the Span Length of the Beam

In order to study the influence of the length of beam on its dynamic response, a simply supported beam with a constant foundation k=1.14e7 N/m^2, damp ratio $\xi = 0.1$ and the load velocity of 90m/s is considered. The length of the beam varies from 30m to 200m and the dynamic normalized deflections on the mid-span are shown in Fig.1 (b). It can be seen that the normalized deflections decrease as the lengths increase. And the decreasing is significant when span length is lower than 120m. When the span length is beyond the value of 120 m, the normalized deflections almost remain constant. So does that of k=1.14e8 N/m^2. However, at lower values of k, it is not the case, as shown in Fig.1 (b). When the foundation stiffness k is reduced to 1.14e2 N/m^2 and 1.14e5 N/m^2, the peak normalized deflections, which initially increase as the span length increases, then decrease with the span beyond the values of 60m. Practical values of k are greater than 1.14e5 N/m^2, so the effect of length for $L \geq 120$m is not significant in this case.

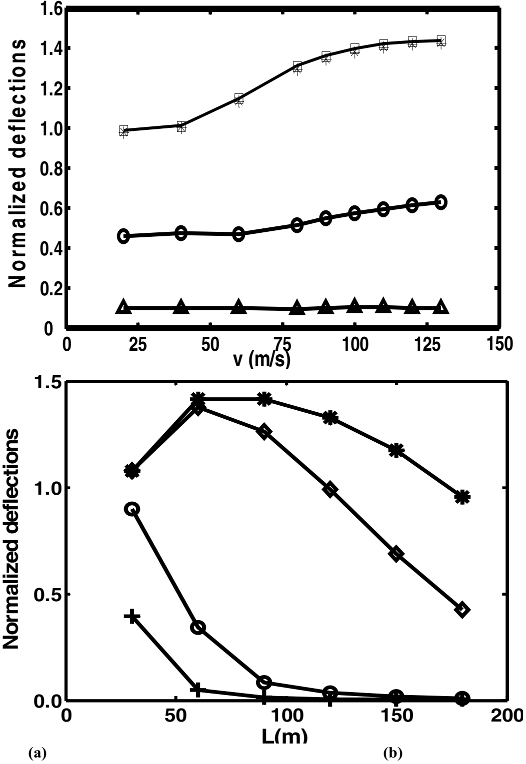

(a) (b)

Fig.1. Variation of peak values of dynamic normalized deflections for different stiffness: (a) with traveling speed; (b) with span length.

CONCLUSIONS

The present paper, based on the mode decomposition and precise time integration method, analyzed the dynamic analysis of beam on a viscoelastic foundation subjected to moving load. This method combines the advantages of the mode decomposition and the precise time integration method. Numerical results are presented for a simply supported beam. The deflections of the beam on Winkler foundation, as a special case, are found to be in excellent agreement with the theoretical analysis. The proposed method is applied to obtain the response time histories in which a more economical computer effort and higher precision could be achieved with the same time step of integration compared with the Newmark method. At the same time, for the beam on viscoelatic foundation, the effects of some important parameters, such as the traveling speed and the length of beam, have also been studied. The comparisons and calculations prove that this method can be used effectively foe forced vibration analysis of beams on foundation.

ACKNOWLEDGMENTS

The author is grateful to the reviewers for their helpful comments.

REFERENECES

A.K. Chopra.(2005). "Dynamic of Structures: Theory and Applications to Earthquake engineering.",second ed. Prentice-Hall (New Jersey).

Andersen L, Nielsen SRK and Kirkegard PH.(2001). "*Finite element modeling of infinite Euler beams on Kelvin foundations exposed to moving loads in convected co-ordinates*." *J. Sound Vib.* Vol.18 (7): 587–604.

Bin Tang.(2007). "*Combined dynamic stiffness matrix and precise time integration method for transient forced vibration response analysis of beams*." *J. Sound Vib.* Vol.118 (1): 1-9.

Hetenyi M. (1946). "In, Beams on elastic foundations*"*. Scientific series, vol. XVI. Ann Arbor: The University of Michigan Press, University of Michigan Studies.

Kenny J T. (1954). "*Steady-state vibration of beam on elastic foundation for moving load"*. *J. Appl. Mech.* Vol.21: 359-364.

LuSun.(2005). "*Analytical dynamic displacement response of rigid pavements to moving concentrated and line loads*.". *Int J. Solids & Struct* .Vol.43(14):1830-1844.

Mengfu Wang. and F.T.K. Au . (2006). "*Assessment and improvement of precision time step integration method*.". *J.Comput & Struc.*Vol.84 (12) :779-786.

Thambiratnam D P and Zhuge Y.(1996). *"Dynamic analysis of beams on an elastic foundation subject to moving loads.". J. Sound Vib.*Vol.198(2): 149-169.

Violeta Medina Andres.(2006). BS. Thesis. Massachusetts Institute of Technology.

W.X. Zhong . and F.W. Williams .(1994). " *A precise time step integration method.". Proc Inst Mech Engrs*.". Part C: J Mech Eng Sci. Vol.208: 427-430.

X.Q.ZHU.and S.S.LAW.(2001)."*Precise time-step integration for the dynamic response of a continuous beam under moving loads*." *J. Sound Vib.*Vol.20(5): 962-970.

Remediation of Liquefaction Potential Using Deep Dynamic Compaction Technique

Sarfraz Ali[1] and Liaqat Ali[2]

[1] National University of Science and Technology (NUST), Pakistan, sarfrazengr@yahoo.com
[2] National University of Science and Technology (NUST), Pakistan, liaqatnit@yahoo.com

ABSTRACT: Deep Dynamic Compaction technique was used to remediate liquefaction potential and enhance soil bearing capacity in one of the construction projects in Pakistan. The soil appeared to be susceptible to liquefaction as cracks of varying sizes were observed in existing structures in the project area during October 8, 2005 earthquake. Among various soil improvement alternatives, deep dynamic compaction technique was used due to its economy. Post compaction liquefaction evaluation indicated remediation of the liquefaction. Study of the project enhanced our understanding of deep compaction behavior of alluvial deposits consisting of alternating layers of fine and coarse grained soils. The paper gives an account of liquefaction evaluation, dynamic compaction program and effectiveness of dynamic compaction program.

INTRODUCTION

In many countries, dynamic compaction technique has successfully been used to remediate liquefaction. Dynamic compaction involves dropping of a heavy tamper repeatedly at same point from a height in a grid pattern. The weight of tamper, height of fall, number of drops, and grid spacing is selected to achieve required depth and degree of improvement. The paper is a case study of a soil improvement project covering an approximate area of 10,000 m^2. The proposed building is a framed structure having column loads varying from 1200 to 2300 kN. The embedment depth of column footings ranged from 2.5 to 4.5 m. The dynamic compaction program was designed empirically and was finalized after a field trial. Post compaction SPT results showed effective improvement in depth and lateral extents.

SITE DESCRIPTION AND SOIL CONDITIONS

Geologically, the project site forms part of Khushalgarh-Rawalpindi fold; a sub-fold of "Himalayan Fold Belt". The faults in the near vicinity are; Nathiagli fault at distance of 6 km (length 395 km), Khaiarabad fault at a distance of 3 km (length 370 km), and Kalabagh fault at a distance of 105 km (length 370 km). The site is composed of alluvial deposits of unconsolidated gravel, sand (course to fine), silt, and clay. The depth of overburden material is 50 to 80 m. The groundwater table exists at a depth of 12 m which rises to 5 m depth in rainy seasons (Khalid, Muhammad Mumtaz, 1995). Soil bearing capacity was evaluated as 100 kPa against 150 kPa required. Sub-surface profile of the site is shown in Figure 1. Loose strata from 3.5 to 5.5 m depth, presented a potential danger to safety and stability of the proposed structure.

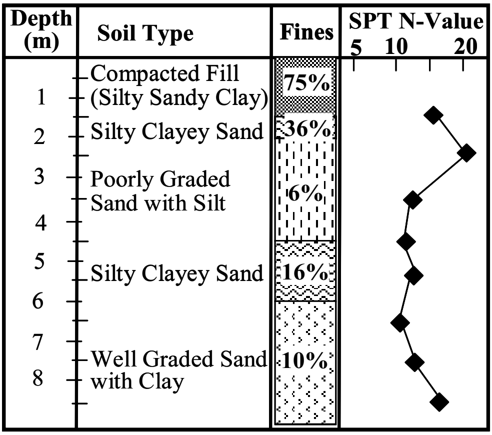

FIG.1. Sub surface profile

EVALUATION OF LIQUEFACTION POTENTIAL

Historical Criteria

The construction site is located in Himalayan seismic zone having a long history of earthquakes in the past and prediction of earthquakes in the future. Seismic maps revised after devastating earthquake of October 8, 2005 in Pakistan, places the construction site in "minor to moderate seismic risk area". An earthquake of 6 to 7.5 magnitudes on Richter scale with peak ground acceleration of 0.03 to 0.1g is predicted. However, design peak acceleration of 0.16g and design period of ground motion of 0.4 seconds is specified for this area (Geotechnical Investigation Report by M/S High Tech, 2004).

Geologic Criteria

Geologic processes that sort soils into uniform grain size distributions and deposit them in loose states, produce soil deposits with high liquefaction susceptibility. Alluvial deposits with high water table (either free or perched) are therefore likely to be susceptible to liquefaction (Kramer, 1996). At the construction site, an alluvial stratum of recent age with un-corrected SPT N-value of less than 12 where water table rises to a 5 m depth in rainy season is susceptible to liquefaction**.**

Compositional Criteria

Compositional characteristics such as particle size, shape, gradation, etc, associated with high volume change potential tend to be associated with liquefaction susceptibility. Well-graded soils are generally less susceptible to liquefaction than poorly graded soils; the smaller particles fill voids between larger particles in well-graded soils result in lower volume change potential under drained conditions and, consequently, lower excess pore pressures under un-drained conditions (Kramer, 1996). From soil conditions given in Figure 1, it is inferred that poorly graded soil layers from 3.5 to 5.5 m depths having fines as low as 6% and low SPT N-values in high water table conditions are susceptible to liquefaction.

EVALUATION FOR INITIATION OF LIQUEFACTION

The fact that a soil deposit is susceptible to liquefaction does not mean that liquefaction will necessarily occur in a given earthquake. Its occurrence requires a disturbance that is strong enough to initiate or trigger it (Kramer, 1996). Most popular methods for evaluation of initiation of liquefaction are "cyclic stress approach" and "cyclic strain approach". In this paper, initiation of liquefaction is evaluated using cyclic stress approach. An earthquake of magnitude 7, peak ground acceleration of 0.16g, and ground motion of 0.4 seconds are used for this evaluation.

Characterization of Earthquake Loading

Earthquake induced loading is characterized by a level of uniform cyclic shear stress that is applied for an equivalent number of cycles (Kramer, 1996). Equation (1), proposed by Seed et al. (1983) is used for calculation of equivalent cyclic shear stress (Table 1). In equation (1), τ_{cyc} = cyclic shear stress at the time of earthquake, $a_{\max}$ = peak ground surface acceleration, c_v = total vertical stress, g = acceleration due to gravity, r_d = value of stress reduction factor for a given depth (0.98 to 0.96 for depth of 3.5 to 5.5 m depth, Seed and Idriss, 1971).

$$\tau_{cyc} = \frac{0.65 a_{\max}}{g \times \sigma_v \times r_d} \qquad (1)$$

Table 1. Equivalent Cyclic Shear Stress Induced by an Earthquake of Magnitude 7 on Richter Scale

Depth (m)	Soil Type	Unit Weight (KN/m^3)	r_d	τ_{cyc}
3.5	Poorly graded sand with silt	17.23	0.98	6.52
4.5	Poorly graded sand with silt	17.23	0.97	8.19
5.5	Silty clayey sand	18.50	0.96	9.96

Characterization of Liquefaction Resistance

Cyclic shear resistance at various depths (shown in Table 2) is calculated using equation (2), (Kramer, 1996).

$$\tau_{cyc,L} = CSR_L \times c'_{v^o} \qquad (2)$$

Where c'_{v^o} = initial vertical effective stress and CSR_L = cyclic stress ratio. SPT N_{Field} values were corrected to $(N_1)_{60}$ by applying appropriate corrections (overburden, energy, borehole diameter, rod length, and sampling).

Factor of Safety

Factor of safety against liquefaction is expressed as **FS**$_L = \tau_{cyc,L}/\tau_{cyc}$. Liquefaction occurs when **FS**$_L$ is less than 1 (Kramer, 1996). From Table 2, it is evident that soil at the project site will liquefy under existing conditions.

Table 2. Cyclic Shear Resistance of Soil and Factor of Safety (FS$_L$)

Depth (m)	**$(N_1)_{60}$**	CSR_L	σ'_{vo} **(kN/m^3)**	$\tau_{cyc,L}$	τ_{cyc}	**FS$_L$**
3.5	6	0.06	64.01	3.84	6.52	0.59
4.5	7	0.07	71.43	5.00	8.19	0.61
5.5	8	0.08	80.12	6.41	9.96	0.64

DYNAMIC COMPACTION PROGRAM

The compaction program comprised two high energy passes and a low energy ironing pass. Each high energy pass comprised 10 blows per impact point from a height of 16 m and the low energy pass comprised 2 blows from a height of 5 m. Grid spacing of primary and secondary pass was 6 m from centre to centre in a square grid pattern. Secondary blows were placed in the centre of primary blows. The ironing pass was performed on overlapping grid with an overlap of one-third of tamper diameter. The circular tamper, 1.5 m high, 2.4 m in diameter and weighing 20 ton, was made of concrete with steel casing.

Effectiveness of Dynamic Compaction Program

Improvement in depth and lateral extent was evaluated by comparing pre to post compaction SPT results at various craters (impact points). All post compaction SPT were performed two weeks after compaction and within 2 m distance of pre compaction SPT. Improvement in depth was evaluated at every 1 m depth interval upto 9 m depth while lateral improvement was evaluated upto a distance of 3D from centre of impact points (D=2.4 m, dia of tamper).

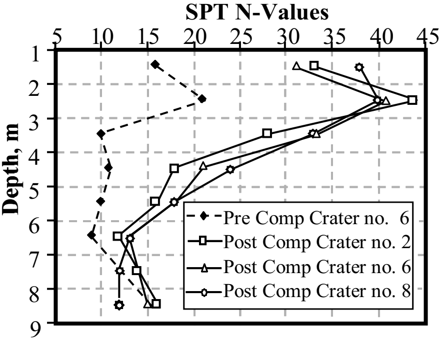

FIG.2.Improvement under impact points

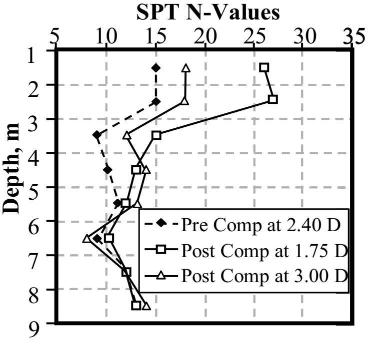

FIG.3. Lateral improvement

Improvement at crater no. 2, 6, and 8 both in depth and lateral extent is shown in Figures 2 and 3 respectively. Pre compaction SPT values at crater no. 2, 6, and 8 were similar therefore only SPT values of crater no. 2 are shown. Large improvement is evident both in depth and lateral extents, especially in the upper 5 m strata. Comparison of depth of improvement achieved in the research project with the depths predicted by empirical correlations and case histories is shown in Table 3. Authors attribute following main reasons to the lower depth of Improvement in the research project:

- The compacted fill layer at top of the strata absorbed relatively more impact energy and transferred less energy to deeper layers. The response of compacted layer can be compared to that of a rigid pavement.
- The depth of improvement is proportional to the grid spacing, closer grid spacing of 6 m in the research project resulted in lower depth of improvement.

Table 3. Comparison of Depth of Improvement Predicted by Empirical Correlations and Case Histories

Reference	Correlation / Method	Improvement in Depth, (m)
Meyerhof (1959)	$D_{\max} = 3.5$ D	$3.5 \times 2.4 = 8.4$
Menard and Broise (1975)	$D_{\max} = \sqrt{WH}$	$D_{\max} = \sqrt{20 \times 16} = 17.88$
Lukas (1986)	$D_{\max} = n\ \sqrt{WH}$	$D_{\max} = 0.65\sqrt{20 \times 16} = 11.62$ $n = 0.65$ for silty soils
Kyle M. Rollins (1994)	Plot of maximum depth of improvement for case histories	7.5 for $W = 20$ Ton and $H = 16$ m
Understudy Research Project	Comparison of pre to post compaction SPT N-values	5
$D_{\max}$ = Maximum depth of Improvement (m), D = Dia of Tamper, W = Weight of Tamper, H = Height of Fall, n = Empirical Coefficient		

EVALUATION OF LIQUEFACTION AFTER DYNAMIC COMPACTION

Earthquake loading (equivalent cyclic shear stress), liquefaction resistance (cyclic shear resistance), and factor of safety evaluated after dynamic compaction is shown in Tables 4 and 5 respectively. Dynamic compaction increased value of factor of safety more than 1 at all three depths.

Table 4. Equivalent Cyclic Shear Stress after Dynamic Compaction

Depth (m)	Soil Type	Unit Weight (KN/m^3)	r_d	τ_{cyc}
3.5	Poorly graded sand with silt	20.50	0.98	7.46
4.5	Poorly graded sand with silt	20.50	0.97	9.46
5.5	Silty clayey sand	19.50	0.96	11.41

Table 5. Cyclic Shear Resistance of Soil after Dynamic Compaction and Factor of Safety (FS$_L$)

Depth (m)	$(N_1)_{60}$	CSR_L	σ'_{v^o} (kN/m^3)	$\tau_{cyc,L}$	τ_{cyc}	FS$_L$
3.5	23	0.24	71.43	17.14	7.46	2.3
5.5	14	0.17	82.12	13.96	9.46	1.5
7.5	12	0.15	92.81	13.92	11.41	1.2

CONCLUSIONS

From results of soil improvement project of alluvial soils, it is concluded that deep dynamic compaction technique can remediate liquefaction potential and enhance bearing capacity upto desired limits at desired depths. The compacted layers at top of strata and reduced grid spacing can significantly reduce the overall depth of improvement.

REFERENCES

Khalid, Muhammad Mumtaz (1995). An investigation into high water table problem at Attock District, an MSc Thesis, National University of Science and Technology (NUST), Pakistan.

Kramer, L., Steven (1996). "Geotechnical earthquake engineering." *Prentice Hall Series*. 351-354, 369-376.

Kyle M. Rollins (1994). In-Situ Deep Soil Improvement, Geotechnical Special Publication No. 45, 37-38.

M/S High Tech, (2004). Report on geotechnical engineering investigation for Attock District, Pakistan.

Seed, H.B., Idriss, I.M. (1971). "Simplified procedures for evaluating soil liquefaction potentials", *J. of Soil Mechanics and Foundation*, ASCE, Vol. 107, 1249–1274.

Seed, H.B., Idriss, I.M., and Arango (1983). "Evaluation of liquefaction potential using field performance data." *Journal of Geotechnical Engineering*, ASCE. 109, 458-482.

Transmitting Artificial Boundary of Attenuating Wave for Saturated Porous Media

Zhi-Hui Zhu[1], Zhi-Wu Yu[2], Hong-Wei Wei[3], and Fang-Bo Wu[4]

[1]School of Civil and Architectural Engineering, Central South University, Changsha, Hunan 410075, People's Republic of China; PH(86-731)265-6471; ZZHH0703@163.COM
[2]School of Civil and Architectural Engineering, Central South University, Changsha, Hunan 410075, People's Republic of China; PH(86-731)265-6166; ZHWYU@CSU.EDU.CN
[3]School of Civil and Architectural Engineering, Central South University, Changsha, Hunan 410075, People's Republic of China; PH(86-731)265-6166; WHW.EDU@163.COM
[4]College of Civil Engineering, Hunan University, Changsha, Hunan 410082, People's Republic of China; PH(86-731)882-3901; WFBPROF@163.COM

ABSTRACT: Based on the constitutive equation of saturated porous media, the attenuating wave multi-transmitting artificial boundaries (AMT-ABs) for transient analysis in case of 2D and 3D are developed and its reflection coefficients are also presented. Compared with the reflection coefficient of homogeneous plane wave multi-transmitting artificial boundary (HMT-AB), the reflection coefficient of AMT-AB is the least. Via programming in APDL provided by ANSYS, AMT-AB was added into ANSYS. Numerical example is given and the analyzed results show that the AMT-AB is the most accurate artificial boundary to analyze sophisticated dynamic problems than other major local artificial boundaries.

INTRODUCTION

An understanding of the dynamic behavior of saturated elastic porous media is a very important topic in the soil-structure dynamic interaction under earthquake and other dynamic loads. Biot (1956) presented the wave motion equation for fluid-saturated two-phase porous media, in which the wave equation is a two dimensional partial differential equation coupled with liquid phase and solid phase. As the analytical solution of fluid-saturated porous media can only be applicable to a few specific boundaries, many practical problems are solved by FEM. To infinite and semi-finite soil in soil-structure dynamic interaction system, the computation is often carried out in a finite zone by applying artificial boundary (AB) in finite zone to simulate wave propagation in truncated boundary. Now, most dynamic ABs are local transmitting ABs, and mainly based on unilateral out-going wave motion theory such as viscous artificial boundary (V-AB), viscous-spring artificial boundary (VS-AB) (Deeks and Randolph 1994, Liu and Lu 1998, Liu and Wang 2005) and multi-transmitting artificial boundary (MT-AB) (Liao 2002). Aimed at solving the complex dynamic problem of fluid-saturated two-phase porous media, Gajo (1996) developed the first-order multi-directional transmitting boundary for two-phase media. Akiyoshi et al. (1998) introduced equivalent Lame's constants, and determined general V-AB, which is suitable for fluid-saturated porous media with isotropic, transversely isotropic and anisotropic properties. Zerfa (2002) proposed a V-AB of fluid saturated porous media which is used for transient analysis in time domain. Zhao (2001) applied local transmitting AB to solve the dynamic problem of fluid-saturated porous media.

Most ABs were deduced based on the assumption of plane wave and the effect of wave amplitudes attenuation ,which is called radiation damping, was not considered. In conditions of wave source problem, to which the effects of radiation damping often dominate those of material damping, this assumption is not rational (Steven 1996). Considering the important role of radiation damping in near field wave motion problems, AMT-AB is deduced in this paper. The comparison between reflection coefficients of AMT-AB and HMT-AB is carried out. By means of a scattering problem, the accuracy of AMT-AB, HMT-AB and VS-AB is compared.

MULTI-TRANSMITTING ARTIFICIAL BOUNDARY (MT-AB)

MT-AB is a kind of displacement boundary, which uses the general expressions of solutions for unilateral out-going wave motion to simulate the process of out-going wave passing the boundary directly. Displacement of points in boundary is represented by the displacement of inner points. By increasing the number of contributing nodes, the accuracy of MT-AB can be improved; in fact, the accuracy of second-order MT-AB is acceptable for practical problem. Since MT-AB has a fairly good universal adaptability, high precision and solid theoretical foundation, a new MT-AB based on assumption of attenuating scattering wave is presented in this paper.

Multi-transmitting Formula (MTF) Based on Attenuating Out-going Wave.

According to the Biot's wave motion theory of two-phase porous media, there exists three kinds of uncoupled waves: two types of compression waves and one type of shear wave. For any of the waves, it is assumed that the waves of liquid phase and solid phase propagate in a certain direction with their respective constant velocity and amplitude. So the solutions of wave motion of liquid phase and solid phase can be solved separately.

Let the *x*-axis be the normal to artificial boundary of a finite discrete model and point to the exterior of the model (fig. 1).

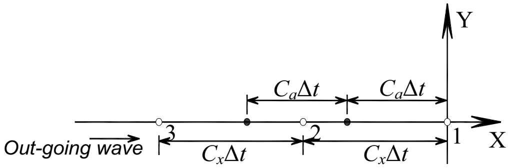

FIG. 1. Multi-transmitting boundary computational model

The wave amplitude based on homogeneous plane wave is supposed to constant, so wave motion equation can be expressed as

$$u(t,x) = f(c_x t - x) \tag{1}$$

So the Nth order MTF of homogeneous plane wave can be written in the form

$$u_0^{p+1} = \sum_{j=1}^{N} (-1)^{j+1} C_j^N u_j^{p+1-j} \tag{2}$$

For the amplitude of attenuating wave attenuates geometrically. The attenuating wave motion equation is

$$\tilde{u}(t,x) = Af(c_x t - x) = Au(t,x) \tag{3}$$

Where c_x is the apparent propagation velocity in normal direction of artificial boundary; A is the attenuating coefficient of scattering wave, $A = 1/\sqrt{r}$ in condition of 2D and $A = 1/r$ in condition of 3D.

According to Eq. (3), by using similar process as deducing Eq. (2), the Nth order MTF of attenuating wave is

$$\tilde{u}(t+\Delta t, x) = \sum_{j=1}^{N} (-1)^{j+1} C_j^N B\tilde{u}\left(t-(j-1)\Delta t, x - j c_a \Delta t\right) \tag{4}$$

Where $B = \sqrt{\dfrac{x_0 - j c_a \Delta t}{x_0}}$ in condition of 2D and $B = \dfrac{x_0 - j c_a \Delta t}{x_0}$ in condition of 3D. The coordinate of boundary point o is $x=x_0$.

The Nth order MTF of attenuating wave can be rewritten as

$$\tilde{u}_0^{p+1} = \sum_{j=1}^{N} (-1)^{j+1} C_j^N B\tilde{u}_j^{p+1-j} \tag{5}$$

Where $\tilde{u}_0^{p+1} = \tilde{u}\left((p+1)\Delta t, x_0\right)$, $\tilde{u}_j^{p+1-j} = \tilde{u}\left((p+1-j)\Delta t, x_0 - j c_a \Delta t\right)$. When x_0 is large enough ($x_0 >> j c_a \Delta t$), Eq. (5) can be simplified as Eq. (2).

The Reflection Coefficient in Frequency Domain.

Through comparing the reflection coefficients of HMT-AB and AMT-AB, the precision of two types of artificial boundary are studied. Since the reflection coefficient analysis is carried in frequency domain, the expression of MTF is also proposed in frequency domain. In order to make the same analysis, assuming the coordinate of boundary point is $x=x_0$ (as shown in fig. 2).

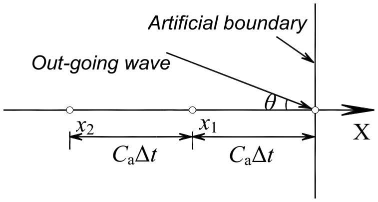

FIG. 2. Schematic illustration of out-going wave in artificial boundary

The MTF of homogeneous plane wave in frequency domain is

$$U_{x_0} = \sum_{j=1}^{N} (-1)^{j+1} C_j^N U_{x_j} \exp(-ij\,\omega\Delta t) \tag{6}$$

The MTF of attenuating plane wave in frequency domain is

$$\tilde{U}_{x_0} = \sum_{j=1}^{N} (-1)^{j+1} C_j^N B\tilde{U}_{x_j} \exp(-ij\,\omega\Delta t) \tag{7}$$

Where U_{x_j} and $\tilde{U}_{x_j}$ are amplitudes at point x_j ($x_j = x_0 - j\,c_a\Delta t$).

Assuming the incident angle of attenuating out-going wave is θ (as shown in fig. 2), the amplitude of out-going wave can be written in the form

$$U_{xj}^I = BU_0^I \exp(ij\,\omega c_a\Delta t\,\cos\theta/c) \tag{8}$$

Analyses of MTF reflection coefficient are usually carried out in the steady-state case. The incident wave is absolutely predominant in total wave field. So $U_{xj} = U_{xj}^I$.

Substituting Eq. (8) into Eq. (6), yields

$$U_{x_0} = \sum_{j=1}^{N} (-1)^{j+1} C_j^N B \exp\left(ij\,\omega\Delta t\,(\cos\theta - 1)\right)U_0^I \tag{9}$$

The total displacement in boundary point is composed of incident wave displacement and reflected wave displacement. The reflected wave displacement is

$$U_{x_0}^R = U_{x_0} - U_{x_0}^I \tag{10}$$

The reflection coefficient of MTF defined by

$$R = \left|\frac{U_{x_0}^R}{U_{x_0}^I}\right| = \left|\frac{U_{x_0}}{U_{x_0}^I} - 1\right| \tag{11}$$

Substituting Eqs. (6) and (8) into Eq. (11), yields the reflection coefficient R_1 of HMT-AB transmitting attenuating out-going wave.

$$R_1 = \left|\frac{U_{x_0}}{U_{x_0}^I} - 1\right| = \left|\sum_{j}^{N} (-1)^{j+1} C_j^N B \exp\left(ij\,2\pi\left(\frac{\Delta t}{T}\right)(\cos\theta - 1)\right)\right| \tag{12}$$

Substituting Eqs. (7) and (9) into Eq. (11), yields the reflection coefficient R_2 of AMT-AB transmitting attenuating out-going wave.

$$R_2 = \left|\frac{U_{x_0}}{U_{x_0}^I} - 1\right| = \left|\sum_{j}^{N} (-1)^{j+1} C_j^N \exp\left(ij\,2\pi\left(\frac{\Delta t}{T}\right)(\cos\theta - 1)\right)\right| \tag{13}$$

In order to clearly illustrate the difference of R_1 and R_2, the curves of relationship between the reflection coefficient to incident angle θ in case of 2D and 3D are reported in figs. 3 and 4 respectively, with $x_0 = 10c_a\Delta t$ and $20c_a\Delta t$ in the conditions of $\Delta t/T = 1/10$ and 1/20.

Conclusions drawn from figs. 3 and 4 are as follows. The first, R_2 are small than R_1 within the entire range of $\theta \le 90^0$. The second, Compared with attenuating plane wave, the amplitude attenuation of attenuating spherical wave is more obvious with same spreading distance. So, R_1 in case of 3D is larger than that of 2D.

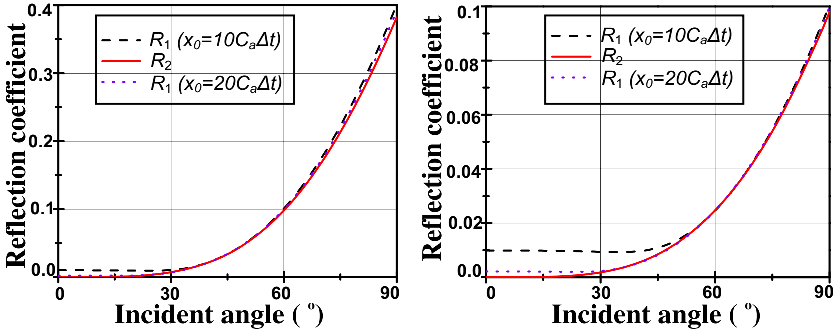

(a) $\Delta t/T$=1/10 (b) $\Delta t/T$=1/20

FIG. 3. The 2nd order MTF reflection coefficient of attenuating plane wave

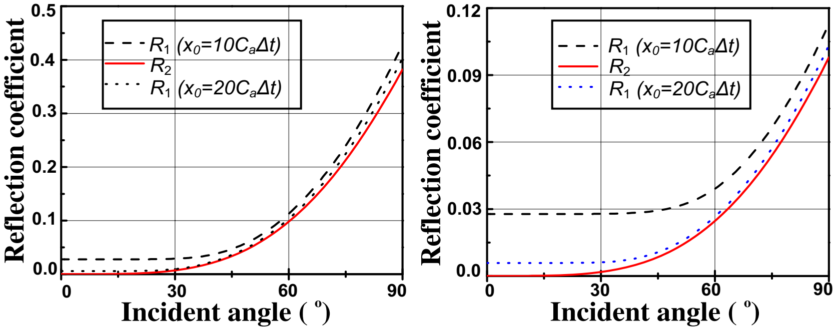

(a) $\Delta t/T$=1/10 (b) $\Delta t/T$=1/20

FIG. 4. The 2nd order MTF reflection coefficient of attenuating spherical wave

NUMERICAL EXAMPLE

In the case of a two-dimensional half-space with a groove at the top, a normal incident pulse wave is imposed on the bottom as shown in the fig. 5. The displacement of pulse wave is written as in Eq. (14). A homogenous, isotropic linear soil half space model is chosen with C_s = 400 m/s, ρ = 2000 kg/m^3 and Poisson's ratio ν = 0.25.

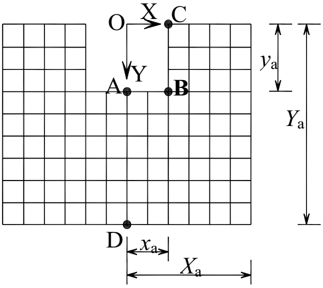

FIG. 5. Computational model of normally incident shear wave

$$U(t) = 16\left[G(t) - 4G\left(t - \frac{1}{4}T_0\right) + 6G\left(t - \frac{1}{2}T_0\right) - 4G\left(t - \frac{3}{4}T_0\right) + G(t - T_0)\right] \quad (14)$$

Where $G(r) = \left(\frac{t}{T_0}\right)^3 H\left(\frac{t}{T_0}\right)$, $H(T) = \begin{cases} 0 & t < 0 \\ 1 & t \geq 0 \end{cases}$, T_0=0.15s.

The computational domain is meshed by square element. The mesh sizes Δx=Δy=2m, the time increment Δt=0.0025s, which satisfy the stability requirement of computation. The computing time is 1.0s. The computational domain data is listed in table. 1.

Table 1. The computational domain

Name	The type of boundary	The computational domain
Scatter1	fixed boundary	X_L=Y_L=250m
Scatter2	VS-AB	X_L=Y_L=30m
Scatter3	2nd order HMT-AB	X_L=Y_L=30m
Scatter4	2nd order AMT-AB	X_L=Y_L=30m

Numerical solutions at three points (A(0,10), B(10,10) and C(0,10)) using different ABs are shown in Fig. 6. The accurate solutions are obtained by Scatter1. In order to assure the accuracy of solutions by Scatter1, the reflected wave is not allowed to arrive in the finite domain.

It is possible to note that the results of Scatter4 with 2nd order AMT-AB is almost close to the accurate solutions of Scatter1. That the 2nd order HMT-AB cannot efficiently absorb the attenuating out-going wave is the major reason of displacement drift occurring in Scatter3 used 2nd order HMT-AB. It also can be seen that the error of Scatter2 is the largest, because VS-AB has only first order computation precision.

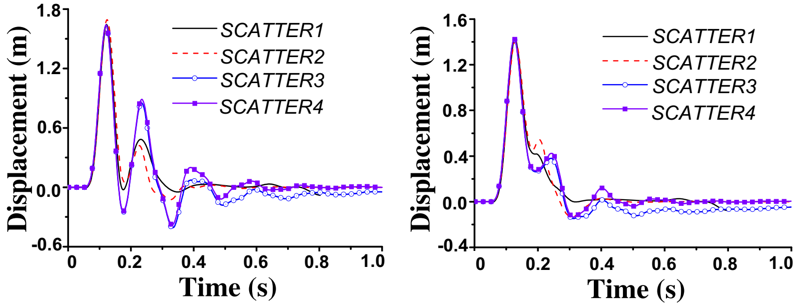

(a) point A (b) point B

FIG. 6. Comparison of displacement at point A, B and C

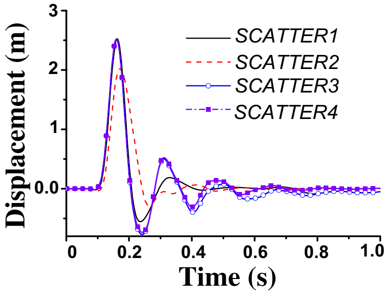

(c) point C

FIG. 6. Comparison of displacement at point A, B and C (continued)

CONCLUSIONS

Through studying the wave motion equation of attenuating out-going wave, the AMT-AB and reflection coefficient are presented in this paper. Comparing the reflection coefficients of homogeneous plane wave multi-transmitting formula with attenuating out-going wave multi-transmitting formula, it has shown that the accuracy of HMT-AB transmitting attenuating wave is lower than that of AMT-AB. This can be find especially in the condition of incident angle equals to zero, because the reflection coefficient of homogeneous plane wave multi-transmitting formula does not equal to zero, but the attenuating wave multi-transmitting formula can transmit the attenuating out-going wave completely.

Via programming in APDL provided by ANSYS, AMT-AB, HMT-AB and VS-AB were added into ANSYS. Through comparing the results of scattering wave problem with three different ABs, it has shown that the precision of MT-AB is higher than that of VS-AB, and the precision of AMT-AB is the highest in three kinds of AB.

ACKNOWLEDGEMENTS

This research was supported by the National Natural Science Foundation of China, No. 50808177, 50778181; the Ph. D. Programs Foundation of Ministry of Education of China, No. 200805331069; China Postdoctoral Science Foundation through Grant No. 20080431033 and Hunan Provincial Science and technology planning project through Grand No. 2008RS4023.

REFERENCE

Biot, M.A. (1956). "Theory of propagation of elastic wave in fluid-saturated porous solid." *The Journal of the Acoustical Society of America*, Vol. 28 (2):168-178.

Zhao, C.G., Du X.L. and Cui, J. (1998). "Review of wave propagation theory in saturated and unsaturated porous medium and its numerical methods." *Advances in Mechanics*, Vol. 28 (1): 83-91 (in Chinese).

Deeks, A.J. and Randolph, M.F. (1994). "Axisymmetric time-domain transmitting boundaries." *J. Engineering Mechanics*, ASCE, Vol. 120 (1):25-42.

Liu, J.B. and Lu, Y.D. (1998). "A direct method for analysis of dynamic soil-structure interaction." Chinese J. Civil Engineering, Vol. 31 (3): 55-64 (in Chinese).

Liu, J.B., Wang. Z.Y., Du, X.L. and Du, Y.X. (2005). "Three dimensional viscous-spring artificial boundaries in time domain for wave motion problems." *J. Engineering Mechanics*, Vol. 22 (6): 46-51 (in Chinese).

Liao, Z.P. (2002). "Introduction to Wave Motion Theories in Engineering (2nd ed)." *Beijing: Science Press* (in Chinese).

Gajo, A., Saetta, A. and Vitaliani, R. (1996). "Silent boundary conditions for wave propagation in saturated porous media." *International Journal for Numerical and Analytical Methods in Geomechanics*, Vol. 20(4):253-273.

Akiyoshi, T., Sun, X. and Fuchida, K. (1998). "General absorbing boundary conditions for dynamic analysis of fluid-saturated porous media." *J. Soil Dynamics and Earthquake Engineering*, Vol. 17 (6): 397-406.

Zohra, Z. and Benjamin, L. (2002). "A viscous boundary for transient analyses of saturated porous media." *J. Earthquake Engineering and Structural Dynamics*, Vol. 33(1): 89-110.

Zhao, C.G., Wang, J.T., Shi. P.X. and Li W.H. (2001). "Dynamic analysis of fluid-saturated porous media by using explicit finite element method." *Chinese Journal of Geotechnical Engineering*, Vol. 23 (2): 46-50 (in Chinese).

Steven, L.K. (1996). "Geotechnical Earthquake Engineering." *Prentice-hall*, *Inc*, 180.

Du, X.L. (2000). "A partially decoupling analytical method for wave propagation problems in time domain." *World Information on Earthquake Engineering*, Vol. 16 (3): 22-26 (in Chinese).

Analysis of the Long-term Settlements of Chimney Foundation on Silty Clay

Xin Xiang[1], Huiming Tang[2], and Lei Fan[3]

[1]Doctor candidate, Faculty of Engineering, China University of Geosciences(Wuhan), 388 Lumo Road, Wuhan City, China; xinxxiang@gmail.com
[2]Professor, Faculty of Engineering, China University of Geosciences (Wuhan), 388 Lumo Road, Wuhan City, China; tanghm@cug.edu.cn
[3]Doctor candidate, Faculty of Engineering, China University of Geosciences(Wuhan), 388 Lumo Road, Wuhan City, China; fanchon1982@126.com

ABSTRACT: As an integral part of foundation design, long-term settlement monitoring is necessary for reasonable estimates of the long-term settlement of chimney foundation bearing on silty clay, particularly of organic soils, for which long-term settlement is significant. The height of the chimney studied in this paper is more than 210 m, and the foundation of chimney is mainly composed of silty clay. The chimney was constructed in stage and surcharged in an attempt to reduce post-constructed settlement. The settlements of subsoil and chimney were instrumented and monitored for about 3 years. Soil properties were determined from laboratory and field testing, and the parameters used for finite-element analysis were determined by back analysis. The settlements predicted by the advanced Grey Model showed reasonable agreement with measured ones. The predicted settlement of finite-element analysis was smaller than the measured values.

INTRODUCTION

The site of chimney is located in Wuhan, middle of China. To explore the subsurface conditions, a number of boreholes were sunk in the preconstruction stage. The nature ground level varies from 37 m to 42 m. The subsoil consists of mainly silty clay and the thickness up to 15 m. The silty clay is underlain by highly weathered argillaceous sandstone.

The moisture content of silty clay is in the range of 22.3% to 26.1%, based on retrieved samples, the soil had a liquid limit of 31.9% - 44.5%, and a plastic limit of 18.8% - 24%. The friction angle varies from 18.1° to 26.1°, and the cohesion is between 58 KPa and 89 KPa. Conventional oedometer tests were conducted as part of the preconstruction site investigation program, which gave a compression index, a , in the range of 0.06 to 0.23.

The foundation settlement was monitored when the construction began, and finished 3 years later than the construction completed. The long-term settlement data, in conjunction with finite element analysis, provide an objective basis for assessing the foundation settlement with time, and final foundation settlement.

ANALYSIS OF PROCESS OF SETTLEMENT

Based on the engineering characteristics of stratum, theoretical formulas were adopted to calculate total settlement. When there is multi-layered soil, total settlement is decided by immediate settlement in the filled soil and clay. In the studied area, the main factor which influences total settlement is settlement of clay bed. Advanced GM(1, 1) model is used to calculate the settlement.

Grey time-varying parameters model is

$$\frac{dx^{(1)}(t)}{dt}+a(t)x^{(1)}(t)=b(t) \qquad (1)$$

The general solution is

$$\bar{x}(T)=[\int_0^T b(s)e^{\int_0^s a(r)dr}ds+c]e^{-\int_0^T a(r)dr} \qquad (2)$$

where $\bar{x}(T)$ is predicted value of $x^{(1)}(T)$.

From formula (1) – (2), $\bar{x}(T)$ could be written as

$$\bar{x}(T)=[\int_0^r b(s)e^{\int_0^s a(r)dr}ds+x^{(1)}(1)]e^{-\int_0^T a(r)dr} \qquad (3)$$

Comparison between the measured value curve and the predicted value curve is presented in Fig. 1-3.

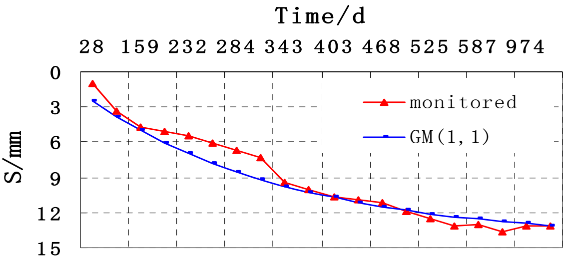

Fig.1. Comparison curves of point 1

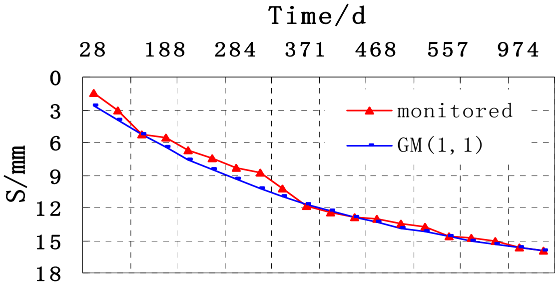

Fig.2. Comparison curve of point 2

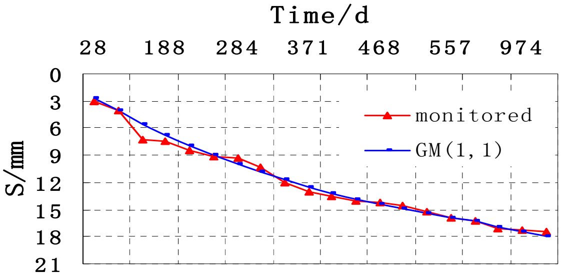

Fig.3. Comparison curves of point 3

ANALYSIS OF FINAL SETTLEMENT

There are many methods to evaluate final settlement, such as hyperbola method, index curve method, Asaoka method and three-point method. Three-point method was applied in this paper to evaluate the final settlement based on three key points. The predicted values of different samples are summarized in Table 1.

Table 1. Predict Sample and Value of Three Point Method

point	Data 1		Data 2		Data 3		Δt	Value (mm)
	day	Σs	day	Σs	day	Σs		
1	284	6.7	404	10.7	524	12.1	120	15.6
2	284	8.3	404	12.3	524	14.3	120	20.5
3	232	8.5	343	13.8	454	15.9	111	24.3

Comparisons of the calculated results against measured ones and results by advanced GM (1, 1) method are given in Table 2.

Table 2. Final Settlement Value

Method	**Settlement/mm**					
	Point 1		**Point 2**		**Point 3**	
	587d	**Final**	**587d**	**Final**	**587d**	**final**
Monitored	13	13.1	14.8	15.6	17.1	18.2
GM(1,1)	12.6	14.4	15	18.6	16.3	17
Three Point		15.6		20.5		24.3

Table 2 shows that the settlement value obtained by Three-Point is slightly larger than measured value, and the value obtained by advanced GM (1, 1) method is much close to monitored value with the error less than 2%.

NUMERICAL SIMULATION BASED ON BACK ANALYSIS PARAMETERS

Based on plane Biot consolidation theory back analysis, the parameters of foundation soil were obtained and used for numerical simulation to predict long term settlements. Plane finite element program of back analysis use optimization method of complex method. The program take the absolute value of difference between monitored value V_{io} of point i and value V_i by finite element as objective function f, through the complex method optimal iterative, searching for minimum of objective function. At this time, the parameters used by finite element are optimum parameters.

Objective function f:

$$f = \sum_{i=1}^{n} \left| v_i - v_{io} \right| \tag{4}$$

where N is the number of observation points.

Using the self-made plane finite element Inversion Program, with optimal method of complex method, the optimal parameters of three back analysis sections could be obtained by iteration. Finally, mean value of all parameters of three back analysis sections are used to finite element analysis.

Numerical simulations were performed by using FLAC. Boundary conditions of chimney foundation are left, right boundary (take X direction as plane normal) and back and front boundary (take Y direction as plane normal), and the length are both 40 m. The bedrock surface was treated as bottom boundary. Boundary constraint conditions are as follows: along front boundary and back boundary, the displacement in Y direction is constrained; along left boundary and right boundary, the displacement in X direction is constrained; along bottom boundary, the displacement in Z direction is constrained. Constitutive relation of rock and soil used Mohr-Coulomb yielding criterion.

FLAC^{3D} is used to calculate the final settlement of chimney foundation (the materials properties as above mentioned). Fig.4 shows the final settlement contour map, and Fig. 5 shows the settlement contour map in Z direction of chimney foundation.

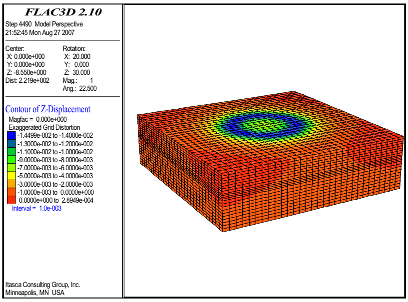

Fig. 4. Settlement contour map of foundation

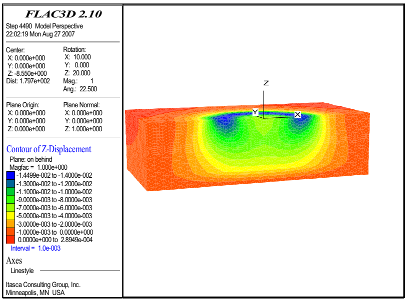

Fig.5. Settlement contour map of Z direction

Tracking the settlement value of three key observation points, and comparing them against the result from advanced GM (1,1) model and the numerical simulation, we summarized the settlement value of three points(Fig 6-8). There is an obvious difference in settlement in early stage between different methods. The difference is decreases gradually with time going on, and the settlements values are tend to coincide after 900 days.

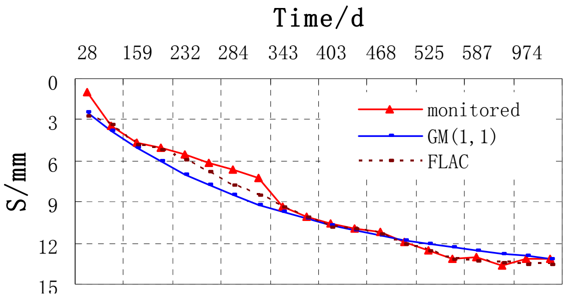

Fig.6. Settlement values of different methods of point 1

CONCLUSION

The settlement value obtained by three different methods based on previous 587 days′ data are close to the result based on the whole data. It means that just 1.5 years′ monitoring is necessary in this project.

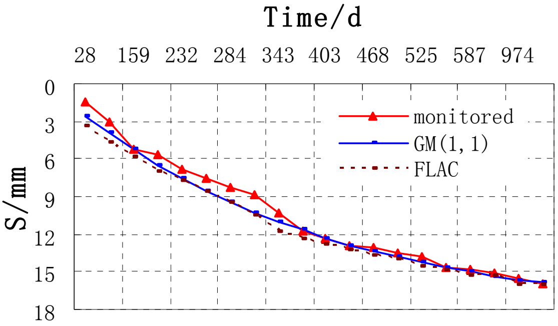

FIG.7. Settlement values of different methods of Point 2

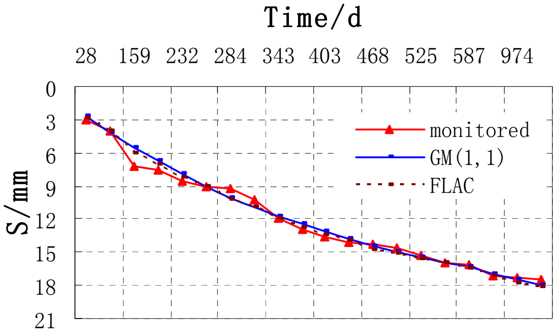

FIG.8. Settlement values of different methods of Point 3

Using the optimal parameters obtained by settlement back analysis to the numerical simulation, the result is more accurate than the result from GM (1,1).

ACKNOWLEDGMENTS

This work was supported by the China Geological Survey, No.1212010640604.

REFERENCES

Jiang, G. and Lin, L.S. (2000). "Study on grey model (GM) apply in prediction of soft foundation of road." Rock and Soil Mechanics. Vol. 21(3): 145-147.

Zhu, J.G, Wang, K.D.(2005). "Back analysis study on consolidation settlement of foundation." Rock and Soil Mechanics. Vol. 266.

Field Tests on Composite Deep-mixing-cement Pile Foundation under Expressway Embankment

Wei Wang[1], Ai-Zhao Zhou[2], and Hua Ling[3]

[1]Department of Civil Engineering, Shaoxing College of Art and Science, Shaoxing City, 312000, China; wellsking.wang@gmail.com
[2]Key Laboratory for Geomechanics and Embankment Engineering of Ministry of Education, Nanjing City, 210028, China; zhouaizhao@126.com
[3]Department of Geotechnical Engineering, Nanjing Hydraulic Research Institute, Nanjing City, 210024, China;lingh@tom.com

ABSTRACT: Anti-slide behavior of road foundation under embankment is of great importance to embankment stability in expressway engineering. Three kinds of field tests on anti-slide behavior of one expressway soft foundation improved by deep-mixing-cement pile (DMCP) are conducted, which include nature soft foundation test, single-pile foundation test and four-pile foundation test. Stress cells are placed in order to investgate the distributions of vertical stresses along the DMCP shaft during the filed tests. The investgated data show that anti-slide strength of the soft foundation increases greatly after the DMCP improvement. Single–pile foundation test and four-pile foundation test provide similar cohesion forces and friction angles, but they have different types of vertical stress growth process. Change of horizontal force only makes a little difference to vertical stress of DMCP below 6.0 m depth. This study can provide good base for relative design of expressway engineering.

INTRODUCTION

Anti-slide behavior of road foundation plays an important role in stability of embankment, and it is essential to operation and management of expressway (Nevzorov, 2002; Motuzov et al, 2004). In soft soil area, many methods are used to enhance its stability, such as cast-in-site concrete pile, preformed concrete pile, sand pile, gravel pile and DMCP (Khamov, 1997; Dong, 2004). In China mainland, DMCP has been used extensively because its cost is small relatively (Deng, 2005; Gao, 2006; Wang et al, 2006). Recently, great efforts have been devoted to studying the DMCP behavior under vertical load, while both theory and test study on DMCP anti-slide behavior under horizontal load are ignored, to some degree (Shan, 1998). In this paper, field tests on anti-slide behavior of nature soft foundation, single-pile foundation and four-pile foundation of one expressway improved by DMCP are performed and investigated, and the distribution of stress along pile is analyzed.

This test field of the expressway is near the seaside, locating in Jiangsu province, China. The nature soil foundation of the expressway is silt with gray-black color and high compressive behavior. The nature foundation has no enough anti-slide stability performance to sustain the above building expressway, because there stands a stiff slope with 8.0 m depth nearby it, shown as figure 1. Hence, it is a must to strengthen the foundation.

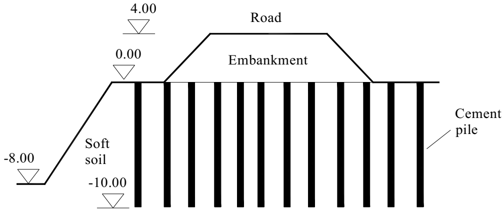

FIG. 1. Typical profile of improvement expressway foundation

Three series soil specimen are obtained form the field for chemical analysis. The average content of organic material in mass of the specimen is 1.0%, so cement with fly ash is designed as original material of DMCP to reinforce the soft foundation. 17% is determined as added ratio in mass of the cement with fly ash.

THE FIELD TESTS

In order to judge the efficiency of DMCP and to obtain reasonable design parameters for this expressway engineering, field anti-slide tests are conducted respectively, including nature soil foundation test, single-pile foundation test and four-pile foundation test. In this project, all the DMCP are with 10.0 m length and 0.5 m diameter. The loading slab is a rectangle concrete slab with 0.3 m thickness. For single-pile test, the plane size of the slab is 0.8m×0.8m. For four-pile test, the plane size of the slab is 1.6m×1.6m. Before loading test, the first step is to construct the DMCP with a flat pile head. The second step is to cast the concrete loading slab in site above the pile head and the soil around it. Age with 60 days is designed before loading test because the DMCP needs a long period to reach its designed strength.

During the single-pile foundation tests, in order to measure the vertical stress along the pile shaft, 8 stress cells are put at two sides of the pile at -0.5 m, -3.0 m, -6.0 m, -9.0 m depth, respectively, shown as figure 2. According to the area of the loading slab and the future height of above embankment, normal stresses during the horizontal shear process, namely the anti-slide tests process, are chosen as 30kPa, 60kPa, 90kPa, and 150kPa. To minimize the effect of shear stress history during the tests, four single-pile foundations are prepared corresponding above four normal stresses. The prepared four single-pile foundations are assumed to have same original property before loading tests. The horizontal force, F, is applied step by step using oil jack. Before applying F, the values of all stress cells are formatted to zero, so the incoming measured stresses by stress cells denote the additional vertical stresses due to horizontal force, F.

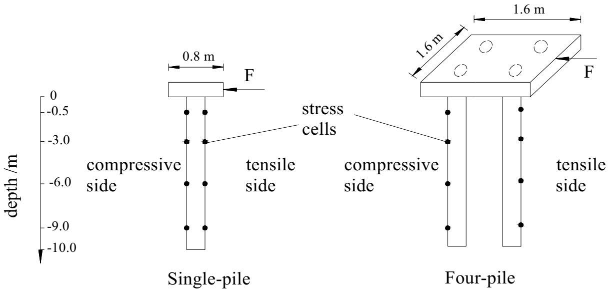

FIG. 2. Sketch of tests and stress cells

Similar to single-pile foundation tests, during the four-pile foundation tests, 16 stress cells are put at two sides of the pile to measure the vertical stress along the pile shaft, seen as figure 2. Here, depths of the cells are same to those in single-pile foundation. Applying step of horizontal force for four-pile foundation tests is same to those of single-pile foundation tests, respectively.

TESTS RESULTS ANALYSIS

Field monitoring demonstrates that the slide failure positions of both single-pile foundation and four-pile foundation are at the contacted face between DMCP and the loading slab under the smaller normal stresses. It also demonstrates that the positions are at the 0.5-2.0m depth under the loading slab under the bigger normal stresses.

Because the number of the investgated data is very large, following discussion is focued on the data investfated with 90kPa normal stress. Figure 3 shows the distribution of vertical stresses along the pile shaft of single-pile foundation under different horizontal forces, F, with 150kPa normal stress. Figure 4 shows the same distribution of four-pile foundation. In figure 4, each value of the stress is the average of two corresponding stress cells measured values, so we can only find 8 measured values while 16 stress cells put.

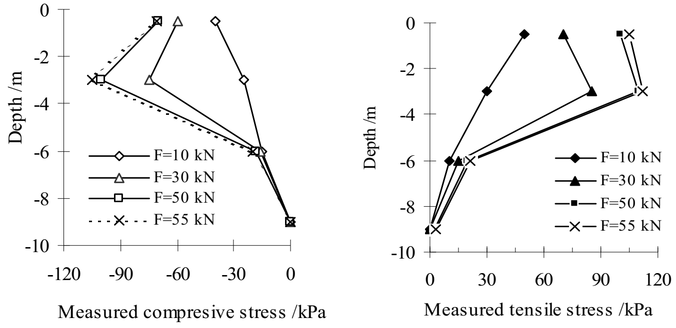

a. left compressive side **b. right tensile side**

FIG. 3. Vertical stress along the pile of single-pile foundation

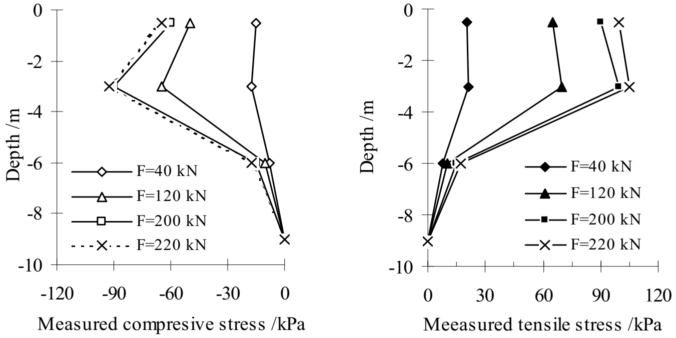

a. left compressive side **b. right tensile side**

FIG. 4. Vertical stress along the pile of four-pile foundation

According to figure 3 and 4 we can draw following conclusions.

(1) To single-pile foundation, under every step of horizontal shear force, the side of pile close to F, namely tensile side in figure 2, experiences tensile state; and the side far from F, namely compressive side in figure 2, experiences compressive state. The magnitude of tensile stress is bigger than the corresponding compressive stress at same depth. The reason may be as followings. The soil under the loading slab can reduce the action result to compressive side by soil-slab-pile interaction, but it cannot reduce the action result to tensile side because the tensile strength of soil is very small. It is evident that the anti-slide behavior of DMCP is different to that of common rigid pile.

(2) To four-pile foundation, under the same horizontal shear stress, both the compressive stress and tensile stress along the pile are smaller than that of corresponding single-pile foundation. Especially, the reduction of compressive stress is significant. The reason may be as followings. Expect for soil-slab-pile interaction like single-pile foundation, the large loading stab and soil around it give rise to arch effect to decrease the compressive stress acutely. The four-pile foundation tests provide enough evidence that the anti-slide behavior of DMCP is different to that of common rigid pile.

(3) Whatever the normal stress is, both compressive stress and tensile stress decrease with increasing depth to some degree. The maximum magnitudes positions are not near the pile head but at 0.5-2.0m depth. Horizontal shear force is mainly balanced by upper soil and pile. Stresses along pile within 6.0m depth increase obviously when horizontal shear force increase. However, when depth is bigger than 06.m, stresses along pile is not sensitive to change of horizontal shear force.

Based on measured data, the normal stress versus shear strength curves of nature soil foundation, single-pile foundation and four-pile foundation, are described as Figure 5. Figure 5 demonstrates that above three foundations all obey the Mohr-Coulomb criterion, and their horizontal shear strengths can be expressed:

$$\tau_f = c + \sigma \tan \phi \tag{1}$$

where τ_f is horizontal shear strength of the foundation; c is cohesion force of the foundation; ϕ is friction angle of the foundation; σ is vertical normal stress.

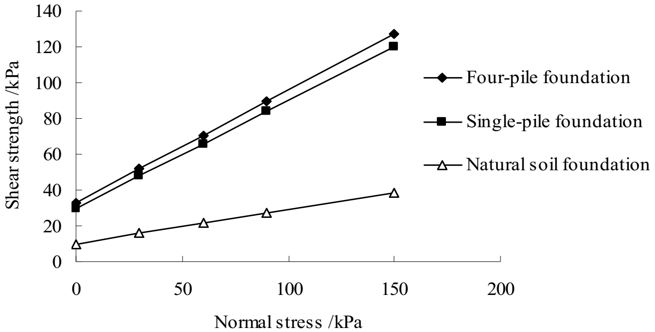

FIG. 5. Normal stress versus shear strength of three kinds foundations

According to equation (1) and Figure 5, cohesion forces of nature soil foundation, single-pile foundation and four-pile foundation are determined as 10kPa, 30kPa, 33kPa, respectively; their friction angles are determined as 11^0, 31^0 and 32^0, respectively. So behavior of foundation improved by DMCP is much better than behavior of nature soil foundation. It should be noted that, cohesion force and friction angle of single-pile foundation are approximately equal to that of four-pile foundation, so we can make use of mechanic parameters from single-pile foundation test to design and manage expressway engineering.

CONCLUSIONS

Anti-slide behavior of one expressway foundation improved by DMCP are investigated and analyzed by field tests, which include nature soft foundation test, single-pile foundation test and four-pile foundation test. According to field tests, following conclusions are drawn for the foundation with horizontal shear force.

(1) Behavior of foundation improved by DMCP is much better than that of nature soil foundation. The increase of cohesion force is more than 20kPa, and the increase of friction angle is more than 20^0.

(2) Cohesion force and friction angle of single-pile foundation are approximately equal to those of four-pile foundation.

(3) Behavior of DMCP foundation is much different to that of rigid pile foundation. Because of soil-slab-pile interaction and arch effect, compressive stress of four-pile foundation is much less than that of corresponding single-pile foundation.

(4) Horizontal shear force is mainly balanced by upper soil and pile. Stresses along pile within 6.0m depth increase obviously when horizontal shear force increase. However, when depth is bigger than 06.m, stresses along pile is not sensitive to change of horizontal shear force.

ACKNOWLEDGMENTS

The authors appreciate the support of Zhejiang Provincial Natural Science Foundation of China under Grant No. Y1080839 and the support of Zhejiang Provincial Excellent Young University Teacher Foundation under Grant No. 2008-176.

REFERENCES

Deng Y. F. (2005). "Maximum lateral deformation of dry mixing column composite foundation in expressway engineering." Rock and Soil Mech., 26(4): 604-607.

Dong P. (2004). "Bearing capacity and settlement of concrete-cored DCM pile in soft ground." Geotech. and Geolog. Engrg., 22(1): 105-119.

Gao J. C. (2006). "DCM and DJM in-situ test of soft clay modification in highway engineering." J. Highway and Transportation Research and Develop., 23(4):53-55.

Khamov A. P. (1997). "Injection of clay-cement grout to strengthen the beds of buildings and structures." Soil Mech. and Found. Engrg., 34(3): 90-93.

Motuzov Y. Y., Ibragimov M. N. and Semkin V. V. (2004). "Experience with stabilization of weak slimy soils." Soil Mech. and Found. Engrg., 41(1): 13-17.

Nevzorov A. (2002). "Experience with the installation of soil-cement piles during the reconstruction of a factory." Soil Mech. and Found. Engrg ., 39(1): 31-34.

Shan L. (1998). "In-site experimental investigation of the horizontal loads for composite foundation of dry-injection cement mixing piles." Water and Hydraulic Tech., 29(5): 13-15.

Wang W., Lu T. H., Wang X. N. (2006). "Study on settlement curve of ramp loading roadbed on soft ground." Rock and Soil Mech., 27(5): 791-794.

Design of Ballasted Railway Track Foundations under Cyclic Loading

Mohamed A. Shahin, M. ASCE

Senior Lecturer, Department of Civil Engineering, Curtin University of Technology, GPO Box U1987, Perth WA 6845, Australia; m.shahin@curtin.edu.au

ABSTRACT: The foundations of ballasted railway tracks are usually consisted of a graded layer of granular media of ballast placed above a naturally deposited subgrade. Available methods for design of track foundations are based on determination of an adequate granular layer thickness of ballast so that subgrade shear failures and plastic deformations produced by the transmission of imposed train loads are prevented. However, the deformation of ballast itself is ignored in almost all available design methods. In addition, most available methods do not represent true cyclic loading situations and rather provide oversimplified solutions based on static loading conditions. In this paper, a method that can be used to calculate the deformation of ballast under train cyclic loading is presented. The method is deemed to complement the existing methods of design of ballasted railway track foundations.

INTRODUCTION

The design of ballasted railway track foundations requires an accurate estimation of the granular layer thickness of ballast that provides protection against subgrade failures and excessive track settlement induced by train cyclic loading. In order to achieve track stability, the total deformation of ballast and subgrade should not exceed an acceptable value. However, the deformation of ballast layer is ignored in almost all available design methods despite the fact that ballast can be responsible for up to 60% of track deformation, as experimentally investigated by Indraratna et al. (2001).

Several simplified theoretical and empirical methods have been proposed in the literature for design of railway track foundations. For example, the British Railways method (Heath et al. 1972) and American Railway Engineering Association method (AREA 1996). However, these methods do not consider the properties of each individual track layer and assume a single homogeneous elastic half-space to represent ballast and subgrade. Other more complex theoretical and numerical solutions have been also developed including the multi-layer theory and finite element method (e.g. Chang et al. 1980; Huang et al. 1986). However, these methods ignore (or improperly represent) the effects of repeated cyclic loads on ballast and subgrade. More recently, Li and Selig (1998) developed a method that considers the plastic deformation of subgrade layer under train cyclic loading but ignores the deformation of ballast layer.

In this paper, a method that can be used to calculate the deformation of ballast layer under true cyclic loading conditions is developed and presented. The method is based on a combination of experimental test results carried out on different types of ballast and 3D finite element simulation (PLAXIS). The method is intended to complement existing design methods of railway track foundations so that ballast deformation can be considered.

DESIGN METHODOLOGY

The proposed design methodology is based on the concept that the total deformation of railway track under repeated train loads is the summation of plastic (permanent) deformations of ballast and subgrade. The plastic deformations of ballast and subgrade can be obtained if their cumulative plastic strains are multiplied by the corresponding track thicknesses. The plastic strain of fine-grained subgrade under repeated train loads can be determined using the model proposed by Li and Selig (1998). In this paper, a laboratory based model that can be used to obtain the plastic strain of three different types of ballast (i.e. basalt, granite and dolomite) under train repeated loads is proposed as follows:

$$\varepsilon_b = a(\frac{\sigma_d}{\sigma_s})^m (1+\ln N)^b \qquad (1)$$

where: ε_b is the percentage cumulative plastic strain of ballast; σ_d is the applied deviator stress; σ_s is the compressive strength of ballast which can be obtained from static triaxial loading tests; N is the number of repeated load applications; and a, b, m are regression parameters depend on the ballast type. Equation (1) above is calibrated using results of a series of large-scale triaxial, isotropically consolidated, drained cyclic compression tests reported by Alva-Hurtado (1980), Lackenby (2006) and Raymond and Williams (1978). The calibration results are shown in Figure (1) in which the solid lines represent the model prediction and $\alpha = \sigma_d / \sigma_s$.

For a certain track of N number of load cycles, ε_b can be determined by knowing σ_d applied on the track ballast layer and using Equation (1). In this paper, it is proposed that σ_d is obtained from a 3D finite element simulation similar to the one described in the next section.

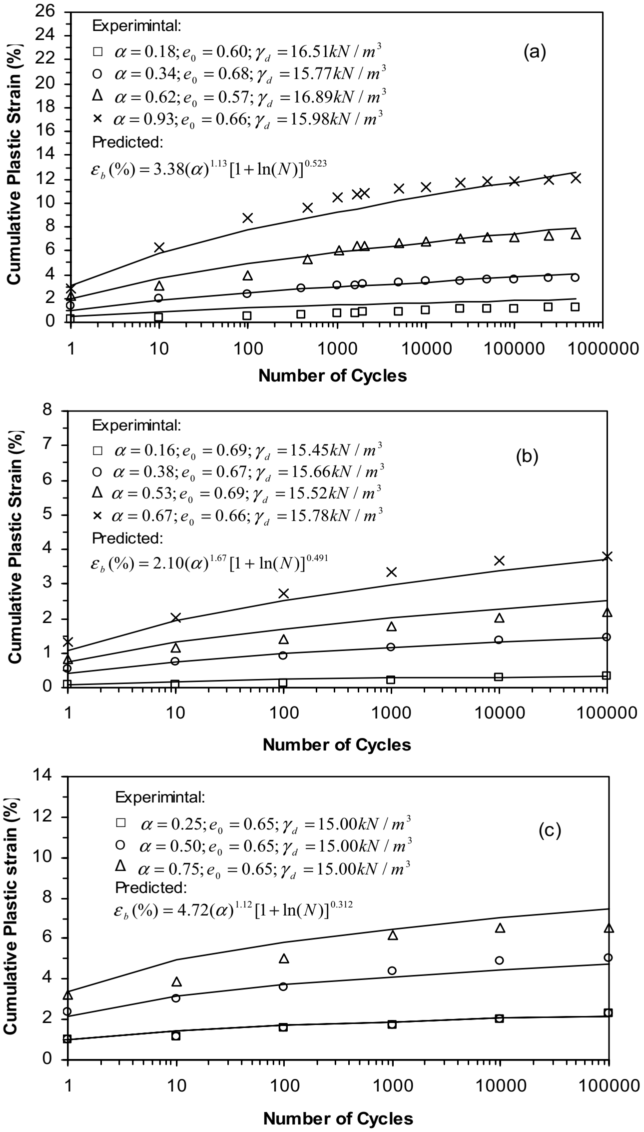

FIG. 1. Comparison of predicted versus measured cumulative plastic strains for: (a) basalt; (b) granite; (c) dolomite.

3D FINITE ELEMENT SIMULATION

Figure 2 shows an example of a 3D finite element simulation that can be used to determine the deviator stress σ_d needed for calculation of ballast plastic strain in Equation (1). The 3D finite element analysis is conducted using PLAXIS 3D Foundation Version 2.1 (PLAXIS 2007). As can be seen from Figure 2, the 3D track section is simulated using five sleepers spaced by a distance of 0.6 m centre-to-centre, therefore, the track has a length of 2.6 m. It should be noted that five sleepers are used in this work as a comparison study carried out by Shahu et al. (1999) using five and seven sleepers indicated that stresses and displacements in railway tracks can be sufficiently simulated using five sleepers. Due to symmetry, only one half of the track is considered in the numerical model.

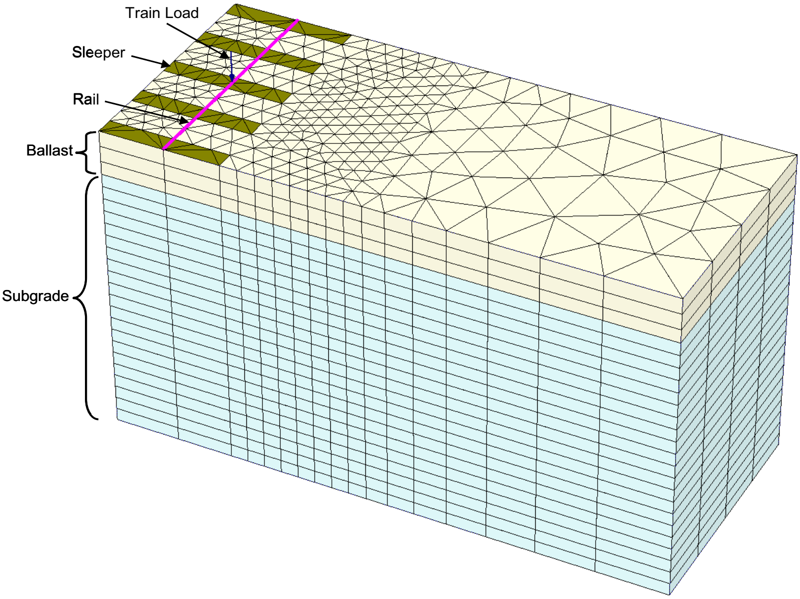

FIG. 2. Finite element configuration used in PLAXIS 3D simulation.

Roller boundary conditions are used in the vertical directions to warrant symmetry and to simulate end of soil, whereas fixed boundary conditions are used at the bottom to simulate bedrock. The track foundation is discretized using 15 node wedge elements available in PLAXIS. The rail is simulated using 3D beam element whereas the sleepers are modeled using 3D floor elements. The minimum required mesh discretization is determined by carrying out a sensitivity analysis on various mesh dimensions until an optimal mesh size is obtained. The gauge length of the track is 1.4 m, and the 3D track dimensions and material properties are given in Table 1. The train wheel load is modeled by applying a concentrated load of 150 kN at the centre sleeper. This load represents an axle train load of 25 tons with dynamic impact of 20%. This track is selected to represent timber sleeper tracks of the New South

Wales State Rail Authority, Australia.

The results of the finite element simulation are shown in Figure 3, from which σ_d applied on the ballast layer can be obtained. It should be noted that similar finite element simulation that was developed by the author and calibrated with published field measurements (see Shahin and Indraratna 2006) indicates the validity of the results obtained from the current model. As mentioned previously, σ_d obtained from Figure 2 can be substituted in Equation (1) so that the plastic strain of ballast can be calculated which then can be multiplied by the ballast thickness to obtain the deformation of ballast layer.

Table 1. Track Properties Used in the 3D Finite Element Analysis

Material Property	**Track Component**			
	Rail	**Sleeper**	**Ballast**	**Subgrade**
Material model	Elastic	Elastic	Mohr-Coulomb	Mohr-Coulomb
Modulus of elasticity, *E* (MPa)	210000	10000	150	10
Poisson's ratio, ν	0.15	0.15	0.35	0.4
Unit weight, γ (kN/m^3)	78	8	16	20
Cohesion, *c* (kPa)	N/A	N/A	0.0	20
Friction angle, φ (degree)	N/A	N/A	45	25
Thickness (m)	0.15	0.2	0.65	3.0
Width (m)	0.15	0.25	6.0	6.0

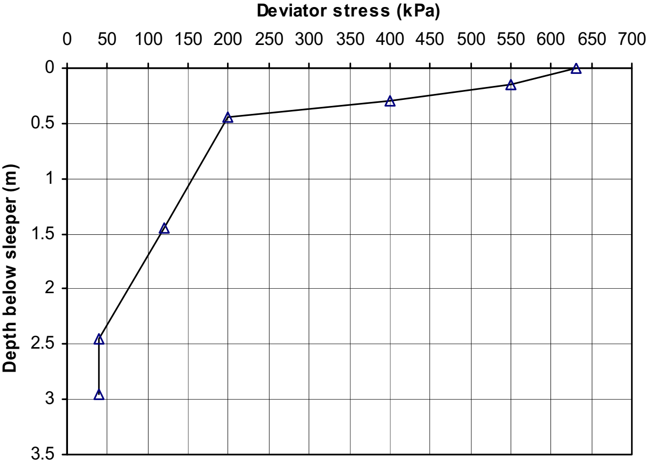

FIG. 3. Deviator stress of the 3D finite element simulation.

CONCLUSIONS

A method was developed and presented to obtain the deformation of ballast in design of railway tracks. The method was based on experimental results carried out on different types of ballast (i.e. basalt, granite and dolomite) and 3D finite element analysis. The method is a useful tool for design of ballasted track foundations and complement existing methods. However, for completeness, further improvement and verification with field cases are needed.

REFERENCES

Alva-Hurtado, J. E. (1980). "A methodology to predict the elastic and inelastic behavior of railroad ballast," PhD Thesis, University of Massachusetts, Amherst.

AREA. (1996). *Manual for railway engineering*, Washington, D. C.

Chang, C. S., Adegoke, C. W., and Selig, E. T. (1980). "GEOTRACK model for railroad track performance." *Journal of Geotechnical Engineering Division*, ASCE, 106(GT11), 1201-1218.

Heath, D. L., Shenton, M. J., Sparrow, R. W., and Waters, J. M. (1972). "Design of conventional rail track foundations." *Proceedings of the Institute of Civil Engineering*, 51, 251-267.

Huang, Y. H., Lin, C., Deng, X., and Rose, J. (1986). "KENTRACK, finite element computer program for the analysis of railroad tracks." Department of Civil Engineering, University of Kentucky, Lexington, KY, USA.

Indraratna, B., Salim, W., Ionescu, D., and Christie, D. "Stress-strain and degradation behaviour of railway ballast under static and dynamic loading, based on large-scale triaxial testing." *Proceedings of the 15th International Conference of Soil Mechanics and Geotechnical Engineering*, Istanbul, 2093-2096.

Lackenby, J. (2006). "Triaxial behavior of ballast and the role of confining pressure under cyclic loading," PhD Thesis, University of Wollongong, NSW.

Li, D., and Selig, E. T. (1998). "Method for railroad track foundation design." *Journal of Geotechnical and Geoenvironmental Engineering*, ASCE, 124(4), 316-329.

PLAXIS, B. V. (2007). *PLAXIS 3D Foundation Version 2.1-Finite element code for soil and rock analysis*, Delft, The Netherlands.

Raymond, G. P., and Williams, D. R. (1978). "Repeated load triaxial tests on a dolomite ballast." *Journal of the Geotechnical Engineering Division*, ASCE, 104(GT7), 1013-1029.

Shahin, M. A., and Indraratna, B. "Parametric study on the resilient response of ballasted railway track substructure using numerical modeling." *ASCE Geocongress 2006*, Atlanta, Proceedings on CD-ROM.

Shahu, J. T., Rao, N. S. V., and Yudhbir. (1999). "Parametric study of resilient response of tracks with a sub-ballast layer." *Canadian Geotechnical Journal*, 36(6), 1137-1150.

Simulation and Amelioration of Wu-Bauer Hypoplastic Constitutive Model under Dynamic Load

Baolin Xiong[1]and Chunjiao Lu[2]

[1]Department of Civil Engineering, Shijiazhuang Railway Institute,Hebei, Shijiazhuang, 050043, People's Republic of China; PH (86-311) 87939195; email: xiongbao77@126.com
[2]Department of Architecture and Art Design, Shijiazhuang Railway Institute,Hebei, Shijiazhuang, 050043, People's Republic of China; PH (86-311) 87939195; email: ruyan1978@126.com

ABSTRACT: The stress-strain relation of sand can be modeled with Wu-Bauer hypoplastic constitutive model, in which the magnitude and direction of stress increment depend on not only the previous stress state, but also the magnitude and direction of current strain increment. The parameters of this model can be determined conveniently by simple triaxial test. Under static load Wu-Bauer hypoplastic constitutive model can well simulate strength and deformation of sand. But under dynamic load, the major shortcoming–ratcheting is produced in Wu-Bauer hypoplastic constitutive model. For eliminating ratcheting, Wu-Bauer hypoplastic model is ameliorated based on intergranular strain tensor. The new parameters in ameliorated model are determined by mode search method. Under cyclic load of oedometric compression and undrained dynamic triaxial, the mechanics features of sand are described by the ameliorated Wu-Bauer hypoplastic constitutive model. Preliminary result shows that stress-strain relation of sand under dynamic load can be well considered and ratcheting may be removed in the ameliorated Wu-Bauer hypoplastic constitutive model.

INTRODUCTION

Hypoplasticity appeared about 30 years ago as an alternative to elasto-plasticity for the description of the irreversible behaviour of soils and has since then attracted the attention of many geotechnical scholars (Dafalias 1986; Kolymbas 1991). The theory is based on nonlinear tensorial functions and is developed without recourse to the concepts in elasto-plastic theory such as yield surface, flow rule and the decomposition of the deformation into elastic and plastic parts (Wu and Kolymbas 1990). The hypoplastic model to describe the mechanical behaviour of cohesionless sand was studied (Wu and Bauer 1994). By adopting a specific function, it is shown that many salient features of sand could be reproduced. The hypoplastic model is called as Wu-Bauer hypoplastic model.

Hypoplastic models have been shown to perform very well for deformations due to rearrangements of the grain skeleton. However, application of hypoplasticity to cyclic stressing or deformation with small amplitudes reveals some defects(Bauer and Wu 1993). The most striking shortcoming is an excessive accumulation of deformation predicted for small stress cycles, called ratcheting. For undrained cyclic shearing the hypoplastic approach predicts too large a build-up of pore pressure. In order to consider mechanics property of sand under dynamic load, Gudehus-Bauer hypoplastic model is ameliorated by introduction of intergranular strain tensor (Niemunis and Herle 1997). Firstly defect of simulation of hypolastic model under cyclic load is given. Then based on intergranular strain tensor Wu-Bauer hypoplastic model is ameliorated. The ameliorated Wu-Bauer hypoplastic model is compared with experiment. Finally conclusion is drawn.

SIMULATION OF HYPOLASTIC MODEL UNDER CYCLIC LOAD

The hypoplastic constitutive model is generally described by a single non-linear tensorial equation:

$$\overset{\circ}{\boldsymbol{\sigma}} = \mathbf{L}\mathbf{D} + \mathbf{N}\|\mathbf{D}\| \tag{1}$$

Now, we demonstrate briefly the major shortcoming of hypoplasticity-ratcheting. For small strain cycles in a 1D case, equation (1) can be simplified to the scalar form:

$$\dot{\sigma} = LD + N|D|\,;\quad 0 < -N < L \tag{2}$$

Values of L and N can be considered constant during a cycle provided that the change of stress is small. The accumulated stress in one strain cycle, $\pm\,\Delta\varepsilon = \pm D\Delta t$, is then

$$\Delta\sigma^{acc} = L\Delta\varepsilon + N|\varepsilon| + L(-\Delta\varepsilon) + N|-\Delta\varepsilon| = 2N|\Delta\varepsilon| \tag{3}$$

An accumulation of strain, viz.,

$$\Delta\varepsilon^{acc} = \frac{\Delta\sigma}{L+N} + \frac{-\Delta\sigma}{L-N} = \frac{-2N}{L^2-N^2}\Delta\sigma \tag{4}$$

is similarly calculated but for a small stress cycle. In both cases the accumulation is generally too large compared with experimental results. So the hypoplastic model needs improvement.

INTRODUCTION OF INTERGRANULAR STRAIN TENSOR

It is convenient to denote the normalized magnitude of $\boldsymbol{\delta}$ as:

$$\rho = \frac{\|\boldsymbol{\delta}\|}{R} \tag{5}$$

and the direction of intergranular strain as:

$$\hat{\boldsymbol{\delta}} = \begin{cases} \dfrac{\boldsymbol{\delta}}{\|\boldsymbol{\delta}\|} & \text{for } \boldsymbol{\delta} \neq \mathbf{0}, \\ \mathbf{0} & \text{for } \boldsymbol{\delta} = \mathbf{0}. \end{cases} \tag{6}$$

The general stress-strain relation is written as:

$$\overset{\circ}{\boldsymbol{\sigma}} = \boldsymbol{\zeta} : \mathbf{D} \tag{7}$$

The fourth-order tensor $\boldsymbol{\zeta}$ represents stiffness and is calculated from the hypoplastic tensors $\boldsymbol{\xi}(\boldsymbol{\sigma})$ and $\mathbf{N}(\boldsymbol{\sigma})$, which may be modified by scalar multipliers m_T and m_R. For general case, we calculate stiffness $\boldsymbol{\zeta}$ using the following interpolation:

$$\boldsymbol{\zeta} = \left[\rho^{\chi} m_T + \left(1-\rho^{\chi}\right) m_R\right]\boldsymbol{\xi} + \begin{cases} \rho^{\chi}\left(1-m_T\right)\boldsymbol{\xi} : \hat{\boldsymbol{\delta}}\hat{\boldsymbol{\delta}} + \rho^{\chi}\mathbf{N}\hat{\boldsymbol{\delta}} & \text{for } \hat{\boldsymbol{\delta}} : \mathbf{D} > 0, \\ \rho^{\chi}\left(1-m_T\right)\boldsymbol{\xi} : \hat{\boldsymbol{\delta}}\hat{\boldsymbol{\delta}} & \text{for } \hat{\boldsymbol{\delta}} : \mathbf{D} \le 0. \end{cases} \tag{8}$$

Where ρ^{χ} is a weighting factor and χ is a constant.

The evolution equation for the intergranular strain tensor $\boldsymbol{\delta}$ is supposed as:

$$\overset{\circ}{\boldsymbol{\delta}} = \begin{cases} \left(\mathbf{I} - \hat{\boldsymbol{\delta}}\hat{\boldsymbol{\delta}}\rho^{\beta_r}\right) : \mathbf{D} & \text{for } \hat{\boldsymbol{\delta}} : \mathbf{D} > 0, \\ \mathbf{D} & \text{for } \hat{\boldsymbol{\delta}} : \mathbf{D} \le 0. \end{cases} \tag{9}$$

Where $\overset{\circ}{\boldsymbol{\delta}}$ is the objective rate of intergranular strain tensor. The exponent β_r is a material constant.

AMELIORATION OF WU-BAUER HYPOPLASTIC MODEL CONSIDERING INTERGRANULAR STRAIN TENSOR

The following expressions substitute for $\boldsymbol{\xi}$ and $\mathbf{N}$ of Eq. (8) and then the ameliorated Wu-Bauer hypoplastic model considering intergranular strain tensor is obtained.

$$\boldsymbol{\xi} = C_1 tr(\boldsymbol{\sigma})\mathbf{D} + C_2 \frac{tr(\boldsymbol{\sigma}\mathbf{D})}{tr(\boldsymbol{\sigma})}\boldsymbol{\sigma} \tag{10}$$

$$\mathbf{N} = C_3 \frac{\boldsymbol{\sigma}^2}{tr(\boldsymbol{\sigma})} + C_4 \frac{\boldsymbol{\sigma}^{*2}}{tr(\boldsymbol{\sigma})} \tag{11}$$

Five constitutive parameters are increased in the ameliorated Wu-Bauer hypoplastic model: R, m_R, m_T, β_r and χ. Experiment of oedometric condition in cyclic load is simulated by the ameliorated Wu-Bauer hypoplastic model. Based on simulation goal function about five parameters is established. The minimum value of goal function is obtained by virtue of mode search method and then corresponding five variables are five parameters that are sought for.

Firstly deformation of Shifosi sand under oedometric condition in ten cyclic loads is simulated by the ameliorated Wu-Bauer hypoplastic model. Weight is increased from 0, 50kPa, 100kPa, 200kPa, 400kPa to 800kPa by grade and then unloaded to 0 by grade. The other nine cyclic loads are in this way. The nine parameters of Shifosi sand are given in table 1. The computed results are compared with experiment (as shown in Fig.1).

Table 1 Nine constitutive parameters in the ameliorated Wu-Bauer hypoplastic model

C_1	C_2	C_3	C_4	R	m_R	m_T	β_r	χ
-74.6	-660.2	-640.3	679.5	0.0001	5.202	2.151	0.258	4.807

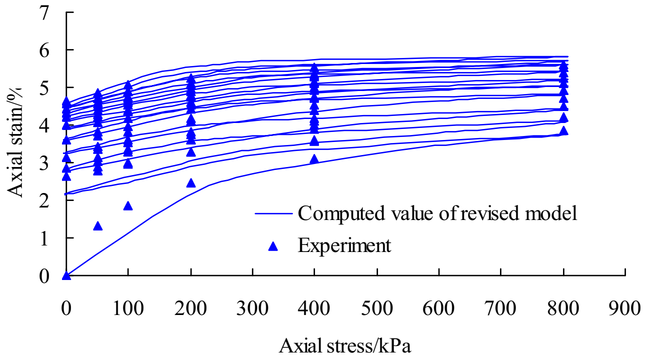

Fig. 1. Contrast of the ameliorated Wu-Bauer hypoplastic model and experiment under 10 cycles in oedometric condition

From Fig.1, strain of sand under cyclic load is well simulated by the ameliorated Wu-Bauer hypoplastic model. With more cyclic times, the degree of deformation becomes less. Relationship curve of axial stress over intergranular strain δ_{11} is shown as Fig. 2.

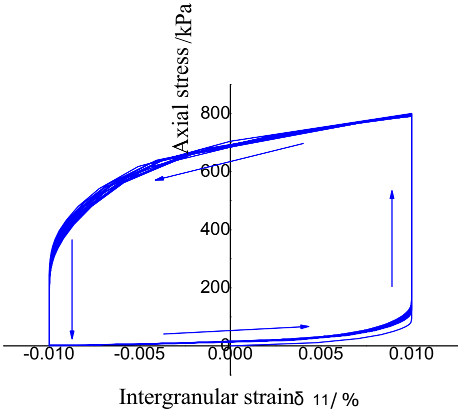

Fig. 2. Relationship curve of axial stress over δ_{11} under 10 cycles in oedometric condition

From Fig.2, in forepart of loading stage of each cycle the absolute value of axial intergranular strain δ_{11} attains maximum value and then keeps constant until axial stress reaches maximum value.

Then pore water pressure and effective stress of Shifosi sand under dynamic triaxial are simulated by the ameliorated Wu-Bauer hypoplastic model. The cell pressure is 300kPa. The computed results are shown in Fig.3.

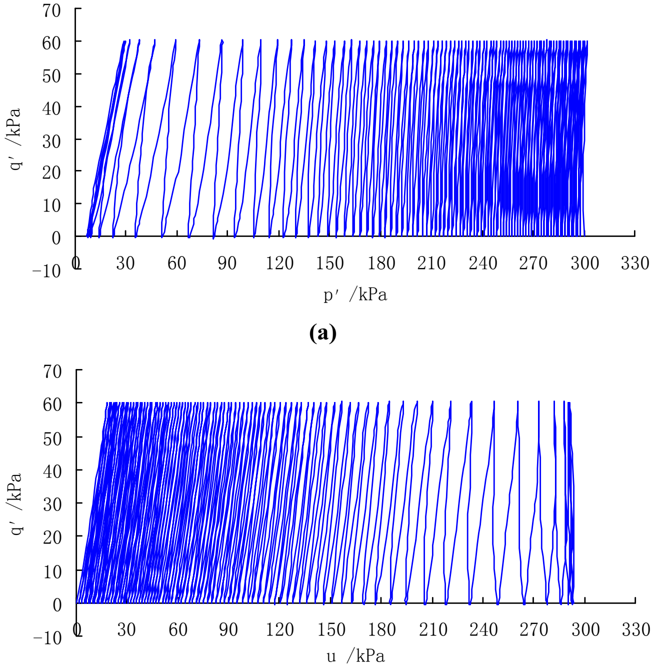

(a)

(b)

Fig. 3. Simulation of the ameliorated Wu-Bauer model (a) q' over p'; (b) q' over u

From Fig.3, the accumulation of pore water pressure and reduction of effective stress can be considered by the ameliorated Wu-Bauer hypoplastic model considering intergranular strain tensor. Under dynamic triaxial relationship curve of deviatoric stress over intergranular strain is shown as Fig. 4.

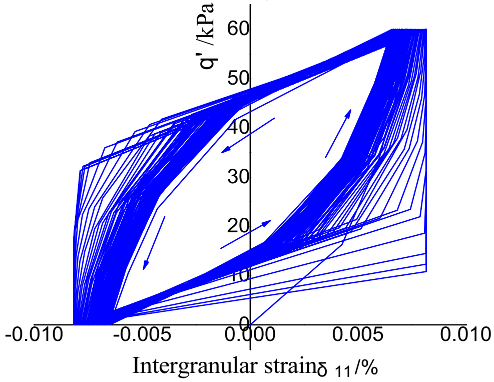

(a)

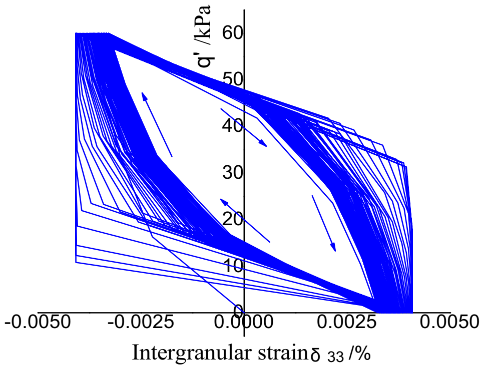

(b)

Fig.4 Relationship curve of deviatoric stress over intergranular strain in the cell pressure of 300kPa: (a) q' over δ_{11}; (b) q' over δ_{33}

From Fig.4, the absolute value of intergranular strain is very small. In the same deviatoric stress, the corresponding absolute value of intergranular strain δ_{11} is two times as large as that of δ_{33}.

CONCLUSION

Aiming at the shortcoming of hypoplasticity under dynamic load, Wu-Bauer hypoplastic model is ameliorated by introduction of intergranular strain tensor. The accumulation deformation of sand in oedometric condition under cyclic load can be considered and accumulation of pore water pressure and reduction of effective stress of sand under dynamic triaxial can be simulated by the ameliorated Wu-Bauer hypoplastic model.

REFERENCES

Dafalias Y. F.(1986) “Bounding surface plasticity, I: Mathematical foundation and hypoplasticity.” *Engineering Mechanics*, ASCE, 112(9): 966-987.

Kolymbas D.(1991) “An outline of hypoplasticity.” *Archive of Applied Mechanics*, 61(2): 143-151.

Wu W. and Kolymbas D. (1990) “Numerical testing of the stability criterion for hypoplastic constitutive equations.” *Mechanics of Materials*, 9(4): 245-253.

Wu W. and Bauer E. (1994) “A simple hypoplastic constitutive model for sand.” *International Journal for Numerical and Analytical Methods in Geomechanics*, 18:833-862.

Bauer E. and Wu W.(1993) “A hypoplastic model for granular soils under cyclic loading.” *Modern Approaches to Plasticity*, Elsevier, 247-258.

Niemunis A.and Herle I. (1997) “Hypoplastic model for cohesionless soils with elastic strain range.” *Mechanics of Cohesive-Frictional Materials*, 2:279-299.

Geotechnical Properties of Controlled Low Strength Materials (CLSM) Using Waste Electric Arc Furnace Dust (EAFD)

Alireza Mirdamadi[1], Shariar Sh. Shamsabadi[2], M. G. Kashi[3], M. Nemati[4], and M. Shekarchizadeh[5]

[1]M.S. in Geotechnical Engineering, Construction Materials Institute (CMI), University of Tehran, Tehran, Iran; mirdamad@gmail.com
[2]B.S. Student in Civil Engineering, University of Tehran, Construction Materials Institute (CMI), Tehran, Iran; shahriarsh86@yahoo.com
[3]PhD. of Concrete Technology, Research Advisor of CMI
[4]PhD. Student in Structural Engineering, University of Tehran, Construction Materials Institute (CMI), Iran
[5]Assistant Professor, Director of Construction Materials Institute (CMI), University of Tehran, Iran

ABSTRACT: Controlled low-strength material (CLSM) is a self-compacted cementitious material used primarily as a backfill in place of compacted soil. It is also known as a flowable fill which is usually a mixture of fine aggregates, small amount of cement, and water. Usage of by-product materials is common as fine aggregates in flowable fill materials. Electric Arc Furnace Dust (EAFD) is a solid waste generated in the collection of particulate material during steelmaking process in electric arc furnace. In this study EAFD was tested for the possibility of producing CLSM with large proportion of this waste. The main properties measured in this research include EAFD chemical properties and EAFD flowable fill geotechnical properties (unconfined compressive strength, California Bearing Ratio (CBR), flowability, and setting time) for different mix proportion. Results indicate that with a good mix design it is possible to produce a CLSM with acceptable mechanical properties to meet design requirements.

INTRODUCTION

Utilization of unmarketable or uneconomic industrial waste materials, has found successful application as backfills, anticorrosion fills, thermal fills, and durable pavement bases (ACI 1999); Controlled low-strength materials (CLSM) are an effective and practical alternative to the above mentioned technologies; A controlled low strength material (CLSM) also known as flowable fill is a self-compact material which is usually a mixture of cement, fine aggregates, water and a by-product material such as fly ash. The American Concrete Institute (ACI) Committee 229 defines CLSM as materials resulting in a compressive strength of 8.3 MPa or less (ACI 1999). Gabr and Bowders (2000) recommend that if the mixture is intended to be removed at a later date the maximum design strength should be around 2 MPa after 28 days of curing in order to be easily excavated by mechanical equipment. A minimum compressive strength of 0.44 MPa should be achieved to provide sufficient support for construction and vehicle loads (Bouzalakos. et al. 2008). Due to this characteristic, EAFD shows passable qualifications as a part of flowable fill mixture. Flowable fill is often proportioned to develop strengths much less than the limit to allow for future excavation, e.g., 0.86 MPa at day 28 for Types A and B flowable backfills as defined by US Pennsylvania Department of Transportation (US PennDOT, 2003). Depending upon the unconfined compressive strength (UCS) and density, US PennDOT (2003) also defines the other two types of flowable fills: Type C non-excavatable flowable fill having 28-day UCS strength over 5.51 MPa, and Type D low-density flowable fill.

Electric Arc Furnace Dust (EAFD), is by-product material disposed during steelmaking process in electric arc furnace. Since Pb and Cd elements are more than exceeding limit permitted by the NBR 10005, according to NBR 10004 it is classified as dangerous solid waste-class I. Mainly, this dust is re-injected into the furnace as the principal ingredient of producing iron. As a result of its huge amount of generation which is between 15 to 25 kg of dust per ton of steel most of EAFD produced during this process is unused (G. Lee and Y. Song 2007), due to this properties, growing generation of this dust have became an environmental concern in many countries, so studying new ways of recycling this material seems to be necessary.

EAFD used in this experiment has been collected from Esfahan’s Mobarake steel company in Iran which produces about 4.5 million tons of steel per year while it’s increasing to 7 million tons in future. Huge amount of EAFD which produces in this company has not been used in a specific way and left in environment without considering its harmful effects. In order to take advantage of economical and environmental benefits of utilization of this material, EAFD can be used as flowable fill component. In order to study the feasibility of applying this by-product in flowable fill, number of tests has been done. All tests were conducted on various mixtures according to ASTM standards contained Initial Flowability, Flow Consistency, Setting time, California Bearing Ratio (CBR) and Unconfined Compressive Strength (UCS).

EXPERIMENTL PROGRAM

Materials

The basic constituent materials used in producing the flowable fill mixtures in this research were: EAFD as fine aggregates, cement as the blinder, and tap water. All flowable fill mixtures use EAFD as the major constituent of the mixture due to maximize the utilization of waste material.

- Electric Arc Furnace Dust (EAFD)

The chemical properties of the EAFD used in this study have been shown in Table 1. Chemical analysis shows significant amount of CaO (Calcium dioxide) in EAFD. Adding water to this mixture causes heat and expansion which is a result of presentation of considerable amount of CaO and should be considered in mixing procedure. A sample of EAFD is shown in Figure 1.

Table 1. Chemical properties of EAFD

Constituents	CaO	MgO	Al_2O_3	Fe	FeO	Fe_2O_3	SiO_2
Percentage	25	3.5	20.2	31.4	8.9	33.7	6

Figure 1. EAFD sample

- Cement and admixture

Type II Portland Cement complying with ASTM C150 to providing proper value of cohesion and strength was used for preparation of the test specimens.

Mix proportions and specimen preparation

The flowable fill compositions used in the experimental studies are presented on Table 2. These compositions were chosen after a series of pre-trials. The testing program was performed on 3 Mixtures. In order to investigate the effect of cement content, the cement range 150 kg/m^3 to 250 kg/m^3 was used in mix proportion. Water content was adjusted to provide a initial flow of about 250 to 350 mm according to ASTM D6103 and ranged 500 to 600 kg/m^3 (Table 2).

Table 2. Mix proportions (kg/m^3)

Mix ID	EAFD	Cement	Water	Tests*
M-1	1410	150	500	F
M-2	1200	200	600	F, ST, UCS, CBR
M-3	1140	250	600	F, ST, UCS, CBR

*F- Flowability
ST- Setting time
UCS- Unconfined Compressive Strength
CBR - California Bearing Ratio (CBR)

The procedure for producing flowable material was according to ACI 229R-99. First, About 70% of water was poured in mixer, and then half of EAFD was added gradually when mixer was working. After about 1 min, cement and after that remaining of EAFD and water were added to mixture respectively. The mixture was blended for approximately 5 min in Hobart mixer, until the produced slurry turned into a homogeneous phase.

Properties of the fresh mix (flowability and setting time) were tested after mixing process. Because of high water content in mixture, setting (according to ASTM C403) in specimens could not be determined, so setting time was not reported.

As a consequence of high flowability, mixtures have been cast into molds with no compaction or vibration. All specimens were kept in molds until test time in moisture room with more than 95% relative humidity and in 38±2 ºC. After curing period, properties of hardened material (UCS and CBR) were performed. Because of expansion effect of CaO, which is the main content of EAFD, it was not possible to de-mold the specimens after the age of 7 days and UCS is performed only in 3 and 7 days after making samples.

RESULT AND DISCUSSION

Fresh mix

The flowability was determined by using an open-ended cylinder according to ASTM D6103. This test was repeated every 15 min after mixture was prepared until 1 hour. Results of flowability and flow consistency are shown in Table 4. The results indicate that the initial amount and permanency of flowability increase by adding cement.

Table 4. Flow consistency

Time (min)	Flow Consistency (cm)		
	M-1	M-2	M-3
0	25	30	35
15	-	28	32
30	-	26.5	29
45	-	26	29
60	-	25.5	29

Unconfined Compressive Strength (UCS)

Unconfined compressive strength tests were performed on 50mm×120mm cylindrical specimens at 3 and 7 days. Smooth sheets were placed at the bottom and top of the specimens during the unconfined compression test to minimize end effects. Results have been given in Figure 2. Results show that the measured UCS for these mixtures is common for most standard flowable fills. As expected, results revealed that compressive strength of mixtures is dependent on cement added, water content and curing time. It seems that high amount of CaO in EAFD which is the cause of the rapid gain in strength may lead the strength of sample M-2 In the day 3 to become higher than M-3.

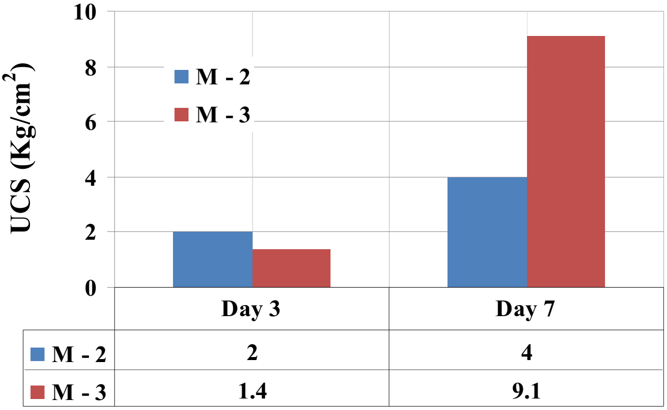

Figure 2. Unconfined Compressive Strength.

California Bearing Ratio (CBR)

The California Bearing Ratio test was done at 1, 3 and 7 days. The CBR value was calculated corresponding to maximum of bearing amount for 2.54 and 5.08 mm penetrations. Results are shown in Figure 3. Same as the UCS, the effect of CaO existence in EAFD has similar influence on CBR results. In addition, a high increase in strength (more than USC) is observed between ages of 3 days and 7 days in CBR results.

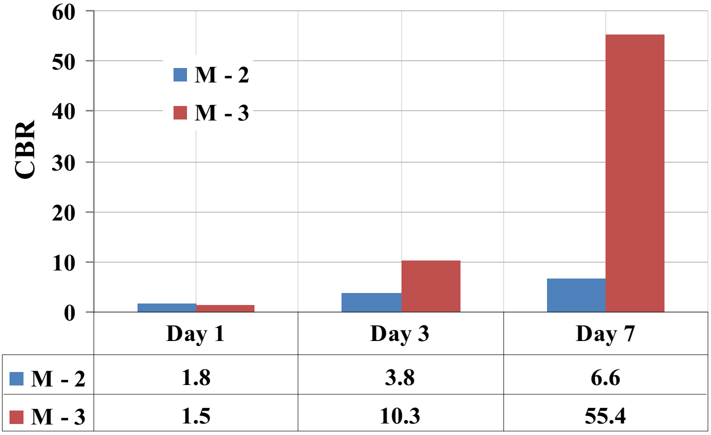

	Day 1	Day 3	Day 7
🟦 M - 2	1.8	3.8	6.6
🟥 M - 3	1.5	10.3	55.4

Figure 3. California Bearing Ratio (CBR)

CONCLUSION

A laboratory test program was conduced to develop a flowable fill material while maximizing waste material utilization and satisfying workability and performance requirement. The test program was designed to investigate fresh and hardened properties of the material. Based on the results obtained in this study, it can be stated, EAFD material which is considered as a waste by-produced can be applied in flowable fill as the economical fine aggregate. The UCS and CBR tests results showed that EAFD flowable gains sufficient adaptable strength for various applications such as back fill, pavement base and sub-base. The strength mainly depends on water and cement content. The lower the water/cement content the higher the strength. The result of flowability consistency shows that this mixture can transport easily while the flowability maintain in adequate amount. Expansibility of this material may be applied for specific situation where a material is required to fill the entire porosity.

REFERENCES

ACI, 1999. Controlled Low-Strength Materials (CLSM) (Reproved 2005). ACI 229R-99, ACI Committee 229, American Concrete Institute, Farmington Hills, MI.

Gabr, M. A., Bowders, J. J. (2000). "controlled low-strength material using fly ash and AMD sludge". *Journal of Hazardous Materials*, 76: 251–263.

Bouzalakos, S., Dudeney, A. W. L., Cheeseman, C. R. (2008). " Controlled low-strength materials containing waste precipitates from mineral processing." *Minerals Engineering*,21: 252–263.

US PennDOT, (2003). "Section 220-Flowable Backfill". *Publication 408/2003. Pennsylvania Department of Transportation*, PA.

NBR 10004 Associação Brasileira de Normas Técnicas (ABNT). (2004). "resíduos sólidos – Classificação".

NBR 10005 Associação Brasileira de Normas Técnicas (ABNT). (2004). "lixiviação de resíduos – procedimentos".

Gye-Seung Lee, Young Jun Song (2007). "Recycling EAF dust by heat treatment with PVC." *Minerals Engineering*, 20: 739–746.

ASTM C 150 (2002). "Standard Specification for Portland Cement".

ASTM D 6103 (1997). "Standard Test Method for Flow Consistency of Controlled Low Strength Material (CLSM)".

ASTM C 403 (1999). "Standard Test Method for Time of Setting of Concrete Mixtures by Penetration Resistance".

T.S. Butalia, W.E. Wolfe, J.W. Lee (2001), "Evaluation of a dry FGD material as a flowable fill", Fuel 80: 845-850

Pendular Element Model for Contact Grouting

Liaqat Ali[1] and Richard D. Woods[2] D.M., ASCE

[1]National University of Sciences and Technology (NUST) Islamabad, Pakistan, liaqatnit@yahoo.com
[2]The University of Michigan, Ann Arbor, USA, rdw@umich.edu

ABSTRACT: Foam grouting can be used to increase the strength and rigidity of unconsolidated sands. Foam grouting consists of reinforcing sands by depositing chemical grout at the inter-particle contacts in the form of pendular elements without filling the voids, contrary to conventional grouting processes, in which soil matrix is saturated with grout. This paper presents a theoretical model for characterizing the grout pendular elements in terms of degree of cementation, fill angle, and the separation distance between the particles. The model is validated by the experimental results obtained from a Resonant Column Device, and micrographs obtained from a scanning electron microscope. The experimental results closely match the results obtained from the theoretical model.

INTRODUCTION

Grout reinforces a soil mass by forming pendular elements at the inter-particle contacts and by filling the leftover pore space. The formation of pendular grout elements at the contacts under partially saturated conditions often suffices to increase strength and rigidity of grouted sands to a desired level (Ali, 1992; Chang, T. S., and Woods, R. D., 1992). Grout pendular elements are analogous to pendular rings and bridges formed by residual liquid in unsaturated porous media. If a saturated sand column is allowed to drain gradually from the bottom, the liquid will be replaced by air, starting from the center of the pores. After free drainage ceases, residual pendular rings and pendular bridges can be observed with the help of a microscope; the interfacial boundary between fluids is curved. The cause of this curvature is the interfacial tension between pore fluids. The capillary pressure is related to the curvature of the meniscus by the Young and Laplace equation: Figure 1 shows the approximate shape of the fluid interface when a small amount of fluid is present between two spherical grains. The forces exerted by a pendular ring or bridges on the soil particles mainly consist of two parts, i.e., a surface-tension force, which resides in the meniscus, and a capillary pressure force, which is transmitted by the liquid but originates in the curvature of the meniscus (Orr et al., 1975). These forces exert a normal or contact stress on the soil particles, and thus provide some stability to the soil matrix.

Investigators from widely divergent fields have studied pendular rings and bridges, shown in Figure 1, from different perspectives. Much work has been done on this subject by chemists, petro-chemical engineers, soil scientists, etc; pendular elements have become a matter of interest to environmental engineers, who are studying them to model the retention of organic contaminants in sandy soil and other aquifer material (Hoag and Marley. 1986: Alharthi et al., 1986; Kia 1988).

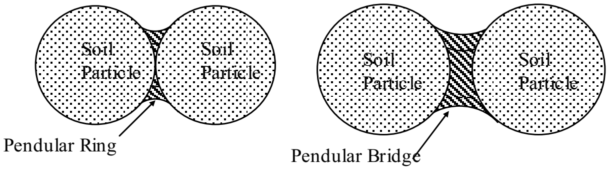

Fig. 1. Pendular ring and bridge between spherical particles.

THEORETICAL PENDULAR ELEMENT MODEL

A theoretical pendular element model is presented for calculation of degree of cementation (C%) as function of the fill angle (θ) and the separation distance between particles (η R).

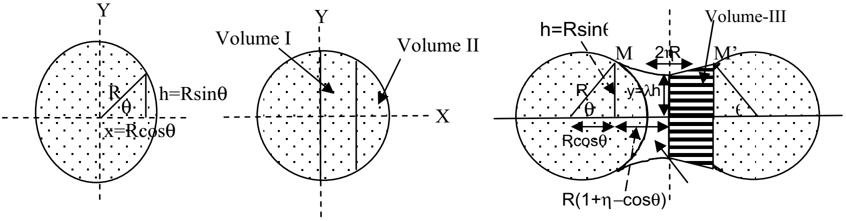

Figure 2. Schematic representation of different terms.

The gelled grout pendular elements can be studied to find the degree of cementation (C%) as a function of the fill angle (θ), and to find the optimum degree of cementation in a soil matrix as a function of packing geometry and grain configuration. The optimum degree of cementation is defined as the grout content at which an increase in strength or stiffness of grouted sand approaches an asymptotic limit. Assuming spherical soil grains and parabolic curvature of the grout-air interface (Figure 1), the volume of different parts of the sphere, shown in Figure 2, can be calculated as follow:

$$\text{Volume of hemi-sphere} = \frac{2}{3}\pi R^3 \tag{1}$$

$$\text{Volume I} = \pi \int_{x=0}^{x=R\cos\theta} (R^2 - x^2)dx = \pi R^3 (\cos\vartheta - \frac{1}{3}\cos^3\vartheta) \tag{2}$$

$$\text{Volume II} = \pi R^3\left(\frac{2}{3} - \cos\vartheta + \frac{1}{3}\cos^3\vartheta\right) \qquad (3)$$

$$\text{Volume III} = \pi \int_{x=0}^{x=R(1+\eta-\cos\theta)} \pi^2 y^2\, dx$$

$$= \pi\left[A^2 R(1+\eta-\cos\theta) + \frac{B^2}{5}R^5(1+\eta-\cos\theta)^5 + \frac{2}{3}ABR^3(1+\eta-\cos\theta)^3\right] \qquad (4)$$

Consider two spherical soil particles connected by a grout bridge as shown in Figure 2. Assuming "λ.h" as the height at the center of the bridge such that " λ h" is less than or equal to h, and that these two particles are *2*η*R* apart, where η is less than 1, then the equation of the grout-air interface shown in Figure 3 is given by :

$y = A + B x^2$ where A and B are constants and $y = \lambda h = \lambda R \sin\theta$ (5)

Applying the boundary conditions

At x = 0 $y = A$ or $A = \lambda h = \lambda R \sin\theta$ (6)

At x = a = R (1+ η - cos θ *)* $y = h = R\sin\theta = A + B R^2 (1+\eta-\cos\theta)^2$

$R\sin\theta = A + B R^2(1+\eta-\cos\theta)^2$

OR

$$B = \frac{(1-\lambda)\sin\theta}{R(1+\eta-\cos\theta)^2} \qquad (7)$$

By solving equation 4, 6, and 7 we obtain the following expression:

$$VolumeIII = \pi\left[\lambda^2 R^3 \sin^2\theta(1+\eta-\cos\theta) + \frac{2}{3}\lambda R\sin\theta\frac{(1-\lambda)\sin\theta}{R(1+\eta-\cos\theta)^2}\right]$$

$$= \pi R^3\sin^2\theta(1+\eta-\cos\theta)\left(\frac{8}{15}\lambda^2 + \frac{4}{15}\lambda + \frac{1}{5}\right)$$

(8)

The volume of the half pendular element "V_f" can be obtained from equation 3 and 8:

$$V_f = \pi R^3\left[\frac{1}{15}\sin^2\theta(1-\cos\theta)(8\lambda^2+4\lambda+3) + \frac{1}{15}\eta\sin^2\theta(1-\cos\theta)(8\lambda^2+4\lambda+3) - \left(\frac{1}{3}\cos^3\theta - \cos\theta + \frac{2}{3}\right)\right] \qquad (9)$$

The degree of cementation (C%) is defined as $\frac{NV_f}{V_v} * 100$ (10)

Where N is the number of interparticle contacts of each particle, and V_f is the volume of the voids associated with each particle. The number of inter-particle contacts depends on the relative density and the configuration of the soil particles. The number of contacts for each particle can be determined either by physical experiment or by the help of the schematic drawings of regular arrays or packing geometries of uniform, spherical particles. From equation 9 and 10:

$$C\% = \frac{\pi R^3 N}{V_v}\left[\frac{1}{15}\sin^2\theta(1-\cos^2\theta)(8\lambda^2+4\lambda+3) + \frac{1}{15}\eta\sin^2\theta(8\lambda^2+4\lambda+3) - \left(\frac{1}{3}\cos^3\theta - \cos\theta + \frac{2}{3}\right)\right] * 100 \qquad (11)$$

Equation 11 is basically derived for pendular bridges, but it can be applied to pendular rings, or a combination of pendular bridges and pendular elements. For pendular rings "η" will be zero; therefore, equation 11 will be reduced to equation 12 as shown below:

$$C\% = \frac{\pi R^3 N}{V_v}\left[\frac{1}{15}\sin^2\theta(1-\cos^2\theta)(8\lambda^2+4\lambda+3)-(\frac{1}{3}\cos^3\theta-\cos\theta+\frac{2}{3})\right]*100 \qquad (12)$$

INFLUENCE OF PACKING GEOMETRY

For spherical particles of identical size, the pore structure is determined from the packing arrangement. Spherical particle arrays have two extremes, i.e., simple cubic with a void ratio of 0.91 and pyramidal with a void ratio of 0.35. Figure 3 shows these two extreme packing and an intermediate packing of cubical tetrahedral/orthorhombic configuration with a void ratio of 0.65. This figure also shows the number of inter-particle contacts, location of each inter-particle contact, and the optimum fill angle for each of these configurations. The optimum fill angle is the maximum angle (measured from the center of a pendular element) which a pendular element makes with an adjacent pendular element without overlapping it.

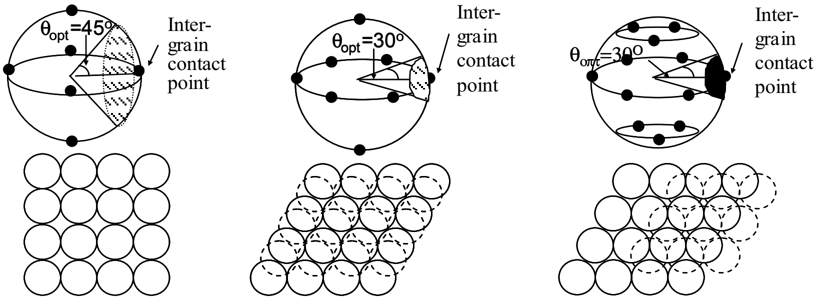

Loose configuration-Simple Cubic; no. of contacts = 6; e=0.91

Medium configuration – Cubic Tetrahedral; no. of contacts = 8; e=0.65

Dense configuration – Pyramidal; no. of contacts =12; e=0.35

Figure 3. Different soil particle configurations and the number of contacts.

When the optimal fill angle is exceeded the radius of curvature in the pendular ring meniscus increases and capillary stresses decreases. As the filling of the pore space continues, radius of the outside surface (MM') of the pendular ring (Figure 2) tends to flatten with loss of most of the capillary stress effect.

Figure 4 shows the effect of fill angle theta (θ) on the degree of cementation for different soil configurations. It shows that as the fill angle increases, the degree of cementation increases. More importantly, the relationships in this figure also establish an optimal degree of cementation corresponding to the optimal fill angle. For example, for a simple cubic configuration the optimal fill angle was 45 degrees (Figure 3). This angle corresponds to a degree of cementation of approximately 36%. For a pyramidal configuration, the optimal degree of cementation is approximately 42% corresponding to a 30° fill angle. In this figure, ideal inter-particle contact has been assumed, i.e., no pendular bridges. However in an actual situation, the inter-particle contacts will consist of both pendular rings and pendular bridges.

In a random array of spheres, the number of contacts may be less than in regular packing; furthermore, it is possible to have contacts which do not transmit any loads (particles that are not in contact with neighbouring particles). The latter are referred to as dead contacts in some research (Petrakis and Dobry, 1986), or pendular bridges in this research.

The number of pendular bridges and their length may vary because of the small difference in size of the spheres and the nature of random packing. Figures 5 illustrate the effect of increase in the number of pendular bridges on the degree of cementation at different fill angles, for pyramidal configurations. The value of "η" has been kept constant (η =0.10) for illustration purposes for these pendular bridges. The degree of cementation was calculated by calculating the amount of grout for each pendular bridge and pendular ring using equation 11 and 12 respectively, and then multiplying them by the respective numbers of the pendular bridges and pendular rings, in any given combination. It is clear from this figure, that as the number of the pendular bridges increases, the degree of cementation increases for all configurations. Figures 6 shows the effect of bridge length on the degree of cementation for pyramidal configurations. In this figure, two pendular bridges have been assumed; the pronounced effect of the separation distance on the degree of cementation can be seen.

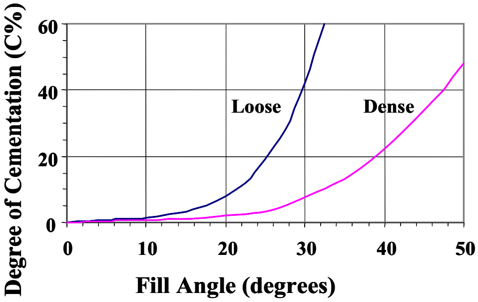

Figure 4. Effect of fill angle on the degree of cementation for idealized loose and dense configurations of spherical soil particles.

EXPERIMENTAL RESULTS

A new grouting technique called "foam grouting" was used to form the pendular elements, in cohesionless soil specimens, in the laboratory. The details about this technique are described elsewhere (Ali, 1992). Three types of sands were grouted to varying degree of cementation (C%) by this process, and after a suitable curing period, the shear modulus (G_s) of the grouted specimens was measured in a Modified Resonant Column Device (Ali, 1992) at small shear strain and at different confining pressure to determine the effect of degree of cementation (C%) on the shear modulus. Figures 7 and 8 show the effect of C% on Ottawa 20-30 sand and Mortar 7-60 sand. In these graphs G_s stands for the shear modulus of the sodium silicate grouted sand, and $G_{s10\text{-}15}$ represents the shear modulus at 10 psi confining measured 15 minutes after application of confining pressure; similarly $G_{s30\text{-}480}$ represents the shear modulus at 30 psi confining measured 480 minutes after application of confining pressure, etc.

All the sands shows a sharp increase in the shear modulus with an increase in C% upto a certain value of C%; and thereafter, either there is no further increase in the shear modulus or it slightly decreases with increasing C%. This value of C% at which the shear modulus is maximum is called the optimum degree of cementation (C_{opt}). The C_{opt} for: (1) Ottawa 20-30 sand - 40%; (2) Mortar 7-60 sand - 50%; and (3) Muskegon sand - 50%.

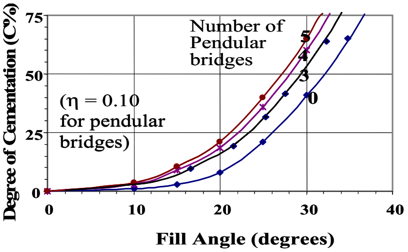

Figure 5. Effect of increase in the number of pendular bridges on the degree of cementation of soil with a dense configuration.

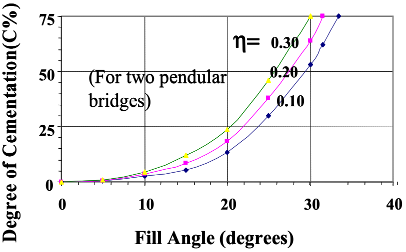

Figure 6. Effect of increase in the length of pendular bridges on the degree of cementation of soil with a dense configuration.

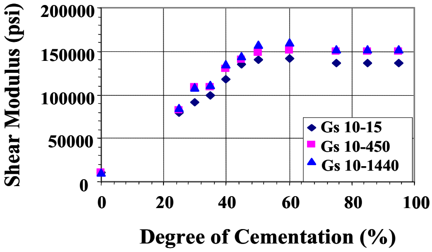

Figure 7. Variation of shear modulus of Mortar Sand with degree of cementation at 10 psi confining pressure.

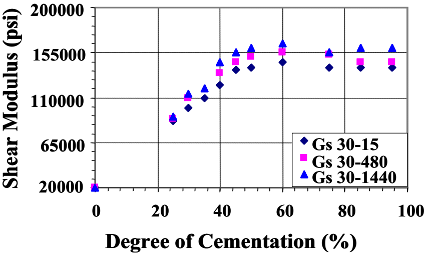

Figure 8. Variation of shear modulus of Mortar Sand with degree of cementation at 30 psi confining pressure.

There is an optimum fill angle for the pendular elements, and if the θ_{opt} is exceeded, the voids will start to fill and menisci will tend to disappear. The optimal degree of cementation determined experimentally is consistent with prediction from the Pendular Element Model. Slightly higher optimal degree of cementation values determined experimentally can be explained by the presence of pendular bridges in the sand which utilizes more grout.

Capillary effects account for the fact that the optimum degree of cementation (Copt) is considerably less than 100%. The effect of capillary forces on the shear modulus of cohesionless (ungrouted) soils was studied by Qian (1990). He tested 13 types of cohesionless soil with different grain shape, size, and gradation to study the effect of capillary forces at different degrees of water saturation. He found that the maximum shear modulus occurs when the degree of water saturation lies between 3% and 13% depending on the grain shape and size, void ratio, confining pressure, etc. As the degree of water saturation is increased beyond these values, the shear modulus decreases because of the destruction of capillary menisci and associated forces. He also showed that degree of saturation is larger for angular sand than the subrounded/ rounded sands.

Therefore by filling the voids beyond a certain limit we lose the beneficial effect of the capillary forces as the menisci associated with the pendular rings flatten out. Loss of beneficial capillary stresses also occurs as water released from the grouts solution continues to fill the residual pore space. O'Connor et al., (1978) showed that as the sodium silicate cures and gains strength, the liquid phase is squeezed out of the gel and a phenomena called syneresis take place: the same phenomena has been observed in this study. The amount of water released by the gel is directly proportional to the quantity of the grout. Thus as the C% is increased in a specimen, more water is released, and the left over voids are smaller. Therefore, the voids are filled more quickly, eliminating the capillary forces.

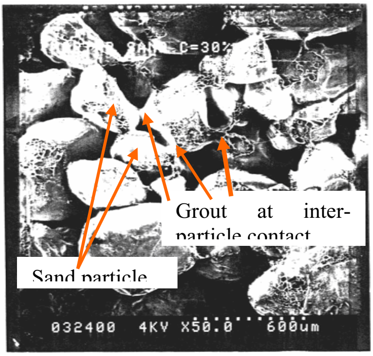

Figure 9. Grout deposited at the inter-particle contacts.

MICROGRAPHS OF CONTACT GROUTED SAND

The micro structure of foam grouted sand specimens was studied by using a Scanning Electron Microscope (SEM). One of the main limitations of these micrographs was that they do not represent the true amount of residual grout, because the specimens had to be dried; as a result over 40% of the grout was lost in the process. However, they do show the shape of the pendular elements.

The micrographs were taken using magnification varying from X25 to X250, to study various aspects of the foamed grouted sand. and foam grout itself. Figure 9 show the grout deposited at the inter-particle contacts in the form of pendular elements.

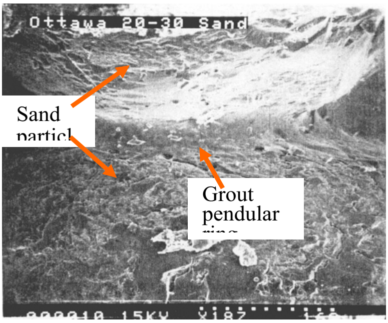

Figure 10. Parabolic curvature of grout pendular element.

Grout deposition at the interparticle contacts in the form of a pendular element with approximately parabolic curvature as assumed earlier in the Pendular Element Model and shown in Figure 10. The volume of the grout in these pendular elements depends on the inter-particle separation at the particle contact, and the degree of cementation. The exact prediction of number of pendular rings and bridges for a given particle configuration and type of sand is difficult, and requires more detailed research at the microscopic level.

CONCLUSION

Foam grouting can be successfully used for bonding particles at their contacts without filling up the pore space. The theoretical model presented in this paper can be used to predict the optimum degree of cementation of contact grouted sands for various particle configurations. The experimental results obtained from the resonant column study and the scanning electron microscope closely match those obtained from theoretical Pendular Elements Model. This study shows that the maximum shear modulus at low shear strain amplitude occurs at less than 50% degree of cementation.

REFERENCES

Ali, L. (1992), "Dynamic Behavior of soils partially grouted by a foaming process", *Ph.D. Dissertation*, The University of Michigan. Ann Arbor.

Alharthi, A., Lange, J. and Whitaker, E. (1986), "Immiscible fluid flow in porous media: dielectroc properties", *J. Contam. Hydrol.,* 1: 107-118.

Chang, T. S. and Woods, R. D. (1992), "Effect of particle contact bond on shear modulus", *J. of Geotech. Engg;,* Vol. 1 , No. X: 1216-1235.

Englehardt,. W. V. (1955), "Interstitial water of oil bearing sands and sandstones", *Proc. Wld. Petrol. Congr.,* Section I/C: 399-416.

Hoag, G. E. and Marley, M. C. (1986), “Gasoline residual saturation in unsaturated uniform aquifer materials", *J. Envir. Engg,* 112: 586-604.

Kia, S. F. (1988), "Modelling of the retention of organic contaminants in porous media of uniform spherical particles", *Wat. Res.,* Vol. 22, No 10: 1301-1309.

O'Connor, K. M. Krizek, R. J. and Atmatzidis, D. K. (1978), "Micro-characteristic of chemically stabilized granular material", *J. of Geotechnical Engng, Div*, Proc. ASCE 104, No. GT 7: 939-952.

Orr, F. M. Scriven, L. E. and Rivas, A. P. (1975), "Pendular rings between solids: meniscus and capillary force", *.J. Fluid Mech.,* Vol. 67: 723-742.

Petrakis, E. and Dobry, R. (1986), "A self consistant estimate of the elastic constants of a random array of equal spheres with application to granular soil under isotropic conditions"*, CE Report No. CE-86-04*, Rensselaer Polytechnic Institute, NY.

Qian, X. (1990), "Dynamic behavior of unsaturated cohesionless sand*", Ph.D. Dissertation*, The University of Michigan, Ann Arbor.

Creating Artificially Cemented Sand Specimen with Foamed Grout

Liaqat Ali[1] and Richard D. Woods[2] D.M. ASCE

[1]National University of Sciences and Technology, Islamabad, Pakistan, liaqatnit@yahoo.com
[2]The University of Michigan, Ann Arbor, USA, rdw@umich.edu

ABSTRACT: It has been shown by researchers that small amount of cementation greatly strengthens and stiffens sands. These improvements help stabilize slopes against earthquake shaking and stabilize loose, saturated sand deposits against liquefaction. Grouting practice and most grouting research has dealt with saturation grouting, however recent research has shown that partial filling of void space with cementitious grout improves strength and stiffness of sand in a very favorable way and at a low cost per unit volume. Upto now there has been no way to artificially create partial void volume grouting of sand except by physical mixing. This paper describes one way of achieving this result by the injection process using a foamed sodium silicate grout.

BACKGROUND

Naturally cemented slopes along the California coast, having an inclination of 60 degrees or steeper and heights of few hundred feet, have withstood many earthquakes, even though individual aggregations of these sands can be crushed by light finger pressure. These sandy slopes have a very small amount of cohesion provided by the natural cementing agents like silica, hydrous silicates, carbonates, etc. (Clough at el., 1981). Ismail at el. (2002) studied the behavior of sand cemented with different types of cements. Experimental work of Estelle at el. (2004), gives the effects of various parameters on damping ratio and shear modulus of grouted sands. Ali and Panos (1997) conducted a laboratory study on sands cemented by Portland Cement and found that a very small percentage of cementing material is required to improve the strength of the soils. Cross hole tests conducted by Woods et ad. (1982) on chemically grouted soil in the field showed that shear wave velocity increased from about 190 m/sec before grouting to 400 m/sec after grouting for a soil having 49% of their voids filled by the chemical grout. Chiang (1986) showed that chemical grouting of only a part of the pore volume significantly increased the shear modulus of sand.

All the above mentioned evidence shows that it is not essential to saturate the soil voids by the cementing/ grouting agent because the desired changes in the properties of the soil can be achieved by partial filling of the soil voids. But, the present practice in chemical grouting is to fill the soil voids entirely by injecting the grout to refusal.

Also the cost of chemical grout is a significant fraction of the total cost of a chemical grouting operation. If there is a large volume of soil to be stabilized by injecting grout, and if the desired changes in the behavior of the soil can be accomplished by depositing grout only at the inter-particle contacts, then it would be uneconomical to completely saturate the soil with grouting material.

There are three distinct stages of grout deposition in the soil matrix as shown in figure 1: 1) in the first stage grout coats the soil particles; 2) in the second stage the grout is deposited at the inter-particle contacts in the form of the pendular elements; and 3) in the third stage grout fills the soil pores. It is not possible to avoid stage 1, but if we could control stages 2 and 3, a substantial amount of grout can be saved.

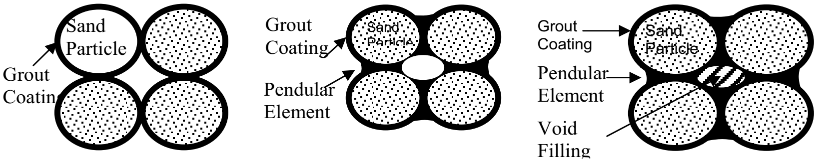

Stage 1. Particle coating **Stage II. Pendular ring development** **Stage III. Void filling**

FIG. 1. Stages of grout deposition in the soil matrix.

FOAM GENERATION PROCESS

A study was undertaken to develop a technique of particle contact grouting with the aim of developing a method with potential field application. One way in which contact grouting might be accomplished is by introducing bubbles into the grout itself so that air in the bubbles occupies some of the void space, and the residual liquid grout forming the bubble film gels at the particle contacts. To introduce bubbles in the grout, a foam method was tried and it proved to be successful. With the proposed foam grouting method, it is possible to grout sand to various degrees of cementation. The degree of cementation (C%) is expressed as a percentage of void space occupied by grout rather than concentration by weight as conventionally expressed. There are two methods of foam generation, i.e., Internal Foaming Process and External Foaming Process.

Internal Foaming Process. In this process foam is generated inside the medium, which is to be grouted, by simultaneous injecting grout-surfactant solution and air pressure or by first injecting grout-surfactant solution and then applying air pressure. Schematic of the process is shown in figure 2.

External Foaming Process. In this process foam is generated by means of a foam generator before injecting it into the soil. A typical foam generator consists of cylindrical tube/ pipe containing glass beads or sand of uniform size or varying size and gradation. Simultaneous injection of grouts-surfactant solution and air supply from one end produces foam from the other end; schematic of the process is as shown in figure 3.

This paper describes the method of preparing contact grouted specimens by the foaming process, and presents some sample micrographs of foam grouted specimens.

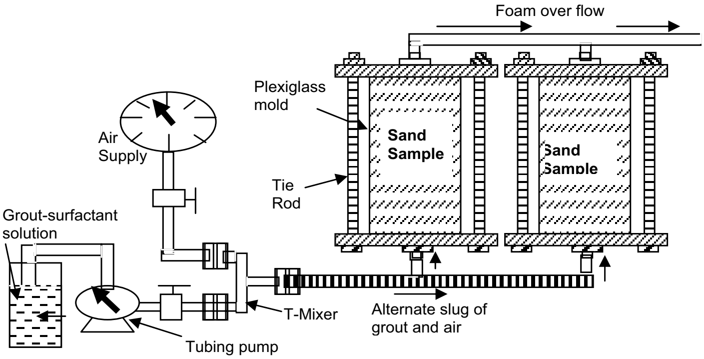

FIG. 2. Schematic of the lab Internal Foaming Process.

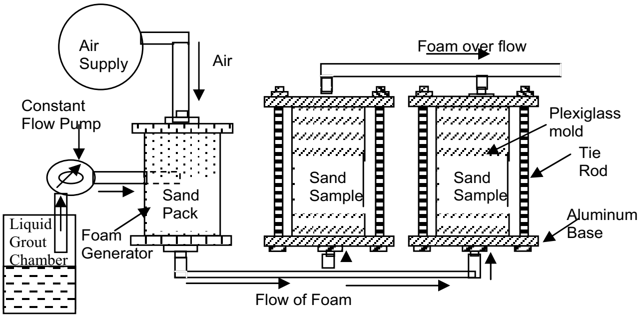

FIG. 3. Schematic of the lab External Foaming Process.

PREPARATION OF AIR DRY SAND SPECIMEN

Split-tube plexiglass molds, having 1.4 inches internal diameter and 3.2 inches length, were used to prepare these air-dry specimens in the following manners:

1) After assembling the plexiglass split-tube mold (less top cap) was held vertically in the holder. One aluminum and two nylon sieves were placed at the bottom to retain the sand particles and obtain a flat-right angle base of the grouted specimens.
2) The air dry specimens were prepared by funneling sand into the molds from a fixed height; by trial and error, the height of fall required to fill the mold to 50% relative density was found.
3) After filling sand in the mold, it's top surface was leveled, and two nylon and one aluminum sieves were placed at the top. The top aluminum cap was then fixed with tie rods and wing nuts as shown in figure 4.
4) O-rings and vacuum grease were used to prevent any leakage in the vicinity of the end caps.

The air-dried specimen was grouted to the desired degree of cementation by using sodium silicate foamed grout and the Internal Foaming Process. A constant flow pump was used to pump the grout mixture at the desired flow rate, an air supply was used to generate the foam and the T-mixer was used to premix air and liquid grout solution before it flowed into the specimen. The grouting proceeded as follows:

1) The air pressure and flow of the grout was controlled by flow regulators.
2) The grout was prepared with the following volume ratios:

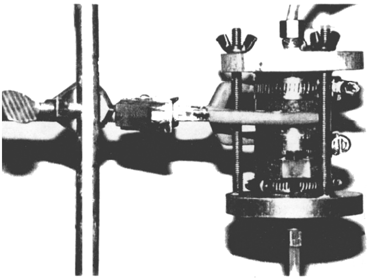

FIG. 4. The plexi-glass mold in assembled form used for preparing grouted specimen.

Sodium silicate solution:	**Distilled water:**	**Ethyl acetate:**	**Formamide:**	**Surfactant solution**
70 parts:	**30 parts:**	**4 parts:**	**12 parts:**	**8 parts**

3) After the sample was connected in the grouting circuit, with suitable pipe fittings as shown in figure 2, the supply line of liquid grout and the air pressure line were opened simultaneously. One could observe the generation and flow of foam through the tygon tubing and sand in the transparent plexiglass split-tube mold.
4) The degree of cementation (C%) was varied by changing the air-liquid ratio of the grout system during injection, keeping all other parameters constant.
5) The supply of the grout solution and air was stopped when at least three volumes of foam had passed through the soil specimen.
6) The valves on the top and the bottom end of the soil specimen were closed after one minute; this time was required for dissipation of air pressure and relaxation of foam.
7) The grouted soil specimens were cured for thirty six hours in the air tight mold, before further testing.

Saturated sand specimens were prepared from the air dry specimens; to enhance saturation, at least five pore volumes of the water were passed through each sample. These samples were then connected in the grouting circuit, and the grouting process was similar to the air dry samples.

MICROGRAPHS OF FOAMED GROUTED SAND

The micro structure of the foam grouted sand was studied by using a Scanning Electron Microscope (SEM). The micrographs were taken using magnification varying from X25 to X250 to study various aspects of the foamed grouted sand, and foam grout itself. Some of the findings from these micrographs are:

1) The foamed grout deposits in the sand matrix in three stages, as follows:
    - **First Stage**; the grout coats the soil particle with a very thin layer as shown in Figure 5a. The thickness of this coating depends upon the surface roughness and chemistry of the soil particles, and is not more than few microns.

- **Second Stage**; the grout deposits at the inter-particle contacts in the form of pendular elements as shown in Figure 5b.
- **Finally**; the grout start filling the empty void spaces as shown in Figure 5c.

2) The grout deposits at the inter-particle contacts in the form of pendular elements with approximately parabolic curvature, as shown in Figure 6a. These pendular elements appear in the form of pendular rings and bridges as shown in Figure 6b. The volume of the grout in pendular elements depends on the inter-particle separation at the particle contact, and the degree of cementation. The prediction of number of pendular rings and bridges for any particles configuration and type of sand is difficult, and requires more detailed research at the microscopic level. Similarly, the inter-particle separation distance (length of pendular bridge) in the soil matrix cannot be ascertained readily.

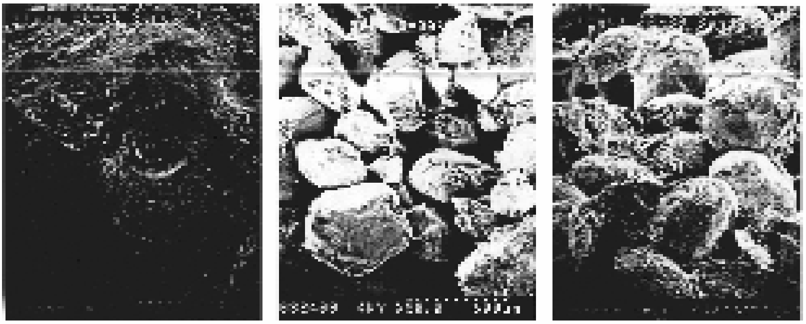

a. Particles coated with grout. b. Formation of pendular element c. Voids filling.

FIG. 5. Micrographs showing various stages of grout deposition.

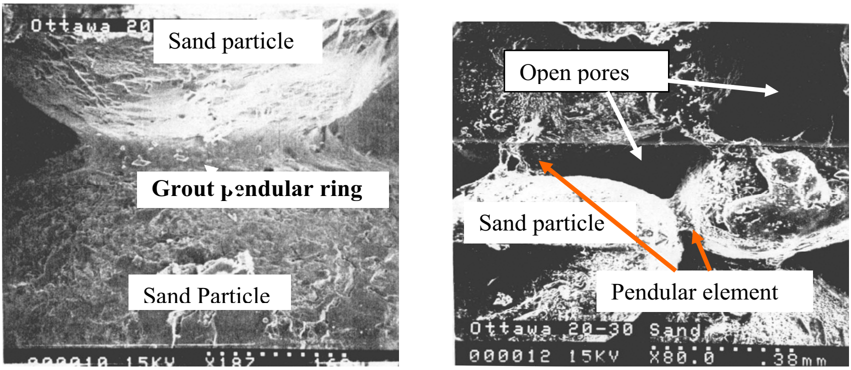

FIG. 6. Micrograph showing open pores and pendular elements formed between Ottawa 20-30 sand particles.

3) The foam grouting process is successful in its main objective, i.e, depositing the grout at the inter-particle contacts and leaving the pores open as shown in Figure 6b.
4) For lower degrees of cementation, the gelled foamed grout in the soil matrix has a honeycomb or vesicular structure as shown in Figure 7, and for higher degrees of cementation, the structure of the gelled foam grout has more solid, "Swiss Cheese" like appearance. Although the lamellae are thin for high quality foam, they are numerous and thus provide stability to the sand.

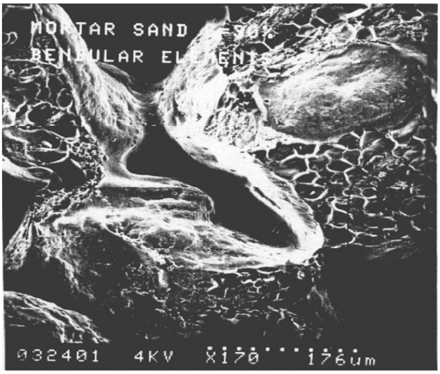

FIG. 7. Vesicular character and honey comb structure of foam.

CONCLUSION

Foamed grout can he successfully used to grout sands to varying degree of cementation. The study has shown that the process has great potential for field applications. The process is simple and cheap, and can be applied in the field with the existing field grouting equipment with negligible addition/ modification. Although only one type of grout has been used in this research but the principle of foam grouting can be applied to any type grout including grouts made from any type of cement.

REFERENCES

M. Ismail *et al*. (2002), "Effect of cement type on shear behavior of cemented calcareous soil". *J. Geotech. Geoenviron*., (June): 520-529.

Estelle. Delfosse-Ribay *et al*. (2004), "Shear modulus and damping ratio of grouted sand". *Soil Dynamics and Earthquake Engineering*, 24: 461-471.

Ali A. Abdulla *et al*. (1997), " Behavior of cemented sands-1. testing" *International journal for numerical and analytical methods*. 21: 533-547.

Ali Liaqat. (1992), "Dynamic behavior of partially grouted sand by a foaming process", *Ph.D. Dissertation*. The University of Michigan, Ann Arbor, USA.

Chang. T, S.. (I986). "Dynamic behavior of cemented sand". *Ph.D. Dissertation*. The University of Michigan, Ann Arhor, USA.

Clough. G. W., Silar, N. and Bachus, R.C., (1981), "Cemented sand under static loading". *J. of Geotech. Engng. Div*., (ASCE) Vol. 107. GT 6: 799-817

Woods. R. D., Partos, A.. and Welsh, J. P. (1982), "Soil modification for relocation of die forging operations", *Proc. of the Conf. on Grouting in Geotechnical Engineering*, ASCE, New Orleans. Louisiana, (Feb.): 938-958.

Zhuque Hole Landslide Disaster Research

Wen Yi[1], Yonghe Wang[2], and Yungang Lu[3]

[1]Central South University, 932 Lushan South Road, Changsha 410083; Central South Forestry University of Science and Technology, 498 ShaoShan South Road, Changsha, 410004;yiwengangbiao@163.com,
[2]Central South University .932 Lushan South Road, Changsha 410083; yonghewang@163.com
[3] Hunan Highway Authority，Changsha 410000; luyungang@163.com

ABSTRACT: This article examines the landslide disasters of July 27, 2008. It was concluded that rock near the road was weakened by water causing creep deformation. Also, heavy long-term rains in the area contributed to conditions right for landslides. Each of the three areas affected along the roadside were approached with a different technique. The landslide on the left side of the road was managed by using bolt reinforcement. The area between roads was managed by changing the line. To the right of the road an anchor line and antiskid stick was used.

INTRODUCTION

Landslide disasters have become the second greatest nature disaster for developed areas [1]. The main cause is heavy rain. Rain-induced landslides account for 90% of total landslides [2]. Most vulnerable are mountainous areas where roads cut through steep inclines. With increased road construction west of the mountains, landslide disasters have become more common, resulting in higher road costs and construction delays, and more seriously, the effects on traffic flow and road safety. An example from the Chang-Ji highway landslide was analyzed for slope stability and proposed government measures for the project were examined.

ZHUQUE HOLE LANDSLIDE DISASTER GENERAL SITUATION

At 1 o'clock on July 27, 2007, in Zhuque Town Village , Dongxi town , Luxi county, Xiangxi Autonomous Prefecture, because of continuous rain, flash floods brought about massive landslides along the highway. The entire roadbed of the contract K196 +720 ~ K197 +180 in Chang-Ji highway sank, Its vertical displacement was more than 20 meters, its horizontal displacement more than 60 meters, sub-base cracking of the entire section, culvert failure, drainage and slope protection deformation also occurred. In K197 +000 ~ K197 +170 horizontal cracks occurred in 6 places, including through the sub-base and roadbed of the pavement. In K196 +720 ~ K197 +180 large areas of mountain soils slid into the bottom of the river, blocking more than 80 meters of Dan River. In addition the landslide brought about the collapse of houses, destruction of rice fields and fruit trees.

LANDSLIDE CAUSES

Rock slopes are generally comprised of soft rock, thus creating conditions for creep deformation. Weak layers of mud sandwiched between dislocated rock layers, provided favorable conditions for a landslide.

Substantial and enduring rains are the direct cause of the landslide. Long-term rainfall brings about three direct affects on the formation, namely, the intensity of lower slope between slopes, the high water pressure of groundwater, and increasing hydrostatic pressure in the landslide trailing edge. Since mid-July Xiangxi Autonomous Prefecture, has suffered landslides where the WuShui River and its tributary the Dan River Basin has received torrential rainfall, and where the steep rock inclination is, cracks in the joints have developed, providing favorable conditions for surface water to enter subsurface layers, potentially making the layers less stable, however, because the slope body has been given water, there is a greater water pressure underground, giving the slope buoyant support from below. Slope comprised of soft rock is easily soften in water and the anti-scouring is bad. The rock layer in the foot of the winding road in ChangDe-side has suffered partial collapse due to long-term water erosion, which eroded the face, providing a favorable environment for a landslide. In the Chang-Ji highway, large-scale landslides happen regularly. The sliding layer typically consists of residual aggregate soil, and strong and weak weathering rock. The thickness of sliding body is approximately 0 ~ 20m, volume about 2,600,000 m^3.

TREATMENT PROGRAM

Calculation on Shear Strength Parameters and the Safety Factor in Slip Surface

According to the terrain of landslide area, the geological survey information and the slope stability in the regular and high-water period, a typical cross-section was selected to calculate the shear strength parameters of sliding surface. The results of each section are shown in table 1. B-B',C-C',D-D',E-E' section pictures are shown in Fig.1, Fig.2, Fig.3, Fig.4.

Calculation Results in K197 +270 ~ K197 +630

According to the terrain area in the roadbed slope, the geological survey data and the stability of the slope, a typical cross-section to anti-count the shear strength parameters of the potential anti-slip surface was selected. The anti-count results are shown in table 2.

Table 1 the safety parameter of the full-section and the shear strength parameters of sliding surface before landslide treatment

calculation section	**Safety parameter**		**shear strength (sliding section)**		**shear strength (anti-sliding section)**	
	Ordinary water level	**high water level**	**cohesion $C(kp_a)$**	**internal friction angle $\varphi(^0)$**	**cohesion $C(kp_a)$**	**internal friction angle $\varphi(^0)$**
B-B'	1.146	0.848	7	14	19	25
C-C'	1.271	0.966	7	14	19	25
D-D'	1.128	0.956	7	14	19	25
E-E'	1.048	0.914	7	14	19	25
F-F'	1.021	0.987	7	14	19	25

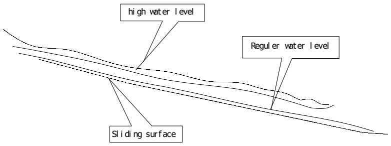

FIG. 1. B-B' cross section.

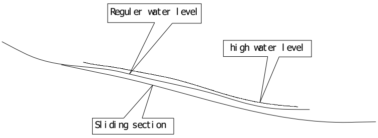

FIG. 2. C-C' cross section.

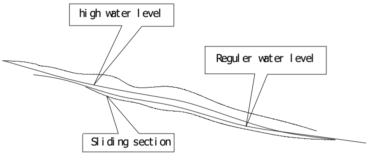

Figure 3 D-D' section calculation picture

FIG. 3. D-D' cross section.

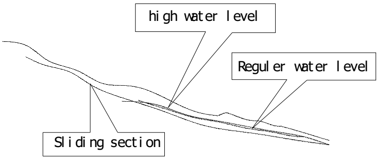

FIG. 4. E-E' cross section.

Table 2 Safety parameter shear strength in unfavorable conditions in rainy season and potential sliding surface

Calculation section	Safety parameter	Shear strength (roadbed section)	
		Cohesion c (kp$_a$)	Friction angle (^{o})
I - I	1.06	10	15

TREATMENT DESIGN

The Overall Design of Treatment

According to the landslide area topography, geological conditions, taking into account economic, environmental protection, facilitating construction and other factors, the overall design of treatments are as follows:

（1）On the left side of the roadbed, the bolt reinforcement was used on the landslide body after clearance slide. A total of clearance is about 210,000 m^3. The bolt + rib beam reinforcement was used in the natural slope of the landslide back margin. The scarp between natural slope of the landslide back margin and clearance was reinforced with framework and anchor. The slope after clearance was reinforced with a concrete skeleton and bolt and is a total of 78544m.

（2）The landslide in the roadbed area after clearance is across a bridge and is a total clearance of about 120,000 m^3. The bridge is T beam of 25m, while in K196 +719 ~ K196 +770, parts to the left of the center-line position of the roadbed have been reinforced with a pile retaining wall plate.

（3）The right side of the roadbed in the lower part of the landslide was cleared and unloaded, reducing the weight of the landslide. After the landslide was cleared within the river front a retaining wall to prevent erosion was set up along the river first-line. Within the landslide body a smooth drainage corridor was set up to reduce the flood level during flood periods and reduce lower power. In addition, 1-2 road piles were set in the landslide body for retention of soil.

Treatment Design in the Lower Part of the Landslide

According to the parameters of the sliding surface, we have analyzed and calculated the strengthening infrastructure after clearing the lower part of the landslide. After clearing in the high-water level conditions the safety parameter is shown as table 3.

Table 3 the safety parameter calculation in adverse conditions before and after landslide reinforcement

Calculation section		B-B’	C-C’	D-D’	E-E’	F-F’
Safety parameter	Strengthening ago	0.78	0.82	1.03	1.02	1.05
	After reinforcement	1.13	1.13	1.10	1.10	1.10

Retaining piles

Piles for retaining the top beam of concrete pressure and intensity level were C25, C20 and C25.

On the right side of the road (Changde paragraph) from the center line of about 160 ~ 220m, 51 anti-slide piles were set up. The pile-section was in the form of 2.0m × 3.5m, the pile center distance was between the level of 5.0m, a length of 20.0 ~ 24.0m, with a pile-thick concrete wall of 25cm, and a piling pressure set-top roof beam.

On the right side of the road (Changde paragraph) from the center line of about 100 ~ 120m the following was set up: 41 anti-slide pile, the pile-section in the form of 2.0m × 3.0m, a pile center distance between the level of 5.0m, length 20.0 ~ 24.0m, pile-thick concrete wall of 25cm, and piling pressure set-top roof beam.

Sliding-zone Ⅰ B pile (front row)

on the right side of the road (Changde paragraph) at the center, about 160m from the line the following was set up: 5 piles, pile-section in the form of 2.0m × 3.0m at the side of the pile, pile center distance between the level of 5.0m, length 16m, pile-thick concrete wall of 25cm, and piling pressure set-top roof beam.

On the right side of the road (Jishou paragraph) about 240 ~ 245m from the center line (Jishou end) the following was set up: 21 anti-slide pile, pile-section in the form of 2.0m × 3.0m side of the pile, pile center distance between the level of 6.0m, pile length 17.0 ~ 20.0m, pile-thick concrete wall of 25cm, and piling pressure set-top roof beam.

A, B-top anti-sliding pile is not exposed to the ground clearance, pile-anchor of the length of the slide from sliding under the rock face, the anchor and the sliding surface of the depth of the pile-length ratio of 1:1. When the excavation of the landslide is less than the thickness of the design, with a difference of less than 1 meter, the increase in anti-slide pile section of the reinforcement anchor paragraph should be reinforced.

Dealing with dynamic landslide design, information-based construction, construction engineers used anti-slide pile digging to confirm the situation. When the smoothness of layers changes in a depth of less than 1 meter, based on the length of the above changes in the principle of supervision by the chief engineer the pile is adjusted accordingly. For other questions or on-site design with a larger difference between the conditions, immediately contact with the designers should be made in a timely manner to take reasonable measures.

In the landslide on the right side of the central location of about 135 ~ 145m (Jishou end) the following was used: 7 set piles, pile-section in the form of 1.5m × 2.0m , the pile center distance between the level of 5.0m, length 16m, pile-thick concrete wall of 25cm, and piling pressure set-top roof beam.
C-top anti-slide pile pressure on the ground exposed roof beam 4.0m, pile-anchor of the length of about 1:1.

Drainage design

Water affected the performance of the major landslide in the body of hydrodynamic pressure and uplift pressure, water caused surface erosion and softening of the soil. The design of the landslide slope stability was based on the cut-off grade, drainage, landslides in the body surface drainage corridor, landslides and cracks in the surface of the slope, as well as measures such as closed surface emissions water and groundwater.

（1）The surface drainage system installed after unloading the slope, according to the terrain, with an elevation of the ground set up three cut-off ditches, which were first set up on the right side of the center line of about 10 ~ 15m, set up in the second line center on the right side about 65 ~ 75m, third set up to the right side of the center, about 190 ~ 210m, and on the surface of the water through the drainage to the edge of the landslide of Dan River, for the rainy season to reduce the flow of the slope erosion, as well as surface water that seeps into the slope, each of which drains the lower part of the front 100m to a sewer. Drainage should be based on the specific location of the Qing side of the slope after a reasonable layout and terrain, about 80m distance, in order to facilitate the slope on the cut-off of the water discharge ditch.

（2）Drainage corridor is set up in a weak watering of sandstone layer under the landslide area. At the same time, the vertical soakage wells are arranged in the top of cave in the drainage corridor.Drainage corridor design included a high-profile excavation 2.45m, a 2.10m wide cross-section, vertical gradient of about 5%, with a total length of 260m; vertical distance between water wells of 6m, design aperture 130mm, pipe of diameter 100m approximately. The drainage corridor intercepted groundwater, deep groundwater and soil from landslide water discharge, and reduced flood water level in the body landslide.

Taking into account the slippery sandstone bed, local cracks, drainage and underground corridor seepage by the long-term impact, to ensure that the drainage corridor and the construction of the security of long-term stability of the operation, after the first excavation of the drainage corridor, a small drain was used for pre-reinforcement. Then the corridor was reinforced with concrete of about 20cm as a permanent support.

Design Anti-erosion

For the landslide along the river, a mortar stone retaining wall was put in place, the upper part of the retaining wall by 1:1.75 to 1:1.5 slope, slope protection was reinforced by using mortar stone tablets. The average retaining wall height was 5.0 ~ 7.0m, Qiang Ding design for the elevation of 130.0 ~ 131.0m, toe wall of soil from a landslide after the removal of weak weathering of bedrock was about 0.5m, the depth of concrete buried under the landslide of high walls was cleared to determine the actual elevation; the base of the retaining walls was a concrete-base, base rock down into the lower part of the vertical row sliding bolt 3, the first row, second row, third row along the bolt vertical spacing of retaining walls was 1.0m, 1.0m, 0.5m, horizontal distance of 1.0m, 1.0m, 1.0m, a single long bolt 4.0m, the upper part of the base depth of about 1 meter between the vertical and horizontal the use of steel bolt connections; Φ28 use the bolt RC-class Ⅱ, for a total length of bond-type anchor; mortar stone slope protection film about 14.0m. Figure 1 shows retaining walls which should be in control point 1 (128112.2889,496284.4641) and control point 3

(127843.7292,495978.2598) as a starting point and end point control, to control the middle point 2 (127970.8814,496112.2172) control. The rest should be based on the river clearance as determined by the Commissioner of the specific location of the engineers to make proper adjustments.

4.3 197 +270 ~ K197 +630 paragraph roadbed

According to the site topography, geology and slope conditions, and other characteristics of the current situation, security, economics, environmental protection and facilitation of the construction and other factors, the right side of the road for the design treatment must be taken into account. According to the "road embankment design specification" (JTJ D30-2004) in 3.7.4, to improve the safety factor, the highway roadbed must ensure the non- Ⅰ under normal operating conditions of security, on the highway embankment reinforcing stability.

The sliding surface of the potential outcome of the parameters, based on the design reinforcement, for embankments to meet the safety factor in the adverse conditions should be 1.10. According to the December 27, 2007 and to December 29, the Hunan-chi-day traffic-building assessment of the Advisory Co., Ltd.: agreed 197 +270 ~ K197 +630 above the right side of the road using pre-reinforced piles in the design was sufficient. After optimization, design specifically as follows.

In this section of the highway embankment near the foot of the slope on the right side of the terrain set up under the 50-D piles (the right side of the road about 40 ~ 55m), pile-section in the form of 2.0cm × 3.0cm side of the pile, the pile level center distance 6.5m, length 21.0 ~ 26.0m, pile-thick concrete wall 25cm, piling pressure set-top roof beam; pile artificial hole pile, pile, and retaining top-pressure concrete beam intensity level of C25, C20 and C25; pile-anchor of the length of the pile since the potential sliding surface located at the top of rock under the date of its anchor and the depth of the potential sliding surface of the Ministry of pile-length ratio is about 1:1.

CONSLUSION

This article introduces the rose-landslide disasters and analyzes the causes of the events. Different sections of the landslide called for different analysis methods. The stability of the road indicates that this method is reasonable and provides a good reference to deal with similar disasters.

ACKNOWLEDGMENTS

The authors appreciate the support of Hunan Science and Technology Hall. It is natural fund project of Hunan Province. Project No. E080602.

REFERENCES

Zheng Yu(2000). "Landslide prediction research methods. "*World Geological,*19 (4): 370.

Li, Meng Hui, Dong Ying, et al(2004). "The type and the characteristics of geological disasters in China --- analysis of the results of the investigation based on of geological disasters in cities and counties nationwide." *Control of Geological Disasters Journal in China,*15 (2): 29 ~ 31.

"International Federation of Red Cross and Red Crescednt Societies." *World Disasters Report 1995 ,* pp150.

"Grifiths D V, Lane P A. Slope stability analysis by finite elements." *Geotechnique*, 1999, 49 (3): 3872403.

Runqiu Huang, Qiang Xu, et al(2002). "Simulation of geological disasters in the course of research and process control." *Science Press*, Beijing.

Ping Kan(1997). "Landslide's study in the role of groundwater. "*Chinese Academy of Sciences Institute of Geology*, Beijing.
Keefer, David K, Schuster Robert L(1993). "Landslides caused by the Klamath falls, Oregon, earthquakes of September 20, 1993. " *Earthquakes & Volcanoes*,24 (3):140~146.
Kun Long Yin, Yang Wang, et al(2002). "Rain on the slide mechanism and dynamic simulation . "*Geological Science and Technology Intelligence*, 21 (1): 75~ 78.

Evaluations of Pullout Resistance of Grouted Soil Nails

Jason Y. Wu,[1] M.ASCE, P.E. and Zhi-Ming Zhang[2]

[1] Associate Professor, Department of Civil and Engineering Informatics, Chung Hua University, Hsinchu, Taiwan, ROC, 30012; jasonwu@chu.edu.tw
[2] Site Engineer, Taipei City Government, Taipei, Taiwan, ROC 11008; m8904003@chu.edu.tw.

ABSTRACT: This study conducted laboratory and field pullout tests on grouted soil nails in sand to examine the interface shear resistance between nails and soil during pullout. The results indicated that the pullout strength found in the laboratory correlated reasonably well with that observed in the field. Such a finding makes the predication of field pullout resistance possible, based on the laboratory protocols developed in this study.

INTRODUCTION

Soil nailing technology has been used widely for the past several decades to stabilize slopes and retain excavations. It is an effective in-situ reinforcement technique, as compared to other soil-retention systems, and presents significant technical advantages (Juran et al., 1990; FHWA, 1993; Bahner, 2005). One of the most important design parameters for the soil nailing system is the ultimate shear strength at the interface between the cement-grout nail and surrounding soil (Chu and Yin, 2005). However, it is difficult to estimate with high accuracy due to the complicated interaction mechanism of the soil-nail. There are a number of influencing factors, such as: soil moisture content, soil properties, roughness of the soil-nail interface, stress conditions, testing methods, and nail installation procedures (Milligan and Tel, 1998; Chu and Yin, 2005; Pradhan et al., 2006; Su et al., 2007). In current practices, pullout resistance is estimated from an assumed skin friction on the interface between soil nail and soil, and it is then verified by field pullout tests during construction. Empirical values are often used for the design but frequently lead to inaccurate results (FHWA, 1993; Chu and Yin, 2005; Su et al., 2007).

Laboratory or field pullout tests have been the most convenient and popular means to obtain the design resistance of a nail (FHWA, 1993; Chu and Yin, 2005; Pradhan et al., 2006). Many researchers have used field and laboratory pullout tests and direct shear box tests to investigate the behavior of soil nails (Franzen, 1998; Milligan and Tei, 1998; Junaideen et al., 2004; Chu and Yin, 2005; Pradhan et al., 2006); however, no standard methods and configurations have been established since the pullout test is very sensitive to the test procedure and boundary conditions. The reported empirical correlations also are limited to the results of laboratory model tests and those obtained from field full-scale tests (Su et al., 2007).

This study conducted laboratory and field pullout tests using 32mmϕdeformed steel bars as model nails in sandy material to investigate the interface shear resistance between the cement-grout nail and soil during pullout. Comparisons were made, and correlations for values derived from the laboratory and in the field were proposed to facilitate the determination of pullout resistance for soil nailing design.

FIELD OBSERVATION

To study the pullout resistance of grouted nail in detail, this research first conducted field pullout tests on true size grouted nails installed on a cut natural slope. The slope had a maximum height of 24m, and was cut at 8m vertical height intervals of 1:1 (V:H) with 2m berms in 3 steps. The site material consisted mainly of medium dense to dense silty fine sand with some clay. The in-situ averaged wet density measured was 19.4 kN/m^3 and the moisture content measured was 15.7±2 %.

At the mid-height of each step of the slope, one grouted soil nail was installed. The nail hole was drilled with a 100 mm diameter rotary drill at a downward inclination of 15 degrees. Casing and water flushing were not used in order to prevent disturbance of the surrounding soil. A standard grade 60 deformed steel reinforcing bar (32mmϕ) with a length of 3m was then inserted into the hole. Two plastic centralizers were placed at equal spacing for each nail to keep the bar in the center of the hole. The grout filled the hole by gravity. The grout mix consisted of cement paste with a water-cement (W/C) ratio of 0.45. The average 28-day strength for samples taken at the site was 55.6 MPa. After 28 days of curing, the load tests were performed by loading the nail until pullout failure occurred. All of the tests were performed in a displacement-controlled manner at 1 mm/min in accordance with the recommendations in FHWA (1994) for sequence loading. After the pullout tests were done, samples of soil and reinforcing bars were collected and sent to the laboratory for further testing.

LABORATORY EXPERIMENT

Testing Apparatus

As shown in Figure 1, the designed pullout test box consists of six circular rings stacked in a vertical direction. Each ring has an outside diameter of 500 mm and a depth of 100 mm. The setup of the pullout test was similar to that described in FHWA (1994) except that it was rotated 90 degrees. Such a test setup avoids sophisticated and expensive system assembling and facilitates the installation of the soil nail. It also eliminated the possible bending and shearing effect of a heavy pullout device loaded on the relatively short test nail if it is inclined. Franzén (1998) concluded that this method has shown the best prediction of the pullout capacity from a pullout test. A center hole hydraulic jack and pump were used to apply the test load to the nail. A reaction plate was installed between the top edge of the test box and the jack. A rubber diaphragm filled with air was placed on the top of the soil sample for applying vertical pressure to the soil-nail system. Friction between the soil and the sidewalls of the box was minimized by lubricated oil. Displacement LVDTs and load cell were used to measure the displacement of the nail head and the applied load.

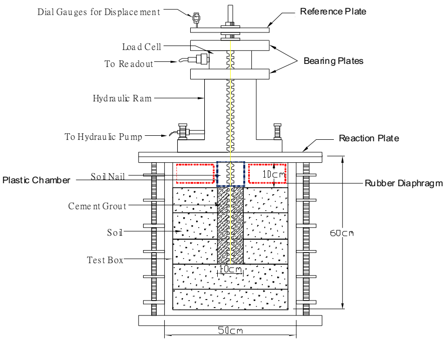

Fig. 1(a). Schematic of laboratory pullout test apparatus

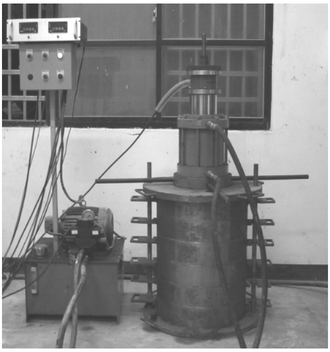

Fig.1(b). Photo of the setup for the laboratory pullout test.

Properties of Soil and Grouted Soil Nail

The soil used for the pullout tests was classified as yellowish brown silty clayey fine sand (SM-SC) collected at the site where field tests were conducted. Index properties, particle size distribution, the shear strength parameters of the soil and the interface of soil-grout were determined in accordance with ASTM protocols. Table 1 presents the test results.

Representative samples of true-size deformed steel bars collected at the site were used as model nails for the experiment. Each model nail had a diameter of 32mmϕ with an embedded length of 400 mm. Cement grout used for the tests was prepared in a manner similar to those in the field test. FHWA (1994) recommended that the grout should have a W/C ratio of about 0.4 to 0.5. The W/C ratio selected for the tests was based on the grout having a 28-day compressive strength of 50 MPa.

Pullout Test Procedures

After the pullout box was assembled and restrained, the soil sample collected at the site was then placed in layers and prepared to the same density and moisture content as in the site condition. Grouted nails were installed in a manner similar to the field practice. After the soil specimen was prepared, a drill hole with a diameter of 100mm was made with a hand auger. The auger was mounted on a steel frame to ensure proper alignment of the drilling. A model nail of 400 mm in length was inserted into the hole and the drill hole was filled with cement grout to bond the nail to the surrounding soil. Grouting was applied under gravity from the bottom of the hole upwards. The pullout box was then sealed with plastic wrap, and stored in a temperature controlled humid room for 28 days of curing. Before the pullout force was applied, specified normal pressures ranging from 0 to 325 kPa were applied through the pressurized rubber diaphragm positioned around the grouted nail to simulate the existing overburden pressures during the field tests. Settlement of the soil was monitored until it was close to final stabilization. A pullout test was then conducted using the controlled displacement method. The nail was put under tension at a displacement rate of 1.0 mm/min. Test procedures were generally similar to those described in FHWA (1993). Four laboratory tests were conducted with a new model nail and a new soil sample prepared for each test. Setup procedures were the same except for the applied normal pressures.

Table 1. Summary of Soil Test Results

Property	ASTM Standard	Value
Liquid Limit of fines	D-4318	23
Plastic Limit of fines	D-4318	18
Plasticity Index	D-4318	5
Specific Gravity	D-854	2.62
% passing #200	D-421	25.5
USCS Classification	D-2487	SM-SC
[a]Cohesion (kPa)	D-3080	12
[a]Friction Angle (°)	D-3080	30
[b]Interface Cohesion (kPa)	D-3080	10
[b]Interface Friction Angle (°)	D-3080	33.5

a. Quick direct simple shear tests for undisturbed soil samples collected at the site.
b. Quick direct simple shear tests performed on the soil-grout interface.

TEST RESULTS AND DISCUSSIONS

FHWA (1993) defined the maximum interface shear stress (q_p) as:

$$q_p = \frac{F_p}{\pi D l} \tag{1}$$

Where, F_p is the measured maximum pullout force; D and l is the diameter and embedded length of the grouted nail, respectively. The interface shear stress is a function of effective normal stress and the interface shear strength between the nail and soil. Chu and Yin (2005) proposed a modified equation for q_p based on Mohr-Coulomb failure criterion:

$$q_p = c'_a + \sigma'_v \tan \delta' \tag{2}$$

Where, c'_a is the soil adhesion at the interface, σ'_v is the effective normal stress, and δ' is the modified interface friction angle with a relationship of:

$$\tan\delta' = \frac{2}{\pi}\tan\delta'' \tag{3}$$

where δ' is the angle of the interface friction. Eq.(2) can be used to fit the shear strength data points to find the interface shear strength parameters of c'_a and δ. The pullout resistance under any effective normal stress thus can be calculated using these parameters (Chu and Yin, 2005).

Figure 2 shows the variations of interface shear stress (q_s) with displacement for the laboratory grouted nails tested under different normal stresses. It can be seen that q_s initially increased with the increase of the pullout displacement until it achieved the peak value (q_p). The observed q_p increased with the increase of normal stress and ranged from 26.2 to 95.8 kPa. Despite the increase of normal stress, the maximum pullout displacement for tested nails required to mobilize the maximum interface shear stress varied little (5 to 7 mm). As in the case of friction piles, the mobilization of interface shear stress requires only a small relative displacement of the nail in relation to the soil. This is generally consistent with observations reported elsewhere (Milligan and Tei, 1998; Junaideen et al., 2004; Chu and Yin, 2005).

Figure 3 presents the effects of normal stress on the pullout shear strength. The results for both laboratory tests and field observations appear to follow the Mohr-Coulomb failure criterion. The apparent cohesion found in the laboratory was only about 39% of that observed in the field. However, their failure envelopes were generally parallel and presented similar values of angle of interface friction (20±1°). As described earlier, the pullout resistance of a grouted nail can be affected by a number of factors. Considering that the laboratory model tests have been conducted in a duplicate manner of field condition, the discrepancy likely could be attributed to higher soil dilatancy in the field. During pullout testing, the dilatancy of the soil was constrained by the surrounding soil. This is capable of developing higher normal pressure at the failure surface and leading to much higher shear strength failure (Chai et al., 2004). The laboratory model nail was much shorter and the surrounding soil mass was significantly less than that in the field and therefore exhibited a lesser effect of soil dilatancy. As shown in Figure 3, such a difference was readily indicated in terms of apparent cohesion of Mohr-Coulomb failure envelope. Based on the relationships indicated in Figure 3 and using Eq. (2), the pullout resistance of a grouted nail at any location of the test site can thus be easily assessed.

The values of shear strength parameters depicted from the laboratory tests correlate reasonably well with those derived from field observations. The laboratory protocols developed in this study suggest an easy scheme for the prediction of the pullout capacity of a grouted soil nail and can save on the costly work of quality verification in the field. Further experimental works are underway to verify the above relationships.

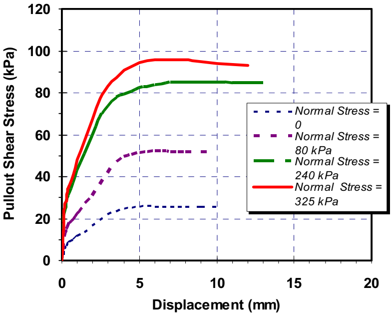

Fig. 2. Shear stress vs. horizontal displacement curves for laboratory pullout tests.

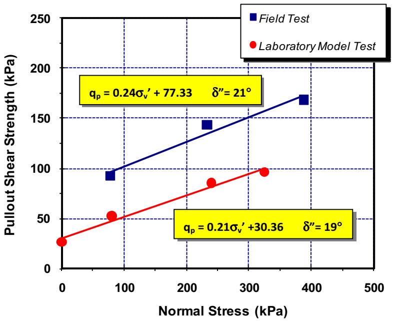

Fig. 3. Comparisons of pullout strength parameters between field observations and laboratory tests.

CONCLUSIONS

Based on the test results presented above, the following conclusions can be drawn:

The pullout shear strength for laboratory tests and field observations increased with the increase of normal stress and generally presented a tendency that appears to follow the Mohr-Coulomb failure criterion.

The apparent cohesion observed in laboratory was substantially lower than that derived from the field due to the effect of soil dilatancy. However, the values of the angle of interface friction were found to be similar for both tests. Such findings make the prediction of field pullout resistance possible based on the protocols developed in this study.

REFERENCES

Bahner, E.W. (2005). "Soil nailing: a local perspective." *Geotechnical Applications for Transportation Infrastructure*, Geotechnical Practice Publication No.3, pp.28-39.

Chu , L.M. and Yin, J.H. (2005). "Comparison of interface shear strength of soil nails measured by both direct shear box tests and pullout tests." *J. Geotechnical & Geoenv. Engrg.,* Vol. 131(9):1097-1107.

Chai, X.J., Hayashi, S., and Du, Y.J. (2004). "Contribution of dilatancy to pullout capacity of nails in sandy clay." Proceedings, Soil Nailing and Stability of Soil and Rock Engineering, Nanjing, China, pp.73-80.

FHWA (1993). "Recommendations Clouterre 1991 (English translation)." *Report on the French National Project Clouterre,* FHWA Rpt. No. FHWA-SA-93-026, Washington, D.C.

FHWA (1994). "Soil nailing field inspectors manual." FHWA, Rep. No. FHWA-SA-93-068, Washington D.C..

Franzén, G. (1998). “Soil nailing: A laboratory and field study of pullout capacity.” Ph.D. Dissertation, Chalmers University of Technoogy, Goteborg, Sweden.

Junaideen, S.M., Tham, L.G., Law, K.T., Lee, C.F., and Yue, Z.Q. (2004). “Laboratory study of soil-nail interaction in loose, completely decomposed granite.” Canadian Geotechnical Journal, Vol. 41(2):274-286.

Juran, I., Baudrand G., Farrg K., and Elias V..”Design of soil nailed retaining structures.” *Design and Performance of Earth Retaining Structures,* GSP 25, ASCE, 1990, 644-659.

Li, J., Tham, L.G., Junaideen, S.M., Yue, Z.Q., and Lee, C.F. (2008). “Loose fill slope stabilization with soil nails:full – scale test.” *J. Geotechnical & Geoenv. Engrg.,* Vol. 134(3):277-288.

Milligan, G.W.E. and Tei, K. (1998). ”The pullout resistance of model soil nails.” *Soils and Foundations,* Vol. 38(2): 179-190.

Pradhan, B., Tham, L.G., Yue, Z.Q., Junaideen, S.M., and Lee, C.F., (2006). “Soil-nail pullout interaction in loose fill materials.” International Journal of Geomechanics, Vol. 6(4):238-247.

Su, L.J., Chan, T.C.F., Shiu, Y.K., Cheung, T., and Yin, J.H. (2007). “Influence of degree of saturation on soil nail pull-out resistance in completely decomposed granite fill.” *Canadian Geotechnical Journal*, Vol. 44(11): 1314-1328.

Microscopic Mechanics for Failure of Slope and PFC: Numerical Simulation

Zhaoyang Xu[1,2], Jian Zhou[1], and Yuan Zeng[1]

1Department of Geotechnical Engineering, Tongji University, Shanghai 200092 P.R.China
2College of Civil Science and Engineer, Yangzhou University, Yangzhou 225009 P.R.China

ABSTRACT: The digital image analysis technology and non-target digital photography deformation measurement system have been adopted to measure the deformation and failure of slope in the model test. Based on the theory of the Particle Flow Code (PFC), the displacement and fracture surface of sand and clay slope are numerically simulated, and the displacement, rotation of granule and the variation of porosity inside the shear band are interpreted from the aspect of meso-mechanics. In addition, various constitutive relationships of particle contacts corresponding to different soil types are introduced to analyze the failure forms and the effect of meso-parameters on the macroscopic mechanical properties of sand and clay slope.

INTRODUCTION

Slope stabilization has been an important issue in civil engineering for many years. Because of the complexity of the stress and geological condition of slope, it is difficult to locate accurately the critical sliding surface and influencing factor of slope by continuum mechanics. PFC(particle flow code), based on the discrete element theory, was introduced to simulate the variation of displacement field of the sliding slope, which overcomes the deficiency of macro-continuity assumption in continuum mechanics and is a more logical method for locating the critical sliding surface compared with conventional ones.

Based on the measurement of the deformation and the failure of the soil slope in the model test, the entire process of the slope fracture, which involves the granule displacement and rotation, the porosity variation, is interpreted from the micro-aspect. Meanwhile, the PFC is introduced to simulate the development of the soil slope failure.

FAILURE OF SLOPE MODEL TEST

The model tests are conducted with Pingtan sand of China in model groove (dimensions include 100mm×40mm×50mm and 50mm×25mm×30mm). The soil slopes are loaded with poises from 20kPa, 40kPa, 70kPa, 80kPa to failure load.

The data are recorded just after each loading level is raised, and the corresponding digital photos are taken continuously using Olympus microscope and CCD video camera throughout the development of soil slope deformation and failure.

The photos of the slope model can be analyzed by Geodog graphical analysis program and then reprocessed by Post-viewer visual software.

The photos are divided into many pixel blocks, and the different pixel blocks can be distinguished by different grey levels. Then, according to the comparison of the location and angle of the pixel under various loadings, the changes of displacement and strain of each pixel can be traced and distinguished.

Fig.1 shows the process of the displacement development for sand slope under three stages of loading. And the displacement variation of clay slope is illustrated in Fig.2.

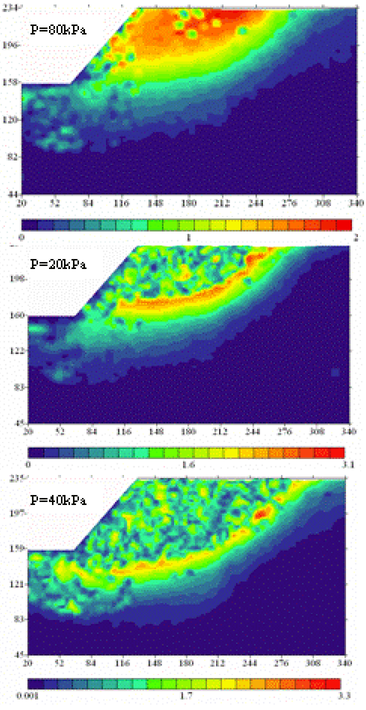

Fig.1. Displacement isoclines of sand slope

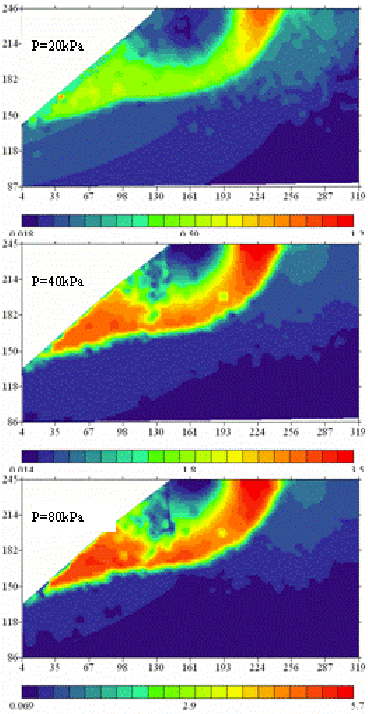

Fig.2. Displacement isoclines of clay slope

It can be seen from the deformation diagrams that the failure forms of sand slope are quite different from that of clay slope. For clay slope, under the first-stage loading, shear deformation on the top of the slope takes place first and then narrow cracks turn out. Under the second and the third-stage loading, the shear deformation further develops, and cracks extend to the middle of the slope and some of them are connected with each other. Therefore the process of clay slope failure turns out to be progressive. While for sand slope, it exhibits an obvious characteristic of suddenness. The soil slope has already failed just after the first two stages of loading, and correspondingly, shear bands stretch from top to base. With the loads being increased, soil piles out unceasingly and sliding surfaces of clay slope become quite different from that of sand slope in shapes. Clay slope soil slides down along circular contour, while for sand, there is a tendency that sliding surface varies from circular on the top of the slope to linear at the base.

Table 1. Meso- parameters of PFC sand

Contact strength /kPa	**Size/mm (height × width)**	**Grain diameter /mm**	$\frac{R_{\min}}{R_{\max}}$	**friction coe.**	**Particle normal rigidity**	**Stiffness ratio**	**Contact strength deviation**	**Velocity of wall /mm**	**Isotropic stress/Pa**
100	80×35	0.5	4.0	0.1-0.5	2.0×10^7	1.50	0.25	10	75×10^3
500	80×35	0.5	4.0	0.1-0.5	2.0×10^7	1.50	0.25	10	75×10^3
1000	80×35	0.5	4.0	0.1-0.5	2.0×10^7	1.50	0.25	10	75×10^3
1500	80×35	0.5	4.0	0.1-0.5	2.0×10^7	1.50	0.25	10	100×10^3

Table 2. Parameters of PFC clay

Density /kg/m^3	**Min. particle diameter /mm**	**Max. particle diameter /mm**	**Initial porosity**	**Frict. coef.**	**Normal stiffness /Pa**	**Tang. stiffness /Pa**	**Cu**	**Cv**	**D_{50} /mm**
2643	0.25	0.65	0.15	0.4	1.25e8	1.25e8	1.29	1.03	0.53

STABILITY ANALYSIS OF SLOPE BY PFC

In order to simulate the deformation of sand material accurately, the determination of the parameters in PFC sample is composed of two steps. Firstly, considering different shapes of particles, particle-cluster element is introduced by using FISH language to simulate interlocking among particles. Consequently, the four basic shapes of particles can be built, shown in Fig.3. Secondly, the size distribution of the particles in PFC should match the particle grading of Pingtan sand. Through the adjustment of meso-parameters in PFC model, the PFC model stress-strain curves agree well with the results in sand modeling experiment. The control parameters are shown in Table 1.

The circular particle in PFC is used to simulate the clay particle. Gradation and parameters are changed so as to make constitutive behavior of aggregate approach real material. In comparison with sand, the contact bond constitutive model is introduced in clay to simulate the adhesion of the particles. Types of contact constitutive models are shown in Fig.4. The clay parameters are shown in Table2.

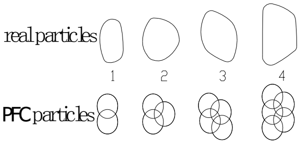

Fig.3. Shapes of particles

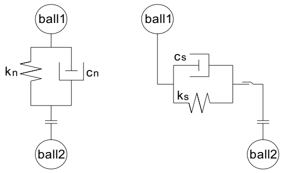

(a) Normal direction (b)Tangential direction

Fig.4. Contact constitutive models of particle

The particles dimensions are magnified during the process of simulation, and the resulting particle number is about 20,000-30,000. It not only solves the problem of the limitation of computer's computational capability and velocity, but also satisfies the precision requirement.

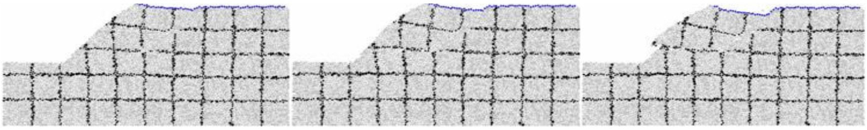

Fig.5. Simulated result of clay slope by PFC under multi-stage loading

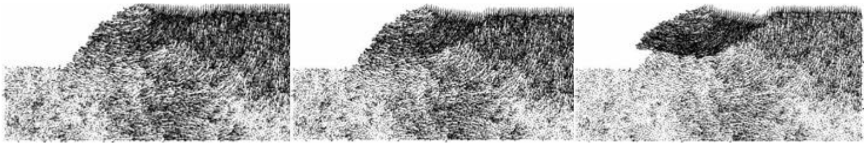

Fig.6. Displacement vector of clay slope under multi-stage loading

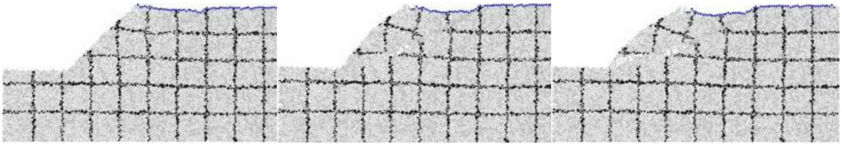

Fig.7. Simulation results of sand slope by PFC under multi-stage loading

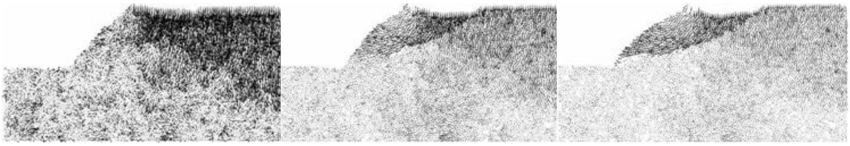

Fig. 8. Displacement vector of sand slope under multi-stage loading

The deformation and displacement simulation of clay slope are shown in Fig.5 and Fig.6. In order to be observed clearly, the model is divided into grids with different colors. The results of sand slope simulation can be seen in Fig.7 and Fig.8.

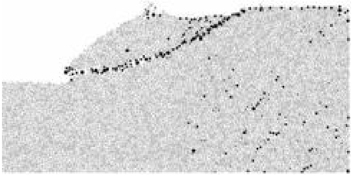

Fig. 9. Diagram of rotation grades of particles

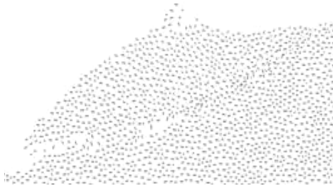

Fig. 10. Diagram of particles direction angle

In displacement diagrams, fracture of sand slope exhibits suddenness.

Fig.9 shows rotation grades of particles. In the diagram the dark color denotes that the rotation angle is larger than 10 degrees. As seen in Fig.9, the particle rotation only occurs within the shear band and most sliding particles keep rigid movement.

The particle angle in Fig.10 has been partially magnified, in which the lines direction represent the angle of each particle. Except the particles in shear band, the directions of the rest particles remain unchanged and keep horizontal. And particles on top of the slope are dense, while the porosity of particles at the bottom becomes larger obviously. The evolution of porosity in different location is shown in Fig.11. At the beginning, the compression of the particles lead to the emergence of shear band and the dilation of material which results in the porosity increasing at the bottom and in the middle of soil slope. When shear band links up, the particles moves and then re-arranges under loading. Finally, the equilibrium condition is reached through the adjustment of the particles inter-force and the sliding surface comes into being as well.

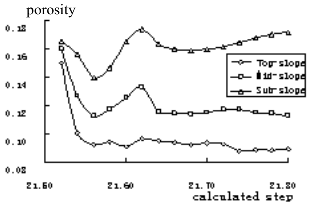

Fig.11. Evolution of porosity

EFFECTS OF MESO-MECHANICS PARAMETERS ON SLOPE FAILURE FORM

It is well-known that slope failure form is influenced by internal structure and external conditions. This paper investigates the effects of meso-mechanics parameters of particle, including linkage strength and friction coefficient. Parameters of PFC model are shown in Table 3.

In Fig.12, linkage strength of particles is zero, which means the soil is non-cohesive and the linkage of particles lies in contact stress completely. Initial failure occurs from the top of the slope, which causes large-scale sliding due to the loss of the support of the top and the middle of the slope. For the clay case, the initial failure occurs at the top of the slope at the beginning, and cracks can be detected from the slope surface. And then at the middle of the slope larger cracks turn out which cause the shear slide. Finally the entire slope slides along the failure surface.

Table 3. Parameters of model PFC

Particle model	Linkage strength (Pa)	Friction coefficient	Density (kg/m^3)	Kn(Pa)	Ks(Pa)
Model-1	0	0.9	2600	6e8	6e8
Model-2	1e5	0.9	2600	6e8	6e8
Model-3	3e5	0.9	2600	6e8	6e8
Model-4	3e5	0.5	2600	6e8	6e8

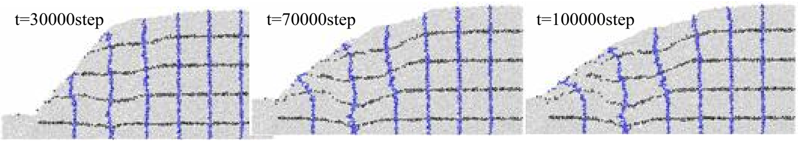

Fig.12. Process of slope failure ($pb=0, f=0.9$)

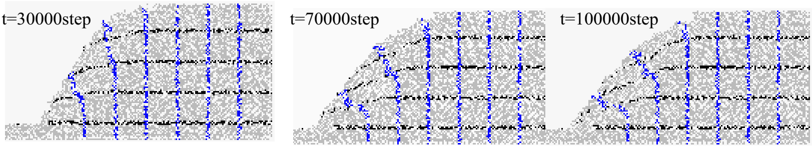

Fig.13. Process of slope failure ($pb=100kpa, f=0.9$ **)**

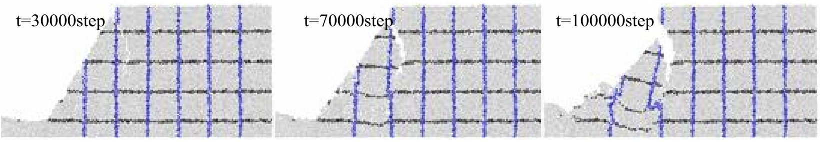

Fig.14. Process of slope failure ($pb=300kPa, f=0.9$ **)**

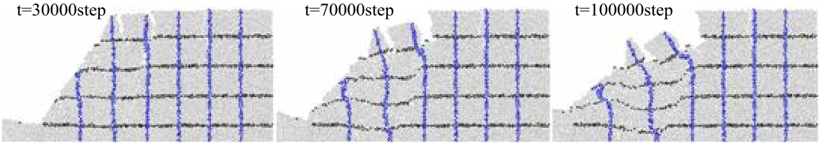

Fig. 15. Process of slope failure ($pb=300kPa, f=0.5$ **)**

Therefore, slope deformation and failure form are influenced by meso-parameters. With the increasing of clay cohesion, slope fracture changes from plastic failure to brittle failure. For non-cohesive slope, the entire slope body presents a plastic flow state, without any obvious cracks.

CONCLUSIONS

Based on the theory of particle flow, the development of displacement field of the sliding slope is simulated without assuming the location and shape of sliding surface, which overcomes the deficiency of macro-continuity assumption in continuum mechanics and is more logical than conventional search method for locating the critical sliding surface. From the displacement field of particles and emergence and development of shear band, it can be concluded that the results of the simulation generally satisfy the test results.

The results of the research help to comprehend mechanical characteristics of soil and the process of successive failure of slope. In future research, we will improve the precision of the results by using three-dimensional approach to simulate the slope deformation.

ACKNOWLEDGMENTS

Funding for this work was provided by The National Natural Foundation of China (50178054).

REFERENCES

Cundall,P.A.(1989).“Numerical Experiments on Localization in Frictional Material.” *Ingenieur-Archiv*, Vol .59:148-159.

JIANG Minjing and SHENG Zhujiang.(1998). “Microscopic analysis of shear band in structured clay.” *Chinese J. of Geotechnical Eng.*, 20(2):102-108

Oda,M. and Kazama,H. (1998). “Microstructure of shear bands and its relation to the mechanism of dilatancy and failure of dense granularsoils.” *Geotechnique*, Vol48(4):465-481

Khalid,A and Alshibli,S. S. (1999). “Sand shear band thickness measurement by digital imaging techniques.” *J. of Computing in Civil Eng.*, 13(2):103-109

White,D. J. and Take,W.A.(2002). “A deformation measurement system for geotechnical testing based on digital imaging,close-range photogrammetry and PIV image analysis.” 15th ICSME, Rotterdam: Balkema :539-542.

ZHOU Jian, et al. (2000). “The method of particle flow and PFC2D code.” *Rock and Soil Mechanics*.Vol.21(3):271–274.

BARDET,J P and PROUBET,J.(1991). “A numerical investigation ofstructure of persistent shear bands in granular media.” G*eotechnique*, 41(4):599–613.

MUHLHAUS,H.B. and VARDOULAKIS,I. (1987). “The thickness of shearbands in granular materials.” *Geotechnique*,Vol.37:271–283.

ZHOU Jian, et al. (2000). “Simulation of biaxial test on sand by particle flow code.” *Chinese J. of Geotechnical Engineering*, .22(6):701–704.

Bardet,J.P. and Proubet,J. (1991). “A numerical investigation of structure of persistent shear bands in granular media.” *Geotechnique*, 41(4):599-613.

ZENG Yuan. (2006). “Microscopic Mechanics of Soil Failure and PFC Numerical Simulation.” *PhD dissertation, Tongji University.*

Influence of Soil Strength on Reinforced Slope Stability and Failure Modes

Hong-Wei Wei[1], Ze-Hong Yu[1], Jian-Hua Zhang[2], Zhi-Hui Zhu[1], and Xiao-Li Yang[1]

[1]Professor,School of civil and architecture engineering, Central south university, Changsha, China, 410075. E-mail: whw.edu@163.com.
[2]Engineer, Ning-Dao Expressway Development Limited Company, Changsha, China,410075.

ABSTRACT: Finite element method was applied to analyze the reinforced slope stability in the paper, and under conditions of reinforcement materials matched with soil of various strengths, the shear zone characteristics and failure modes, as well as the influences of the soil strength parameters on reinforced effect, were also investigated. Results showed that reinforcement had increased significantly the apparent cohesion of soil, the reinforced sandy slope was damaged along a certain sliding arc, and appeared the cohesive slope destruction characteristics, the failure modes of the traditional sand slopes were varied correspondingly, and the integrity and stability of sandy slopes were all improved. Even with the same reinforcement material, reinforcement effect on the stability of the slope differed with various index of soil strength. The selection of the strength combinations of reinforcement and soil within a certain range could sufficiently mobilize the interactions to improve the reinforcement effect. Results also showed that reinforcement could improve the soil strength and enhance the stability of the slope to a certain extent, but could not change the main body of soil in the reinforced slope. Considering the combination of reinforcement and soil is crucial to ensure the reinforced effect in reinforced slope design.

INTRODUCTION

In the past 10 years of highway construction projects, Application of reinforced embankment slope with geosynthetics had developed very rapidly, Reinforced soil with geosynthetics improved soil strength and the overall stability of the embankment slope, particularly in mountain highway, through rational design of the reinforcement, the height of reinforced slope could increase by 10% to 30% compared with that of soil slops, thus reduced significantly the field occupation and fill construction. Reinforcement technique possesses a good application prospect.

Influence factors on reinforced soil strength are complex, not only depended on the strength of reinforced material, but also on that of the soil, as well as the interaction between soil and reinforcement. For a certain strength of the reinforced material, matched with the soil of different strengths, the interaction characteristics differed, reinforced soil appeared different strength characteristics, the research can be found in the literature of O'Rourke & Druschel (1990), Zou & Zhang (1998), Wei & Yu (2005) et al. As a result, ignorance of the combination of reinforcement and soil in the reinforced slope designs might usually be the key reason to cause failure of reinforced slopes, the related work accidents had been discussed in literature [7].

Influences of reinforcement modulus and layers on shear zone yield characteristics and failure modes of the reinforced slope had been investigated by Yu in 2003-2004, but the impact of soil strength on the stability of reinforced slope might be the same important factor. Finite element analysis models of a reinforced embankment slopes were established and the visual graphics technology was also applied to research reinforced soil slope stability, as well as the shear zone yield characteristics and failure modes with various soil friction angle φ and cohesion c, and its influences on the reinforced effect. In comparisons with test results, the calculation models and analysis results were reasonable.

FINITE ELEMENT METHOD FOR REINFORCED SLOPE STABILITY

The stability of the reinforced slopes was determined by the combination work of soil and reinforcement. Therefore, the plane units, one-dimensional linear units were all set up to simulate soil and reinforcement material respectively, and only the reinforcement axial stress were considered, while the bending stress were ignored in finite element calculation. Between soil and reinforcement the contact friction units were used to simulate their interactions. The slope stability analysis was simplified by plane strain problem in the paper.

In the reinforced slope, reinforced materials and soil went through almost the same strain due to the extensity of Geosynthetics, only when collapse happened in reinforced slope, a relatively small slide emerged, therefore, within a certain range of deformation, soil and reinforced materials deformation were compatible, in order to simplify the calculation, assuming that the node-node contact on two surface, and maintaining a small amount of deflection, contact elements were applied to simulate the state of the work on reinforcement and soil interface. The reinforced materials were laid on all around the whole width of embankment with uniform distribution. The boundary conditions were given as vertical rollers on the left and right boundary, full fixity at the base, and free boundary at the rest .

The Soil model used in this study consists of six parameters: internal angle φ cohesion c, elastic modulus E, Poisson's ratio μ dilatancy angle ψ unit weight γ

The dilatancy angle ψ affects the volume change of soil during yielding , if $\phi=\psi$ then plasticity flow rule is associated, and direct comparison with the classical plasticity theory can be made, but the calculation of dilatancy is too large than that is observed in reality. This in turn leads to increased failure load prediction, especially in confined problems, the constitutive soil models to incorporate non-associated plasticity are used to resolve. Slope stability analysis is relatively unconfined, so the choice of dilation angle is less important. The value $\psi= 0$ had been used in the paper, corresponding to a non-associated flow rule with zero volume change during yield. Griffiths (1999) studies showed that this option enabled the model to give reliable factors of safety and reasonable potential failure surface shapes and locations.

Mohr-Coulomb yielding criterion remains widely used in geotechnical practice, but Mohr-Coulomb yielding surface was an irregular hexagonal section with cone angles, brought the numerical difficulties. Broading Mises yield criteria is cone-shaped surface, and can be written as follows:

$$\alpha I_1 + \sqrt{J_2} = k$$

(1)

Where: I_1, J_2 are the first invariant of stress tensor and the second invariant of stress tensor deviator. α,κ are constants related with the rock material. In plane π, α,κ represent various circles, and through different transformation of expressions of α,κ, various yielding criterions can be realized in the finite element .In order to compare with the traditional method, Xu, Gan-Cheng, Zheng, Ying-ren (1990) put forward equivalent area with Mohr-Coulomb criterion in place of traditional Mohr-Coulomb yield criterion, the calculation results were close to that with Mohr-Coulomb criterion, compared with Bishop simplified method, the average error of the slope safety factor calculated was 5.7%, and calculation dispersion was smaller. α,κ can be written as follows:

$$\alpha = \frac{2\sqrt{3}\sin\varphi}{\sqrt{2\sqrt{3}\pi\left(9-\sin^2\varphi\right)}} \qquad k = \frac{6\sqrt{3}c\cos\varphi}{\sqrt{2\sqrt{3}\pi\left(9-\sin^2\varphi\right)}} \tag{2}$$

The factor of safety of slope was defined in the paper as the number by which the original shear strength parameters might be divided in order to bring the slope to point of failure. The soil friction angle and cohesion were input, and gravity load were imposed step-by-step during calculation. And then the soil strength parameters c, φ were gradually reduced uptill to the reinforced slope sliding appearance, the factored shear strength parameters c', φ' were just the required strength of soil to remain the equilibrium of slope. The factor of safety of slope was therefore given by:

$$c' = \frac{c}{F_s};\ \tan\varphi' = \frac{\tan\varphi}{F_s}$$

(3)

The stresses and strains were redistributed in reinforced slope, due to the finite element method solutions would give information about the internal stresses and deformations of slope, therefore, the influences of reinforcement force on stresses on the potential sliding surface, and the stabilizing effect of reinforcement were considered more comprehensively.

The shear zone going through was taken as an indicator of failure in the paper. During calculation, slope failure and numerical non-convergence occurred simultaneously, and were accompanied by a dramatic increase in nodal displacements within the mesh, when close to the real safety factor F_s.

INFLUENCES OF SOIL STRENGTH PARAMETERS ON REINFORCED SLOPE STABILITY

In the examples studied, the slope was inclined at an angle of $\beta=40^0$, the height H=20m. Calculation parameters included: unit weight γ=21kN/m^3, elastic modulus E=20MPa, Poisson's ratio μ=0.3; tensile modulus of reinforcement E_R=200kN/m, the number of reinforcement layer n=8. Normal rigidity coefficient of interface between soil and reinforcement FKN=1E6kN/m^2, and tangential rigidity coefficient FKT≤320 kN/m^2.

Effects of cohesion on reinforced slope stability

Given the soil friction angle$\varphi=15^0$ and$\varphi=30^0$, the safety factors of reinforced and unreinforced slopes were all calculated with various cohesion c, the safety factor increments with increasing cohesion c of reinforced slopes in comparison with that of soil slope were summarized in Table1, and illustrated in Fig.1.

For the same reinforcement modulus and layer, the increments of reinforced slopes differed with the various cohesions. Due to the reinforced soil significantly improving the apparent cohesion the safety factor increased larger relatively when the soil cohesions were low. Reinforced effect of the stability were not the same either under different friction angles, in particular, when both the friction angles and cohesion were lower, the safety factor increments of reinforced slopes increased more significantly. Therefore, the main contributions to the slope stability made by reinforcement attributed to the increase of soil cohesion.

Table 1. Safety Factor Increments of Reinforced Slope in Relation to Soil Slope with Various Cohesion *c*

	Cohesion *c*/ kPa									
	120	100	80	60	40	20	10	5	1	0.1
Safety factor increments/%, whenφ=30°	5.86	6.51	7.33	9.95	6.59	7.69	9.17	9.18	9.20	9.52
Safety factor increments/%, whenφ=15°	3.54	4.17	9.84	8.50	9.02	10.3	8.82	10.5	12.2	14.3

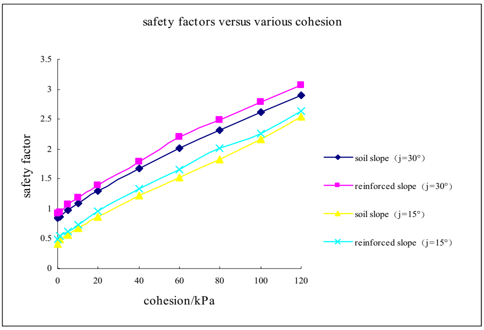

Fig.1. Safety factor of slopes versus cohesion *c*

In the soil slope, safety factor appeared linear increase with the cohesion increase, while in the reinforced slope the safety factor increment varied with the different cohesion c. In the range of cohesion c less than 20kPa, the space of safety factor envelopes of the reinforced slope and soil slope were smaller relatively compared with that of the cohesion in 20kPa ~100kPa, and when cohesions were greater than 100kPa the space tended to be stable. These showed that within cohesion of 20kPa to 100kPa, the interaction between soil and reinforced material appeared coordinating, and reinforced effects on stability safety factor increase were more significant. Taking into account the slope safety factor value in the Norm, in this example, the filling material cohesions should be chosen in range of 20kPa~100kPa.

Effects of cohesion on reinforced slope shear zones and failure modes

The shear zones of soil slope when the cohesion close to c=0 were illustrated in Fig.2 (a). As a result of the limitation of calculation model, c=0.1kPa was used to simulate the soil without cohesion, in this situation, the shear zones calculated of the reinforced slopes were similar with that of sandy slopes, the results at the same time showed the rationality of calculation model.

The reinforced slope shear zones moved towards the internal slopes and foundation as illustrated in Fig.2 (b), the failure modes appeared destruction characteristics of the cohesive slopes, the slope integrity was enhanced, and the tendency to soil cohesion increase was conformed to the test results.

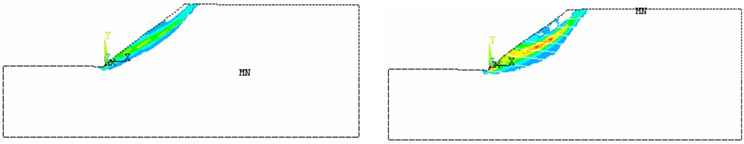

（a） c=0.1kPa, Fs =0.42 （b） c=0.1kPa, Fs =0.48

Fig.2. The shear zones of soil slopes versus various cohesion

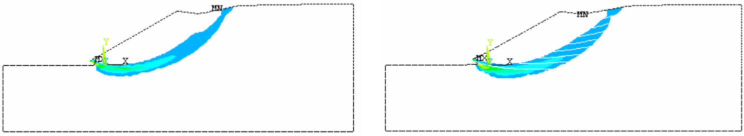

（a） c=100kPa, Fs =2.16 （b） c=100kPa, Fs =2.78

Fig.3 Shear zones of reinforced slopes with various soil cohesion

With the reduction of soil cohesion, the shear zones of both the reinforced and soil slopes moved towards the surfaces of slope, as illustrated in Fig.2 and Fig.3. But the shear zone width of the reinforced slope along the reinforcement direction was wider apparently, and showed more soil near the shear zone was involved in resistance to slope sliding due to the friction and bite between soil and reinforcement, in addition, the tensile strength and separation of reinforcement all prevented the partial damage from the continuity, and enhanced the stability of the slope. At the same time, even if the cohesion c=0.1kPa, the shear zone of reinforced slope still possessed a certain angle with the slope surface, and tended to slip along a certain arc, with a cohensive slope failure feature. The plane failure modes of non-cohesive sand slope had been revised due to reinforcement, as showed in Fig.2 (a) (b).

The cohesion strength of reinforced soil consists of two parts, one was possessed by soil itself, and the other was reinforced by the interaction of reinforcementl and soil. The triaxial test and direct shear test results all showed that the strength increase of reinforced soil mainly caused by the apparent cohesion increase, seen in literature [7-8]. These calculation results not only showed the effects of reinforcement on slope stability differed with various soil cohesion, but also the reinforced slopes differed essentially from the unreinforced in the safety factors, performances of shear zones and failure modes, as illustrated in Fig.2 (a) (b). In particular, when the soil cohesion reduced down to c=0.1kPa, this appeared more intuitively. Therefore, for the sandy slope, reasonable reinforcement enabled slope stability improved, but the failure mode of sliding parallel to the slope surface also varied correspondingly.

Effects of various friction angles φ on reinforced slope stability

In the examples studied, the soil cohesion were given as c=40kPa and 60kPa respectively, other calculation parameters were the same as that above.

Safety factors of reinforced and unreinforced soil slopes were summarized in Table2. The safety factor of slopes were significantly reduced with the soil friction angle reduction, down close to $\varphi 0^0$, the safety factors of the reinforced and unreinforced slopes were almost equal, and reinforcement had no action on slope stability, as illustrated in Fig. 4, whether reinforced or soil slope, their safety factors reduced with the friction angle, the decrement of safety factor increased at $\varphi \leq 5^0$.

Table 2. Slope Safety Factors with Various Soil Friction Angles

	Friction Angle φ							
	45°	35°	25°	15°	10°	5°	1°	0°
Soil Slope (c=60kPa)	2.56	2.17	1.85	1.54	1.35	1.15	0.94	0.845
Reinforced Slope(c=60kPa)	2.70	2.38	2.03	1.68	1.46	1.21	0.95	0.854
Safety Factor Increment/%	5.47	9.68	9.73	9.09	8.15	5.23	1.06	1.06
SoilSlope(c=40kPa)	2.25	1.87	1.52	1.22	1.07	0.86	0.65	0.556
Reinforced Slope(c=40kPa)	2.34	1.95	1.66	1.31	1.13	0.92	0.67	0.563
Safety Factor Increment/%	4.00	4.28	9.21	7.38	5.61	6.98	3.08	1.26

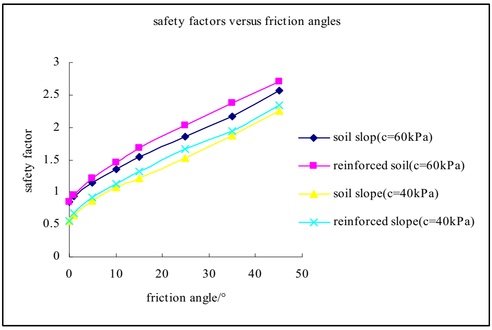

Fig.4. Safety factor versus friction angle

The spaces of safety factor envelopes of reinforced and unreinforced slope were varied with various friction angles, as illustrated in Fig.4. Under cohesion *c*= 40kPa condition, the safety factor envelope space of the reinforced and unreinforced slopes was smaller, only nearby *c*=25kPa did the greater distance occur. While under *c*=60kPa condition, the space between safety factor envelopes appeared more far relatively within the range of 15~45kPa of cohesion. The relationship between increment of reinforced slope safety factor and soil cohesion and friction had just reflected the complexity of interaction between the reinforcement and soil.

Effects of various frictions on reinforced slope shear zones and failure modes

The shear zones of soil slopes moved gradually into the slope and foundation with reduction of soil friction angle, φ as illustrated in Fig.5. When the friction angle dropped down to 0^0, the shear zones went completely through the foundations, appeared the destruction characteristics of soft ground. With the friction angle decreases the shear zones of reinforced slopes also gradually moved into the slope, and with φ=0° went through the foundations in Figure 6, these tendencies were consistent with that of soil slopes. But under the same condition, the widths of shear zones of reinforced slopes increased compared with that of soil slopes, as showed in Fig.5 and Fig.6. It was just did the shear bonds appear that more soil strengths were mobilized to resist the slope slip, and raised safety factors of reinforced slope. On $\varphi=0^0$ condition, due to no friction between the reinforcement and soil, the soil shear strengths were not improved, the shear zones of reinforced slopes were basically the same with that of the soil slope, and the slope safety factor had no increase. These were conformed to the undrained shear test results in the literature [8].

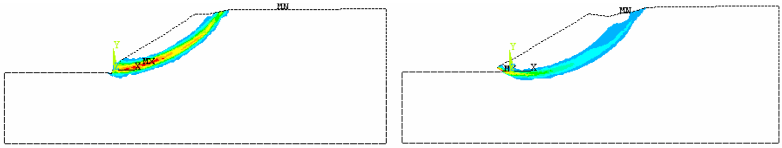

(a) φ=45°, Fs =2.25 (b) φ=10°, Fs =1.07

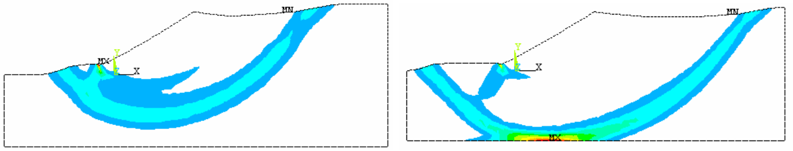

（c） φ=1°, Fs =0.65 （d） φ=0°, Fs =0.56

Fig.5. Compaction of soil friction on shear zones of soil slope

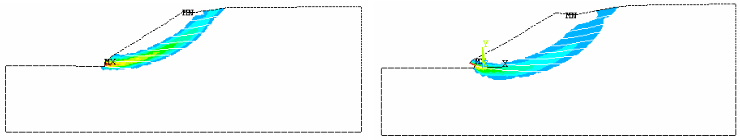

(a)φ=45°, Fs =2.34 (b) φ10 °, Fs=1.12

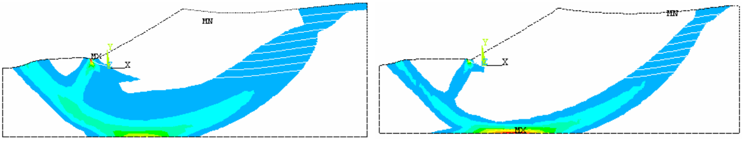

(c)φ=1°, Fs =0.67 (d)φ=0°, Fs =0.56

Fig.6. Impaction of soil friction on the shear zones of reinforced slopes

On the rapid filling construction or poor drainage conditions, reinforcement effects on improving the slope stability was not too significant. As a result of poor drainage, the collapse of reinforced slope occurred frequently in actual projects. Analyses of the causes of the accident had been usually attributed to the reinforcement, in fact, reinforcement could improve the force states in slopes, but could not enable all problem to be resolved. Soil is still the main body in reinforced slopes, the basic engineering design principles still have to be complied with in reinforced slope designs. Designers must consider sufficiently a reasonable selection of reinforcement material and construction scheme under the specific circumstances and the soil nature in order to achieve the best reinforced effects.

Analyses also showed that on a poor drainage condition, sliding arc was unlikely to be a damage mode in the embankment slope, but might be asymmetric destruction mode squeezed out of the deep soil, as showed in Fig. 5 (c) (d).and Figure 6 (c) (d), thus, the assumption of traditional circular sliding in limit equilibrium analysis method needs further discussion.

SUMMARY AND CONCLUSIONS

The following conclusions can be made from this study:

Reinforcement had increased significantly the apparent cohesion of soil, the reinforced sandy slopes were damaged along a certain sliding arc, and appeared destruction characteristics of cohesive slope, the failure modes of the traditional sand slope were varied correspondingly, and the integrity and stability of sandy slope were all improved.

Even with the same reinforcement material, reinforcement effects on the stability of the slope differed with various soil strength index. The selection of the strength combinations of reinforcement and soil within a certain range could sufficiently mobilize the interactions to improve the reinforcement effects.

On poor drainage conditions, effects of reinforcement on the slope stability was not significant, even act on a positive role. The collapse of reinforced slope relating to poor drainage occurred frequently in actual projects. Analyses of the causes of the accident had been usually attributed to the reinforcement. In fact, reinforcement could improve the force states in slopes, but could not enable all problem to be resolved. Soil is still the main body in reinforced slopes, the basic engineering design principles still have to be complied with in slope reinforced designs. Designers must consider sufficiently a reasonable selection of reinforcement material and construction scheme according to the specific circumstances and the soil nature in order to achieve the best reinforced effects. Compared with reinforcement strength and layer, drainage condition and construction speed is more critical to slope stability.

The analyses showed that the reinforced slope failure modes of reinforced slope were varied with the reinforcement conditions, the assumption of traditional arc sliding in limit equilibrium method were needed further discussion, while slope safety factors given by finite element method were perhaps more reasonable.

ACKNOWLEDGMENTS

The writers acknowledge the support of the National Science Foundation of China, Grant No. 50778181 & 50808177. Additional founding was also provided by the Water Conservancy Department of Hunan, Grant No. 2007Z08, the Science & Technology Department of Hunan, Grant No. 2007FJ4188, the Construction Department of Hunan, Grant No. 06hnjs007. All these supports are gratefully acknowledged.

REFERENCES

McGown, et.al(1978), “Effect of Inclusion Properties on the Behavior of Sand”, *Geotechnique*, 128(3): 327-346.

Tumay, M. T., Antonini, M., and Arman, A.(1979), “Metal Versus Nonwoven Fiber Fabric Earth Reinforcement in Dry Sands: A Comparative Statistical Analysis of Model Tests”, *Geotechnical Testing Journal*, ,2(1): 44-56.

O’Rourke, T., Druschel, S., and Netravali, A. (1990), “Shear strength characteristics of sand-polymer interfaces”, *J. Geotech. Eng.*, 116(3): 451-469.

Zhou,X.H, Zhang,Q.S(1998). “Test report on engineering performances of geogrid”.*Journal of Hunan University* (natural sciences), (3):55-61

Wu Jing-hai,Wang De-qun, Chen Huan(2000), “Triaxial test on sand reinforced withgeosynthetics” *Chinese J. of Geotechnical Engineering*, 22(2):199-204

Bao Fu-hua, Zou Yi-tang, Zhao Chuan(1999), “Study on geogrid reinforced stone”, *Chinese Journal of Geotechnical Engineering,* 21(2):217-221

Analysis for deformation and shear zones of reinforced embankment, A dissertation submitted in partial satisfaction of the requirements for the degree of Doctor of engineering, Hunan University, Changsha, Hunan, China,2004.

Wei Hong-wei, Yu Ze-hong, Zou Yin-sheng(2005), "Shear characteristics of soil reinforced with geosynthetic material", *J. of Hydraulic Eng.,* 36(5):555-562

Duncan, J. M.(1996), "State of the art: limit equilibrium and finite-element analysis of slopes", *J. Geotech. Eng.*, ASC,122(7):577-596.

Jorge G. Zornberg, Nicholas Sitar, James K. Mitchell(1998). "Performance of geosynthetic reinforced slopes". *J. of Geot. and Geoenv. Eng.*, 124(8).

Griffiths. D. V. &Lane. P. A.(1999), "Slope stability analysis by finite elements", *Geotechnique*, 49(3): 387-403

Xu Gan-cheng, Zheng Ying-ren(1990). "Application of yielding criterion in geotechnical engineering". *Chinese J. of Geotechnical Eng.*, 12(2):93-99

Yu Ze-hong, Zou Yin-sheng, Wang Yi-sun(2004), "Influence of modulus of soil and reinforcement analysis of slopes reinforced with geosynthetics", *Chinese Journal of Geotechnical Eng.*, (6): 787-791.

Design of a Hybrid Reinforced Earth Embankment for Roadways in Mountainous Regions

Chia-Cheng Fan[1] and Chih-Chung Hsieh[2]

1Associate Professor, Dept. of Construction Engrg., National Kaohsiung First University of Science and Technology, Taiwan, R.O.C.
2, Jhuoyue Rd., Nanzih District, Kaohsiung City, Taiwan, R.O.C.; ccfan@ccms.nkfust.edu.tw
2Formerly Graduate Student, Dept. of Construction Engrg., National Kaohsiung First University of Science and Technology, Taiwan, R.O.C.

ABSTRACT: This paper presents the mechanical behavior of a hybrid reinforced earth embankment, incorporating reinforced earth embankments with soil nails, built in limited fill space. Soil nails are installed on back of reinforced earth embankments to provide additional resisting forces to stabilize the embankment. This study aims to analyze nail forces developed within a hybrid reinforced earth embankment with various geometric conditions in the fill space. Influence of reinforcement length and slope gradient of the embankment facing on the distribution of nail forces was analyzed and discussed. Simple design charts for determining the nail forces mobilized on back of hybrid reinforced earth embankments in narrow fill space were established in this research.

INTRODUCTION

Reinforced earth retaining structures are conventionally used in areas where the fill space is sufficiently wide for placing reinforcements with the required length. Reinforced earth embankments are being used increasingly in transportation projects throughout the world. In a mountainous region, however, building a stable reinforced earth embankment may be very difficult due to steep slopes or insufficient spaces for placing reinforcements. In addition, mountain roadways may suffer from failures during heavy rainfall events or in seismic conditions. The width of collapsed roadways may be inadequate for building a stable reinforced earth embankment. A hybrid earth embankment system was developed to use in mountain roadways with a limited fill space (Fan and Hsieh, 2007). The hybrid system incorporates a reinforced earth embankment which is connected to the existing ground slope with soil nails, as shown in Figure 1(a). Soil nails provide additional resisting forces to stabilize the reinforced earth embankment which is potentially unstable due to insufficient reinforcement lengths. A flexible connecting system was developed to tie the reinforcements within a reinforced earth embankment to soil nails installed in the firm ground behind the embankment. This hybrid reinforced earth embankment system can also be used in widening existing embankments, repairing collapsed mountain roadways, and other conditions with limited fill space. The key to properly design this hybrid reinforced earth embankment for a given loading condition is to determine the stress distribution to the reinforcements, connecting elements, and soil nails. The idea of the hybrid reinforced earth embankment is highly feasible in engineering practice and has been used in a few cases recently. However, there is no theory or methodology, e.g. limit equilibrium methods, so far to analyze this proposed system.

This study aims to investigate the mechanical behavior of the embankment system using the finite element method and to develop design charts for soil nails. Static loadings were accounted for in the FE analyses. The influence of the reinforcement length and slope gradient of the embankment facing on the distribution of nail forces was also analyzed and discussed in this paper.

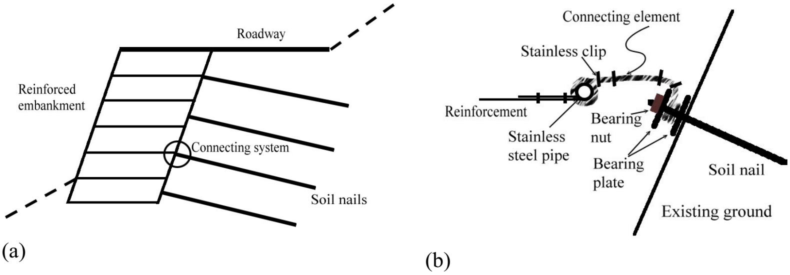

Figure 1. Illustration of a hybrid reinforced embankment system used for mountain roadways. (a) a hybrid embankment system; (b)details of connecting elements (Fan and Heish, 2007).

COMPONENTS OF THE HYBRID REINFORCED EARTH EMBANKMENT

A series of connecting elements are used to incorporate reinforced earth embankments with soil nails, as shown in Figure 1(b). The connecting element, improved from a patented connecting method (Chou and Fan, 2004), consists of a series of stainless steel wire ropes and stainless steel pipes. Stainless steel wire ropes are used to connect soil nails with reinforcing materials by binding the nail head and the steel pipe. At least a pair of stainless steel wire rope clips are used to tie the stainless steel wire rope at both ends. Horizontal spacing for the connecting elements is typically 1 to 1.5m.

Numerical modeling

The finite element procedure was used to model the construction of the hybrid reinforced earth embankment system. The non-linear finite element program PLAXIS (PLAXIS BV, 2002), which can reasonably model the mechanical behavior of soil-nail interactions and reinforcing elements, was used to analyze the stress distribution of reinforcements and soil nails. Typical geometry of the hybrid reinforced earth embankment used in the numerical analyses is shown in Figure 2.

The top of the embankment supports a typical mountain roadway, assumed to be 6m wide (W) in this study. The reinforcement length (L_R) remains identical from the top to the bottom of the embankment. Both the vertical and horizontal spacing of soil nails installed at back of the embankment are 1m. Soil nails are placed at an orientation of 20° with respect to the horizontal, which is within the 15°-20° range typically used in practice. The reinforcing material used in the reinforced embankment is geogrid, with a vertical spacing of 0.5m. A one-meter stabilization berm (B) was arranged on the facing of the embankment every 5m high, which is typically used in engineering practice. The finite element mesh for modeling the hybrid reinforced earth embankment ($H=9m$; $\beta=80°$; $L_R=4m$) support a mountain roadway is shown in Figure 3. The mesh, consisting of 9594 elements, was examined to eliminate the influence of the mesh size effect and the boundary on results of the analyses. The boundary at the bottom of the mesh is fixed against displacements in any direction. Both of the vertical boundaries in the mesh are fixed only against displacements in the horizontal direction. The initial stresses for the existing ground were generated using the procedure of gravity loading. The analyses were carried out according to the construction sequence of the embankment in the field. Soil nails were installed following the excavation of the slope, then the reinforced earth embankment was built by placing the fill and reinforcements from the bottom to the top surface. The existing ground was in dry condition.

Modeling of soils, reinforcements, nails and soil-nail interfaces

The Mohr-Coulomb constitutive model was used to model the stress-strain behavior of backfill and existing ground. Table 1 shows the parameters used in the analysis. The parameters for the existing ground are soil properties typically used for a rock formation with slight to moderate weathering conditions.

Reinforcing elements can sustain only tensile forces and were modeled as elastic materials. A typical value of 1000 kN/m was used as the axial stiffness of reinforcements (e.g., geogrid) in the analysis.

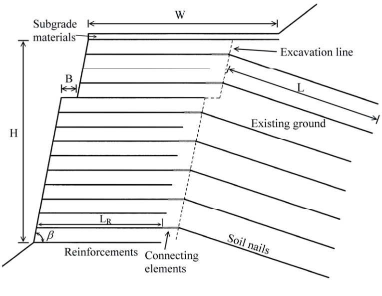

Figure 2. Typical geometry of the hybrid reinforced earth embankment system used in the analyses.

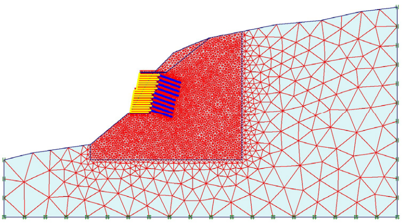

Figure 3. The finite element mesh for the hybrid reinforced earth embankment ($H=9m$;$\beta=80°$;$L_R=4m$).

Soil nails used are #9 rebar (29mm in diameter) surrounded by a 10 cm diameter ring of cement mortar. Nail length used in the analyses is 6m. In 2-D finite element analysis (plane strain condition), nails were modeled using the "equivalent plate model" approach (Unterreiner et al, 1997) and elastic perfectly-plastic behavior. Table 1 illustrates the properties of nails used in the analyses.

Moreover, interfaces were placed on both sides of nails and reinforcing materials. The Mohr-Coulomb model was used to model the behavior of soil-nail interfaces. Material properties for the interface element are identical to those used for its surrounding soil element, except that a strength reduction coefficient (R_{inter}) was used to determine the strength parameters of the interface. The adhesion (c_{inter}) and friction angle ($\tan\phi_{inter}$) of the interface are estimated as the ratio of c_{soil}/R_{inter} and $\tan\phi_{inter}/R_{inter}$, respectively, where c_{soil} and ϕ_{soil} are the cohesion and friction angle of the soil, respectively, adjacent to the interface. A R_{inter} value of 1.0 is considered reasonable for the soil-nail interface (Chu and Yin, 2006). The R_{inter} value for the soil-reinforcement interface used in the analyses is 0.6, based on the experimental results by O'Rourke et al (1990).

MECHANICAL BEHAVIOR OF THE HYBRID REINFORCED EARTH EMBANKMENT

To determine the required reinforcement length for a stable reinforced earth embankment, conventional methods, e.g. the limit equilibrium method, can be used. The computer program ReSSA (Adama Engineering Inc., 2001), based on the limit equilibrium method (Elias et al, 2001), was used to conduct this task. The required reinforcement length for a stable reinforced earth embankment can be analyzed to meet a desired factor of safety. For example, the required reinforcement length to reach a factor of safety of 1.5 in normal conditions is about 6.5m for a 9m-high embankment with a slope gradient of 80° and the backfill properties listed in Table 1. Thus, the 9m-high reinforced earth embankment with a reinforcement length of 4m needs additional resisting forces to meet the safety requirement.

Table 1. Parameters for soil materials and reinforcing materials

Soil parameters		
Backfill	**Existing ground**	**Subgrade materials**
$\gamma_t=19.5kN/m^3$ $\gamma_{dry}=16.5kN/m^3$ $c=5kPa$ $\phi=30°$ $E_s=50MPa$ $\nu=0.3$	$\gamma_t=22kN/m^3$ $\gamma_{dry}=20kN/m^3$ $C=200kPa$ $\phi=35°$ $E_s=2200MPa$ $\nu=0.2$	$\gamma_t=19.5kN/m^3$ $\gamma_{dry}=16.5kN/m^3$ $c=10kPa$ $\phi=30°$ $E_s=70MPa$ $\nu=0.3$
Reinforcing materials		
Soil nails	Reinforcements	Connecting elements (Stainless steel wire ropes)
$EA=138000$ kN $EI=7.29$ kN-m^2 $\nu=0.15$ M_p (Ultimate bending moment) = 1.71kN-m N_p (Ultimate tensile force) = 277 kN	$EA=1000$ kN/m	$EA=23560$kN

Stress distribution

The stress distribution of reinforcements, connecting elements, and nails in a 9m-high embankment system (β=80°; W=6m; LR=4m) following the construction is shown in Figure 4. For reinforcements in approximately the lower half of the embankment, maximum reinforcement stresses are located within the length of the reinforcement. For reinforcements connecting with soil nails in approximately the upper half of the embankment, maximum reinforcement stresses are located at the connection of soil nails and reinforcements. In other words, nails bear most of the driving forces induced during the backfilling in approximately the upper half of the embankment. The maximum nail force at different elevations is mobilized at the head, and the tensile forces fade away along the length of the nail. Most of the nail forces are mobilized above the two-third embankment height following the construction, and they are partly induced by the settlement of the embankment during the backfilling and partly transferred from the reinforcement stress mobilized within the embankment. The role of soil nails in the hybrid reinforced earth embankment proposed is clearly identified in the finite element analyses conducted herein.

Effect of reinforcement length on the nail force

Numerical analyses were carried out to investigate the effect of the reinforcement length (L_R) on the nail forces mobilized during the construction. For a 9m-high embankment with a slope gradient (β) of 80° and a road width (W) of 6m, the distribution of the maximum nail force, occurring at the head, with the depth at various reinforcement lengths following the construction is shown in Figure 5. The data below the depth of about one-half of the embankment height show that nail forces increase with decreasing reinforcement length, whereas the nail forces above the depth of about one-third of the embankment height do not show a clear trend with the reinforcement length. The maximum nail force along the depth occurs at a depth of about 0.5H~0.6H. Reinforced earth embankments with short reinforcements need greater resisting forces provided by nails to stabilize the embankment compared with those with long reinforcements.

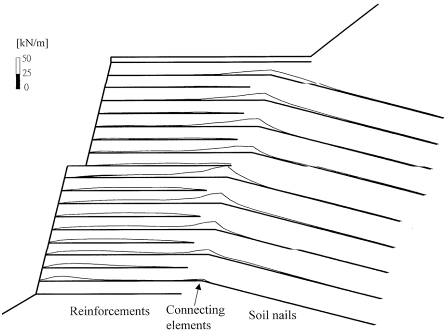

Figure 4. Stress distribution of reinforcing elements in a 9m-high embankment system.

Effect of slope gradient of the embankment on the nail force

Figure 6 shows the effect of the slope gradient (β)of the embankment facing on the variation of the maximum nail force with the depth following the construction of a 9m-high embankment. The reinforcement length (L_R) is 4m. The maximum nail forces for the embankment with a steep facing are noticeably greater than those with a moderate slope gradient at the upper half-height of the embankment. Nevertheless, the mobilized nail force decreases slightly with the β angle for nails located at approximately the lower one-third of the embankment height.

DESIGN FOR THE HYBRID REINFORCED EARTH EMBANKMENT

The maximum reinforcement stresses mobilized at various elevations of a 9m-high hybrid reinforced earth embankment with a slope gradient of 80° following the construction range from about 2.5kN/m to 11.5kN/m. The reinforcement stresses are considerably less than the tensile strength (T_{ult}) of normally used reinforcing materials (geogrids), e.g. $T_{ult} \approx 150 \sim 250$kN/m. Therefore, the stability of the hybrid reinforced earth embankment relies mainly on the understanding of the nail forces that may develop following the construction of the embankment and under static loading conditions.

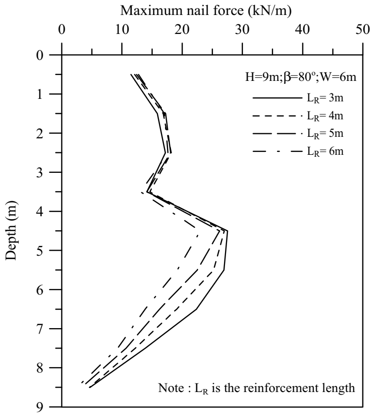

Figure 5. Effect of reinforcement length on the distribution of the maximum nail force with the depth following the construction.

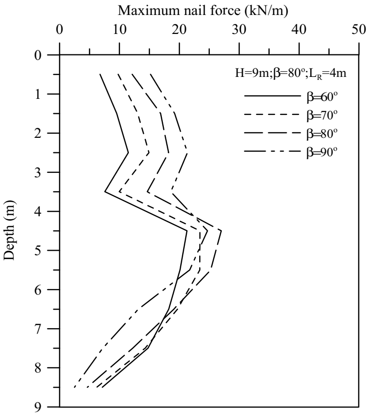

Figure 6. Effect of slope gradient on the distribution of the maximum nail force with the depth following the construction.

Numerical analyses for the hybrid reinforced earth embankments with various slope gradients (β=60°~90°), various embankment heights (H=7~12m), and various reinforcement lengths (L_R=3~9m) were carried out to investigate the distribution of nail forces developed following the construction and under 10kPa static loadings. The nail forces induced by normal traffic loading are less than those induced by a 10kPa static uniform loading (Fan and Hsieh, 2007). Therefore, the nail forces mobilized under a 10kPa static uniform loading are used to develop design charts for the hybrid reinforced earth embankment proposed.

The nail forces mobilized at the back of the reinforced earth embankment with various geometric conditions in narrow fill space were obtained, and design charts for nail forces were summarized in this research. The design charts for soil nails were presented in terms of the normalized depth (z/H) vs. normalized nail force ($T/\gamma HS_HS_v$), where H is the embankment height; T is the maximum nail force (developed at the nail head); γ is the unit weight of fill; S_H and S_v are horizontal and vertical spacing of nails, respectively. To simplify the design procedure, stress envelopes for nail forces in the embankment with various fill geometries were established. Figure 7 shows nail force envelopes of (z/H) vs. ($T/\gamma HS_HS_v$) for hybrid reinforced earth embankments with various reinforcement lengths (L_R) at a slope gradient (β) of 60°, 70°, 80°, and 90° if the friction angle of the backfill is 30°. For a moderate slope gradient (β=60°), the influence of the reinforcement length on the stress envelope is not noticeable. Thus, the design chart for the hybrid reinforced earth embankment with a β angle of 60° is presented using a single stress envelope. For the embankment with steep facing (β=70°, 80°, and 90°), nail force of the envelope increases with decreasing reinforcement length. Additionally, it is recommended to install soil nails from the top surface to about the two-third of the embankment height to ensure the effectiveness of the nails based on the research conducted herein. The design chart established herein can be easily used in the design of soil nails in the hybrid reinforced earth embankment.

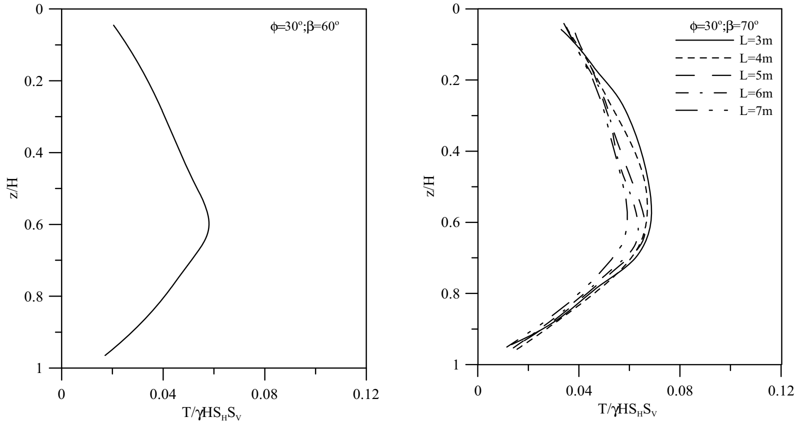

(a) (b)

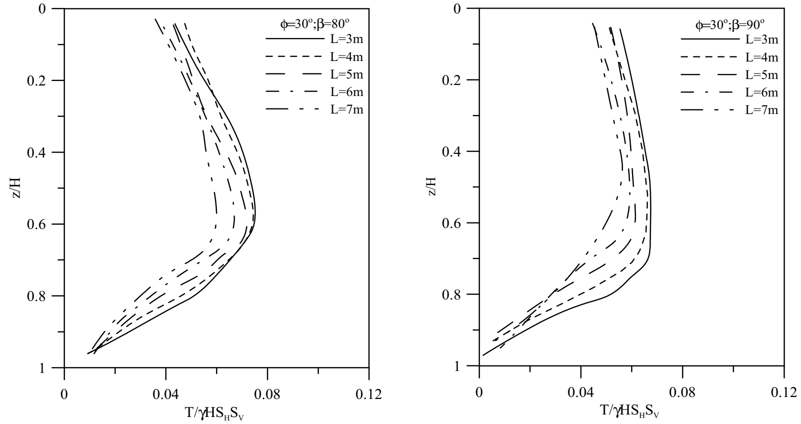

(c) (d)

Figure 7. Design charts of nail forces for the hybrid reinforced earth embankment. (a)β=60°; (b)β=70°; (c)β=80°; (d)β=90°.

CONCLUSIONS

This paper presents the mechanical behavior of a hybrid reinforced earth embankment built in limited fill space. Soil nails are installed on back of the reinforced earth embankment to provide additional resisting forces to stabilize the embankment with limited fill space. Influence of the reinforcement length and slope gradient of the embankment on the distribution of nail forces was analyzed and discussed in this paper.

The stability of the hybrid reinforced earth embankment during the construction and subjected to loading on the roadway relies mainly on the resistance that nails can provide. Simple design charts for estimating the nail forces mobilized within the hybrid reinforced earth embankment with various geometric conditions were established for fill materials with a friction angle of 30° in this research.

ACKNOWLEDGMENTS

This research work was sponsored by the National Science Council in Taiwan under the grant number NSC 94-2622-E-327-007-CC3. This support is gratefully acknowledged.

REFERENCES

ADAMA Engineering Inc. (2001). *The computer software ReSSA(2.0).*

Chou, N. N.S. and Fan, Chia-cheng (2004). *Structure for fastening soil nails to reinforced soil retaining walls*. U.S. Patent No. US6742967B1.

Chu, L.M., and Yin, J.H. (2005). "A Laboratory device to test the pull out behavior of soil nails." *ASTM Geotechnical Testing Journal*, Vol. 28(5), 499-513.

Elias Victor, Barry, R. Christopher, and Berg, Ryan R. (2001). *Mechanically Stabilized Earth Walls and Reinforced Soil Slopes Design and Construction Guidelines*. Federal Highway Administration, Pub.No. FHWA-NHI-00-043.

Fan, Chia-Cheng and Heish, Chih-chung (2007). "A Hybrid Embankment System Used in Repairing Collapsed Roadway in Mountainous Area". *the 16th Southeast Asia Geot. Conf.*, May 8-11, Kuala Lumpur, Malaysia.

O'Rourke, T. D., Druschel, S. J., and Netravali, A. N. (1990). "Shear strength characteristics of sand-polymer interfaces.'' *J. Geot. Eng* , 116(3): 451–469.

PLAXIS BV (2002). *User's manual of PLAXIS*. A.A. Balkema.

Unterreiner, P., Benhamida, B., and Schlosser, F. (1997). "Finite element modelling of the construction of a full-scale experimental soil-nailed wall, French Nat. Research Project CLOUTERRE." *J. of Ground Improvement*, 1(1): 1-8.

Analysis of Overturning Stability for Broken Back Retaining Wall by Considering the Second Failure Surface of Backfill

Heping Yang[1], Wenzhou Liao[2], and Zhiyong Zhong[3]

[1]Professor, School of Communication and Transportation Engineering, Changsha University of Science and Technology; PH (86) 731-2309581; cscuyang@163.com
[2]Graduate research assistant, School of Communication and Transportation Engineering, Changsha University of Science and Technology; PH (86) 731-2309581; liaowenzhou@163.com
[3]Engineer, Roadway administration of Zhuzhou;cscuzzy@163.com

ABSTRACT : In the traditional analysis of overturning stability for broken back retaining wall, pressures acting on the upper and the lower parts of wall are calculated independently based on the hypotheses that earth pressure is linear distribution, and its resultant thrust is the vector sum of the pressures acting on the two parts; The existence of the second failure surface of backfill is judged by the formula of the critical angle for wall with gentle back as derived from Rankine theory. Not only this method is complicated, but also the relevant calculating results are tend to be unsafe Therefore, aiming at these problems, formulas for calculating the pressure on the second failure surface and the safety factor against overturning were derived by the horizontal differential element method considering the occurrence of the second failure surface. Then the traditional methods and the proposed one were compared by case studies. The results show that it is unsafe to design broken back retaining wall by these traditional methods and the critical angle formula for wall with gentle back is not suit for broken back retaining wall.

INTRODUCTION

The current methods to calculate earth pressure on broken back retaining wall are incomplete yet, such as the extending method, the forces polygon method and the correcting method. In these methods, the sliding soil behind wall is divided into two parts and the trial failure surfaces include not only the first surface which passes though the heel of wall, but also another one passing the point of intersection of the broken back surface. The evaluations of earth pressures acting on the two parts of wall and also the locations of the two surfaces are independently, which violates the principle of motion coordination of soil. Therefore, in literature 1, the two failure surfaces were assumed to be parallel and the bound of the sliding soil was obtained from two points of view which were the minimum safety factor against overturning, denoted by k_{smin}, and the maximum earth pressure, respectively. It shows that the two results are almost identical with small obliquity of the upper part of wall back. In practice, the most common failure mode of wall is overturning but not sliding, so it is suggested to design retaining wall by k_{smin}. As for the authenticity and rationality of the hypotheses that the failure surface has a deviation to the right and passes the point of intersection of the broken back surface, there are no proofs by test or theory yet. At present, the non-linear theory based on the horizontal differential element method as the main analysis method is relatively perfect, and the non-linear distribution of earth pressure is confirmed by the laboratory test and engineering detection. In the analysis of broken back retaining wall by the horizontal differential element method, the sliding wedge can be treated as a whole and the resultant thrust can be obtained by once calculation, moreover, the hypotheses used in traditional methods can be avoided. In literature 4, the non-linear distribution of earth pressure on gravity-balanced wall was analyzed by the horizontal differential element method, but the second failure surface was not considered. In literature 1, whether there exists the second failure surface of backfill was judged by the critical angle formula (α_E=45-φ/2) derived from Rankine's theory for wall with gentle back, but the rationality of this formula being used for broken back retaining wall is not confirmed yet. Therefore, aiming at these problems in the analysis of broken back wall and under the condition of the sandy backfill, formulas for calculating the pressure on the second failure surface and the safety factor against overturning are derived by using the horizontal differential element method and considering the second failure surface.

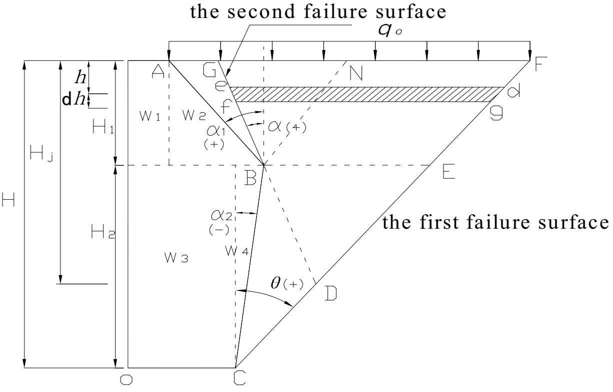

Fig. 1. Schematic diagram of a broken back retaining wall

THEORETICAL ANALYSIS

Basic assumptions

The backfill is single, homogeneous, anisotropic and cohesionless.

The positive direction of the inclination of the wall back is in the counterclockwise direction; the inclination of the trail second failure surface is positive (referring to Fig.1).

The sliding soil mass fails as a whole, and the first and the second failure surfaces are planes which pass through the heel of wall and the point of intersection of the broken line back surface, respectively(referring to Fig.1).

The angle of external friction δ_i between wall and soil and the angles of internal friction φ at the first and the second failure surfaces are uniform distribution, respectively. (Where i=1, 2, which represent the upper and lower wall, respectively)

Occurrence conditions of the second failure surface

The inclination of the upper part of wall is bigger than the critical angle of the second failure surface;

The inclination of earth pressure with respect to the normal of the upper wall back is smaller than or equal to δ_1.

Derivation of the distribution of the earth pressure on the second failure surface

With reference to Fig.1 and based on geometric analysis, we can get the relevant geometric parameters and the calculating height of wall $H_j = \overline{GF} \times H_1 / (\overline{GF} - \overline{BE})$.

Taking the horizontal differential element d-e-f-g to analyze: $\overline{ef} = dh / \cos\alpha$ $\overline{ed} = (H_j - h)\sin(\theta + \alpha)/(\cos\alpha\cos\theta)$, $\overline{fg} = (H_j - h - dh)\sin(\theta + \alpha)/(\cos\alpha\cos\theta)$, and $\overline{gd} = dh / \cos\theta$.

Therefore, the dead weight of the differential element d-e-f-g is expressed as:

$$dw = \gamma S_{defg} = \frac{1}{2}\gamma(\overline{ed} + \overline{fg})\overline{ef}\cos\alpha = \gamma(H_j - h)\frac{\sin(\theta + \alpha)}{\cos\alpha\cos\theta}dh$$

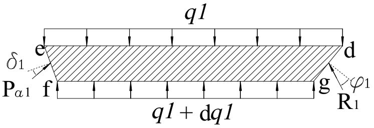

Fig. 2. Schematic diagram of a differential element analysis of forces

Analyzing the differential element d-e-f-g, three static equilibrium equations can be established letting $\sum X=0$, $\sum Y=0$ *and* $\sum M_C=0$(with respect to the midpoint of edge g-d).After simplifying and neglecting higher order term, they become: (referring to Fig.2, n and τ represent the normal component and tangential component, respectively.)

When the ruptured angle of the second failure surface $\alpha = \alpha_1$,then $\delta = \delta_1$;and when $\alpha < \alpha_1$,then $\delta = \varphi$.

$$p_{a1}\cos(\alpha + \delta) - R_1\cos(\theta + \varphi)\cos\alpha / \cos\theta = 0 \qquad (1)$$

$$p_{a1}\sin(\alpha+\delta)dh+R_1\sin(\theta+\varphi)\frac{\cos\alpha}{\cos\theta}dh-q_1\times\frac{\sin(\theta+\alpha)}{\cos\theta}dh$$
$$+dq_1\frac{\sin(\theta+\alpha)}{\cos\theta}(H_j-h)-\gamma\frac{H_j-h}{\cos\alpha}\frac{\sin(\theta+\alpha)\cos\alpha}{\cos\theta}dh=0$$

(2)

$$-p_{a\ln}\sin(\alpha+\delta)dh+q_1\sin\alpha\times dh-dq_1\frac{H_j-h}{\cos\theta}\times\frac{\sin(\theta+\alpha)}{2}$$
$$+\gamma\frac{H_j-h}{\cos\alpha}\frac{\sin(\theta+\alpha)\cos\alpha}{2\cos\theta}dh=0$$

(3)

Dividing Eq.2 by 2 and adding to Eq.3 gives an expression. Substituting Eq.1 to it and simplifying, the expression becomes:

$$p_{a1}=n_1q_1$$

(4)

Where $n_1=\cos(\theta+\varphi)\sin(\theta-\alpha)/[\cos\theta\sin(\theta+\varphi-\alpha-\delta)]$.

Substituting Eq.4 to Eq.3 gives $dq_1/dh-aq_1(H_j-h)=\gamma$ and the expression:

$$q_1=e^{-\int\frac{-a}{H_j-h}dh}\left(\gamma e^{-\int\frac{-a}{H_j-h}dh}+D\right)=\left(H_j-h\right)^{-a}\left[\int\gamma\left(H_j-h\right)^a dh+D\right]$$

Where $a=1-n_1\cos\theta\sin(\theta+\varphi+\alpha+\delta)/[\cos(\theta+\varphi)\sin(\theta+\alpha)]$.

For $a\neq$-1 or 0, there is $q_1=-\gamma(H_j-h)/(1+a)+D/(H_j-h)^a$.

When $h=0$,substituting $q_1=q_{1o}=q_o$ into the above equation gives :

$D=\left[\gamma H_j/(1+a)+q_o\right]H_j^a$,

hence :

$$q_1=\left(\gamma\frac{H_j}{1+a}+q_o\right)\left(\frac{H_j}{H_j-h}\right)^a-\gamma\frac{H_j-h}{1+a}\quad (0\leq h\leq H_l)$$

(5)

For $a=0$, there is $q_1=\int\gamma dh+D$.

When $h=0$, Substituting $q_1=q_{1o}=q_o$ into the above equation gives :

$q_o=D$,hence :

$$q_1=\gamma h+q_o\quad (0\leq h\leq H_l)$$

(6)

For $a=-1$, there is $q_1=\left(H_j-h\right)\left[\int\gamma\left(H_j-h\right)^{-1}dh+D\right]$.

When $h=0$,Substituting $q_1=q_{1o}=q_o$ into the above equation gives :

$$q_1=-\gamma\left(H_j-h\right)\ln(1-\frac{h}{H_j})+q_o(1-\frac{h}{H_j})\quad (0\leq h\leq H_l)\qquad (7)$$

When $a>0$, substituting $h=H_j$ to Eq.5 gives $q_1\to\infty$; when $a<-1, h\to H_j$, q_1 may be negative value. To avoid the negative q_1, in literature 3, Wang Weizhang suggested that when $a>0$ Eq.6 should be adopted and when $a<-1$, Eq.7 should be adopted. In this paper, his suggestion was accepted.

Safety factor against overturning

With reference to Fig.1, the wall is divided into four parts whose weights are w_1, w_2, w_3 and w_4, respectively, and the corresponding moments are M_{w1}, M_{w2}, M_{w3} and M_{w4}. The weight of soil wedge between the upper wall back and the second failure surface is w_5, and the corresponding moment is M_{w_5}. The surcharge acting on the soil wedge A-B-G is Q, and the corresponding moment is M_Q. The horizontal and vertical components of resultant force on the second failure surface are E_{a1x} and E_{a1y}, respectively, and the corresponding moments are $M_{E_{a1x}}$、$M_{E_{a1y}}$, respectively. Note that all the moments mentioned in this paragraph are calculated with respect to rotation point o.

For the lower part of wall, a differential element located in triangle B-C-E is taken to analyze. Let the calculated height of wall $H_j=H_2$, the vertical load q_{2o} may be determined by Eq.5, 6 and 7. And also, the distribution of earth pressure acting on the back of the lower part of wall may be obtained. The moments caused by the horizontal and vertical components of earth pressure acting on the lower wall with respect to point o are $M_{E_{a2x}}$、$M_{E_{a2y}}$, respectively.

For $\alpha_2+\delta_2\le 0$

The resisting moment is $M_r = M_{w1}+M_{w2}+M_{w3}+M_{w4}+M_{E_{a1y}}+M_{w_s}+M_Q$

The overturning moment is $M_t = M_{E_{a1x}}+M_{E_{a2x}}-M_{E_{ayy}}$

The safety factor against overturning is $k_s = M_r / M_t$

For $\alpha_2+\delta_2>0$

$$M_r = M_{w1}+M_{w2}+M_{w3}+M_{w4}+M_{E_{a1y}}+M_{E_{a2y}}+M_{w_s}+M_Q$$

$$M_t = M_{E_{a1x}}+M_{E_{a2x}}$$

$$k_s = M_r / M_t$$

Solution and Process

In general, the ruptured angles of the first and the second failure surfaces and k_{smin} are obtained by the two equations $\partial k_s(\alpha,\theta)/\partial\theta=0$ and $\partial k_s(\alpha,\theta)/\partial\alpha=0$. However, the process of calculation of these non-linear equations is complex. Therefore, with the help of the highly developed computing technology and the trail method, the calculation adopts internal and external nested loop mode in which internal recycle is performed under $\theta \in (20°, 45°)$. The results show that $k_s(\alpha, \theta)$ and θ have the concave curve relationship and there exists a minimum of $k_s(\alpha, \theta)$. A two-dimensional array is used to record the values of $k_s(\alpha, \theta)$ and the corresponding θ. The external recycle is performed under $\alpha \in (\alpha_1, 0°)$. The results show $k_s(\alpha, \theta)$ and α also have the curve relationship and there exists a minimum of $k_s(\alpha, \theta)$. The value of k_{smin}, the ruptured angles θ and α and the active earth pressure can be obtained by using internal and external nested loop calculation. The step of both loops is 1°. The judgment of the sliding of soil wedge A-B-G is made and recorded on an array after each internal loop. In the loop, when $\delta \neq \varphi$ and α_1 is big, the value of n_1 may be negative which will lead the earth pressure to be negative by Eq. 4. In order to help program to find k_{smin}, let the value of k_s to be bigger, as in this paper k_s is set to 100. By using MATLAB, a program of easily calculating k_{smin} and analyzing the associated results has been compiled.

CASE STUDIES

Example 1(from literature 1)

A broken back retaining wall is 8m high (both the upper and the lower part of the wall is 4m high). The backfill surface is horizontal and the surcharge pressure is zero. The top of the wall is 2.5m in width. The inclinations of the upper and the lower of the wall are 18° and -15°, respectively. The backfill is cohesionless, and the density $\gamma=18kN/m^3$, the angle of internal friction $\varphi=35°$. The angles of external friction between the two parts of wall and backfill are 35^o, 10^o, respectively. The unit weight of the wall material being $\lambda_C=24kN/m^3$. Whether there exists the second failure surface of backfill is judged. The relevant results are given in Table 1 and Table 2.

Table1. The calculation results of example 1

$\alpha_1-\alpha$ (°)	k_s	**Is the soil wedge ABG sliding?**	$\alpha_1-\alpha$ (°)	k_s	**Is the soil wedge ABG sliding?**	$\alpha-\alpha_1$ (°)	k_s	**Is the soil wedge ABG sliding?**
0	2.550	—	7	2.763	Y	14	3.003	Y
1	2.579	Y	8	2.795	Y	15	3.040	Y
2	2.609	Y	9	2.829	Y	16	3.044	Y
3	2.639	Y	10	2.863	Y	17	3.021	Y
4	2.669	Y	11	2.897	Y	18	2.999	Y
5	2.700	Y	12	2.931	Y			
6	2.731	Y	13	2.967	Y			

Note: Y represents ABG slide, N represents ABG keep static and the symbol — represents ABG is not existed.

Table.1 shows that when $\alpha-\alpha_1=0$, the safety factor against overturning is the minimum; and when $\alpha-\alpha_1\neq0$, the soil wedge A-B-G is sliding. Therefore, the second failure surface does not occur.

Table2. Comparison with the results calculated by linear methods

methods of calculation	The first ruptured angle θ (°)	The second ruptured angle α_E (°)	Active earth pressure E_a (kN/m)	$k_{S\min}$ (k_s)
the proposed method	33	18	121.20	2.55
literature1	34	—	115.06	3.74
The wall back extending method	36	—	116.32	3.38
The forces polygon method	34	—	114.56	3.19

Note: the symbol — represents the second failure surface is not considered. The results of the extending method and the forces polygon method are determined according to principle of the maximum earth pressure. The results of the proposed method and the method in literature 1 are determined according to the principle of the minimum safety factor of wall stability against overturning.

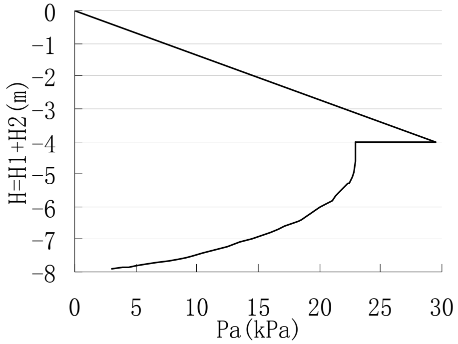

Fig. 3. Distribution of earth pressure along the height of wall

By comparing the results in table.2 with that of other methods, the active earth pressure obtained by the proposed method is the biggest and k_s is the smallest. The reason is that the method used in literature 1, the extending method and the forces polygon method are based on the hypotheses that earth pressure is linear distribution, whereas the earth pressure distribution obtained by the proposed method is nonlinear distribution (as shown in Fig.3). When the resultant forces in different methods are close to each other, the overturning moment obtained by the curve distribution is bigger than that by linear distribution, but the resisting moment is much smaller. So it is relatively unsafe to design broken back retaining wall by using the traditional methods.

Example 2

A broken back retaining wall is 8m high (both the upper and the lower part of the wall is 4m high). The backfill surface is horizontal and the surcharge pressure is zero. The width of the top of the wall is 1m. The inclinations of the upper and the lower of the wall are 40°, -10°, respectively. The backfill is cohesionless, γ=18*kN/m*^{3}, φ=35°. The angles of external friction between the two parts of wall and backfill are 35°, $\varphi/3$ respectively. The unit weight of the wall material being λ_C=24*kN/m*^{3}. The position of the second failure surface and the safety factor against overturning are obtained and the results are given in Table 3.

Table3. The calculation results of example 2

$\alpha_1-\alpha$ (°)	k_s	**Is the soil wedge ABG sliding?**	$\alpha_1-\alpha$ (°)	k_s	**Is the soil wedge ABG sliding?**	$\alpha-\alpha_1$ (°)	k_s	**Is the soil wedge ABG sliding?**
0	4.261	N	7	3.562	N	14	3.632	N
1	4.188	N	8	3.543	N	15	3.651	N
2	4.120	N	9	3.558	N	16	3.671	N
3	4.057	N	10	3.566	N	17	3.691	N
4	3.999	N	11	3.579	N	18	3.712	N
5	3.944	N	12	3.595	N	19	3.734	N
6	3.893	N	13	3.613	N			

Note: this table contain only a partial dates. Y represents soil wedge ABG slide, N represents ABG keep static

Table.3 shows that when α_1-α=8°, the k_s is the minimum （k_{smin}=3.543） and the soil wedge A-B-G is stable, which shows that the second failure surface exists and the ruptured angle is 32°. If α_1 changes to 35°and other conditions keep invariant, the same conclusion can be obtained. Moreover, example 1 and 2 show that the critical angle of rupture really exists and equal to 32°, furthermore, when α is bigger than it, the second failure surface would occur, or else would not. However, according to literature 1, for retaining wall with gentle back, the critical angle is α_E=45-φ/2=45¯35/2=27.5°. Therefore, the difference of the two results indicates that the critical angle formula for wall with gentle back is not suit for broken back retaining wall.

CONCLUSIONS

(1) In the analysis of overturn stability of broken back retaining wall by using the horizontal differential element method, the sliding wedge can be treated as a whole and the resultant thrust can be obtained by once calculation, so it is more reasonable. The safety factor against overturning obtained by the proposed method is smaller, making it safer to design broken back retaining wall.

(2) The results show that, for broken back retaining wall, the relationship between the critical angle of the second failure surface and the friction angle is nonlinear. The critical angle formula obtained by Rankine's theory for wall with gentle back is not suit for broken back retaining wall.

REFERENCES

Yang Xueqiang.(2000). "Research on active soil pressure and stability of retaining wall with broken back surface. " *China Journal of Highway and Transport*, 13(3), 15-19(in Chinese)

Yang Xueqiang, Fan Yin. (2001). "Research on the second failure surface of backfill behind retaining wall with gentle back surface. "*Geotechnical Engineering Technique*, 1,14-17(in Chinese)

Wang Weizhang, Wu Yazhong. (1996) "*New theory of calculation of earth pressure on retaining wall and its application in practice*." Beijing: China Communications Press, (in Chinese)

Zong Quanbing, Dai Zihang, Liao Huomu.(2005). "Analysis of non-linear distribution of earth pressure on the back of balance weight retaining wall ." *Geotechnical Engineering Technique*, 19（2）,55-58(in Chinese)

Wang Yuanzhan, Wang Hailong, Li Liang.(2000) . "Distribution of earth pressure on retaining wall." *China Harbour Engineering*, 14（4）,1-5(in Chinese)

Wang Shichuan, Ling Jianming.(2000). "Nonlinear analysis of active earth pressure on a rigid retaining wall." *Chinese J. of Underground Space and Eng.*, 14(4),1-5 (in Chinese)

Li Junli, Yao Dailu.(2004). "*Design theory and calculation of roadbed* ." Beijing: China Communications Press, (in Chinese)

Gu Weici.(2004). "*Calculation of earth pressure on retaining wall*." Beijing: China Building Materials Industry Press, (in Chinese))

The Upper Bound Calculation of Passive Earth Pressure Based on Shear Strength Theory of Unsaturated Soil

L.H. Zhao[1], Q. Luo[2], L. Li[3], F. Yang[4], and X.L. Yang[5]

[1] Doctoral candidate, School of Civil and Architectural Engineering, Central South University, Changsha, Hunan Province, People's Republic of China, +86(731)564-1684; zlh8076@163.com
[2] Doctoral candidate, School of Civil and Architectural Engineering, Central South University, Changsha, Hunan Province, People's Republic of China, +86(136)0851-6622; luoqiang@vip.sina.com
[3] Professor, School of Civil and Architectural Engineering, Central South University, Changsha, Hunan Province, People's Republic of China, +86(731)887-6678; liliang_csu@163.com
[4] Doctoral candidate, School of Civil and Architectural Engineering, Central South University, Changsha, Hunan Province, People's Republic of China, +86(135)4964-1242; yf5754@126.com
[5] Professor, School of Civil and Architectural Engineering, Central South University, Changsha, Hunan Province, People's Republic of China, +86 (731)265-6248; yangxl@mail.csu.edu.cn

Abstract: Based on the shear strength of unsaturated soil, the passive earth pressure of unsaturated soils is studied by means of the kinematical approach of limit analysis theory, in which not only the saturated shear strength parameters φ′, c′ and (ua-uw), but also the soil-water characteristic curve and the engineering practice are analyzed synthetically. The result of upper bound method for passive earth pressure is obtained via the sequential quadratic programming. The numerical results show that the existing of soil suction and the distribution mode of soil suction exert a significant effect on the passive earth pressure. Meanwhile, if the yield criterion of unsaturated soils turns into the yield criterion of saturated soils, then the solutions presented here ameliorate appreciably with available predictions.

INTRODUCTION

In several situations, soil retaining walls are located above the ground water table where the soil is typically in a state of unsaturated condition. Therefore, estimation of the passive earth pressure of retaining walls using the conventional approaches, which assumed fully saturated conditions ignoring the influence of the soil suction (u_a-u_w), may not lead to economical designs. Several approaches are available for determination of the passive earth pressure based on the saturated shear strength parameters (Sokolovskii 1965, Chen 1975, Soubra and Macuh 2002, Gao, et al. 2003, Fan, et al.2005, Yang and Yin 2006). However, limited researchers have carried out investigations on the passive earth pressure of unsaturated soils (Fredlund 1993), and these works have shown that the contribution of the soil suction to strength is considerable, and using strength parameters reasonable based on the unsaturated soil theory may be worthy for practical. Thus, the goal of this paper is to evaluate the influence of soil suction and its distribution mode on the passive earth pressure.

THE PRINCIPLE AND METHOD

The shear strength theory of unsaturated soil

On the assumption that the failure criterion of unsaturated soils is the extension of the linear M-C failure criterion of saturated soils, a linear shear strength formula for the shear strength τ_f of unsaturated soil has been proposed by Fredlund in 1978 (Fredlund 1993), can be expressed as Equation (1) and the sketch of it is shown in Fig. 1.

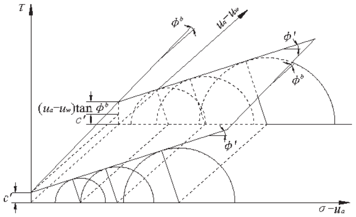

$$\tau_f = c' + (\sigma - u_a)\tan\phi' + (u_a - u_w)\tan\phi^b \qquad (1)$$

Fig.1 Shear strength of unsaturated soil

where c'=effective cohesion intercept, σ=the total normal stress on the failure plane, u_a =the pore-air pressure, u_w =the pore-water pressure, $(\sigma-u_a)$ =the net normal stress, (u_a-u_w)= the soil suction, ϕ'=the effective angle of internal friction and ϕ^b= the angle defining the rate of increase in shear strength with respect to soil suction, which is assumed to be constant for convenience analysis.

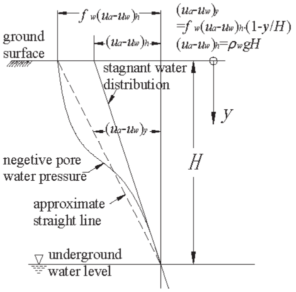

Fig.2 The Hdistribution ofH matric suction

Let be $c = c' + (u_a - u_w)\tan\phi^b$, Equation (1) could be expressed as (Fredlund 1993)

$$\tau_f = c + (\sigma - u_a)\tan\phi' \qquad (2)$$

When soil mass reaches the saturation state, u_w equals to u_a and (u_a-u_w)=0, the shear strength of an unsaturated soil transformed reposefully into saturated soil's.

The typical distribution of soil suction varying with the depth, which is directly related to the water content of soil mass and could be described as the soil-water characteristic curve (*SWCC*). The soil suction along the depth direction is presumed to be a straight line. The approximate straight line of soil suction is shown in Fig.2 (Fredlund 1993).

The negative pore water pressure at ground surface under the condition of the stagnant water could be expressed as $(u_a-u_w)_h = \rho_w gH$, where $(u_a-u_w)_h$ is the soil suction at the ground surface, H is the embedment of ground-water level. Therefore, when the depth y is less than or equal to H , the soil suction of this point in unsaturated soil is

$$(u_a - u_w)_y = f_w \cdot (u_a - u_w)_h \cdot (1 - y/H) \qquad (3)$$

where f_w is a certain percentage of soil suction under the hydrostatic condition.

The total cohesion (c) of this point in unsaturated soil can be expressed as

$$c = c' + f_w \cdot (u_a - u_w)_h \cdot (1 - y/H)\tan\phi^b \tag{4}$$

The research method and basic hypothesis

In the present analysis, some assumptions have been made as follows. (1) The retaining wall is long enough, and the problem can be regarded as plane strain problem; (2) The filling is idealized as a perfectly plastic material. Suppose the failure surface pass through the heel of the retaining wall and does not penetrate the foundation material. (3) The backfill is assumed to follow the shear strength of unsaturated soil and the energy consumption calculation indexes are c and Φ'. (4) The friction angle δ at the soil-wall interface is assumed to be constant. For the relative clean surface, $\delta < \Phi'$ and for the relative rough surface, $\delta \geqslant \Phi'$. (4) The change of soil bulk density (γ) due to the different water content is neglected.

THE TRANSLATIONAL FAILURE MECHANISM

The multiple rigid block translational failure mechanism

Based on the upper bound theorem, the passive earth pressure corresponds to an inward movement of the wall with the velocity V_0 horizontally, which causes the wedges to move up, and the backfill is divided into a number of triangular wedges (Soubra 2002, Yang 2006, Fan 2005). Each of the triangular wedges moves as a rigid wedge. The geometry of wedge i is characterized by the length of the base D_i , the angles α_i and β_i , and the length of interface L_i (i = 1, ……, n), as shown in Fig. 3.

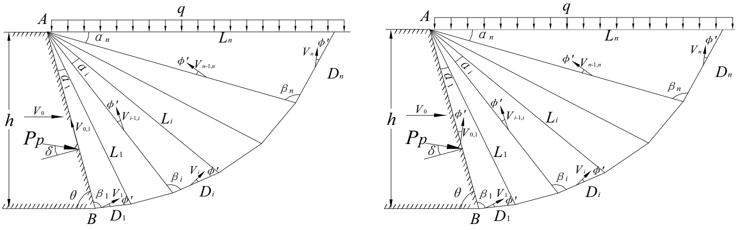

(a) for relative clean surface **(b) for relative rough surface**

Fig.3 Multi-wedge failure mechanism for passive earth pressure

The simple geometry of any wedge can be obtained according to Fig. 3. Take the retaining wall with a relative clean surface ($\delta < \Phi'$) as a example, the relative velocities at the discontinuous surface of any wedge are shown in Fig. 4 and could be calculated as follows.

$$V_1 = V_0 \cdot \frac{\sin(\theta)}{\sin(\beta_1 - \phi')} \qquad (5)$$

$$V_i = V_{i-1} \cdot \frac{\sin(\pi + 2\phi' - \alpha_{i-1} - \beta_{i-1})}{\sin(\beta_i - 2\phi')} \quad (i = 2,...n) \quad (6)$$

$$V_{0,1} = V_0 \cdot \frac{\sin(\pi + \phi' - \theta - \beta_1)}{\sin(\beta_1 - \phi')} \qquad (7)$$

$$V_{i-1,i} = V_{i-1} \cdot \frac{\sin(\alpha_{i-1} + \beta_{i-1} - \beta_i)}{\sin(\beta_i - 2\phi')} \quad (i = 2,...n) \quad (8)$$

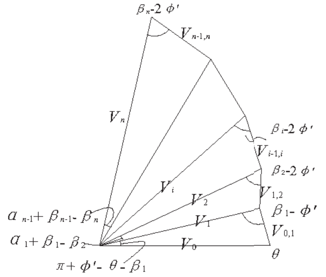

Fig.4 HVelocityH hodograph for the relative clean surface

The energy consumption calculation

Under these assumptions mentioned above, the rate of external work due to soil weight W_{soil}, external loads at the top of filling W_q and passive earth pressure W_P ($W_P = P_p V_0 \cos(\pi/2 - \delta - \theta)$) can be calculated respectively.

Since the backfill is regarded as perfectly rigid and no general plastic deformation is permitted to occur, the contribution to energy dissipation is provided along the failure surface L_i、D_i (i=1,……,n) and the soil-wall interface *AB*.

For the relative clean soil-wall surface, energy dissipation along the soil-wall interface *AB* can be expressed $G_{AB} = P_P \cdot \sin\delta \cdot V_{0,1}$, and for the relative rough soil-wall surface $G_{AB} = c' \cdot h \cdot V_{0,1} \cdot \cos\varphi' / \sin\theta$.

The total cohesion c_{Li} and c_{Di} $(i = 1,...n)$ along the velocity discontinuity line L_i and D_i $(i = 1,...n)$ can be calculated respectively by the Equations (9) and (10) for the reasons that all of the velocity discontinuities are straight lines and the total cohesion of any point above the underground water level processes a linear increasing trend with increasing depth.

$$c_{Li} = c' + f_w \cdot (u_a - u_w) \cdot (1 - y_{Li}/H) \cdot \tan\phi^b \quad (i = 1,...n-1) \qquad (9)$$

where $y_{Li} = 1/2 \cdot L_i \cdot \sin(\theta - \sum \alpha_i) \quad (i = 1,...n-1)$

$$c_{Di} = c' + f_w \cdot (u_a - u_w) \cdot (1 - y_{Di}/H) \cdot \tan\phi^b \quad (i = 1,...n) \qquad (10)$$

where $y_{D1} = L_1 \cdot \sin(\theta - \alpha_1) + 1/2 \cdot D_1 \cdot \sin(\pi - \beta_i - \theta)$

$$y_{Di} = L_i \cdot \sin(\theta - \sum \alpha_i) + \frac{1}{2} \cdot D_i \cdot \sin\left[\pi - \beta_i - (\theta - \sum \alpha_{i-1})\right] \ (i = 2,...n)$$

Therefore, the total arithmetic expression of the contribution to energy dissipation along the failure surface L_i 、 D_i (i = 1…n) can be calculated as $\sum G_i = \sum c_{Li} \cdot L_i \cdot V_{i-1,i} \cdot \cos\phi' \ (i = 1,...n)$ and $\sum Q_i = \sum c_{Di} \cdot D_i \cdot V_i \cdot \cos\phi' \ (i = 1,...n)$ respectively.

Calculation the passive earth pressure

Finally, equating the rate of energy dissipation to the rate of work of external force leads to the expressions for the upper bound to the passive earth pressure of unsaturated soil. For the relative clean soil-wall surface, the passive earth pressure of unsaturated soil P_p can be expressed

$$P_p = \left(\sum G_i + \sum Q_i - W_{soil} - W_q\right) \Big/ \left[V_0 \cdot \cos(\pi/2 - \delta - \theta) - \sin\delta \cdot V_{0,1}\right] \ (i = 1,...n) \qquad (11)$$

For the relative rough soil-wall surface, the passive earth pressure of unsaturated soil P_p can be expressed

$$P_p = \left(\sum G_i + \sum Q_i + G_{AB} - W_{soil} - W_q\right) \Big/ V_0 \cdot \cos(\pi/2 - \delta - \theta) \ (i = 1,...n) \qquad (12)$$

In Equations (11) and (12), h 、 H 、 θ 、 γ 、 q 、 Φ' 、 c' 、 Φ^b are regarded as invariables, α_{i} , β_{i} (i=1…..n) are regarded as independent variables and c_{Li}, c_{Di} (i=1…..n) are regarded as dependent variables. As shown in FIGs.3 and 4, the independent variables of α_{i} , β_{i} (i=1…..n) should assure the geometry conditions of failure mechanism (the constraint conditions of geometric) and velocity hodograph (the constraint conditions of velocity vector). It is well-known that the litter the upper-bound solutions the more close to the truth value in the process of the limit analysis. Therefore, the solving of the upper-bound of the passive earth pressure is converted to a constrained extreme value of the multivariate nonlinear function, and an optimization procedure with sequential quadratic programming algorithm (*SQP*) had been compiled to get the minimum P_p in the present paper.

CALCULATIONS AND DISCUSSIONS

Comparisons to other solutions

Comparison has been adopted to show the validity of the presented method with other solutions (Sokolovskii 1965, Chen 1975, Gao, et al. 2003), as shown in Table 1.

Table 1 Comparison of P_P in sand (horizontal angle of filling β=0°)

<table>
<tr><td colspan="7">θ=70°, γ=18 kN/m^3, h=2m</td></tr>
<tr><td>φ' (°)</td><td>δ (°)</td><td>Coulomb (<i>kN</i>)</td><td>Sokolovskii (<i>kN</i>)</td><td>Gao (<i>kN</i>)</td><td>Chen (<i>kN</i>)</td><td>This paper (<i>kN</i>)</td></tr>
<tr><td rowspan="2">20</td><td>0</td><td>70.0</td><td>68.4</td><td>71.6</td><td>70.0</td><td>69.9</td></tr>
<tr><td>10</td><td>83.2</td><td>83.2</td><td>83.2</td><td>83.2</td><td>83.0</td></tr>
<tr><td rowspan="2">30</td><td>0</td><td>86.4</td><td>86.4</td><td>90.8</td><td>91.2</td><td>91.0</td></tr>
<tr><td>15</td><td>126.4</td><td>126.4</td><td>126.4</td><td>126.4</td><td>126.4</td></tr>
<tr><td colspan="7">θ=90°, γ=18 kN/m^3, h=2m</td></tr>
<tr><td>φ' (°)</td><td>δ (°)</td><td>Coulomb (<i>kN</i>)</td><td>Sokolovskii (<i>kN</i>)</td><td>Gao (<i>kN</i>)</td><td>Chen (<i>kN</i>)</td><td>This paper (<i>kN</i>)</td></tr>
<tr><td rowspan="2">20</td><td>0</td><td>81.6</td><td>81.6</td><td>81.6</td><td>81.6</td><td>81.6</td></tr>
<tr><td>10</td><td>105.6</td><td>102.0</td><td>103.2</td><td>103.2</td><td>103.2</td></tr>
<tr><td rowspan="2">30</td><td>0</td><td>120.0</td><td>120.0</td><td>120.0</td><td>120.0</td><td>120.0</td></tr>
<tr><td>15</td><td>199.2</td><td>184.8</td><td>187.6</td><td>188.4</td><td>187.6</td></tr>
</table>

As can be seen from Table 1, the values of P_P calculated by means of the present study are in agreement well with the existing research results, and the comparison shows that the proposed method is an effective method for evaluating the passive earth pressure under the saturated soil theory.

Parameters analysis with shear strength theory for unsaturated soil

Fig. 5 shows the change of the passive earth pressure corresponding c'=10kPa, ϕ'= 30°, φ^b=15°, θ=70°、90°, γ=20kN/m^3, q=10 kPa, h=2m, H=4m and the ground surface soil suction of filling behind the retaining wall (u_a-u_w) in the range from 0.0 kPa to 40.0 kPa, with the underground water level unchanged.

From Fig. 5, it can be seen that the existing of soil suction take a significant effect on P_P in unsaturated soils. The rate of P_P shows a linear increasing trend with increasing the ground surface soil suction of filling, resulting in an enhanced coefficient against passive failure of the retaining wall.

Fig. 6 shows the change of the passive earth pressure corresponding c'=10kPa, ϕ'= 30°, ϕ^b=15°, θ=70°、90°, γ=20kN/m^3, q=10 kPa, h=2m and the ground surface soil suction of filling behind the retaining wall (u_a-u_w) = 40.0 kPa, with the underground water level H varying from 0 m to 10 m.

It can be seen from Fig. 6 that the higher the underground water level the lower stability of retaining wall, and the rate of P_P indicates that the underground water level possess nonlinear infection on P_P. Furthermore, changes in underground water level will obviously influence P_P, particularly for high underground water level under the condition of rainfall infiltration.

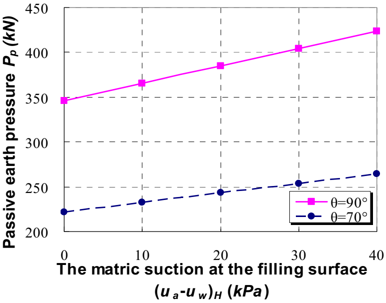

Fig.5 P_P **vs.** $(u_a - u_w)_H$

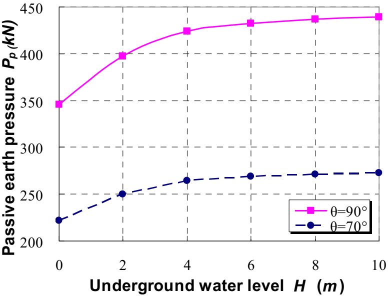

Fig.6 P_P **vs.** H

CONCLUSIONS

Based on the existing researches, the passive earth pressure of the unsaturated soils has been studied. The main conclusions as follows: (1) The unsaturated condition of filling behind the retaining wall takes a significant effect on the passive earth pressure. The development of soil suctions in soils contributes to their shear strength, resulting in an enhanced passive earth pressure. (2) Changes in underground water level under the condition of rainfall infiltration obviously have a great effect on the passive earth pressure.

ACKNOWLEDGMENTS

Thanks should go to Miss Zhang Ting for her assistance. The present work was sponsored by the Nation West Traffic Construction Science and Technology Item of China (No. 2006318802111). The financial support is greatly appreciated.

REFERENCES

Chen W. F. (1975). “Limit analysis and soil plasticity.” Amsterdam: Elsevir Science.

Fredlund D.G. and Rahardjo H. (1993). “Soil Mechanics for Unsaturated Soils. ”,1st Ed. Wiley, NewYork.

Fan W., Sheng Z.J. and Yu M.H. (2005). “Upper-bound limit analysis of earth pressure based on unified strength theory.” *Chinese Journal of Geotechnical Engineering,* Vol. 27(10):1147-1153. (in chinese)

Gao H.B., Zhu B.Z. and Zhu D.Y. (2003). “Upper-bound limit analysis of passive earth pressure coefficients.” *Subgrade engineering*, (3):14-17. (in chinese)

Sokolovskii V.V. (1965). “Statics of Soil Media.” Translator Jones R.and Schofield A. London:Butterworths Science.

Soubra A.H. and Macuh B. (2002). “Active and passive earth pressure coefficients by a kinematical approach.” *Proceeding of the Institution of Civil Engineers, Geotechnical Engineering*, Vol. 55 (2):119-131.

Yang X.L. and Yin J.H. (2006). “Estimation of seismic passive earth pressure with non- linear failure criterion.” *Engineering Structures*, Vol. 28(3): 342-348.

Bearing Capacity Analysis of Beam Foundation on Weak Soil Layer: Non-linear Finite Element versus Loading Tests

Ze-Hong Yu[1], Hong-Wei Wei[2], and Jian-Hua Zhang[3]

[1]Professor, Changsha Science &Technology University, Changsha, China,410076.E-mail:yzh.edu @ 163.com.
[2]Professor,School of civil and architecture engineering, Central south university, Changsha, China, 410075. E-mail: whw.edu@163.com.
[3]Engineer, Ning-Dao Expressway Development Limited Company, Changsha, China,410075.

ABSTRACT: Considering the interfacial contact between beam and foundation, as well as the weak layer and adjacent soil, the nonlinear finite element model of beam-foundation-underlying weak layer system was proposed and the foundation bearing capacity on weak soil layer was analyzed in the paper. Compared with standardized methods and static load test results, the proposed method was feasible and more reasonable to evaluate the bearing capacity of beam foundation on weak soil layer. According to the calculation results the corresponding ground treatment was proposed, and saved more than 2,000 million Yuan in Tai-Zhong-Yin railway project in China.

INTRODUCTION

The planning beam prefabricated plant of Tai-Zhong-Yin Railway Engineering was situated in Qingxu of Shang Xi province in China. The foundation soil layers in 30m depth range from top to bottom are: the late Quaternary Holocene alluvium layer, demarcated at the bottom of the second silty clay layer; the early or middle Quaternary Holocene alluvium layer, demarcated at the bottom of the fourth silty clay layer; the rest are the Quaternary Pleistocene alluvium layers.

The proposed buildings rested heavily on the first silt and silty clay layer, and silt and silty sand layer acted as the first underlying layer. In the horizontal direction, the rock characteristics of supporting and underlying layers varied greatly, according to soil distribution characteristics and the variability analysis of physical and mechanical index, the building foundation was heterogeneous ground, which hard shell was 1.5~3.0m thick, and the underlying weak laminated arch clay appeared mud and plastic flow, with thickness of 2.5~6.0m. On this field condition, a large-scale gantry crane system of lifting weight of 180t and self-weight of 130t was planned to be erected, with two arranged parallel within 10m distance.

As poor drainage conditions and by the local law and regulation constraints the that engineering field must be rehabilitated to cultivate after the completion of engineering, the soft-processing program by gravel piles put forward by the original design was infeasible, and the bearing capacity and stability of the natural foundation needed a reliable safety evaluation.

The foundation bearing capacity was predicted currently by the depth of the plastic zone under foundation, theoretical equations or specified methods, but the calculation results generally tended to be too conservative relatively, related studies can see in Griffiths(2002), Kumar and Kouzer (2004, 2007). The static load tests were also adopted to determine directly the capacity. The results were reliable but representative inadequately. Consequently, that establishing the finite element model of capacity analysis to calculate the whole foundation and combining the calculation results with test results, might be more feasible to put forwards the reliable capacity evaluation for engineering.

Finite element methods were adopted widely in slope stability analyses, and to calculate stresses, strains in soil structures under working conditions (Hird et al. 1990, Yu & Han 1996), but in fewer literatures were applied in predictions of foundation bearing capacity. In current methods to estimate the bearing capacity of foundation, two idealized situations were usually involved: perfectly smooth or perfectly rough footings, which means no horizontal shear stresses allowed at the beam base or no relative horizontal sliding between beam and soil. In reality, beams were usually constructed by pouring concrete directly on underlying soil, the beam-soil interface was rough enough to resist the slip tendency, in finite element analyses beam was assumed to be extensible, satisfying no slip and compatibility condition at the interface between the beam and the neighboring soil. The influences of the section and stiffness of beam foundation had been also considered in analysis, and the calculation results were compared with tests and those available in literatures.

FOUNDATION SOIL AND NATURAL BEARING CAPACITY

According to the Geological Survey, the foundation soil layers formation were as followed:

Layer.1: silty clay, the thickness of 0.8~2.10m, the average thickness of 1.62m; SPT(standard penetration test) blow count in the range of 2.0~ 4.0, with an average of 3.0. Compression coefficient a1-2 in the range of 0.23 ~ 0.63MPa-1, with an average of 0.40MPa-1;

Layer.2: silt, silty sand, the thickness of 1.9~6.60m, the average thickness of 4.15m; SPT blow count in the range of 1.0~4.5, with an average of 2.2. Compression coefficient a1-2 in the range of 0.12 ~ 0.40MPa-1, with an average of 0.20MPa-1;

Layer.3:

(1) silt, the thickness of 1.1~8.70m, the average thickness of 5.71m; Compression coefficient a1-2 in the range of 0.10~0.31MPa-1, with an average of 0.16MPa-1; SPT blow count in the range of 4.0~12.0, with an averaging of 6.4.

(2) silty sand, the thickness of 1.1~11.1m, an average thickness of 4.88m; SPT blow count in the range of 6.0~ 16.0, with an average of 12.5.

Layer.4: silty clay, the thickness of 3.6~8.0m, the average thickness of 5.76m; Compression coefficient a1-2 in the range of 0.14 ~ 0.65MPa-1, with an average of

0.43MPa-1, SPT blow count in the range of 6.0~16.0, with an average of 9.9. Under natural foundation conditions, by the basement pressure of gantry crane of 150kPa, the foundation bearing capacity varied with various embedded depth (reversed by depth) were summarized in Table.1.

When the foundation embedded depth arrived 3.0m, the bearing layer was the second silt and silty clay layer, the natural soil strength satisfied the loading requirements of the upper structure, and the raft foundation was applicable, as a result of heterogeneous distribution in horizontal and vertical directions, the ground treatment should be still carried out.

Table 1. The Natural Foundation Bearing Capacity with Embedded Depth

Embedded Depth/m	Supporting Layer	the First Underlying Layer	Characteristic Value of Bearing Capacity（kPa）	Conclusion
1.50	①Silty Clay	②Silt,SiltyClay	89	Ansatisfied
2.00	②Silt,Silty Clay	③Silt,Silty Sand	125	Ansatisfied
2.50	②Silt,Silty Clay	③Silt,Silty Sand	140	Unsatisfied
3.00	②Silt, Silty Clay	③Silt,Silty Sand	156	Satisfied

PLATE BEARING CAPACITY TEST AND ANALYSIS

The bearing capacity tests were divided into three groups of A, B and C, 3 points were measured in each group. The distance between points was about 2-3m. A, B was situated in the vicinity of the 6th and 9th holes drilled previously, which limited in the scope of the gantry crane foundation (the width of 5m considered). While C was arranged between the 10th and 11th holes, which limited under beam deposit (distance between center lines of 3.5m). Three groups spanned the space of 400m.

Table 2. Plate Bearing Tests Results

No.	Type	Max. Load /kPa	Bearing Capacity/kPa	Measured Characteristic Values/kPa	Max. Settlement/mm	Notes
1#	Cushion Coat	405	375	187.5	60.41	Area A
2#	Cushion Coat	468	438	219.0	60.58	Area A
3#	Cushion Coat	330	313	156.5	60.76	Area A
4#	Cushion Coat	468	438	219.0	61.73	Area B
5#	Cushion Coat	440	438	219.0	61.61	Area B
6#	Cushion Coat	500	438	219.0	62.17	Area B
7#	Original Foundation	260	250	125.0	60.83	Area C
8#	Original Foundation	270	260	130.0	60.00	Area C
9#	Original Foundation	260	250	125.0	60.67	Area C

Two working situations were simulated in bearing tests, The first was in accordance with the situation that excavating 1m in the original ground, then filling 70-80cm, and compacting to about thickness of 50cm (the data calculated by 1.0m high-beam). For group A, the original ground elevation was +758.856 m, after excavation and backfill compaction, the south elevation was +757.932m, and the north was +757.995m; For group B, the original ground elevation was +758.840m, after excavation and backfill compaction, the south and north elevation was +758.343m and +758.327m respectively. The second situation was that tests were run on after roller compaction, the south elevations of original and rolling were 758.983m and 758.979m, and the north were 758.905m and 758.775m respectively. The request of the bearing capacity characteristics value must be more than 250kPa after the upper treatment.

The bearing capacity tests of filling cushion layers had 3 groups in area A, and the other three in area B. the bearing capacity characteristics value of A was 156.5kPa, and B of 219kPa, both could not meet design requirements (design characteristics values were no less than 250kPa).

Test-bearing capacity characteristics value:

Area. A: 1# 187.5kPa, 2# 219kPa, 3# 156.5kPa, the area bearing capacity characteristics value was 156.5kPa.

Area. B: 4# 219kPa, 5# 219kPa, 6# 219kPa, the bearing capacity characteristics value was 219kPa.

Area.C: 7# 125kPa, 8# 130kPa, 9# 125kPa, the bearing capacity characteristics value was 125kPa, and could not satisfy design requirements.

FINITE ELEMENT ANALYSIS OF BEARING CAPACITY

Finite element method

The bearing capacity analyses were carried out by the finite element method using a viscoplastic algorithm and the elastic-perfectly plastic Tresca yield criterion. The six-node linear strain triangle was used to modeling foundation soil, this element was capable of correctly modeling collapse behavior under undrained conditions for plane stain problem. And beam element was incorporated to model beam foundation.

A six-node quadrilateral element developed by Goodman et al was adopted in order to model the interface between beam and foundation soil. The element had been used to simulate the interface between soil and geosynthetics in analysis of a reinforced embankment approach bridge abutment(Yu et al. 1996). The maximum shear resist of this element was equal to soil shear strength.

Table 3. Calculation Parameters of Soil

	Cohesion c/kPa	**Friction Angle φ^0**	**Unit Weight /kN/m^3**
Crushed Stone Cushion	0	40	17
Silty Clay	16.5	5.1	16.9
Silty Soil and Sand(Weak Layer)	17.2	1.8	12.3
Silty Soil	20	10	18
Silty Sand	24	15	19.5

The boundary conditions were given as vertical rollers on the left and right boundary, full fixity at the base, and free boundary at the rest. In undrained conditions, a large volume of shear modulus should be used as possible in analysis, but the parameters were too large, the numerical problem might occurred. The bulk modulus =5.6×10^5kPa was found to be satisfactory.

The beam stiffness was used 2.05×10^7kPa/m, and adjacent soil strength was chosen by test information as summarized in Table.3. To limit the relative displacements prior to slip and normal to interface, the stiffness parameters were set to high values, k_s=6.5 ×10^3kPa/m, and k_n=10^6kPa/m.

In order to decrease boundary effects on calculation results, the calculation width and depth of foundation was adopted 5 times and 10 times of that of beam.

Finite element calculation results

When the thickness of crushed stone cushion layer was only 0.5m, the beam foundation of 1.8m-wide beard the load of 28 tons, the calculation vertical stress was 236kPa, the vertical displacement was 6.5cm in foundation, and the plastic shear zone went completely through the foundation, as illuminated in Fig.1.

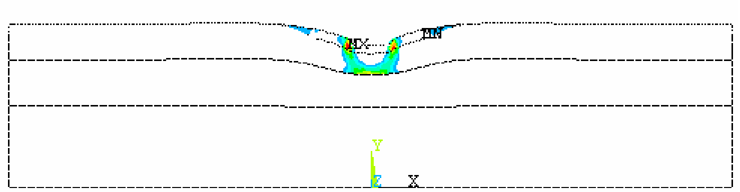

Fig.1. The foundation plastic failure zone under 1.8m-width beam (crushed stone cushion thickness of 0.5m)

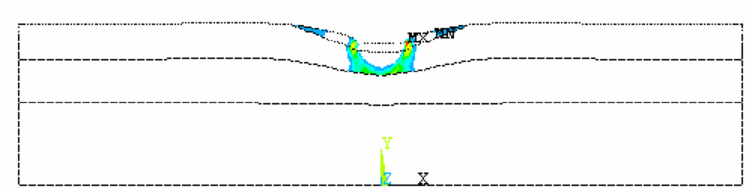

Fig.2. The foundation plastic failure zone under 2.8m-width beam (crushed stone cushion thickness of 0.5m)

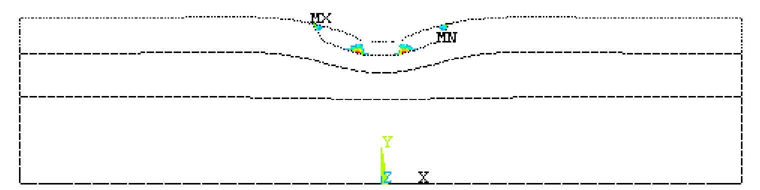

Fig.3. The foundation plastic deformation under 2.4m-width beam (crushed stone cushion thickness of 0.8m)

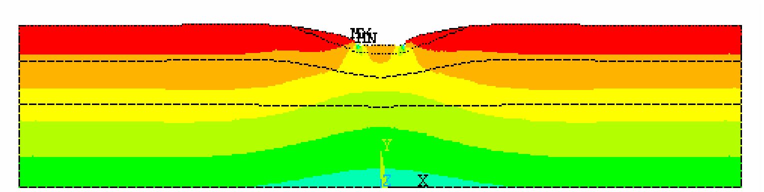

Fig.4. Vertical stress state cloud in foundation under 2.4m-width beam (crushed stone cushion thickness of 0.8m)

Under 2.8m-wide beam foundation and endured load of 28 tons conditions, the plastic failure zone also went completely through the foundation, as showed in Fig.2, the vertical stress was 146kPa, and the vertical displacement was 7.9cm.

When the cushion thickness and beam width increased up to 0.8m and 2.4m, under loading of 28 tons, only some of the plastic deformation emerged, as illuminated in Fig.3, the vertical stress was 132kPa and the displacement was 4.7cm, the bearing capacity was improved. The vertical stress state cloud under the track beam cross-section showed in Fig.4.

Comparisons between the calculated and measured results

The finite element calculation results of foundation bearing capacity and the measured in bearing capacity tests had been summarized in Table.4

Table 4. Calculated and Measured Values of Bearing Capacity

Beam Width	1.8	2.4	2.8
Calculation σ (Cushion Thickness of 0.5m)	236	204	146
Calculation σ (Cushion Thickness of 0.8m)	151	132	129
Measured σin Area A （Cushion Thickness 0.5m）	156		
Measured σin Area B （Cushion Thickness 0.5m）	219		
Measured σin Area C (Original Foundation)	125		

As to the broken stone cushion thickness of 0.5m and track beam width of 1.8m, 2.4m, 2.8m, the calculated stresses at the bottom were 236kPa, 204kPa, 146kPa respectively, less than or close to the measured σ= 219 kPa in area B, but greater or close to the measured value 156 kPa in area A.

Area A was situated in the vicinity of the 6th hole, the original Geological cross-section had been illuminated in Fig.5, we can see, the Layer.1 was silty clay, the thickness of 1.5m, SPT blow count in the range of 2.0~ 4.0, with an average of 3.0. Compression coefficient a1-2 in the range of 0.23 ~ 0.63MPa-1, with an average of 0.40MPa-1. Layer.2 was silt, silty sand, the thickness of 5.0m, SPT blow count in the range of 1.0~4.5, with an average of 2.2. Compression coefficient a1-2 in the range of 0.12 ~ 0.40MPa-1, with an average of 0.20MPa-1. the soil is a typical weak laminated arch clay.

Area B in the vicinity of the previously drilled 9th hole, the original Geological cross-section showed in Fig.6, Layer.1 was silty clay layer, the thickness of 1.3m, Layer.2 was silt and silty clay, the thickness of 4.3m. the observed laminated soft soil appeared completely plastic flow in field. Due to the weak soil thickness were high up to 1.9~6.60m, the average of 4.15m, the measured bearing capacity from area A and B were influenced greatly by the second layer.

In view of heterogeneity of the soil mechanics distribution in the vertical direction, the final design scheme adopted 2.4m width track beam and 0.8m thick crushed stone cushion. The calculated stress by finite element at the bottom of track beam was 132kPa and displacement of 4.7cm, less than the measured stress of 156 kPa in Area A. The Project had been put into operation since March, 2007, and the measured settlements were within 0.8cm~2.1cm, less than calculated vertical displacement of 4.7cm.

Track beam foundation does not approached the ultimate bearing state, and the track beam cross-section design and ground treatment programs were reasonable.

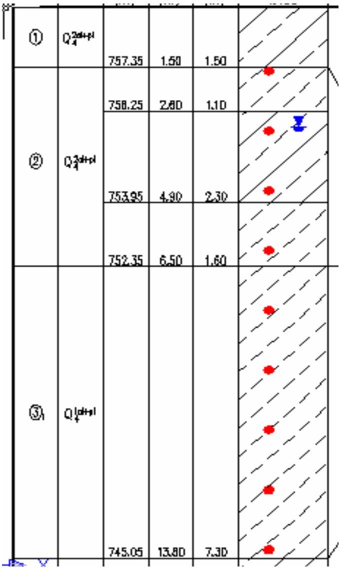

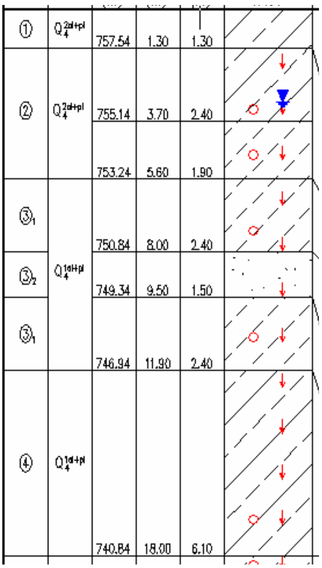

Fig.5. Soil column on the 6th hole **Fig.6. Soil column on the 9th hole**

CONCLUSIONS

The finite element program had been used successfully to predict the beam foundation bearing capacity and settlement. The calculation results agreed well with the measured in the field, the reliability and feasibility has been confirmed. Considering the interactions between track beam and foundation, as well as between the adjacent layers, finite element could effectively simulate the force transfer between layers in foundation, and more reasonable than the traditional methods. Results also showed the foundation bearing capacity was influenced by beam width and cushion thickness, while the thickness of weak laminated arch layer also played a key role.

ACKNOWLEDGMENTS

The research presented in this paper was supported by the National Science Foundation of China, Grant No.50778181. Additional founding were also provided by the Water Conservancy Department of Hunan, Grant No.2007Z08, the Science & Technology Department of Hunan, Grant No.2007FJ4188, and the Construction Department of Hunan, Grant No.06hnjs007. All these supports are greatly appreciated.

REFERENCES

Arindam Dey, Prabir K. Basudhar,A.M (2008). “Flexural response of beams on reinforced foundation beds”, *Proc. of 17th analysis and computation specialty conference*.

C.C. Hird, I.C.Pyrah and D.Russell (1990). “Finite element analysis of the collapse of reinforced embankments on soft ground”, *Geotechnique*, 40(3):633-640.

D.V.Griffiths, Gordon A.F(2002). “Bearing capacity of rough rigid strip footing on cohesive soil: probabilistic study”, *J. of Geot. & Geoenv. Eng.,* ASCE, 128(9):743-755.

Jyant Kumar and K.M.Kouzer(2007). “Effect of footing roughness on bearing capacity factor N_γ”, *J. of Geot. & Geoenv. Eng.,* ASCE, 133(5):502-511.

Jyant Kumar(2004). “Effect of footing-soil interface friction on bearing capacity factor N_γ”, *J. of Geot. & Geoenv. Eng.*, ASCE, 54(10):677-680.

Soubra,A.H(1999). “Upper-bound solutions for bearing capacity of foundation”, *J. of Geot. & Geoenv. Eng.*, ASCE, 125(1):59-68.

Yu Ze-hong, Han Li-an(1996). “Finite element analysis of alleviating bridge approach settlement with geonet”, *Chinese Journal of geotechnical engineering*, 16(6): 24-30.

Stability Analysis of Cutting Slope Reinforced with Anti-slide Piles by FEM

Ren-Ping Li[1]

[1]Associate professor, College of Civil & Hydroelectric Engineering , China Three Gorges University, Yichang 443002, Hubei province of China; l.r.p@163.com

ABSTRACT: Stability of cutting slopes reinforced by anti-slide piles is analyzed with finite element method (FEM) under the hypothesis of plane strain in this paper. The soil is idealized to be elastoplastic, obeying Mohr-Coulomb yield criterion. Equivalent sheet-pile is adopted in which the plastic bending failure will occur as soon as it reaches the ultimate allowable moment (UAM). The safety factor of the pile-reinforced slope is calculated through strength reduction method. The effects of types of piles, flexural rigidity (FR), UAM and location of piles-row on safety factor are discussed in this paper.

INTRODUCTION

Setting piles in slopes is one of the commonly-used methods to improve slope stability, which makes reasonable calculation of safety factor (SF) between reinforcing pile and slope interaction system a key problem in reinforcing design process. The transfer coefficient method (Pan Jiazhen, 1980) is widely used to analyze stability of slopes and the design is based on the residual thrusting force. Furthermore, many researchers, such as Tomio Ito (1979), R. Cantoni (1989), Shen Zhujiang (1992), Poulos (1995) and S. Hassiotis (1997) etc., have proposed several methods for the design of slopes reinforced by a single row of piles. All the above methods are common in the ultimate counterforce or bending moment which piles can supply is calculated under the assumption that piles are rigid and then the factor of safety of the whole system is achieved according to its conventional definition, simultaneously considering the stabilizing state of piles. Different aspect of these methods is only the approaches of calculating lateral forces acting on the piles. Because of different hypothesis, ultimate lateral force (Pu) through every approach varies much. Further study shows in fact that the lateral force also depends on other factors, such as horizontal bearing capacity, deformation of piles and relative displacement between the piles and soils. Present methods can't take effects of all the factors into account, which leads to inaccurate SF of the slope and pile system.

FEM has become a powerful alternative to solving complicated geotechnical engineering problem. D.V. Griffiths (1999), E. M. Dawson (1999) and Steve Laudeman(2004) etc. have used FEM to analyze stability of slopes and determine the critical slip surface. To calculate the stability of slopes with FEM has fewer assumptions than conventional methods, which makes the minimum safety coefficient more accurate than that from slice method.

With FEM to analyze the reinforcing pile-soil interaction system, piles are usually treated as elastic, which leads to the fact only deformation and inner force can be analyzed while the system stability and damage can't. In this paper, a new method is proposed to analyze the stability of pile-soil interaction system. With the assumption that both soils and piles are elastoplastic and the idealization of pile bent to be equivalent sheet piles, the plastic bending failure will occur as soon as sheet piles bears the UAM and then SF of the reinforced slopes can be attained. Results indicate that the proposed method has its feasibility. The effects of types of reinforcing piles, flexural rigidity, UAM and location of piles-row on safety factor are mainly discussed. Examples show that the analytical procedure and conclusion have important value to the design of reinforcing pile, and this procedure can also be extended to the stability analysis of foundation pit bracing, pile foundation of pier etc.

ANALYTICAL METHODS OF SLOPE STABILITY ANALYSIS

Traditional Methods

The method of slice is an earliest and commonly in the stability analysis of slopes, which is suitable for homogeneous or heterogeneous clay soils. It is based on the assumption that soils are elastoplastic. Stability of slopes can be analyzed according to the limit equilibrium principle irrespective of stress and strain equations of soils. Differences among any slice methods lie in the equilibrium conditions and assumptions of slice surface shape, as shown in the following table:

Method	**Equilibrium condition**				**Slip surface shape**
	Integral moment	**Soil slices moment**	**Vertical force**	**Horizontal force**	
Fellenius method (1936)	√	×	×	×	arc
Bishop's Simplified method (1955)	√	×	√	×	arc
M-P, S and J-method*	√	√	√	√	arbitrary

* M-P-method (Morgenstern-Price, 1965), S-method (Spencer, 1967), J-method (Janbu, 1968) Present the mostly used are Fellenius and Bishop's Simplified method.

Brief Description of the Finite Element Method

Advantages of FEM to slope stability analysis over traditional limit equilibrium methods can be summarized as follows:

(a) No assumptions about the shape or location of the failure surface are required;

(b) No assumptions about slide forces between slices and how to divide soil slice are required;

(c) Deformation information of soil element under working stresses is available;

(d) Progressive failure can be simulated.

In this paper, parametric studies of piles-row and slope interaction system are performed with PLAXIS (Vermeer, 1998). This program employs 6-noded or 15-noded triangular elements as well as interface elements soil and the wall.

To achieve SF of slopes with FEM, soil element adopts the Mohr-Coulomb model, which includes six parameters: E (Young's modulus), ν (Poisson's ratio), γ(Unit weight), φ '(Effective friction angle), c' (Effective cohesion), ψ (Dilation angle). Although elastic parameters (E, ν) have a profound influence on deformation prior to failure, they have little influence on SF in stability analysis of slopes. Thus, in the absence of E andν, they can be endued with nominal values (e.g. E=105 kN/m^2 andν=0.35). The total unit weightγassigned to the soil is proportional to the nodal self-weight loading generated by gravity. Dilation angle (ψ) affects volume change of soils during yielding. Slope stability analysis is relatively unconfined, which makes choice of dilation angle less important. As the main objective of the current study is the accurate prediction of SF of slopes, a compromise value of ψ=0 , corresponding to a non-associated flow rule with zero volume change during yield, has been used throughout this paper.

Mohr-Coulomb failure criterion has been used throughout this paper, which can be written as:

$$F = \frac{\sigma_1' + \sigma_3'}{2}\sin\varphi - \frac{\sigma_1' - \sigma_3'}{2} - c\cdot\cos\varphi \tag{1}$$

Where $\sigma_1^{'}$ and $\sigma_3^{'}$ are the maximum and minimum principal effective stresses.

The failure function *F* can be interpreted as follows:

$F < 0$, stresses inside failure envelope (elastic state)

$F \geq 0$, stresses on or outside failure envelope (soils yield and stress redistributes)

Definition of safety factor (F_s) adopts from strength reduction method. Trial strength indexes (φ_f, c_f) are used during calculation, which have following relation with φ, c and F_S:

$$c_f = c / Fs \quad , \qquad \varphi_f = \arctan\left(\frac{\tan\varphi}{Fs}\right) \tag{2}$$

This method is referred to as the 'shear strength reduction technique'. To find the 'true' F_s, it is necessary to initiate a systematic search for a suitable value of F_s that will exactly cause the slope to fail. It can be achieved with the program *PLAXIS*, which solves the problem by repeating a sequence of user-specified F_s values.

Plane Strain

To perform two-dimensional analysis of antislide plies-slopes system, spaced piles (flexural rigidity=E_pI_p) set in a slope are simplified as an equivalent sheet-pile wall (flexural rigidity=EI), which converts complicated three-dimensional problem to plane strain problem (see Fig.1 (E_sI_s is flexural rigidity of soils between piles)). The equivalent sheet-pile wall is modeled with elastoplastic beam elements through the finite element mash. The soft stratum is represented by ideal elastoplastic model, which conforms, to Mohr-Coulomb yield criterion. When the deformation of a pre-selected point in the slope or soils increases suddenly as *Fs* increases gradually, this indicates that plastic slip occurs in the point and the slope comes into critical state. In

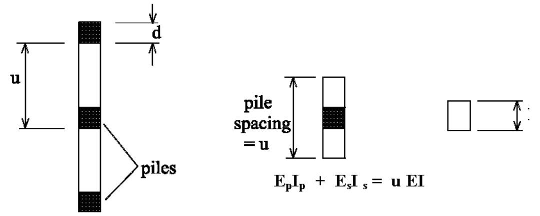

Plan on pile group **Wall stiffness per pile** **Equivalent sheet-pile wall stiffness per meter width**

Fig. 1 Equivalent sheet-pile wall representation of piles for plane strain finite element analysis

the meantime the bending moment of the sheet-pile wall usually reaches the UAM if its location is proper and. This *Fs* is exactly the safety factor of the slope.

Relation between the bending moment (Mz) of pile at depth *z* and its flexural rigidity (EI) can be given as follows:

$$M_z = -EI\left(d^2y/dz^2\right) \tag{3}$$

Eq (3) indicates that the allowable moment is direct proportional to its flexural rigidity, which means that increasing pile diameter or decreasing pile spacing can significantly improve the flexural rigidity of pile and the allowable moment.

STABILITY ANALYSIS OF UNREINFORCED SLOPE

Example ①: Homogeneous slope (see Fig. 2①).

Here Fs is 1.08, which has been given by S.Hassiotis (1997) with friction circle method (Taylor, 1937). Hull & Poulos (1999) gave a slightly higher value of Fs (=1.11) with the same method and a somewhat different result (Fs =1.12) with Bishop's modified slip circle analysis for the same slope. Calculated result of Fs in

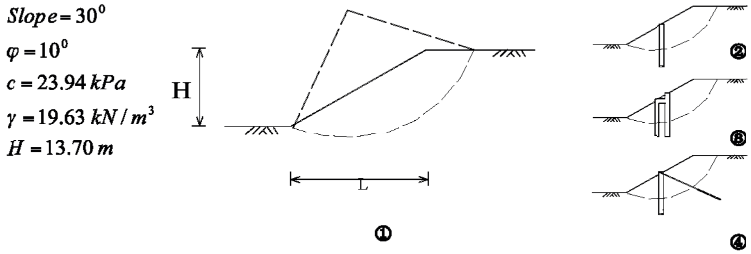

Fig.2 Example①~④: ①—critical surface of unreinforced slope

this paper is 1.096, which is very close to values gained by researchers mentioned above.

Parameters of friction circle method used for analysis of the critical surface of the homogeneous slope are shown in Fig.2 while results through FEM are shown in Fig.3.

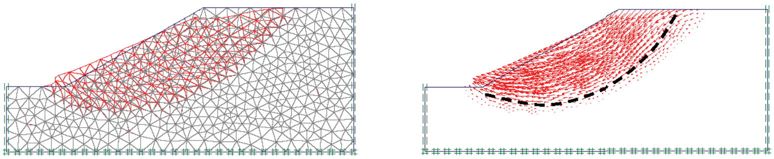

(a) (b)

Fig.3 Example①: (a) deformed mesh (b) nodal displacement vectors

Fig.3(a)and 3(b) give deformed mesh and nodal displacement vectors corresponding to the situation with Fs=1.096. The deformed mesh gives a rather diffuse indication of the failure mechanism. Comparing Fig.3 with Fig.2①, it can be shown that the shapes and positions of the critical surface are very close to each other. In Fig.3, the configuration of slide slope is helical, which coincides with the result with plastic theory.

In summary, FEM to determine SF and critical slip surface of unreinforced slopes has shown as a reliable method. D.V. Griffiths (1999) also comes to the same conclusion, who adopted FEM to analyze stability of slopes in some more complex conditions. Comparison with results from other slice methods indicates FEM is more accurate.

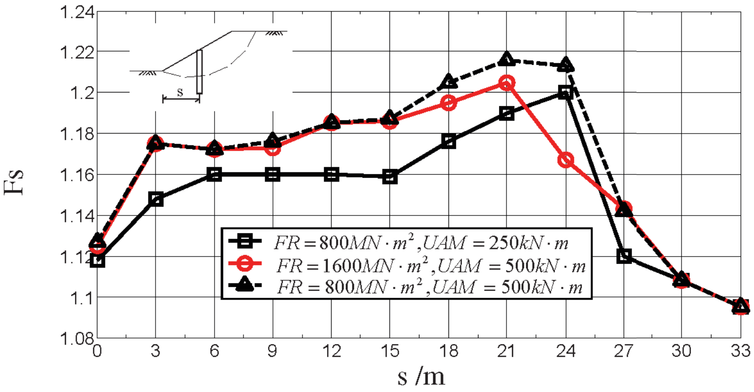

Fig.4 Effect of one-row piles location on safety factor of slope

FINITE ELEMENT ANALYSIS OF PILE-REINFORCED SLOPE

Reinforcing piles set in the slope commonly adopt the type of piles-row, such as cantilever, h shape retaining wall and tie-back reinforcing piles (shown in Fig.2②③④)etc. (Shao 1999, Wei 1999). The effect of these three structural types on the stability of slope (as shown in example ①) reinforced with piles-row is to be studied.

Example ②: FEM analysis of slope reinforced with cantilever piles (Fig.1②)

Results are shown in Fig.4 (pile length≤20 m) that makes it clear that reinforced effect is different when the location of reinforcing pile changes. Reinforced effect is relatively better near slope shoulder and in the center and upper part. Fig.4 also indicates that increasing the UAM of reinforcing piles can improve the reinforced effect greatly. However, only increasing the flexural rigidity while keeping the UAM invariable will decrease the reinforced effect, especially near the slope shoulder.

Example ③: FEM analysis of reinforced slope with h retaining wall piles(Fig.1③)

Results are shown in Fig.5, and it indicates that there are two peak values of SF when adopting h retaining reinforcing piles (pile length≤20 m), which respectively appears in the middle-bottom of the slope surface and near the slope shoulder.

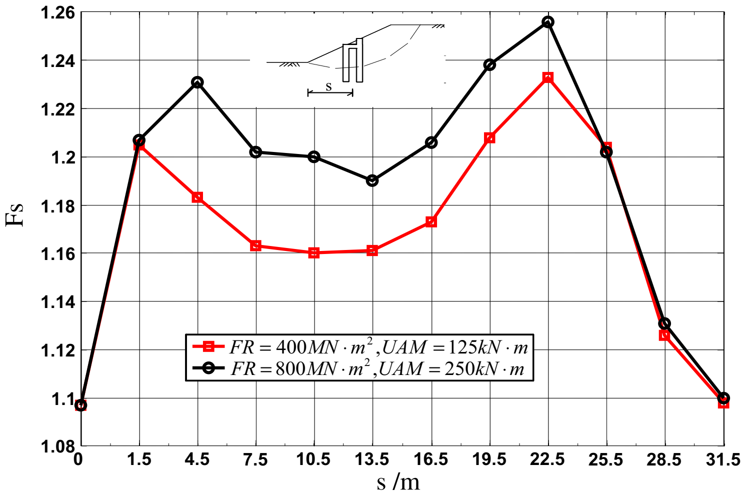

FIG.5 Effect of double-row piles location on safety factor of slope

Fig.5 also shows that it is insignificant to increase the UAM of reinforcing piles near the base of slope and in the slope shoulder, because lateral force applied to piles by soils is too small to reach the allowable lateral force. Failure is difficult to appear and the reinforced effect can't be expressed. The maximum safety factor is respectively 1.233 and 1.200 by comparing parameters from Fig.5 (UAM=125*kN·m*) and Fig.4 (UAM=250*kN·m*), which mean pile density in the former figure is a half of that in the latter. This means that the reinforced effect of h retaining wall piles is slightly better.

Example 4:FEM analysis of slope reinforced with tie-back reinforcing piles(Fig.④)

To express clearly, an elastic strut substitutes anchor at the top of piles.

Fig.6 shows that peak value of SF appears in the distance s=9.0m. (pile length≤20 m). Comparison in Fig.6, Fig.5 and Fig.4 shows that SF for slopes reinforced with tie-back reinforcing piles increases fast, which is from 1.096 to 1.315 (UAM= 250*kN·m*) until 1.403 (UAM=500*kN·m*). However, SF for slopes reinforced with cantilevers piles is 1.20 and 1.217 respectively while SF for slopes reinforced with h retaining wall piles is 1.233 and 1.253 respectively. It shows that the reinforced effect of tie-back reinforcing piles is the best approaches.

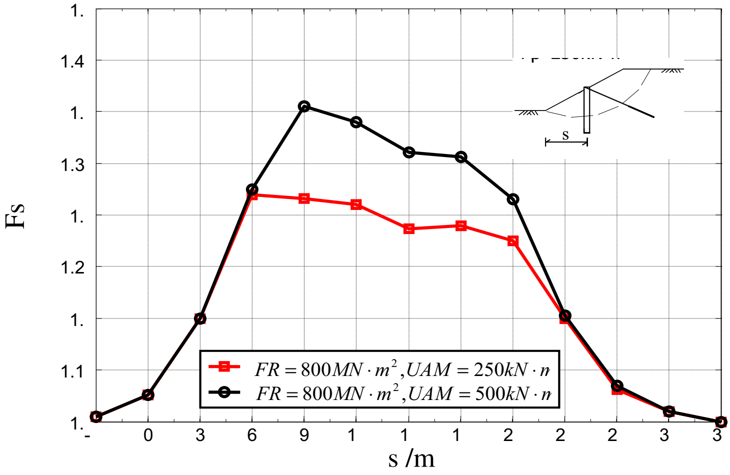

Fig.6 Effect of top anchor-hold one-row piles location on safety factor of slope

CONCLUSIONS

According to results presented in this paper, conclusions can be drawn as follows:

FEM can be used to analyze stability of slopes and safety factor and slip surface location can be precise enough.

Safety factor of reinforcing pile slope interaction system can be calculated by FEM proposed in this paper, which considers the effect of complex factors such as allowable moment, flexural rigidity etc. on the stability of reinforced slope.

In the three mentioned structural types, the reinforced effect with tie-back reinforcing piles is the best. All the reinforced effect varies with the change of piles' location. Selecting appropriate structural type and increasing the allowable moment of piles can promote the reinforced effect.

The stability analysis method presented in this paper is helpful in the design of reinforcing piles reinforcing slopes, which considers complex interaction between piles and soils in the slope. Obviously it is better than present design methods of reinforcing pile.

REFERENCES

Griffiths, D. V. & Lane, P. A.(1999). "Slope Stability Analysis by Finite Elements." *Geotechnique* 49(3): 387-403.

Dawson, E. M. Roth, W. H. & Drescher, A.(1999). "Slope Stability Analysis by Strength Reduction." *Geotechnique* 49(6): 835-840.

Poulos, H.G.(1995). "Design of Reinforcing Piles to Increase Slope Stability." *Can Geotech.*32: 808–818.

Pan Jiazheng(1980), "The Anti-slides Stabilization of Building and the Landslide Analysis. " *The water Conservancy Publishing Company*.

Steve Laudeman, P. E. & Nien-Yin Chang, P. E.(2004). "Finite Element Analysis of Slope Stabilization Using Piles." *Geotechnical Engineering for Transportation subjects*: 2000-2009.

Hassiotis, S. Chameau, J. L. and Gunaratne, M.(1997). "Design Method for Stabilization of Slopes with Piles." *J. Geotech. Engrg.*, ASCE. Vol.123(4): 314-323.

Shao Qihao(1999), "Several Structure Types of Anti-slide Pile for Chengdu-Kunming Line and Its Scope of Application." *Subgrade Engineering* No.1:65-67

Shen Zhujiang(1992). "The Anti-sliding Resistance of Pile and the Ultimate Design of Anti-slide Piles." *Chinese Journal of Geotechnical Engineering*, 14(1):53-58.

Tomio Ito et al(1979). "Design Method for the Stability Analysis of the Slope with Landing Pier." *Soils and Foundations*, 19(4)：152-159.

Wei Yongxing(1999). "Prevention and Practice of Landslide." *Subgrade Engineering*, No.3：44-47.

Optimization Methods for Design of the Stabilizing Piles in Landslide Treatment

Wu-Qun Xiao[1] and Bo Ruan[2]

[1]Associate Professor, School of Civil Engineering and Architecture, Central South University, Changsha, Hunan, 410075, China; wqxiao@mail.csu.edu.cn
[2]Lectuer, School of Civil Engineering and Architecture, Central South University, Changsha, Hunan, 410075, China); ruanboxiao@mail.csu.edu.cn

ABSTRACT: In this paper, the authors have studied the optimization of design schemes of the stabilizing piles and the detailed structure of the selected pile in middle-large landslide treatment. Using multi-objectives decision making fuzzy analysis and analytical hierarchy process (AHP), the optimized design scheme of the stabilizing piles, which is of the multiple attribute and fuzzy property, is done. Through the selection of decision variables, objective function, constraint condition (i.e. strength, size, reinforcement etc.) and optimization algorithm, the detailed structure of the selected stabilizing piles can be optimized to minimize the cost of construction. By the software, it is easy to solve this minimized value of nonlinear constraint multi-function. A case analysis proves that there is lower cost of construction by optimization of both schemes of stabilizing piles and the detailed structure of the selected pile in landslide treatment.

INTRODUCTION

The stabilizing piles are effective engineering measure which is used to prevent the slope sliding and improve the stability of the slope and are widely used in middle-large scale landslide treatment. However, the design method and theory is still empirical and need unceasing improvement (Zou and Chen 2003). The pile parameters, such as the length, the pile spacing, the cross-section size, the reinforcing bars and the number of the pile rows are determined by empirical method at first and then checked, adjusted to satisfy standard demand. Generally, there are several feasible schemes of the stabilizing piles in the same landslide treatment. By contrasting different design schemes of the stabilizing pile on the basis of present criterion and experience, a suitable one of the lowest cost is qualitatively chosen. However, the selected scheme is only a practical one, not the best one. In this paper, the main content is how to obtain a series of parameters for the design of the stabilizing piles which not only satisfy the demand of the landslide treatment but also is effective, economical, and safe. The optimizing design includes the optimization of the design schemes of the stabilizing piles and the detailed structure of the selected pile in landslide treatment.

OPTIMIZATION OF DESIGN SCHEMES OF THE STABILIZING PILES

Optimization of design schemes of the stabilizing piles in landslide treatment means that the best one is chosen among many feasible schemes. The feasible schemes are given in the light of the characteristics of a landslide and the treatment target. The main content of optimization includes the number of pile rows, the pile spacing, the pile types (with or without anchor and the number of anchor layers). The landslide treatment is quite complicated engineering system and the optimization of the pile design scheme is restricted by a lot of definite or indefinite factors. It is difficult to choose the best scheme only on basis of single-target optimization rule (generally, the lowest cost). The attributes of the pile design scheme in landslide treatment include reliability, cost, construction difficulty, time limit for a project, environment influence. Some attributes are fuzzy. Fuzzy Multi-objective decision making theory is used to optimize the design schemes of the stabilizing pile which have multi-attributes and fuzzy properties (Xu 2001).

Steps of the scheme optimization

Step 1 Set up target (index) eigenvalue matrix which is used to evaluate the design scheme of the stabilizing piles

If n stands for the number of the design scheme and every one is evaluated with the index number m (such as reliability, cost, time limit), the target eigenvalue matrix (decision matrix) is as follows:

$$X_{m\times n}=\begin{bmatrix} x_{11}\ x_{12}\ \ldots x_{1n} \\ x_{21}\ x_{22}\ldots x_{23} \\ \ldots. \\ x_{m1}\ x_{m2}\ldots x_{mn} \end{bmatrix}=(x_{ij}) \qquad (1)$$

In Eq. (1), x_{ij} is the ith index value corresponding to the jth design schemes.

The value in Eq. (1) can be divided into quantitative (such as cost) and qualitative index (such as reliability). The former is directly expressed with number and the latter is shown with grade, that is, value 2, 1.5, 1, 0.5 and 0, standing for the best, the better, the middle, the lower and the lowest, respectively.

Step 2 Normalization of index value

To compare and calculate, the target value of Eq. (1) is needed to normalize. By normalization, the optimal index (target) membership degree matrix is as follows.

$$R_{m\times n}=\begin{bmatrix} r_{11}\ r_{12}\ldots r_{1n} \\ r_{21}\ r_{22}\ldots r_{2n} \\ \ldots \\ r_{m1}\ r_{m2}\ldots r_{mn} \end{bmatrix}=(r_{ij}) \qquad (2)$$

Where r_{ij}(i=1,…m; j=1,…n) is a relative optimal membership degree of the ith value corresponding to the jth scheme. The calculation of value r_{ij} has two types.

One type of r_{ij}, called as a type-benefit index (the greater value r_{ij}, the more excellent), e.g. reliability, stability, advanced feature, is calculated according to Eq. (3).

$$r_{ij}=\frac{x_{ij}-\min(x_{ij})}{\max(x_{ij})-\min(x_{ij})} \qquad (3)$$

The other type of r_{ij}, called as a type-cost index (the smaller value r_{ij}, the more excellent), e.g. cost, time, difficulty, bad influence, is calculated according to Eq. (4).

$$r_{ij} = \frac{\max(x_{ij}) - x_{ij}}{\max(x_{ij}) - \min(x_{ij})} \qquad (4)$$

Step 3 Ascertainment of the most excellent scheme through fuzzy multi-objective comprehensive judgment

The optimal stabilizing pile design scheme is determined in accordance with the scheme membership degree u_j relative to the best excellent. The maximal value u_j is the optimal design scheme. The calculation formula of u_j with fuzzy multi-objective comprehensive judgment method is shown in Eq. (5).

$$u_j = \frac{1}{1 + \left[\frac{\sum_{i=1}^{m} (w_i |r_{ij} - 1|)^p}{\sum_{i=1}^{m} (w_i r_{ij})^p} \right]^{2/p}} \qquad (5)$$

Where p is distance parameter and is equal to 1 or 2, representing Hamming distance and Euclidean distance respectively. In this study, p is 2. And w_i is weight-vector of objective or index, requiring

$$\sum_{i=1}^{m} w_i = 1 .$$

Ascertainment method of w_i has subjective and objective weighing approach (Fan and Zhao 1997). There are many subjective and objective weighing approaches, such as TOPSIS, ELECTRE, AHP (Hwang and Yoon 1981; Mousseau et al. 2001; Saaty 1977). Among these methods, analytic hierarchy process (AHP) which can reflect the will, engineering experience and expert judgment from decision makers is one of widely used subjective weighing approach (Zhao et al. 1986). The calculating step of AHP is as follows.

Steps of calculating weight-vector with AHP

Step 1 Set up analytic hierarchy model

Based on four basic rules which are secure and practical, economical and reasonable, protecting environment, convenient construction, the analytic hierarchy model (Fig.1) is constituted to estimate the stabilizing pile scheme in landslide treatment.

In Fig.1, values of C_1, C_6 are calculated according to actual criterion and conventional design method, C_{10} is given by construction company, and other values, C_2, C_3, C_4, C_5, C_7, C_8, C_9, C_{11} and C_{12}, are given by local experienced and professional experts.

Step 2 Construct judgment matrix

Element value of judgment matrix which reflects people's knowledge to relative importance of every factor is generally denoted with 1~9 scale (Zhao et al. 1986). Relative to the optimal scheme (A), judgment matrix of relative importance of four factors in rule hierarchy, including safety and feasibility (B_1), economy and reasonableness (B_2), environment protection (B_3), convenience of construction (B_4), is given as Tab.1.

In other hierarchy, judgment matrix of factors relative to a factor of upper hierarchy can be obtained according to above method in turn.

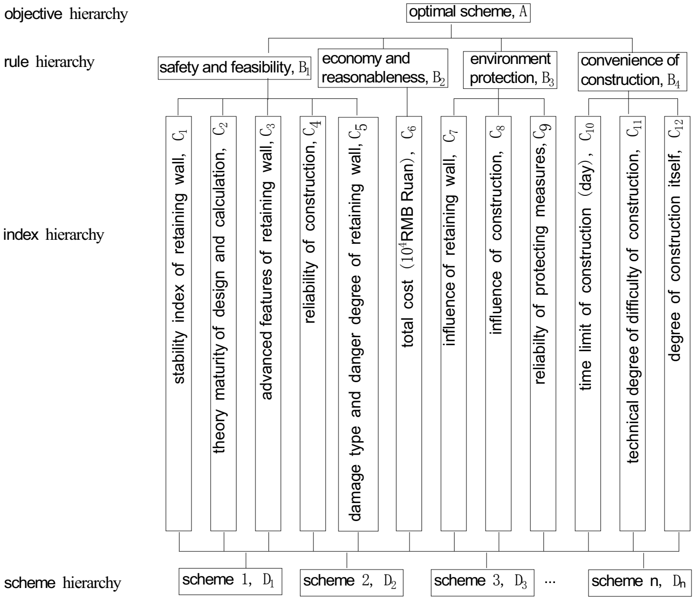

Fig.1. Hierarchy model of the stabilizing piles design scheme

Table 1. A-B Judgment Matrix and Consistency Checking

A	B_1	B_2	B_3	B_4	W_{Bk} (k=1,…,4)
B_1	1	1	2	3	0.351
B_2	1	1	2	3	0.351
B_3	1/2	1/2	1	2	0.189
B_4	1/3	1/3	½	1	0.109
$\lambda_{max}=4.012$ CI=0.004 RI=0.9 CR=0.0044<0.1					

Step 3 Single sorting of hierarchy and consistency checking

By using square root method, calculate the sorting weight-vector of every factor in the same hierarchy relative to a factor of upper hierarchy, and at the same time, get the eigenvector solution λ_{max} of judgment matrix (Wang 2004). This process is called as single sorting of hierarchy. According Eq. (6), calculate the consistency index CI and ratio CR .

$$CI=\frac{\lambda_{\max}-n}{n-1} \qquad \mathrm{CR}=\frac{\mathrm{CI}}{\mathrm{RI}} \tag{6}$$

Where, n is order of judgment matrix, and RI is mean stochastic consistency index that can be consulted.

When CR<0.1, consider that the result of single sorting of hierarchy is of satisfying consistency. Otherwise, it is necessary to adjust the element value of judgment matrix. λ_{max}, W, CI, CR of judgment matrix A-B are listed in Tab.1. Judgment matrix, relative weight vector w_j and consistency checking of every factor of the same hierarchy relative to a factor of upper hierarchy in other hierarchy is done in the light of above method and steps. The calculated result of single sorting of hierarchy is shown in Tab.2.

Step 4 Total sorting of hierarchy and consistency checking

Total index weight-vector is relative weight-vector of every index in index hierarchy relative to the top hierarchy. This calculation process is called as total sorting of hierarchy and the result is listed in Tab.2.

Total index weight-vector W is expressed in Eq. (7).

$$W = (W_1 \;\; W_2 \ldots \; W_n) \qquad (n = 12) \qquad (7)$$

According to Tab.2, total index weight-vector of evaluation index system in stabilizing pile design scheme is as follows.

$$W = (0.137 \;\; 0.069 \;\; 0.075 \;\; 0.042 \;\; 0.027 \;\; 0.351 \;\; 0.14 \;\; 0.032 \;\; 0.018 \;\; 0.081 \;\; 0.018 \;\; 0.01)$$

OPTIMIZATION OF DETAILED STRUCTURE OF STABILIZING PILES

After optimization of the design scheme, the detailed structure of the stabilizing pile in the chosen design scheme is needed to be further optimized. Under premise that the supporting function of the pile is satisfied according to actual criterion and conventional design method, the optimized goal is to minimize the engineering cost. For example, as for the anchor stabilizing pile, the optimized aspects mainly include cross-section size, location of anchor, reinforcement, etc..

Table 2. Single and Total Sorting of Hierarchy

		C_1	C_2	C_3	C_4	C_5	C_6	C_7	C_8	C_9	C_{10}	C_{11}	C_{12}
B_1	0.351	0.391	0.198	0.215	0.12	0.076	0	0	0	0	0	0	0
B_2	0.351	0	0	0	0	0	1	0	0	0	0	0	0
B_3	0.189	0	0	0	0	0	0	0.74	0.167	0.094	0	0	0
B_4	0.109	0	0	0	0	0	0	0	0	0	0.74	0.167	0.094
Total index weight W_i		0.137	0.069	0.075	0.042	0.027	0.351	0.14	0.032	0.018	0.081	0.018	0.01

Optimization of anchor location

Location of anchor (or anchor depth) is the vertical distance of anchor apart from the pile top. The optimization goal of the location is to minimize the endured moment of the pile in order to reduce reinforcement amount and cost.

Calculation result shows that, with falling of the anchor location (or increment of anchor depth), the pile moment of anchor point (axial intersection between the pile and anchor) increases and the maximum moment of total pile decreases. Because of increment of the anchored depth, the designed tension of anchor increases. When the moment of anchor location (or anchor point) is equal to the maximum moment of the pile, the moment of the pile is lowest, and, of course, the cost is lowest (Qin & Gao 1997). Therefore, when the moment of anchor location is the maximum moment of the pile, the location of anchor is the optimal location of anchor. But, in practical engineering, other factors, such as anchor anchorage, techniques, the calculating maximum anchor tension that is limited by field strata, should be taken into consideration in determining the optimized location of anchor.

Optimization of cross-section size and reinforcement of the pile

After the number, type and plane location of the pile in the process of design scheme optimization and the above anchor location have been established, the design residual thrust, length, internal force distribution, tensile force and length of anchor in each pile are accordingly formed. On basis of these known parameters, the cross-section size (generally, the section being of rectangle) and reinforcement of the pile are optimistically chosen in order to get the lowest cost of each pile. The optimized design includes four contents, decision (design) variable, objective function, and constraint condition and optimization algorithm respectively.

Establishment of decision variable

Decision variable X is expressed with following formula

$$X = \{x_1, x_2, x_3)^T$$

Where x_1, x_2 represents cross-section height (m) and width (m) of the pile and x_3 means cross-section area (m^2) of the longitudinal tension bar in the reinforced concrete pile.

Establishment of objective function

Cost of a single stabilizing pile is objective function *f(X)*, representing as following formula.

$$\begin{aligned} f(X) &= f(x_1, x_2, x_3) = Z_c + Z_{As} + Z_{As}' + Z_g \\ &= C_c \cdot x_1 \cdot x_2 \cdot L + \gamma \cdot L \cdot x_3 (C_{As} + C_{As}'\beta) + \gamma \cdot C_g (4x_1 + 2x_2 - 8a_0 + e) A_g \cdot L / S_y \rightarrow \min \end{aligned} \tag{8}$$

Among the variables, Z_c, Z_{As}, $Z_{As'}$, Z_g are cost (RMB yuan) of concrete, longitudinal tension bar, compression reinforcement and stirrup, and C_c、C_{As}、$C_{As'}$、C_g are unit price (RMB yuan per kilogram) of these four materials, respectively. And variables L, γ, β, a_o, e, A_g, and S_y are length of the pile (m), unit weight of reinforcement (kg/m^3), the ratio of cross-section area between compression and longitudinal tension bar, thickness of concrete cover (m), length of reinforcement hook (m), cross-section area (m^2) of a piece of stirrup and stirrup spacing (m).

Constraint condition

(1) Strength constraint

a. Strength constraint of cross-section

Strength constraint of cross-section is shown as Eq. (9).

$$M \le M_u = f_y \cdot x_3 (1 + \beta)(x_1 - a_o) \cdot \gamma_s \tag{9}$$

Thereinto, $\gamma_s = 1 - 0.5 \cdot \dfrac{f_y \cdot x_3 (1 + \beta)}{f_{cm} \cdot x_2 (x_1 - a_o)}$

b. Strength constraint of inclined section

Strength constraint of inclined section is shown as Eq. (10).

$$V \le 0.07 f_c \cdot x_2 (x_1 - a_o) + 1.5 f_{yg} \cdot \frac{n.A_g}{S_y} (x_1 - a_o) \tag{10}$$

Where M = design section moment of an stabilizing pile (N·m)
f_y = design tensile strength of longitudinal reinforcement (MPa)
f_c = axial compression design strength of concrete (MPa)
f_{cm} = flexural compression design strength of concrete (MPa)
f_{yg} = design tensile strength of stirrup (MPa)

n - number of stirrup

(2) Reinforcement constraint

a. Longitudinal reinforcement should be limited by Eq. (11).

$$0.0015 \le \frac{(1+\beta)x_3}{x_2(x_1-a_o)} \le 0.544\frac{f_{cm}}{f_y} \tag{11}$$

b. Stirrup should be limited by Eq. (12).

$$0.02\cdot\frac{f_c}{f_{yg}} \le \frac{n\cdot A_g}{x_2\cdot S_y} \le 0.12\frac{f_c}{f_{yg}} \tag{12}$$

(3) Size constraint

The size of the pile should be restricted by Eq.(13).

$$\begin{gathered} 1.5 \le x_1 \le 5 \\ 1.2 \le x_2 \le 3.5 \\ x_1 \le 1.5x_2 \\ x_2 \le x_1 \end{gathered} \tag{13}$$

Optimization algorithm

The detailed structure optimization of the stabilizing pile belongs to nonlinear programming issue of inequality constraint in maths. The issue can be solved by dynamic programming technique and also can be solved by known software, such as Matlab 6.5.

EXAMPLE

Xiaojianwan landslide in Beijing – Zhuhai Expressway is located in Chenzhou, Hunan Province, China. Volume of landslide body is up to 60×10^5 m^3, belonging to a large scale soil deposit landslide (Xiao Wu-quan, Li Liang and Ruan Bo, 2002). Typical landslide section is shown in Fig. 2. Shear strength index of soil of sliding surface is below: c=22kPa, $\varphi=12°$.

Optimization of the landslide treatment scheme with anti-sliding pile

Based on the field condition of hydrogeology and engineering geology, characteristic of surrounding building and environment limitation, experts have taken three available anti-slide pile scheme of landslide treatment into account. They are: two rows of pile (scheme 1, D_1), one row of pile (scheme 2, D_2), one row of anchor pile (only one anchor per pile) (scheme 3, D_3). Index of three schemes is listed in Table 4.

Table 4. Index Value of Each Anti-sliding pile Scheme

	C_1	C_2	C_3	C_4	C_5	C_6	C_7	C_8	C_9	C_{10}	C_{11}	C_{12}
D_1	1.5	1	0.8	1	0.6	885	0.6	0.6	1	90	0.6	0.6
D_2	1.2	1	0.7	0.9	0.9	817	0.7	0.8	0.9	120	0.8	0.6
D_3	1.7	0.7	1	0.7	1	762	1	1	0.7	120	1	1

According to Eq. (2), (3) and (4), optimal membership degree matrix R after normalization is as follows.

$$R=\begin{pmatrix} 0.6 & 1 & 0.33 & 1 & 1 & 0 & 1 & 1 & 1 & 1 & 1 & 1 \\ 0 & 1 & 0 & 0.67 & 0.25 & 0.55 & 0.75 & 0.5 & 0.67 & 0 & 0.5 & 1 \\ 1 & 0 & 1 & 1 & 0 & 1 & 0 & 0 & 0 & 0 & 0 & 0 \end{pmatrix}^T$$

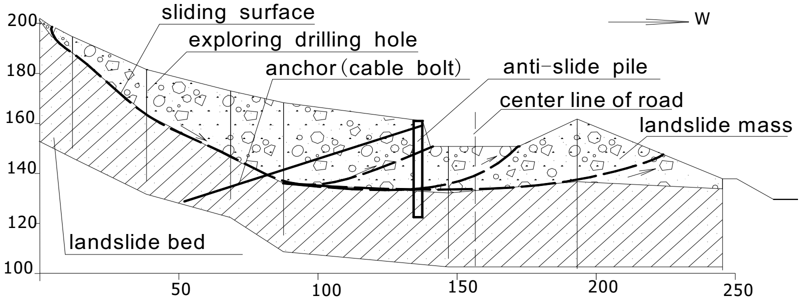

Fig. 2. Typical landslide cross-section (unit of size is meter)

Each scheme membership degree u_j relative to the best excellent is calculated according to Eq. (5) and on the basis of weight value w_i from Tab.2. Value u_j of each scheme is respectively as follows:

$u_1 = 0.249, \quad u_2 = 0.481, \quad u_3 = 0.807$

Obviously, the optimal scheme in above three schemes is scheme 3 (D_3), which is one-line pile with one anchor. In this scheme, the pile spacing is 6 meter. But the length and cross-section size of pile, length and bundles of anchor cable, etc. are best chosen based on the plane location of a pile in the landslide.

Optimization of the stabilizing pile detailed structure

Landslide thrust of different location is calculated respectively and the stabilizing pile of different location is optimized on basis of the thrust and sliding-surface depth. The detailed optimization process of the stabilizing pile with one anchor cable in Fig.2 is as follow.

(1) Location optimization of anchor cable

By calculation, the anchor cable with 54.5 m in length is 3.2 m apart from the pile top with the pile length of 37.2 m. The anchor cable consists of 8 lines of strand with a norm of $7\varphi 5$ in each line.

(2) Optimization of cross-section size and reinforcement of the pile

The chosen cement concrete grade of the pile body is C25 and the reinforcement is grade II. The chosen diameter of compressed and tensile reinforcement, supplementary reinforcement and stirrup is 32 mm, 22 mm and 16 mm respectively. Optimal decision variables are solved by means of solving minimum value of nonlinear programming function of many variables of inequality constraint. Optimal decision variable values are as follows.

$x_1 = 2.8m$

$x_2 = 2.2m$

$x_3 = 0.029m^2$

The other parameter values in Eq. (8) can be determined or consulted after x_1, x_2 and x_3 is optimized. Calculation from Eq. (8) shows the lowest cost of the pile is 1.035×10^5 RMB.

After various construction factors have been taken into account, detailed structures of each stabilizing pile is optimized in the same way. The total cost of the chosen stabilizing pile design scheme (D_3) is 7.62×10^6 RMB which is 1.23×10^6 RMB (about 16%) less than the cost in ordinary design.

CONCLUSIONS

(1) The optimizing design of stabilizing pile includes the design scheme optimization and the detailed structure optimization of the chosen pile in landslide treatment.

(2) Because the design scheme of stabilizing pile is of multi-attributes and fuzzy property, the scheme can be optimized on the basis of multi-objective fuzzy group decisions theory and analytic hierarchy process.

(3) Through the selection of decision variables, objective function, constraint condition (i.e. strength, size, reinforcement etc.) and optimization algorithm, the detailed structure of the selected stabilizing piles can be optimized to minimize cost of construction.

(4) A case analysis shows that the optimization method is viable and economical.

REFERENCE

Fan Zhi-ping, Zhao Xuan (1997). "An objective and subjective synthetic approach to determine weights for multiple attribute decision making. " *Journal of Decision Making and Decision Support Systems,* Vol.7(4):87-91.

Hwang C., Yoon K. (1981). "Multiple attribute decision making methods and applications: A state-of-the-art survey." New York: Springer

Mousseau V., Figueira J., Naux J. (2001). "Using assignment examples to infer weights for ELECTRE TRI method: Some experimental results." *European Journal of Operational Research*, 130 (2):263-275.

Qin Si-qing, Gao Ling-qin (1997). "Optimum design theory of anchor pile." *Journal of Engineering Geology*, Vol.5 (3) :237-241.

Saaty T. (1977). "Modeling unstructured decision problems: A theory of analytical hierarchies." Proceedings of the first international conference on mathematical modeling. 69-77.

Wang Guang-yue (2004). "Information entropy fuzzy analytic hierarchy process model for retaining decision making of deep foundation pits." *Rock and Soil Mechanics*, Vol. 25(5): 737-739.

Xiao Wu-quan, Li Liang, Ruan Bo (2002). "Analysis on the formation and characteristics of Xiejiawan landslip located in Beijing - Zhuhai expressway." *Site Investigation Science and Technology*, Vol.(4):30-34

Xu Yang-qing (2001). "Study of optimum-design theory and dynamic displacement-controlling of deep excavation." Wuhan: Wuhan University of Technology Press

Zhao Huan-chen, Xu Shu-bo, Jing-sheng (1986). "Analytic hierarchy process." Beijing: Science Press

Zou Guang-dian, Chen Sheng-shui (2003). "A design method of stabilizing piles and its optimized numeral model." *Chinese Journal of Geotechnical Engineering*, Vol. 25(1): 11-17

Search for Critical Slip Surface and Reliability Analysis of Soil Slope Stability Based on MATLAB

Sheng Zeng[1], Bing Sun[2], Shijiao Yang, and Kaixuan Tan

1 School of Nuclear Resources and Safety Engineering, University of South China, Hengyang, China, zeng0808@126.com
2School of Resource and Safety Engineering, Central South University, Changsha, China, sunbing0734@126.com

ABSTRACT: The stability analysis of slope is a popular topic in geotechnical engineering, however, the key of stability analysis is how to determine the most dangerous sliding surface, but the traditional method is determined according to experience. Because the genetic algorithm has powerful adaptability and does well in searching the global optimum solution, it was applied to analyze the stability of slope based on the premise of circular sliding surface and the ideal of genetic algorithm. The realization on the genetic algorithm of circular sliding surface is to found circular failure analysis model based on the Bishop method and to search the circle center coordinate of the most dangerous sliding surface with the genetic algorithm toolbox of MATLAB. Then an interface program for the reliability analysis of soil slope stability is developed depended on the platform of MATLAB. The analysis of the numerical example shows that the method of this paper has a higher accuracy, higher iterative convergence speed and stronger adaptability than the traditional calculation method, and that the reliability of the most dangerous sliding surface is the minimum reliability, which provides reference for the optimization design of slope.

INTRODUCTION

The criterion on how to evaluate the stability of soil slope and the way to find the critical slip surface are the main purpose in stability analysis of soil slope. The traditional slope stability analysis based on the circular slip surface such as the golden section, coordinate alternation and dichotomy method are easy to fall into local minimum, although they are widely used in practice. In the stability analysis of slope under complex geological conditions, the objective function is often highly irregular and peaky non-convex function, while it may be the most local optimal solution using the traditional optimal method. In recent years, a number of bionic algorithm such as genetic algorithm have strong fitness and robustness, which are good at searching the global optimal solution, even if the defined objective function is not continuous, non-rule or noisy, it is able to find the global optimum with a great probability. As a result, the genetic algorithm is introduced to analyze and design the slope stability by many scholars, so the traditional methods' shortcomings are overcome and a series of results are obtained.

With the use of MATLAB genetic algorithm toolbox in different fields, it provides a new way for the soil slope stability analysis and the genetic algorithm search procedures of a critical slip surface are avoided to be compiled. Based on the simplified Bishop method, the center coordinates of the most dangerous slip surface has been searched using the genetic algorithm toolbox of MATLAB, then the critical slip surface slope is obtained, and the interface procedures of soil slope stability analysis is developed on the basis of MATLAB platform. The example shows that the study has higher accuracy, faster iteration and more adaptation than the traditional method.

SEARCHING THE MOST DANGEROUS SLIP SURFACE WITH GA

According to the basic idea of genetic algorithms, the paper determines the most dangerous slip surface and the solution corresponding to the minimum safety factor with the genetic algorithm of the MATLAB toolbox.

The objective function shown as Equ.(1) adopts simplified Bishop method when the most dangerous slip surface is searched,

$$F_s = \frac{\sum_{i=1}^{n} \frac{1}{m_{\theta_i}} \left[c_i l_i \cos\theta_i + W_i tg\varphi_i \right]}{\sum_{i=1}^{n} W_i \sin\theta_i} \tag{1}$$

Where, $m_{\theta i} = \cos\theta_i + \frac{1}{F_s} tg\varphi_i \sin\theta_i$, W_i is the soil gravity, c_i, φ_i is the effective cohesion and internal friction angle, θ_i is the angle between normal and the vertical of the soil slice *i* slip surface, l_i is the arc length of the soil slice *i* circular arc in the sliding surface, n is the total number of the soil slices.

Through the study of this section, the program searching the most dangerous slip surface is compiled based on MATLAB genetic algorithm toolbox. In the specific settings of the genetic evolution, the fitness function also adopted the Bishop safety factor calculation equation.

GENETIC ALGORITHM OF SLOPE RELIABILITY BASED ON MATLAB

(1) Limit state equation

The limit state equation must be founded when the slope stability reliability is analyzed. Based on the Equ.(1), F_S is equal to 1 when the slope is in the limit equilibrium state, and then the limit state equation as follows,

$$g(x) = \sum_{i=1}^{n} \frac{c_i l_i + \gamma h_i b_i tg\varphi_i}{\cos\theta_i + \sin\theta_i tg\varphi_i} - \sum_{i=1}^{n} \gamma h_i b_i \sin\theta_i \tag{2}$$

Where, γ is bulk density of soil slices, h_i is the central height, b_i is the width, and the others are equal to Equ.(1).

(2) The realization of reliability index based on GA

x_1, $x_2 \ldots\ldots x_n$ are the hypothesis arbitrary distribution independent random variables, and after the variables were normalized, and then the equivalent normal distribution mean value $\mu_x^{'}$, standard deviation $\sigma_x^{'}$ and reliability index β.

$$\sigma'_{xi} = \phi\left\{\phi^{-1}[F_{xi}(x^*_i)]\right\} / f_{xi}(x^*_i) \tag{3}$$

$$\mu'_{xi} = x^*_i - \phi^{-1}[F_{xi}(x^*_i)] / \sigma'_{xi} \tag{4}$$

$$\beta = (\sum[(x^*_i - \mu'_{xi}) / \sigma'_{xi}]^2)^{1/2} \tag{5}$$

The reliability index is the minimum distance from the central point M to the limit state hypersurface $Z = 0$ in the U space. In the hypersurface, the shortest distance point $P^*(u_1^*, u_2^*, \ldots, u_n^*)$ apart from M is checking point.

At beginning, the checking point is unknown, β is looked as the function of P (x_1, $x_{2,}\ldots\ldots, x_n$) on the limit state hypersurface. Through the genetic algorithm optimization solving, the minimum of β is gained, which means that reliability index and checking point P^* (x^*_1, $x^*_2, \ldots\ldots, x^*_n$) is obtained. The solution of reliability index can be come down to the following constrained optimization model,

$$\text{Min} \quad \beta^2 = \sum_{i=1}^{n}[(x^*_i - \mu'_{xi}) / \sigma'_{xi}]^2 \tag{6}$$

$$\text{s.t.} \quad Z = g(x_1^*, x_2^*, \cdots\cdots, x_n^*) = 0 \tag{7}$$

The Equ.(7) is used as constraint function. The constrained nonlinear programming problem adopts penalty strategy, and the value of penalty coefficient is based on the actual project. The fitness function is constructed with addition form. The optimum value of fitness function is searched by genetic algorithm, and the reliability index β is obtained. The failure probability P_f is gained by the function cdf('norm',－β,0,1) , i.e. the reliability probability P_r=1－P_f.

Through the study of this section, the genetic algorithm program solving the reliability index is compiled based on MATLAB, while the program is only applicable to the stability analysis of homogeneous soil slope.

EXAMPLE OF APPLICATION

A soil slope is located in national highway NO. 107 K8+615-641. The height of slope is 9m, the length is 26m, the angle is 76^0, the soil layer is alluvial sediments clay layer. The soil parameters of this slope are obtained by laboratory test. The cohesion force c is 20kPa, and its standard deviation is 7.7kPa. The internal friction angle φ is 19^0, and its standard deviation is 3.950. The soil bulk density is 19kN/m^3. Considering engineering demand, the analysis of slope stability is necessary, which may provide instructions for design and construction.

According to the study, the SLIDE-SURFACE.M, the SLOPE-GA.M, the CONSTRAINT-CONDITION.M and SLOPE-GA-MIN.M（fitness function）four program module are compiled. SLIDE-SURFACE.M program based on the assumption of circular slip surface and idea of genetic algorithm, a method which uses genetic algorithm to determine the most dangerous slip surface and the corresponding minimum safety factor is presented. The others three programs are used to calculate the reliability index of soil slope in the most dangerous failure slope surface. When the MATLAB genetic algorithm toolbox GUI is used to solve optimal value of the four program module functions, the data input type of the fitness function is double vector, the population size is 20, the selection parameter is stochastic uniform function, the mutation parameter is Gaussian function, the cross parameter is scattered function, and the setting cross probability is 0.8. The iteration number Generation of genetic algorithm is equal to 100. The best fitness value Stall time equal to 20.

With the SLIDE-SURFACE.M program, the position of the most dangerous failure slope surface is obtained, the coordinates of center of circle are（-10.4683, 23.4136）, and the radius of arc sliding is 25.5961m, the safety factor of the soil slope is 1.0097. At this time, the computing terminates, and just the iteration number of genetic algorithm is 95. The Fig.1 and Fig.2(a) are shown the solving process.

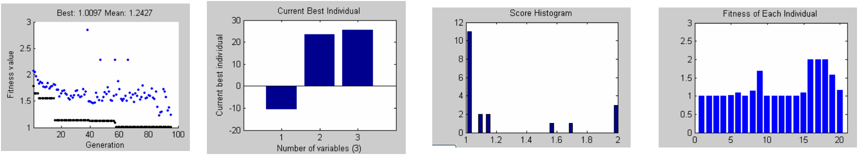

(a) (b) (c) (d)

Fig. 1. Optimization tracking of GA in SLIDE SURFACE.M function

Remarks: (a) the most optimal fitness value and even fitness value of each generation, (b) the most optimal fitness value corresponding point coordinate in current generation, (c) the scores of histogram in each generation, (d) the individual scores of histogram in each generation.

Because this is constraint nonlinear programming problem, penalty coefficient is defined 0.8 in CONSTRAINT-CONDITION.M program. Call SLOPE-GA.M, CONSTRAINT-CONDITION.M and SLOPE-GA-MIN.M programs, a series of results are obtained. Using cohesion force and internal friction angle as the checking point, the coordinates are (23.4049, 0.2633). The safety factor of the soil slope is 1.1308. The reliability index is 1.063. The failure probability is 14.38%. The reliability is 85.62%. At this time, the computing terminates, and just the iteration number of genetic algorithm is 51. The Fig.2(b) and Fig.3 show the solving process.

In order to verify the reliability index of the most dangerous sliding surface is the minimum reliability index of slope, this paper provided 10 groups of sliding surface reliability index for the comparative analysis, and the results are as shown in Table 1.

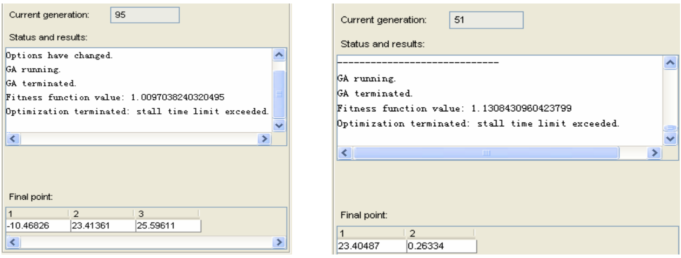

Current generation: 95

Status and results:

```
Options have changed.
GA running.
GA terminated.
Fitness function value: 1.0097038240320495
Optimization terminated: stall time limit exceeded.
```

Final point:

1	2	3
-10.46826	23.41361	25.59611

Current generation: 51

Status and results:

```
------------------------------
GA running.
GA terminated.
Fitness function value: 1.1308430960423799
Optimization terminated: stall time limit exceeded.
```

Final point:

1	2
23.40487	0.26334

(a) (b)

Fig. 2. Calculation status and final result

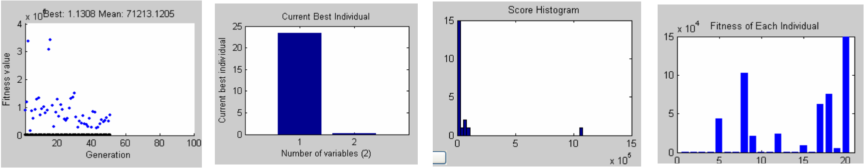

(a) (b) (c) (d)

Fig. 3. Optimization tracking of GA in SLOPE-GA-MIN.M function

Remarks: (a), (b), (c), (d) significance equal to Fig.1.

Table 1. Reliability Index of Different Sliding Surface

Radius (*m*)	Cohesion Force	Internal Friction Coefficient	Reliability Index	Radius (*m*)	Cohesion Force	Internal Friction Coefficient	Reliability Index
21	5.3500	0.3996	2.15	26	4.5395	0.2634	2.39
22	9.1052	0.3356	1.49	27	9.4876	0.1509	2.92
23	12.835	0.3287	1.31	28	2.7005	0.2478	2.59
24	11.6558	0.4212	1.74	29	11.3152	0.1211	4.66
25	15.2025	0.3876	1.12	30	17.7588	0.0457	4.91

CONCLUSIONS

(1) The reliability index of the different radius sliding surfaces is more than the most dangerous sliding surface, and the reliability of the most dangerous sliding surface is the minimum reliability of slope.

(2)The assessment formulation of slope stability is set up based on BISHOP method. Based on the MATLAB genetic algorithm toolbox, a method searching for the most dangerous sliding surface is determined. With the genetic algorithm, the search for the most dangerous sliding surface is accurate, quick and practicable.

(3)With the MATLAB toolbox, checking point method and genetic algorithm, an interface program for the reliability analysis of soil slope stability is developed. The results show that this program is effective to analyze the stability of soil slope.

(4)The selection of penalty coefficient has important influence on the minimum reliability index of slope, which should be further studied. This can improve the method.

(5)This study twice uses genetic algorithm to analyze the reliability of the soil slope, which provides reference for the stability of soil slope.

ACKNOWLEDGMENTS

This work was supported by the education department of Hunan, China under Grant NO. 08C758.

REFERENCES

Wen Xin-li, Guo Qiang. (2007). "Application of Genetic Algorithm on Non-circular Slip Surface of the Slope." J . Zhejiang Wat. Cons & Hydr. College, Vol. 19(4):51-54.

AN Guan-feng , YIN Kun-long , TAN G Hui-ming. (2002). "Appl ication of Genetic Algorithm in Numerical Simulation of Slope Stabil ity Analysis." Earth Science-Journal of China University of Geosciences, Vol. 27(2):177-180.

WAN Wen, CAO Ping, FENG Tao, et al. (2006). "Searching for the most dangerous failure surface of complex slope based on accelerating hybrid genetic algorithm." Chinese Journal of Geotechnical Engineering, Vol. 28(4): 475-479.

MI Hong-liang, CHEN Zu-yu. (2003). "Genetic algorithm used in determining the global minimum factor of safety of slopes." Chinese Journal of Geotechnical Engineering, Vol. 25(6):671-675.

SRINIVASA L R. (1996). "Optimal land grading based on genetic algorithms." Journal of Irrigation and Drainage Engineering, Vol. 122(4):183–188.

HU Song-bo. (2006). "The Research and Application on Optimization Design of Highway Soil Side Slope Based on the Economical Risk Analysis." HengYang: University of South China.

ZHOU Zhi-gang; YIN Hua-jie (2006). "Stability Analysis of Soil-nail Bracing Unsaturated Slope Based on Genetic Algorithm." Journal of Changsha Communications University, Vol. 22(2): 24–28.

Rock Slope Quality Evaluation Based on Matter Element Model

Zhi-Qiang Kang[1], Run-Sheng Wang[2], Li-Wen Guo[1], and Zhong-Qiang Sun[3]

[1] College of Resources and Environment, Hebei Polytechnic University, Tangshan 063009, Hebei, China, kzqzsh@163.com
[2] Department of Civil Engineering, Tangshan College, Tangshan 063009, Hebei,China;
[3]College of Environmental Science and Engineering, Hebei University of Science and Technology, Shijiazhuang 050018, Hebei, China

ABSTRACT: To solve the problem of rock slope failure in mountain express highway construction, extenics predicted method of rock slope stability of highway rock slope was proposed on the basis of extenics theory analysis based on matter element model. Classical and section field were established by using stable rank and influence factor of rock slope. By the usage of associated function in extenics sets, extenics forecast model of synthesis judgment of rock slope stability rank was set up, and the prediction results were obtained through extenics evaluation analysis. The example analysis shows that this extenics forecast method can forecast the rank problem of rock slope quality further accurately and scientifically, which provides more reliable basis for taking economic and reasonable reinforcement protection steps.

INTRODUCTION

With the high speed development of economy, the construction of express highway is playing an important role, especially in the development of the West Region in China. While, located in mountains or canyons, the highway rock slope stability problem stands out as an urgent issue[1]. The quantification of rock slope stability situation is a little hard to express from macrography and integrality. It's no doubt that the macro-analysis of slope stability through rock quality classification can provide an valuable information for the slope safety. In recent years, extenics rising and application in engineering have brought a new idea of highway rock slope quality evaluation. Rock slope evaluation based on extenics theory is an ideal rock classification project evaluation method. So this paper precedes a number of new explorations on the slope quality classification by using extension theory. And the achievement provides theories and methods for high slope stability intelligence analysis.

BASIC THEORY OF EXTENICS

By using extension of matter to calculate qualitatively and using extenics set theory and correlation function to calculate quantitatively, extenics method, which is a combination of qualitative and quantitative, evaluates on the study object from the aspects of feasibility and optimization. It, a new evaluation method, can transform the various indicators into a kind of compatibility problem. The conclusions accorded with the state facts can be obtained through establishing matter model.

Extenics[2-6] sets the matter and mathematics theories as its theoretical framework in which the matter element is the logic cells. V is the quantity value of c about the given matter N. An orderly triples R=(N,c,v) is used as a basic matter to descript N, shortened matter element. The name N, characteristic c and quantity value v are the three basic elements of the matter element. If N has various characteristics, that is

$$R=\begin{bmatrix} N & c_1 & v_1 \\ & c_2 & v_2 \\ & \cdots & \cdots \\ & c_n & v_n \end{bmatrix}=\begin{bmatrix} R_1 \\ R_2 \\ \cdots \\ R_n \end{bmatrix}$$

where R is named as n-dimension matter element presented as R=(N,C,V).

When N_{ot} is a standard thing, quantity value range about characteristic C_i is $V_{oti}=<a_{oti}, b_{oti}>$, the matrix of the classical and section domain can be respectively expressed as:

$$R_{ot}=(N_{ot},\ C,\ V_{ot})=\begin{bmatrix} N_{ot}, & c_1, & <a_{ot1},b_{ot1}> \\ & c_2, & <a_{ot2},b_{ot2}> \\ & \cdots, & \cdots \\ & c_n, & <a_{otn},b_{otn}> \end{bmatrix};\ R_p=(N_p,\ C,\ V_p)=\begin{bmatrix} N_p, & c_1, & <a_{p1},b_{p1}> \\ & c_2, & <a_{p2},b_{p2}> \\ & \cdots, & \cdots \\ & c_n, & <a_{pn},b_{pn}> \end{bmatrix}$$

R_{ot} is the classical domain matter element and R_p is the section domain matter element, while $v_{pi}=<a_{pi}, b_{pi}>$ is the expanded range of quantity value about characteristic c_i of section domain matter element .It is clear that $<a_{oti}, b_{oti}> \subset <a_{pi}, b_{pi}>$ (i=1,2,…n) 。

Several experts make an evaluation of various features of a certain material unit N_j (j=1,2,…m, and in accordance with the standards a score is set from which the matter element under test is gained.

$$R_j=\begin{bmatrix} N_j & c_1 & v_{j1} \\ & c_2 & v_{j2} \\ & \cdots & \cdots \\ & c_n & v_{jn} \end{bmatrix}$$

The correlation function of the matter element N_j about the grade it is:

$$k_{tj}(v_{ti})=\frac{\rho(v_{ji},v_{oti})}{\rho(v_{ji},v_{pi})-\rho(v_{ji},v_{oti})}\quad i=1,2,\ldots n\ ;\ j=1,2,\ldots m\ ;\ t=1,2,3,4,5 \tag{1}$$

In the formula (1),

$$\rho(x_o,\mathrm{x})=\begin{cases} \mathrm{a}-x_o, x_o \le \dfrac{\mathrm{a}+\mathrm{b}}{2} \\ x_o-\mathrm{b}, x_o \ge \dfrac{\mathrm{a}+\mathrm{b}}{2} \end{cases} \tag{2}$$

Where x_o is numerical value, x(a,b) is space interval; $k_{tj}(v_{ti})$is the correlation of characteristic i in matter element j about standard matter element grade t. Given a weighting coefficient W_i on each characteristic c_i, k_{tj} （N_j） about grade t of matter element N_j is:

$$k_{tj}(N_j) = \sum W_i k_{tj}(v_i) \tag{3}$$

$$k_{jt_0}(N_j) = \max\{k_{tj}(N_j) | t = 1,2,3,4,5\} \tag{4}$$

where this matter element grade is t_0.

QUALITY EVALUATION OF HIGHWAY ROCK SLOPE BASED ON EXTENICS

An extenics evaluation on the quality grade of large rock slope is made in this paper using the highway rock slope as an example, which provides reliable bases for the project stability analysis and the rocks reasonable utilization.

Guangnan highway, located in China's Guangxi Zhuang Autonomous Region, is one of tactic project of the Western Development projects. With complex rock slope and typical mountain terrain, this region exists important issues of slope destruction and instability.

Highway Slope Geological Conditions

The main rock slope of five slope strata (B_1,B_2,B_3,B_4,B_5) were selected that the slope stability grade extension evaluation were proceeded.

Strata 1(B_1): the bottom of the selected slope with sandstone and complete rock mass;

Strata 2(B_2):a overall complete rock mass mainly with siltstone and argillite that has steep rake angle, weak joint and small scale;

Strata 3(B_3):a overall complete rock mass mainly composed of argillite the joint of which is weak with some sandstone and siltstone;

Strata 4(B_4): mainly composed of thin and middle thick siliceous argillite with some siltstone;

Strata 5(B_5):the top of the selected slope, mainly composed of strong differentials litho logy with slack relief, opening joint, good connectivity, complete secondary silt.

Selection of the Slope Evaluation Index

According to the test results and data analysis of highway, six factors selected as slope stability complex index are as follows.

1) Compressive strength of wet rock, Rc, reflects the hard extent and litho logy of the rock;

2) Rock deformation modulus, E, reflects the rate of stress and strain under the load;

3) Rock gravity, γ （the weight of unit rock, reflects the density of the rack;

4) Rock shearing strength, including cohesive strength C and internal friction angle φ, reflects the hard extent and combination degree of their own;

5) Rock Poisson's ratio, reflects the ratio of the main stress and the strain on the vertical direction under external force.

As the national standards [7,8], rock slope quality is divided into 5 grades with single parameter, which was shown in table 1. According to the design report of highway slope, the parameter indexes of 5 main adjacent rock(B_1,B_2,B_3,B_4,B_5) were obtained, as it shown in table 2.

Table 1. Rock mass quality classification with single parameter

level	I	II	III	IV	V
R_c/MPa	120~200	60~120	30~60	15~30	0~15
γ/ （KN/m^3	28~30	26.5~28	24.5~26.5	22.5~24.5	0~22.5
E/GPa	33~60	33~20	20~6	6~1.3	0~1.3
μ	0~0.2	0.2~0.25	0.25~0.3	0.3~0.35	0.35~0.5
C/MPa	2.1~8	2.1~1.5	1.5~0.7	0.7~0.2	0.05~0.2
φ(o)	60~90	50~60	39~50	27~39	0~27

Table 2 Parameters of wall rock slope

type	B_1	B_2	B_3	B_4	B_5
R_c/MPa	100	80	50	50	20
γ/ （KN/m^3	27.3	20	15	15	5
E/GPa	22	20	15	15	5
μ	0.24	0.25	0.27	0.27	0.35
C/MPa	2.45	1.96	1.48	1.48	0.5
φ(o)	56.3	53.5	47.7	47.7	30

Dimensionless Parameters

For ease of calculation, the different indexes must be made dimensionless, the methods of which are as follows:

$$q'_{ti}=\begin{cases}\dfrac{q_{ti}-q_i^{\min}}{q_i^{\max}-q_i^{\min}}, \text{for the large factors}\\[2ex] \dfrac{q_i^{\max}-q_{ti}}{q_i^{\max}-q_i^{\min}}, \text{for the small factors}\end{cases} \qquad d'_{ti}=\begin{cases}\dfrac{d_{ti}-q_i^{\min}}{q_i^{\max}-q_i^{\min}}, & \text{for the large factors}\\[2ex] \dfrac{q_i^{\max}-d_{ti}}{q_i^{\max}-q_i^{\min}}, & \text{for the small factors}\end{cases}$$

In the formula, q_{ti} is evaluation standard value of i factor in the t sort, q'_{ti} is the dimensionless evaluation standard value of i factor, $q_i^{\max}$ is the maximum evaluation standard value of i factor, $q_i^{\min}$ is the minimum, d_{ti} is the evaluation standard value of i factor in the under test rock t, d'_{ti} is the dimensionless evaluation standard value of i factor in the under test rock t.

After the dimensionless treatment on table 1 and 2, table 3 and 4 with corresponding value were obtained.

Table 3 Rock mass quality classification with single parameter (dimensionless)

level	I	II	III	IV	V
R_c	0.6~1.0	0.3~0.6	0.15~0.3	0.08~0.15	0~0.08
γ^3	0.93~1.0	0.88~0.93	0.82~0.88	0.75~0.82	0~0.75
E	0.55~1.0	0.33~0.55	0.1~0.33	0.02~0.1	0~0.02
μ	0.6~1.0	0.5~0.6	0.4~0.5	0.3~0.4	0~0.3

C	0.26~1.0	0.19~0.26	0.09~0.19	0.03~0.09	0~0.03
φ	0.67~1.0	0.56~0.67	0.43~0.56	0.3~0.43	0~0.3

Table 4 Parameters of wall rock slope (dimensionless)

type	B_1	B_2	B_3	B_4	B_5
R_c	0.5	0.4	0.25	0.25	0.1
γ^3	0.91	0.91	0.9	0.9	0.89
E	0.37	0.33	0.25	0.25	0.083
μ	0.52	0.52	0.46	0.46	0.3
C	0.31	0.25	0.185	0.148	0.063
φ	0.63	0.59	0.53	0.53	0.33

Definition the classical domain and section domain matrix

According to table 3, the corresponding range of I~V rock slope quality index were taken as classical domain. The six factors are c_1, c_2, c_3, c_4, c_5, c_6 respectively. Therefore, the classical domains of slope matter element are as follows. Section domain matrix, R_p, is based on the range of rock slope quality index. In general, it is the total of the rock slope grades.

$$R_{01}=\begin{bmatrix} N_{01}, & c_1 & <0.60,1.0> \\ & c_2 & <0.93,1.0> \\ & c_3 & <0.55,1.0> \\ & c_4 & <0.60,1.0> \\ & c_5 & <0.26,1.0> \\ & c_6 & <0.67,1.0> \end{bmatrix} \quad R_{02}=\begin{bmatrix} N_{02}, & c_1 & <0.30,0.60> \\ & c_2 & <0.88,0.93> \\ & c_3 & <0.33,0.55> \\ & c_4 & <0.50,0.60> \\ & c_5 & <0.19,0.26> \\ & c_6 & <0.56,0.67> \end{bmatrix} \quad R_{03}=\begin{bmatrix} N_{03}, & c_1 & <0.15,0.30> \\ & c_2 & <0.82,0.88> \\ & c_3 & <0.10,0.33> \\ & c_4 & <0.40,0.50> \\ & c_5 & <0.09,0.19> \\ & c_6 & <0.43,0.56> \end{bmatrix}$$

$$R_{04}=\begin{bmatrix} N_{04}, & c_1 & <0.08,0.15> \\ & c_2 & <0.75,0.82> \\ & c_3 & <0.02,0.10> \\ & c_4 & <0.30,0.40> \\ & c_5 & <0.03,0.09> \\ & c_6 & <0.30,0.43> \end{bmatrix} \quad R_{05}=\begin{bmatrix} N_{05}, & c_1 & <0.0,0.08> \\ & c_2 & <0.0,0.75> \\ & c_3 & <0.0,0.02> \\ & c_4 & <0.0,0.30> \\ & c_5 & <0.0,0.03> \\ & c_6 & <0.0,0.30> \end{bmatrix} \quad R_p=\begin{bmatrix} P, & c_1 & <0.0,1.0> \\ & c_2 & <0.0,1.0> \\ & c_3 & <0.0,1.0> \\ & c_4 & <0.0,1.0> \\ & c_5 & <0.0,1.0> \\ & c_6 & <0.0,1.0> \end{bmatrix}$$

Definition the under test matter element of highway rock slope

The under test matter element were defined as follows according to table 4.

$$B_1: R_{10}=\begin{bmatrix} N_{10}, & c_1 & 0.50 \\ & c_2 & 0.91 \\ & c_3 & 0.37 \\ & c_4 & 0.52 \\ & c_5 & 0.31 \\ & c_6 & 0.63 \end{bmatrix}; \quad B_2: R_{20}=\begin{bmatrix} N_{20}, & c_1 & 0.40 \\ & c_2 & 0.91 \\ & c_3 & 0.37 \\ & c_4 & 0.52 \\ & c_5 & 0.31 \\ & c_6 & 0.63 \end{bmatrix}; \quad B_3: R_{30}=\begin{bmatrix} N_{30}, & c_1 & 0.25 \\ & c_2 & 0.90 \\ & c_3 & 0.25 \\ & c_4 & 0.46 \\ & c_5 & 0.185 \\ & c_6 & 0.53 \end{bmatrix}$$

$$\mathrm{B}_4\text{: } R_{40} = \begin{bmatrix} N_{40}\,, & c_1 & 0.25 \\ & c_2 & 0.90 \\ & c_3 & 0.25 \\ & c_4 & 0.46 \\ & c_5 & 0.148 \\ & c_6 & 0.53 \end{bmatrix} ;\quad \mathrm{B}_5\text{: } R_{50} = \begin{bmatrix} N_{50}\,, & c_1 & 0.10 \\ & c_2 & 0.89 \\ & c_3 & 0.083 \\ & c_4 & 0.30 \\ & c_5 & 0.063 \\ & c_6 & 0.33 \end{bmatrix}$$

Definition the weight coefficient by analytic hierarchy process

1) The judgment matrix was set up by defining every evaluation factor of highway rock slope and dealing with the evaluation index. In this paper, the relative important comparison matrix, S, by the usage of the numbers 1 to 9 and their reciprocal values was constructed.

$$S = \begin{bmatrix} 1 & 7 & 3 & 5 & 6 & 8 \\ 1/7 & 1 & 1/5 & 1/3 & 1/2 & 2 \\ 1/3 & 5 & 1 & 3 & 5 & 6 \\ 1/5 & 3 & 1/3 & 1 & 3 & 4 \\ 1/6 & 3 & 1/5 & 1/3 & 1 & 4 \\ 1/8 & 1/2 & 1/6 & 1/4 & 1/4 & 1 \end{bmatrix}$$

2) The maximum characteristic root of the above judgment matrix, $\lambda_{\max}$ =6.444,was calculated by extract method. The weight assemble W= （0.456, 0.051, 0.254, 0.128, 0.079, 0.032） of evaluation index is got by normalizing the corresponding exigent vector.

3) Consistency check of the above calculation was made. The consistency index CI is 0.088, the randomness index RI 1.24, then the rate of random consistency index CR is 0.072.As CR<0.10,the result has satisfied consistency. Therefore, the assembly W is the weight of the evaluation factors.

Calculate the association of the rock slope

According to the formula (1) and (2), the association degree about every quality grade of the under test rock slope was calculated. Then the complex association degree about every quality grade of the under test rock slope was obtained through W_i and formula (4).The results are shown in table 5.

Table 5 Calculation results of relational degree of rock slope

type	k1	k2	k3	k4	k5
B_1	-0.1748	0.1577	-0.2003	-0.3894	-0.4568
B_2	-0.2232	0.1777	-0.1266	-0.3709	-0.4485
B_3	-0.4760	-0.1391	0.2418	-0.3251	-0.4050
B_4	-0.4873	-0.1545	0.0271	-0.2615	-0.4156
B_5	-0.7492	-0.6062	-0.2624	-0.3049	-0.2157

Following the evaluation rules (4), the under results were acquired:

$\mathrm{Maxkj}(B_1)=k_2(B_1)$;$\mathrm{Maxkj}(B_2)=k_2(B_2)$;$\mathrm{Maxkj}(B_3)=k_3(B_3)$;

$\mathrm{Maxkj}(B_4)=k_3(B_4)$; $\mathrm{Maxkj}(B_5)=k_5(B_5)$

It can be seem from the results that strata one and two belong to the second level, strata three and four belong to the third and the fifth strata belongs to the fifth level.

Through the analysis of the Guangnan highway rock slope, the strong differential litho logy B5 must be excavated and at the same time, effective reinforcement should be carried out. Large fault and distribution sometimes play an important role in the deformation of the slope. Bedding fault will speed up the gliding while the inverse fault will prevent it. As for strata B4 and B3, with the influence of the shape and differentiation of fault and slope, it is importance to reinforce the anchor wire and the anchor arm .This measures can prevent the destruction of rock, slow down the creep deformation of the rock and strengthen the safety of highway slope.

CONCLUSIONS

The highway rock slope stability evaluation is a complicated process. Through the construction of matter element by extenics method to evaluate rock slope stability grades, the project problem brought by rock slope quality can be predicted more accurately and scientifically. This paper sets up the matter element of extenics evaluation of highway rock slope based on the analytic hierarchy process against the Guangnan highway slope. The results show that this assessment method, which is reasonable and feasible with better practicability, can provides a new thinking method when dealing with the similar highway engineering problem.

ACKNOWLEDGEMENTS

Authors acknowledge the support of the International Engineering Foundation and the Education Science foundation of Hebei (2007454)

REFERENCES

Feng Xiating, Wang Yongjia, Ding Enbao(1995). "Intelligent Method of Stability Analysis of Open-Pit Slopes." *Journal of Northeastern University*(*Natural Science*),Vol.16(5): 453-457.

Cai Wen(1990). "The Extension set and non-compatible problem [A].In:Chien Weizhang ed.Advances Mathematics and Mechanics in China." *Beijing*: *International Academic Publishers*,23-26.

Cai Wen(1994). "Matter element model and its application."*Beijing* : *Science & Technology Press*: 10-13.

Cai Wen, Yang Chunyan, Lin Weichu(1997). "Extension engineering method." *Beijing*:*Science & Technology Press*:34-38.

Chen Julong(1997). "From matter element analysis to extenics." *Beijing*:*Science & Technology Literature Press*:18-22.

Zhang Bin,Yong Qidong,Xiao Fangchun(1997). "Fuzzy matter elemetent analysis". Beijing:Petroleum Industry Press:45-49.

"Classification criterion of engineering rocks.(1995)" *Beijing*: *Ministry of Water resouces P.R.China*

"Code for water resources and hydropower engineering geological investigation [S](1998)." *Beijing*:*Ministry of Water resouces P.R.China*

Study on the Application Performances of Saponated Residue and Fly Ash Mixture as Geogrids Reinforced Earth Retaining Wall Filling Material

Ji-Shu Sun[1], Yuan-Ming Dou[2], Chun-Feng Yang[2], and Jian-Cheng Sun[2]

[1]Doctoral student, Dept. of Civil Engineering, Hebei University of Technology, Guangrong Road #8, Tianjin 300130, People's Republic of China; Tel:(86)022-60435971; E-mail: sunjishu76@126.com
[2] Professor, Dept. of Civil Engineering, Hebei University of Technology, Guangrong Road #8, Tianjin 300130, People's Republic of China; Tel: (86)022-60204020; E-mail: douyuanming@163.com

ABSTRACT: The filling material performances and its interface friction properties with the geogrids would directly influence the application properties of the geogrids reinforced earth retaining walls. Through systematical experiments, the technical performances which include strength and rigidity of saponated residue and fly ash mixture were studied in this paper. Moreover, the interface friction properties between geogrids and the mixture were studied. The results indicate that the mixture of saponated residue and fly ash have higher strength and rigidity, good interface friction with the geogrids. The technical performances of the mixture conform to the requirements of geogrids reinforced earth retaining walls, so it can be used as the filling material of geogrids reinforced earth retaining walls.

INTRODUCTION

Because of the good engineering performances, a large number of reinforced earth retaining walls have been constructed throughout the world. Compared with the traditional gravity earth retaining walls, geogrids reinforced earth retaining walls have the better engineering characteristics of light deadweight, beautiful shape, construction convenience and etc. Especially on the soft ground, the better performances would be embodied in virtue of their light deadweight.

Filling material's performances and interface friction properties with the geogrids directly influenced the application performances of the geogrids reinforced earth retaining walls. The commonly used filling materials are lime soil, graded gravel, fly ash and so on. As the filling material of geogrids reinforced earth retaining walls, it should have the following engineering properties: (1) good mechanical properties which include the strength and rigidity; (2) better interface friction property with the geogrids; (3) the material had better be lightweight. Ke Zhao, et al. (2001) studied the performances of saponated residue and added-calcium fly ash mixture in highway application. Cancelli A, et al. (1992) studied the frictional characteristics of geogrids with fly ash by means of direct shear and pull-out tests. Nicola Moraci and

Piergiorgio Recalcati (2006) analyzed the factors affecting the pull-out behaviour of geogrids embedded in a compacted granular soil.

Through experiments, the technical performances of saponated residue and fly ash mixture, and the interface friction properties between geogrids and the mixture, were studied in this paper. The purpose was to investigate the application properties of the mixture used as filling material of geogrids reinforced earth retaining walls.

PROPERTIES OF RAW MATERIALS

Saponated Residue and Fly Ash

Saponated residue is one kind of industrial waste residue discharged by chemical plant in producing epoxy propane. Saponated residue has higher fineness, but no cohesion itself. It can be easily dispersed in other material through mixing. Fly ash is another industrial waste discharged by coal power plant. The primary chemical compositions of saponated residue and fly ash are shown in Table 1.

Table 1. Chemical Composition of Saponated Residue and Fly Ash (%)

Material type	CaO	Al_2O_3	SiO_2	Fe_2O_3	MgO	K_2O	Others
Saponated residue	48.45	8.58	14.28	2.15	3.2	0.23	23.11
Fly ash	3.97	32.16	48.94	6.79	0.71	0.74	6.69

Table 1 indicates that the primary composition of saponated residue is calcium oxide. It can be used as an inorganic binder. In terms of chemical composition, saponated residue and fly ash mixture is approximately same as lime-fly ash.

Geogrids

The geogrids used in the experiment was specification TGS-2 of polyester fiber. Its unit area weight is 558g/m2, ultimate tensile strength is 56.1kN/m, limit elongation is 23.4% and mesh size is 25×25 mm.

MECHANICAL PROPERTIES OF SAPONATED RESIDUE AND FLY ASH MIXTURE

Compressive Strength

Based on the standard test method (Ministry of communications, 1995), test cylinder samples of saponated residue and fly ash mixture at different mix ratio were made and cured. The unconfined compressive strength (Degree of compaction is 95%) at different curing ages was tested. The results are shown in Table 2.

Table 2. Compressive Strength of Saponated Residue and Fly Ash Mixture at Different Age (*MPa*)

Mix Ratio	7d	28d	90d	180d	Notice
15:85	0.827	1.434	1.792	2.152	Mix ratio is the dry mass ratio
20:80	0.832	1.527	2.247	2.726	
25:75	0.846	1.669	2.614	3.053	

Table 2 indicates that the seven days-age compressive strength of every mix ratio is more than 0.8MPa. The compressive strength of saponated residue and fly ash mixture is higher. Furthermore, the compressive strength of the mixture would increase with the curing age or saponated residue content increasing. Compactness is another factor influencing the strength. The strength would decrease about 2 to 7 percent while compactness decreases 1 percent.

Clearage Strength and Modulus of Resilience

Test results of clearage strength and modulus of resilience of saponated residue and fly ash mixture are shown in Table 3. The test results indicate that the mixture has higher clearage strength and modulus of resilience. Its clearage strength is a little higher than that of lime-ash-soil. Their modulus of resilience is equal in the gross.

Table 3. Clearage Strength and Modulus of Resilience (*MPa*)

Mix Ratio	Clearage Strength	Modulus of Resilience	Notice
15:85	0.235	652	① Compactness is 95 percent ② Cured age is 180 days
20:80	0.328	875	
25:75	0.357	1025	

Water Stability

Water stability of saponated residue and fly ash mixture was tested by wetting-drying test (Ministry of communications, 1995). The results indicate that water stability coefficient of saponated residue and fly ash mixture of every mix ratio is bigger than 1, as shown in Table 4. Water stability of the mixture is good.

Table 4. Water Stability Test Results (Compactness 95 percent)

Mix Ratio	Strength of Contrast Sample（*MPa*）	Strength after Wetting-drying(*MPa*)	Water Stability Coefficient
15:85	1.508	1.622	1.08
20:80	1.804	2.021	1.12
25:75	2.061	2.328	1.13

INTERFACE FRICTIONAL PROPERTIES

Test Apparatus and Test Method

Direct shear apparatus: the shear box size 150mm×150mm, vertical load was tested through lever system and, horizontal load was tested through worm gear plus hand wheel. Pull-out test device: test box size 500mm×240mm×300mm, vertical load was tested through oil pressure jack plus stress ring and horizontal load was tested through jack plus pressure sensor. Tests were conducted in strain-controlled mode, and both the shear rate and pull-out rate were 0.5mm per minute.

Direct Shear Test and Results Analysis

According to the selected test methods, interface friction properties between geogrids and the mixture of saponated residue and fly ash were tested by a direct shear test. The friction angles and direct shear coefficients could be calculated by the Eq. (1) and Eq. (2) respectively. The results are shown in Table 5.

The relationship of shear strength and normal stress is:

$$\tau = c + \sigma_n \tan \varphi \tag{1}$$

Where: τ—Shear strength (kPa);
c—Cohesion (kPa);
σ_n—Normal stress (kPa);
φ—Internal friction angle (°).

Direct shear coefficients (Jing-hai Wu et al. 2001) could be calculated as follow:

$$C_{ds} = \tan \varphi_{sg} / \tan \varphi_{ss} \tag{2}$$

Where: C_{ds}—Direct shear coefficient;
φ_{sg}—Interface friction angle between geogrids and the mixture (°); a_s—Internal friction angle of the filling material (°).

Table 5. Direct Shear Coefficients of Geogrids with Saponated Residue and Fly Ash

Mix Ratio		**Friction Angle φ (°)**	**Cohesion c (kPa)**	**Regression Coefficient R^2**	**Direct Shear Coefficient C_{ds}**
15:85	The mixture	28.1	12.8	0.9965	0.84
	Interface	24.3	9.4	0.9887	
20:80	The mixture	30.1	15.9	0.9969	0.90
	Interface	27.6	9.8	0.9894	
25:75	The mixture	31.9	19	0.9979	0.92
	Interface	29.9	13.7	0.9899	

The direct shear test results indicate that: (1) shear strength of the mixture of saponated residue and fly ash is higher; the friction angle reached to approximately 30°, slightly smaller than it is in the coarse sand; (2) direct Shear coefficient is relatively high, from 0.84 to 0.92, slightly bigger than lime-fly ash. These indicate that geogrids and the mixture have a better interface friction property.

Pull-out Test and Results Analysis

The interface friction property between geogrids and the mixture of saponated residue and fly ash is generally investigated by pull-out test and is characterized by pull-out coefficient. Pull-out coefficients (Wu et al., 2001) could be calculated as follow. The results of pull-out test are shown in Table 6.

$$C_{po} = \tan \varphi_{sg} / \tan \varphi_{ss} \tag{3}$$

Where C_{po}—Pull-out coefficient; φ_{sg}—Interface friction angle between geogrids and the mixture (°); a_s—Internal friction angle of the filling material (°).

Table 6. Pull-out Coefficients of Geogrids with Saponated Residue and Fly Ash Mixture

Mix Ratio	Friction angle φ_{sg} (°)	Cohesion c (kPa)	Regression Coefficient R^2	Pull-out Coefficient C_{po}
15:85	15.1	5.6	0.9869	0.51
20:80	18.4	6.7	0.9879	0.57
25:75	20.7	8.2	0.9846	0.61

From Table 6, we can determine that: 1. there is a linear relationship between the pull-out stress and the normal stress; 2. the interface friction angle (φ_{sg}) between geogrids and the mixture is 15.1° to 20.7° and Pull-out coefficient is 0.51 to 0.61.The pull-out coefficient is bigger than that of sand (0.37) and appropriately same with that of lime-fly ash. These show the better interface friction properties between geogrids and the mixture of saponated residue and fly ash once again.

CONCLUSIONS

Through systematical experiments, the application performances of saponated residue and fly ash mixture were studied in this paper. The main conclusions obtained are summarized below.

(1) The mixture of saponated residue and fly ash has higher strength, rigidity, and good water stability.

(2) The strength of saponated residue and fly ash mixture would increase when saponated residue content, the curing age or degree of compaction, is increased.

(3) Both the direct shear coefficient and pull-out coefficient of the mixture of saponated residue and fly ash are relatively higher. These indicate the better interface friction between geogrids and the mixture of saponated residue and fly ash.

(4) The performance of saponated residue and fly ash mixture conform to the requirement of filling material of geogrids reinforced earth retaining walls. So it can be used as a good filling material of geogrids reinforced earth retaining walls.

REFERENCES

Ke Zhao et al. (2001). “A Research on the Performances of Saponated Residue Added-Calcium Fly Ash in Highway Application”. *Chinese Journal of Fly Ash Comprehensive Utilization*, 14 (1):6-10.

Cancelli A, Rimoldi P, Tongi S. (1992). “Frictional characteristics of geogrids by means of direct shear and pull out tests”. *Proceedings of Earth Reinforcement Practice*. Kyushu, Japan: A. A. Balkema, 1992. 141-146.

Nicola Moraci and Piergiorgio Recalcati. (2006). “Factors affecting the pullout behaviour of extruded geogrids embedded in a compacted granular soil”. *Geotextiles and Geomembranes* 24(2006):220-242.

Ministry of communications. (1995). “Test Methods of Materials Stabilized with Inorganic Binders for Highway Engineering”. *China Communication Press*.

Jing-hai Wu, Huan Chen et al. (2001). “Study on soil interaction characteristics of geosynthetics”. *Chinese Journal of Geotechnical Engineering*, 23 (1):89-93.

Study of Mouzhudong Landslide Mechanism

Lei Guo[1,2], Helin Fu[1], and Hong Shen[1]

[1] Civil Engineering College, Central South University 410075
[2] Tunnel Engineering Bureau,Luoyang China, 471009

ABSTRACT: Mouzhudong landslide lies in Guixin Express, and it was a big landslide which occurred previously. The main part of the landslide is sequence shale with lime stone. After being repaired for serval times, there are still new cracks existing in the potential landslide. In this paper, through the stability analysis to the right landslide of Maozhoudong with Limit Balance Method, current slope stability also can be disclosed. The possible slide faces include the arc face slide from the bottom of retaining wall and the polyline face slide from the top of poles along mudstone.

SURVEY OF MOUZHUDONG LANDSLIDE

Mouzhudong landslide includes the right and left landslide, which lie in the right of K48+085～K48+210m and the left of K47+942～K48+041 respectively. The direction of the line is NE71.17^0. This road section is cutting shape, the tallest slope is more than 60m high. The right slope slided in 2000, the original retaining wall could not withstand the current slope thrust, there were many cracks in different angles developing inside the wall, and the facing wall had been pressed and hunched, and in 2001, the improvement measure was taken by local Highway Bureau. The basic principle for the improvement was[1]: reinforcing the current retaining wall, setting prestressed anchor cables to withstand collapse force, to bare slope, measure of hanging net and ejecting concrete was taken, i.e. on the toe of left slope with 2m tall retaining wall, in excavated slope land the hanging net and ejecting concrete defense was adopted, the anchor pole was 5m long, and the space distance is 2m. But now, there are new cracks appearing in the slopes (Fig.1(a)), it needs to be repaired again[2]. Before repairing, it is essential the mechanism of Mouzhudong Landslide to be disclosed.

CALCULATION THE RIGHT MOUZHUDONG LANDSLIDE STABILITY WITH LIMIT EQUILIBRIUM METHOD

Calculation models

Considering of the fault development, rock fragmentation and limestone with mud thin, and slope treated as decentralization structure, the slide face is arc desalt rock sandwich; Consideration of the combination of consolidate terrain structure and slope body affected by water pressure in F_1 and density, and when slide along general obliquity limestone with mud, it will easily slide down in inclined. It was a credible method to take stability calculation to these two landslide models synchronously [3], and analyze the safety factor lesser model as practical landslide. The arc slide model can be calculated with more accurate and relative simple Predigestion Bishop Method, for incline slide model, slide body can be regarded as a whole to analyze the stability and calculated with Transfer Coefficient Method.

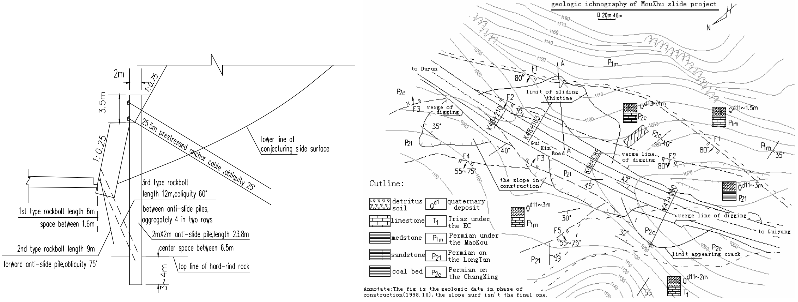

(a) **(b)**

Fig.1. Geology plan of Maozhudong landslide

According to shape, geological constitution, slide situation and cracks distribution of this slope, there are three kinds of possible slide types: along original face or the top of spud for antislip or slope face cracks appeared. In addition, cracks and loosened piles distributions are somewhat affected by the combination of stratum direction and spud for antislip, landslide moving trend is about the angular bisector of the slope surface direction and terrain proneness, where appeared the first slide face possibly. There are two kinds of slide face, and six potential sliding planes in the original landslide. Due to the angle of nip mud face and F_1 is much big, the transfer coefficients in the corner are small or even minus possibly when stability calculated with Transfer Coefficient Method. To avoid of this situation and considering F_1 to be steep incline with 80°, the rear limestone cliff of F_1 to be integrity , when slide happens, the slide body and limestone will cut from F_1, the weight of landslide is all assumed on the slide face of nip mud layer, there is only groundwater pressure in F_1. Maozhoudong landslide geotechnical parameters are in table1.

Slope Stability calculation

1)Determination of slope admit stability coefficient

The rock slope belongs to the types of IV, the highest part is 65m. If the slope being destroyed , the traffic will be break off . According to the safety grade standard of construction slope engineering technical criterion, the sliding stability coefficient of wedge slide is 1.30, of arc slide is 1.25; the sliding stability coefficient of highway is 1.20～1.30,and according to the relative prescription of highway roadbed design criterion. When calculated with Transfer Coefficient Method, slope stability is 1.30, when calculated with Predigestion Bishop Method ie becomes to 1.25.

Table1. Maozhoudong landslide geotechnical parameters

Type	Cohesion C(KPa)	Frication angleφ(°)	Saturated unit weight(KN/m3)	Wed unit weight(KN/m3)
shale	10	6.9	23	20
Limestone with mud	10	36.75	25	22
coal stratum	15	30	25	22
Limestone	500	60	27	25

2) Procedure of slope stability calculation

Assume thrust distribution of landslide behind the retaining wall lies between triangle and rectangle, resultant force P acting on 0.4H of wall above slide face. Since the terrain in the bottom of retaining wall is soft, assume turn center is the center of the retaining wall foot, during stability calculation, the effect of wall foot obliquity when inclined angle α＝10° needs to be considered. According to the slope reinforce data in existence, anchor poles are N.o8 channel steel, diameter of anchor bore is 110mm, the availability length of anchor poles, Ⅰ, Ⅱ and Ⅲ are 4.5m, 6.5m and 8.5m. Anchor pole, I, which disposed straightly in the bottom of the retaining wall, where rock is soft and fragmentation, only little effect to stability of retaining wall, the effect of anchor poles, I, for predigesting calculation is not considered. Upright resistance of anchor poles should be the less value in shearing resistance of mortar and rock mass near the bore cliff and stretching resistance of channel steel, for cracked coal stratum, according to experience, the adhesion strength of mortar and rock is 150kPa according to construction slope engineering technical criterion (considering terribly soft rock). These pulls provided by mortar and rock mass in the bore cliff of anchor poles Ⅱ and Ⅲ are 337KN and 440 KN, which are greater than stretching resistance of No.8 channel steel 215KN. So, upright resistance of anchor pole is 215KN, and 165.4 KN/m when convert unit breadth. Show in table 2, according to the weight of retaining wall, the complex sliding resistance is 240.23KN/m, which controlled by antidumping stability.

The total length of anti-sliding pile is 23.8m, 11.2m long above slide face, and the average distance between two piles is 6.5m, there are two prestressed anchor cables with obliquity 25° in each piles, the stretching resistance design value of single bundle prestressed anchor cables is 600KN, the pull value of anchor cable on each pile is 1200KN. Assume sliding resistance acting pot of spud for antislip is the center of landslide and the inclined angle is 10°. Shown in table 3, combines with the effect of anchor cables, the sliding resistance of single anti-sliding pile is 7118.8KN, if calculated by shear section , along the pile sliding resistance become to 1095.2 KN/m.

For the potential slide face 5 and 6 in A-A, the angle of section and exposure is about 35°, trusting resistance of retaining wall and spud for antislip needs to be divided by the coefficient sin35°.

Table 2. The retaining wall trusting resistance calculation

W(KN/m^3)	x(m)	α(^{o})	β(^{o})	δ(m)	B(m)	h(m)	f	Kf	Kc	T1(KN/m)
667	1.18	10	49.2	0.54	6	3.04	0.4	1.3	1.2	165.4
Sliding resistance P1(KN/m):			453.1	Floor stressσ_{max}、σ_{min}(Kpa):				56.92	218.86	P(KN/m)
Inclining resistance P2(KN/m):			240.2	Floor stressσ_{max}、σ_{min}(Kpa):				155.4	108.21	240.23

Table 3. Spud for antislip trusting resistance calculation

a (mm)	A_g (㎜^{2})	A_g' (㎜^{2})	Ak/S (㎜)	f_y (Mpa)	f_{yk} (Mpa)	f_c (Mpa)	M_p (KN.m)	Q_P (KN)	a (mm)	A_g (㎜^{2})
1500	2000	70	28149	24932	4.41	310	310	12.5	16231	5923.13
H_1(m)	H_2(m)	H_p(m)	α(o)	T(KN)	β(o)	Ho(m)	PQ(KN)	PM(KN)	P(KN)	P(KN/m)
23.8	11.12	5.56	10	1200	25	2.5	7118.849	16839	7118.8	1095.21

3) Result of calculation

Calculated the right landslide of Maozhoudong and the result is showed in table 4.

Table 4. The result of stability calculation

NO.	Slide face	Method	Safety coefficient F	Admit F_{min}
Presumed face 1	Arc	Predigestion Bishop	1.10	1.25
Presumed face 2	Polyline	Transfer Coefficient	1.212	1.3
Potential face 1	Polyline	Transfer Coefficient	0.994	1.3
Potential face 2	Polyline	Transfer Coefficient	1.567	1.3
Searching face 1	Arc	Predigestion Bishop	1.162	1.25
Searching face 2	Polyline	Transfer Coefficient	1.05	1.3
Potential face 3	Arc	Predigestion Bishop	1.286	1.25
Potential face 4	Arc	Predigestion Bishop	1.565	1.25
Potential face 5	Arc	Predigestion Bishop	1.256	1.25
Potential face 6	Polyline	Transfer Coefficient	0.980	1.3

4) Parameter sensitivity analysis

According to geological condition, the groundwater pressure distribution is gained, which has close relation with rainfall, it is fluctuant and changes frequently, so its sensitive to slope stability needs to be analyzed. During calculation, assume groundwater pressure equipotential line begin with 3/4 height of F_1, along the line of the top of retaining wall, reaching F_2 through limestone with mud , and connecting with roadbed side ditch in coal stratum. Now, the water table of F_1 is 5m, 10m and 20m away from slope face, in addition, the groundwater pressure were converted with 1.0, 0.75 and 0.5 to analyze the change of calculation stability coefficient.

The calculation results are shown in table 5-8, they are relative stability coefficient, the ratio of the corresponding coefficient in table 2 for analyze more conveniently. The key problem is to find potential dangerous slide face, so the face selected in parameter sensitivity analysis is the calculation stability coefficient fall short of demand in table 2.

Table 5. Slope stability sensitivity caused by groundwater content

F1grondwater depth(m)	Presumed 1	Presumed 2	Potential 1	Potential 6	Searching 1	Searching 2
	Arc	Polyline	Polyline	Polyline	Arc	Arc
5	0.961	0.882	0.849	0.846	1.001	0.964
10	0.935	0.934	0.916	0.920	1.000	1.000
15	1.000	1.000	1.000	1.000	1.000	1.000
20	1.041	1.042	1.052	1.053	1.000	1.000
25	1.083	1.094	1.116	1.098	1.000	1.000
The most difference	0.083	0.118	0.151	0.154	0.001	0.038

Table 6. Slope stability sensitivity caused by groundwater pressure

Groundwater stress minus coefficient	Presumed 1	Presumed 2	Potential 1	Potential 6	Searching 1	Searching 2
	Arc	Polyline	Polyline	Polyline	Arc	Polyline
0.5	1.128	1.143	1.089	1.045	1.000	0.909
0.75	1.064	1.070	1.044	1.022	1.000	0.909
1	1.000	1.000	1.000	1.000	1.000	1.000
The most difference	0.128	0.143	0.089	0.045	0	0.091

Table 7 . Slope stability sensitivity caused by mud density inside limestone

Saturation unit weight	Savageness unit weight	Presumed 1	Presumed 2	Potential 1	Potential 6	Searching 1	Searching 2
		Arc	Polyline	Polyline	Polyline	Arc	Polyline
24	22	0.978	1.006	1.003	1.003	1.000	1.000
25	22	1.000	1.000	1.000	1.000	1.000	1.000
26	22	1.003	0.994	0.996	0.997	1.000	1.000
25	20	1.006	1.009	1.013	1.022	1.017	1.025
25	21	1.003	1.004	1.006	1.011	1.008	1.012
25	23	0.996	0.995	0.994	0.990	0.988	0.990
The most difference		0.022	0.009	0.013	0.022	0.017	0.025

Table 8. Slope stability sensitivity caused by mud c、 φ inside limestone

Limestone with mud		Presumed 1	Searching 1	Shale		Presumed 2	Potential 1	Potential 6	Searching 2
φ(°)	C(Kpa)	Arc	Arc	φ(°)	C(Kpa)	Polyline	Polyline	Polyline	Polyline
33	10	0.903	0.907	5	10	0.872	0.837	0.815	0.791
35	10	0.950	0.949	6	10	0.939	0.923	0.902	0.901
36.75	10	1.000	1.000	6.9	10	1.000	1.000	1.000	1.000
39	10	1.063	1.061	8	10	1.074	1.094	1.077	1.121
36.75	6	0.984	0.971	6.9	8	0.961	0.939	0.916	0.861
36.75	8	0.992	0.997	6.9	10	1.000	1.000	0.981	1.000
36.75	12	1.007	1.021	6.9	12	1.034	1.056	1.046	1.049
36.75	15	1.122	1.118	6.9	15	1.358	1.345	1.207	1.305
The most difference		0.122	0.118	The most difference		0.358	0.345	0.207	0.305

CONCLUSIONS

The main reasons of Maozhoudong landslide including followings:(1) the abundant groundwater source in this section;(2) the poor geological conditions, i.e. permeable and impermeable terrain inter-beds, rock fragmentation, the geology of joint and fold ;(3)the past large-scale excavated, especially in bulge landform zone excavated propitious to the form of landslide;(4) general incline terrain constitution with soft shale is related with the form of landslide tightly.

Through the stability analysis to the right landslide of Maozhoudong with Limit Balance Method, current slope stability also can be disclosed. The possible slide faces include the arc face slide from the bottom of retaining wall and the polyline face slide from the top of poles along mudstone.

ACKNOWLEDGMENTS

This paper is sponsored by Chinese Natural Science Foundation (50878213), West science and technology construction projects of ministry of communications (2003-318-802-01), Hunan Communication project(200506), here thank them.

REFERENCES

Fu Helin. Theoretical Analysis Model for Block Crack Rockmass Slope Stability and Its Application：[D].Changsha：Central South University, 2000:20~50

Zhao Shangyi, Shi Weiming, Zhen Yinren. The Finite Element Method of Slope Stability Analysis [J]. Underground Space, 2001.12, 21(5)：450～454

R.E.Goodmam. Methods of Geological Engineering in Discontinuous Rock [M].West Publishing Company, 1976:30~66.

Study of Deep Drain Stability in High Steep Slope

Zhibin Qin[1] and Xudong Zha[1]

[1]School of Traffic and Transportation Engineering, Changsha University of Science and Technology, Changsha, Hunan, 410076, P.R.China, e-mail: zhibinq@126.com

ABSTRACT: The seepage situation of cutting slope groundwater is simulated and analyzed with the finite element software ANSYS. Comparing and analyzing the seepage field distribution of setup plan for hole diameter, hole long, hole distance to different drainage holes, it gets that the incidence and effect for changes of hole diameter, long hole, hole distance to drainage seepage field distribution. Combined with the real project, it discusses the distribution of slope seepage field under drainage holes laying double row along elevation, and draws that drainage holes laying multi-row along elevation can significantly improve drainage effect. So it determines the design project for drainage curtain of water-rich and high-steep cutting slope. Then, through the geological prospecting and the hydrological conditions survey in the real engineering, combined with the results of drainage pipes with finite element analysis, the specific buried project of deep drainage pipes is identified. Moreover, according characteristics of deep drainage, the technology and the control requirements of corresponding construction are established. Finally, slope surface deformation and internal displacement are monitored by using GPS and inclinometer. Monitoring results for many times in 18 months are analyzed. The largest surface deformation is 41.4 mm, and the largest internal deformation is only 10 mm, all are less than the first order of allowing deformation 123.75 mm of $0.0025h$ (h is the height of slope). Slope stability is got, and it is further validated the slope has a good stability after the deep drainage treating.

INTRODUCTION

With the great improvement of the rural road situation, the roadbed is becoming much higher. In the western mountainous area, where fragment characterizes the geological structure, the key point falls on the design of the cutting slope. The anchor rod timbering technique that is newly developed from the neo-construction program of the mine tunnel has been used as an important construction form in cutting-slope timbering and foundation pit blocking. Under the circumstances where the plane projected angle of the shovel-shaped angle in the rock stratum is larger than that of the slope, because of the affluent water from the rock stratum itself and the rain, the stability of the internal structure of the slope shall be mainly affected by the joint force due to the sudden fall of the water level. The essay shall discuss on how to stabilize the cutting slope by researching on the deep drainage method, whose main principle is blocking and draining. As further references, the author shall take some examples to clearly state the application conditions, the construction techniques and the economical considerations, etc of this method in question.

FINITE ELEMENT ANALYSIS OVER THE DESIGN OF THE DRAIN HOLES IN THE CUTTING SLOPE

Finite element value calculation mould

The mould shall be applicable to solving the seepage field, by means of simulating the drain hole and its effect for the convenience of analysis. Thus, the essay adopts a completed mould, which can be freely dissected using the gridding method. Closely imitate the drain hole through changing the parameter of its material and the conditions of the edges.

The two-dimensional drainage analyzing method shall be adopted in the essay. Take the supreme value of the water level, i.e. 49.5m as the height of the cutting slope. Adopt the Descartes right-angle coordinate, with X axis representing the leaning direction of the slope, Y axis the height of the slope, and Z axis the tendency direction.

On the left side of the coordinate, the fixed supreme water level is 49.5m; the gradient of the slope is 1:0.5. The port on the right side of the drainpipe is 1m above the slope bottom. Refer to picture 1 for the finite element mould, 8-joint plane is applied.

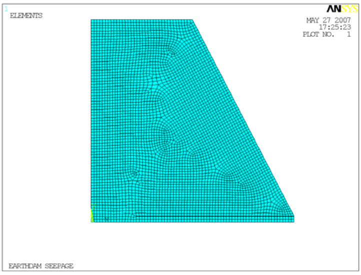

Figure1 Finite element model

Parameters of the materials used in the mould: the draining parameter of sand is 1.673×10-4cm/s; suppose there is no block in the drainpipe and the water is directly let out; the upper part of the drainpipe is 70% permeable, while the lower part 30% impermeable.

Suppose the slope is made of homogeneous isotropy materials, in which case the infiltration of objects cannot be compressed. Follow the Darcy Law when the slope of the water seepage in a small hydraulic pressure gradient on the. With the fluid gap function, the material of the cutting slope shall comply with the revised Terzaghi effective laws.

Result

1) The basic algorithmic principle

The basic algorithmic principle is as follows: since the size of the drain area is unknown to us and the water level is changeable, it is necessary to fix a level that is the same as the upstream water level as the boundary, which is obviously higher than that of the final water level. As the iteration process moves forward, in step r, compare the head of pressure and the Gravity of the joint point, if lower, then this joint point can be taken as the Zero water head. As for one specific unit, if all its joints are judged to be zero water head, then this unit will not be involved in the cycle, which may eliminate the influence of the non-saturated area on the drain area. Otherwise, the unit shall participate in the next cycle and the initial water head of the zero water head joints shall be zero in value. Recalculate until the absolute difference of the head of pressure and the Gravity is lower than the limit value.

In the process of calculating the finite element value, we analyzed the drainage from two different ways. The saw tooth curve in the picture represents the flexible water level. If we interpolate the head of pressure and the Height value, divide it into more grids, find out and connect the same value point of the head of pressure and the Height value, then we can get the flexible water level line that is more reality-based and much smoother.

2) Analyzing results

(1) To change the diameter of the drain hole can influence the draining effect, but only to a minor extent.

(2) The length of the hole has a great influence over the draining effect. After we get the drilling materials, i.e. through drilling the top slope to find out the flexible surface and the water-abundant stratum, we will adopt the plan of lengthening the drain hole.

(3) As the hole distance increases, along the direction of the cutting slope, the step-down function out of the drainage will wear off, but that of the whole area will maintain strong. According to the analysis over the step-down effect of finite element drainage, the hole distance is 7m.

(4) Through analyzing the seepage fields of the double-row drain holes, if the drain holes of the upper row are distributed under the flexible surface, the row distance will affect the distribution of the seepage field. We recommend that the setup of double-row drain holes which can greatly improve the draining effect be adopted. The distance between the upper row and the lower row is 12m.

REAL PROJECTS

General information

The K39+240 section of the HUAIXIN express highway lies in an unfavorable terrain, where the rain easily gathers, the ground water is mainly supplied from other places, and it is the drainage area for ground water, thus the area is always immersed in water. Though the cutting slope is mainly composed of non-dissoluble rocks, under the hydrating function, the surface of the slope is vulnerable to soakage and efflorescence, which may widen the crack, weaken the structural strength between rock stratums, and enhance the physical and chemical efflorescence effect. The gravity density of the effloresced rocks can increase from 8kN/m^3 to 20.4kN/m^3; the cohesion of the rocks can be raised to 65kPa from 5kPa, which is quite sensitive to the change of the ground water, thus leading to the drop of the parameters like C and φ, producing more indefinite factors and resulting in such geological problems as slippage, landslip, cracking, etc.

Implementation plans

Through the geological prospection and the hydrological conditions survey in the real engineering project, combined with the results of drainage pipes with finite element analysis, the specific buried project of deep drainage pipes is identified. Moreover, according to the characteristics of deep drainage, the technology and the control requirements of corresponding construction are established.

(1) Taking into account of the constructional conditions, 100mm-hole in diameter is recommended.

(2) Taking into account of the potential risks induced by the sliding strip and the effloresced intermediate zone, the hole shall go through the calculated sliding arc in length and be 3 to 5m deep into the bedrock. In this project in discussion, the hole is defined as 10 to 35m deep. The average value is 25m.

(3) According to the water level, the flow rate and the flow velocity, Computable diving for a radius of affected water diversion is 3.5 to 6.5m. When the holes on the two sides fall in the seepage scope, in the light of the results of the finite element analysis, the optimum hole distance is 7m.

(4) Adopt the double-row drain hole setup plan. The distance between the upper and the lower row is 12m. Since it is better to set the holes in the center of the Diving water network "channels", the holes in the two rows shall be arranged in a staggered way, forming an Abatis.

Constructional techniques

Survey and plan —→ Dig holes —→ Take out the tubes —→ Fix the drainage pipe and the tube—→Remove the machine and finish other follow-up work

Since the external surface of the cutting slope is greatly effloresced, it will maintain wet for some time after the water from the hill has drained away. Thus, after the deep drain holes are accomplished, we should increase the arch-like frameworks, with turf stuck inside to effectively ensure that the water in the hole drains away along the intercepting water curb in the framework, and meanwhile, to avoid the partial collapse of the cutting slope due to water immersion. The turf can lower the possibility of further effloresce.

Quality control

(1) We can adopt the submersible drilling dry holes to make the holes. Ensure that the hole diameter is 100mm, with the difference value at ±1~2mm.

(2) To avoid the collapse of the holes and ensure that tubes can be smoothly fixed, it is necessary to adopt the circulation drilling methods in the process of making holes.

(3) After the installation of the seepage pipes is accomplished, take out the tubes without affecting the seepage pipe.

(4) The hole shall be slightly tilting upward horizontally, with the obliquity controlled between 2° to 3°. Ensure that the hole stretches to the point designed ahead in depth.

(5) The difference value of the hole length shall be controlled within the scope of ±5cm.

Cutting slope monitoring analysis

1) Deployment of the monitoring system

Taking into account of the destructive mechanism, the conditions for stabilization, the integral stability and the partial stability, K39+300, K39+330 and K39+380 are defined as the three monitoring sections for stability analysis. On each section, there should be three to four monitoring points, with more or less the same distance between every two points. The monitoring point should be marked on the section in obvious places using concrete. Set up the hole with inclinometer that is 6m, 12m and 15m long.

2) Monitoring over the displacement of the slope surface

After the drain pipes are fixed, we have monitored the three sections for 18 months using GPS techniques, during which period, the measurement was carried out for 6 times. For the monitoring results, refer to picture 2-4.

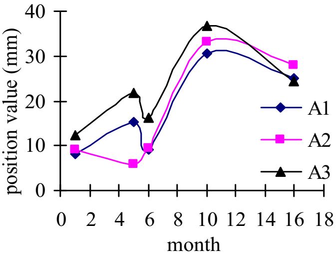

Figure 2 the section of K39 +300

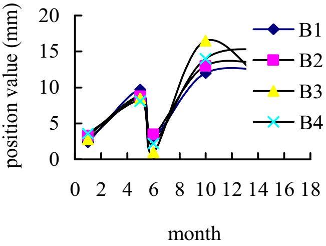

Figure 3 the section of K39 +300

After the drain pipes were fixed, we monitored the three sections for 18 months using GPS techniques, during which period, the measurement was carried out for 6 times. In the first-time measurement, we fixed the coordinate of the datum mark. The results of the follow-up measurements are the relative displacement value to the datum mark. The measurement results showed that the slope was just slightly deformed, and that there was a trend of palliation.

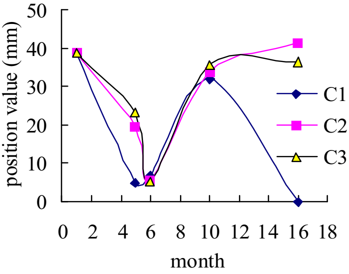

Figure4 the section of K39 +300

Since the beginning of October, deformation could hardly be found. The largest surface deformation is 41.4 mm, and the largest internal deformation is only 10 mm, all are less than the first order of allowing deformation 123.75 mm of 0.0025*h* (*h* is the height of slope). Thus slope stability is ensured.

3) Changes of the Measurement of ramps

The measurement of ramps were monitored 8 times from October 2006 to May 2007. For the monitoring results, see picture 5, 6 and 7.

From the pictures, we know that the internal part of the slope is just slightly deformed. The maximum displacement value is 10mm, appearing at the point of 2m to the end of 6m-long inclinometer pipe. Since the allowable difference value is ±10mm, it can be confirmed that the slope is quite stable and the drain pipe functions well.

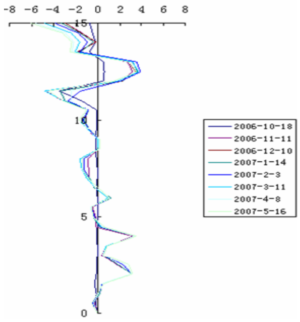

Figure 5 the inclinometer data of 15m

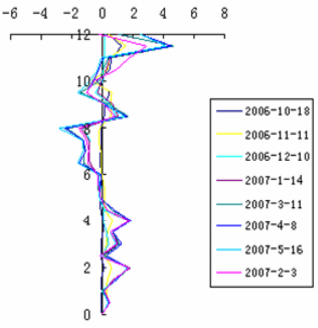

Figure 6 the inclinometer data of 12m

As the diameter diminishes, the water level in the hole will drop and the water head will maintain low, which can enhance the internal stress of the rock. As the cracks of the rock become dry and full, the performance of the rock will improve. However, the seepage along the cracks still exists, which can make the slope surface wet for a long time. Thus, surface preservation activities like preventing from efflorescence and exfoliation are indispensable.

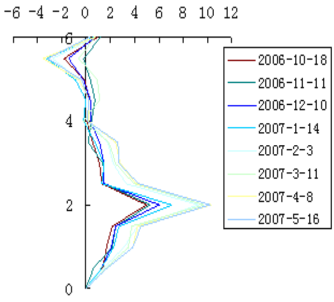

Figure 7 the inclinometer data of 6m

CONCLUSIONS

The deep drainage method can effectively drain away water. The water head in the water-level monitoring hole should be kept lower than the pre-determined value. Although problems like edge crashes and joint development may occur, there is no trend of collapse. Deformation is not found through the monitor over the inclinometer hole.

REFERENCES

Chen S H, Wang W M, She C X,etc. (2000)Unconfined seepage analysis of discontinuous rock slope[J].Hydrodynamics Ser.B, 23(3), 60~66.

Fipps, Get al. (1986)Drains as a boundary condition in finite elements, Water Resources Research, 22(11), 57~60.

Mechanism Analysis and Treatment of Landslide of Changtan New River

Jinshan Lei[1], Junsheng Yang[1], Dadong Zhou[2], Zhiai Wang[2]

[1] Central South University , School of Civil Engineering and Architecture, 22# South Shaoshan Road, Changsha 410075, P R China;jslei@mail.csu.edu.cn
[2] China Hydro Mid-South Design & Research Institute, Changsha, 410014, P R China

ABSTRACT: Due to the continual rainfall and creep deformation occurring to the slope on left bank of the new river in the flood control projects in Liye west of Hunan, and a serious landslide was likely to occur to the slope. Based on the analysis of the mechanism of landslide and slope stability, and the stratum layer parameter inversion carried by the Least Square method, we finally decided to use pre-stressed cable and anchor for the treatment to the slope. The monitoring result indicated that this treatment plan is reliable and safe.

INTRODUCTION

The ancient town of LiYe is located in the middle of the central reservoir area of the WanMi hydropower station of YouShui River, on the left bank of YouShui river . The flood prevention project of the town, subordinate to the reservoir project, consists of flood prevention dike, tunnel, dam and the new river. Changtan new River from 0+300 to 0+830 has undergone the test of rainy seasons and flood seasons thoroughly after completion. Creep deformation was firstly found on the slope from 0+480 to 0+530 on the left bank, and landslide cracks were found on the slope of pile 0+460 later, as shown in Fig.1 and Fig.2.

Fig.1. Slope with creep deformation on the left bank (0+480~0+530)

Fig.2. The muddy sandwich in the terrain of the landslide(0+460)

ENGINEERING GEOLOGY AND HYDROGEOLOGY

Topography

According to the topography, the new river can be divided into three parts: entrance part, middle part and exit part. The middle part is located in the combination part of the II and III class bands and the hills; the shape of the valley is shaped like "V"; and the valley floor is 250~257m high and 5~17m wide. The slopes on both banks can be divided into two parts: the upper-part and the under-part. Most of the slope on the both sides of the under-part near the valley floor is steep, and forms an angle of about 60 degrees; the slope is 3~14m high. In the upper-part, the slope on the right bank consists the II, III class bands, 5~12m high, and forms an angle of 20~50 degrees. The left bank is a hill slope with a gradient between 20 to 40 degrees.

Formation Lithology

In the middle section of the new river, the bed rock is mostly exposed to the air and relatively complete, On the depth of the severely weathered sandstone shale on the 9th layer is 1 ~ 7m ,the depth of the slightly weathered sandstone shale on the 10th layer is 0.5~5.58m. In this section, the rock occurrence is 10°~60°/NW<20°and the slopes on both valley banks are inclined. The quaternary loose accumulation in the section is mainly the broken stone on the 8th layer, scattered, generally 0.5~1.0m deep, and in a few gullies the maximum thickness reaches to 3m. After excavation, the geological plane figure of slope is shown in Fig.3.

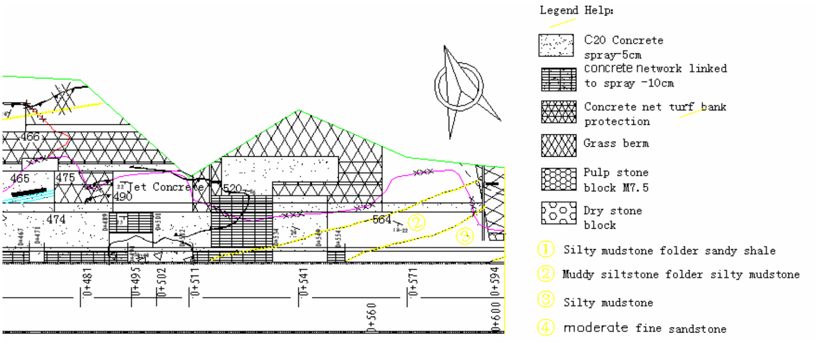

Fig.3. Engineering geological plane figure of the Changtan new river slope (0+400~0+600 section)

Physical and Mechanical Properties of Rock and Soil

We mainly got samples of slightly weathered sandy shale for tests on the physical and mechanical properties, with the results as shown in Table 1. Because of the limited conditions, we failed to identify and take the weak sandwich, and thus could not provide the location and mechanical parameters of the sandwich.

Table 1. Physical and Mechanical Index of the Rock

indicators layer		Specific gravity	Dry density (KN/m^3)	Saturated water absorption (%)	Compressive strength (MPa)
slightly weathered sandy shale	The scope of value	2.69~2.80	24.07~24.71	2.44~4.98	3.8~10.2
	Average value	2.75	24.4	3.82	7.9

Hydro-geological Conditions

The location has the subtropical monsoon climate: warm, humid and rainy; and the rainy seasons last from April to August. The groundwater mainly consists of the upper water of the quaternary layer and fractured bedrock water, and mainly comes from precipitation; the water level and quantity are greatly affected by season, groundwater was found at the foot of the hill on an altitude of 252.5m when we were investigating. According to the analytical results of the water sample, the groundwater has no corrosive effect on the concrete structure.

ANALYSIS OF LANDSLIDE MECHANISM

Natural Factors

The disadvantageous rock layer structure: The slope is located in the area where the rock is muddy shale, water-soft *and* collapse, and there is muddy sandwich in the shale, as shown in Fig. 2, which provides a good sliding surface for the slope out of mechanical balance. The water, especially the water from paddy fields, seepages from the top of the slope to accelerate the speed at which the rock becomes soft, causing the creep deformation. The characteristic that the slope rock tendency is in line with the slope tendency also provides a precondition for the massive landslide slip.

Because of the continual heavy rain before landslide, the groundwater environment was worsened, which reduced the stability of the slope, On the one hand it increased the glide strength of the slope, on the other hand generous surface water permeated through slipping surface into the slippery body, softening the body of rock, greatly reducing the intensity of cutting of the slippery body, accelerating the destroy of slope and aggravating the sliding.

The above adverse natural factors provided basis for the landslide.

Human Factors

Because of the excavation of the new river, a deep-cutting formation, which was 26m wide at the bottom, 8~15m high on the backs, the anti-slide section of the slope was partly destroyed, which meant to destroy the mechanical balance of the slope. And it also provided a leisure face for the slope to form a new landslide. Because of the leisure face, the front page of the slope will be firstly out of mechanical balance in unfavorable conditions described above, which will cause the upper part of the slope to slide. Then gradually the whole slope will be out of balance and finally form a landslide.

In sum, besides the natural stratum geological condition of the Changtan new river slope, excavation and precipitation caused its landslide.According to the analysis of its causes and characteristics, the landslide is a traction-landslide, which should be taken into fully account in the future landslide rectification.

STABILITY ANALYSIS OF LANDSLIDE

Identifying Slip Surface

The slope has undergone several design changes, and the slope ratio has been changed from 1:0.75 to 1:1.5. But it still has the tendency to slip, mainly due to the inaccurate judgment of the location of the sliding surface and geotechnical parameters.

In this exploration we still failed to get the weak sandwich, but we could accurately identify the burial depth of the weak sandwich according to the rock and soil taken out from the drillings. According to the cracks on the top of the slope and the location of the cutting outlets of the landslides and the situation of the drillings, we found the rough location of the sliding surface on the profiles above, as shown in Fig.4~Fig.6.

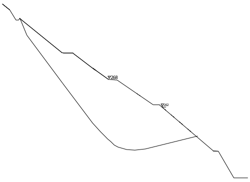

Fig.4. Determined sliding surface (0+460)

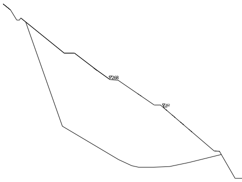

Fig.5. Determined sliding surface(0+480)

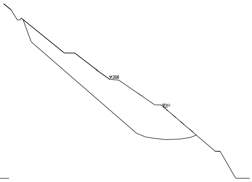

Fig.6. Determined sliding surface(0+510)

Identifying the Anti-shear Parameters

Identifying the slip-shear parameters of the rock and soil on the sliding surface is the basis of stability analysis of landslide; here the landslide stability inversion analysis method is adopted to identify the slip-shear parameters and the sensitive analysis on slip-shear parameters is also carried out.

I Get the sliding surface through geological survey, and divide the sliding body into blocks according to the situation of the slope and the sliding surface.

II Measure the slip-angleα,slip-length L, and slip-weight W by AutoCAD.

III According to the Geotechnical Engineering Investigation norms, suppose the safety coefficient K to be 1.0, adopt Calculating Equality 1 to set up the linear equation about $\tan\varphi$ and C:

$$K=\frac{\sum W_i\sin\alpha_i\cos\alpha_i+(\sum W_i\cos^2\alpha_i+\sum Wj\cos^2\alpha j)\tan\varphi+\sum(L_i\cos_i+L_i\cos_i)c}{\sum W_j\sin\alpha_j\cos\alpha_j} \qquad (1)$$

IV If you want to calculate n profiles, then you will get n linear equations, expressed with matrix as follows:

$$\begin{bmatrix} a_{11} & b_{11} \\ a_{21} & b_{21} \\ \vdots & \vdots \\ a_{n1} & b_{n1} \end{bmatrix}_{n\times 2} \begin{bmatrix}\tan\varphi & c\end{bmatrix}=\begin{bmatrix} c_{11} \\ c_{21} \\ \vdots \\ c_{n1} \end{bmatrix}_{n\times 1} \quad A=\begin{bmatrix} a_{11} & b_{11} \\ a_{21} & b_{21} \\ \vdots & \vdots \\ a_{n1} & b_{n1} \end{bmatrix}_{n\times 2},B=\begin{bmatrix} c_{11} \\ c_{21} \\ \vdots \\ c_{n1} \end{bmatrix}$$

The result worked out by the least square method can be got by A/B in MATLAB quickly as follows: c=20.67kPa, φ =18.060°

Sensitivity Analysis of Parameters

Carry out the sensitivity analysis on c and φ , as shown in table 2. .The sensitivity of friction angle was great. In combination with the similar engineering experience, as the horizontal deformation reached to 111mm on the profile, the value c is appropriate between 5 kPa and 20kPa, and the friction angle φ is appropriate between 9 degrees and 20 degrees. The actual situation can be reflected when C equals to 20kPa and φ equals to 18 degrees under the conditions without the influence of heavy rain etc.

Table 2. Parameter Inversion and Sensitivity Analysis of the Rock on the sliding Surface

C(kPa)	18	20	9	10	5	5
φ (°)	18	18	20	20	21	22
Safety factor	1.006	1.03	0.991	1.002	0.993	1.042

TREATMENT

According to the analytical data and considering field conditions, construction and technical conditions, the cable and anchor combined supporting program as follows was adopted: a anchor supports the superficial section of the landslide; a pre-stressed cable supports the internal section of the landslide; and the displacement of the sliding body can be well controlled, so the width of the crack can also be well controlled, which is favorable to the waterproofing effect on the strengthening body. The main profiles strengthened are as shown in Fig.7. and Fig.8. And the designs of waterproofing, drainage and grouting enforcement of the landslide are also applied.

Waterproofing: fill all the kinds of existing cracks on the surface. In the landslide area, the cracks were filled with clay, tamped and then covered by mortar.

Drainage: built drainage holes, top gutters and hill gutters to set up a perfect waterproofing and drainage system. Set up two kinds of soft water pipe scuppers, the depth of which was separately 8m and 5m; the angle of gradient was 5 degrees; the diameter was 80mm.

Grouting and reinforcement: adhere the crack in order to enhance the anti-slide function of the slope and prevent the ground water from penetrating and gathering. Simultaneously the construction can be operated conveniently. According to the weathered and broken situation of the rock, the static pressure grouting can be properly carried out to the weathering layer before drilling, and the pressure should be no more than 0.3MPa.

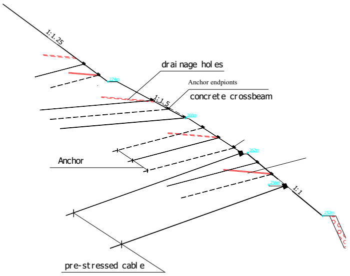

Fig.7. Cable and anchor combined support of deep slide

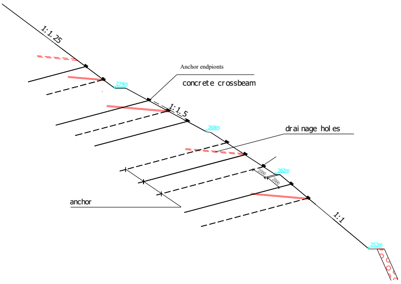

Fig.8. Anchor support of the superficial slide

CONCLUSIONS

Besides the natural stratum geological condition of the Changtan new river slope, Excavation and precipitation caused its landslide.

It is a key step to determine sliding surface and select geotechnical parameters of the rock in sliding zone for analyzing safety of the landslide. Here,using the least square method to carry on inversion analysis of the geotechnical parameters of the rock in the sliding zone is helpful to improve the reliability of the results.

Based on these analysis and calculation, we adopted that anchor supports the superficial section of the landslide, and pre-stressed cable supports the internal section of the landslide. The monitoring results show that the landslide is effectively controlled; and the safety of the slope and river is ensured.

ACKNOWLEDGEMENTS

The work was supported by Hunan Provincial Natural Science Foundation of China. The support is gratefully acknowledged.

REFERENCES

David Jarman.(2006) "Large rock slope failures in the Highlands of Scotland: Characterisation, causes and spatial distribution"*Engineering Geology*, 83(1-3): 161-182

D. Kinakin, D. Stead.(2005) " Analysis of the distributions of stress in natural ridge forms: implications for the deformation mechanisms of rock slopes and the formation of sackung"*Geomorphology*, 65(1-2): 85-100

J. Kodama, E. Nishiyama, K. Kaneko. (2009) . "Measurement and interpretation of long-term deformation of a rock slope at the Ikura limestone quarry, Japan" *International Journal of Rock Mechanics and Mining Sciences*, 46 (1):148-158

R.J. Pine, W.J. Roberds. (2005)" A risk-based approach for the design of rock slopes subject to multiple failure modes—illustrated by a case study in Hong Kong" *International Journal of Rock Mechanics and Mining Sciences,* 42 (2):261-275

Mechanical Analysis of Retaining Structure Considering Deformation and Validation

G.X. Mei[1], L.H. Song[2], and J.M. Zai[3]

[1]Professor, College of Civil Engineering and Architecture; Nanchang Hangkong University; Nanchang 330063; meiguox@163.com
[2]Ph. D. Department of mechanics, Nanjing University of Technology, Zhongshan North Road 200, 224#, Nanjing, 210009; h27991@163.com
[3]Professor, College of Civil Engineering, Nanjing University of Technology, Nanjing, 210009.

ABSTRACT: The non-linear relationship between displacement and earth pressure indicates that the earth pressure varies with the displacement, which affects the mechanical analysis of retaining structures. A model, based on commonly observed characteristics of earth pressure-displacement relationship, is developed to describe the relationship between earth pressure and displacement. The solution of the proposed is given in the paper. The comparison between the literature data and the predicted values from proposed model shows that the proposed model provides a good prediction of lateral earth pressure at relatively small displacement. Moreover, the results indicate that the displacement has a significant effect on earth pressures, which justifies the necessity of the proposed model.

INTRODUCTION

With the increased use of underground space, more and more research is being focused on the proper design of deep foundations as well as earth retaining structures. The estimation of the earth pressure magnitude and distribution is one of the necessary steps during the design. This is usually achieved by assuming a linear distribution of earth pressure and using active or passive earth pressure coefficients obtained by limit equilibrium or limit analysis. The influence of different parameters on the earth pressure has been continuously studied to improve the earth pressure theory.

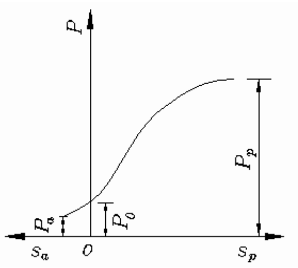

Figure 1. Earth pressure - displacement relationship

The classical form of the relationship between the earth pressure and the displacement is shown in figure 1. As can be seen from the figure, the earth pressure distribution along the retaining structures is dependent on the displacement of the structures. Therefore, if the earth pressure-displacement relationship, shown in figure 1, can be appropriately modeled, the problem of earth pressure can then be solved.

FORMULA OF EARTH PRESSURE CONSIDERING DISPLACEMENT

Characteristics of earth pressure

As mentioned earlier, the earth pressure acting on the retaining structures is different at the different displacement. The main characteristics of earth pressure-displacement relationship, as shown in Figure 1, can be described as:

(1) The earth pressure, at the displacement of $s=0$, is equal to the earth pressure at rest p_0.

(2) The earth pressure, at the displacement of $s=s_a$, is equal to the active earth pressure determined by Rankine's earth pressure theory p_a, which is the minimum value

(3) The earth pressure, at the displacement of $s=s_p$, is equal to the passive earth pressure p_p, which is the maximum value.

(4) The value of p_a decreases with the increase of the displacement of s_a. On the other hand, the value of p_p increases with the increase of the displacement of s_p. s_a is the displacement of retaining structures moving away from soil, and s_p is the displacement of retaining structures moving towards soil. The values of displacements s_a, or s_p for different types of soil and different modes of retaining structures movement can be obtained from Liu & Hou (1997).

(5) There is an inflection point at $s=0$, which is the dividing point between active earth pressure and passive earth pressure. This characteristic of earth pressure - displacement relationship can be mathematically expressed as:

$$\frac{\partial^2 p}{\partial s^2} > 0 \quad \text{(For the active earth pressure, } s<0\text{)}$$

$$\frac{\partial^2 p}{\partial s^2} < 0 \quad \text{(For the passive earth pressure, } s>0\text{)}$$

Formulation

The earth pressure-displacement relationship, as shown in Figure 1, has the form of sigmoid function, which can be expressed as

$$f(x)=\frac{1}{1+e^{-(x/T)}} \tag{1}$$

The sigmoid function has several desirable mathematical attributes, e.g., $f(x)=0.5$, $f(+\infty)=1$, and $f(-\infty)=0$. Moreover, the parameter T in the sigmoid function can be used to describe the property of material. As such, the sigmoid function can be used as the basis function for developing a model to describe relationship between earth pressure and displacement.

Based on the above-mentioned characteristics of earth pressure, the following model was developed:

$$p=\left(\frac{k(\varphi)}{1+e^{-b(s_a,\varphi)s}}-\frac{k(\varphi)-4}{2}\right)\frac{p_0}{2} \tag{2}$$

where p_0 is earth pressure at rest; $k(\varphi)$ is a function of the soil friction angle; $b(s_a, \varphi)$ is a function of the displacement at the active condition and soil friction angle, and $b(s_a, \varphi)>0$; p is earth pressure at a displacement of s.

Solution

In equation (2), there are three unknown parameters of $k(\varphi)$, $b(s_a, \varphi)$ and p_0, which can be determined by two methods. The first one is the back-calculation method in which three parameters are determined from three measured value pairs of the earth pressure (p) and displacement (s), i.e. (p_1, s_1), (p_2, s_2), and (p_3, s_3). Although this method is relatively easy, the three measured pairs of the earth pressure (p) and displacement (s) are not easy to obtain. As such, the second method will be discussed and used in this study. In this method, the values of p_a, p_p and p_0 can be determined from classical theory of earth pressure, e.g., Rankine's theory.

From equation (2), the values of earth pressure at $s=0$, $s\rightarrow+\infty$, and $s\rightarrow-\infty$ can be obtained as:

$$p_{(0)}=p_0 \tag{3}$$

$$p_{(\rightarrow+\infty)}=\frac{k(\varphi)+4}{4}p_0 \tag{4}$$

$$p_{(\rightarrow-\infty)}=\frac{4-k(\varphi)}{4}p_0 \tag{5}$$

Actually, the displacement s ranges between s_a and s_p, and can never approach infinity, The corresponding values of earth pressure at $s= s_a$, and $s= s_p$ can be obtained as:

$$p_{(s_a)}=\left(\frac{k(\varphi)}{1+e^{-bs_a}}-\frac{k(\varphi)-4}{2}\right)\frac{p_0}{2} \tag{6}$$

$$p_{(s_b)}=\left(\frac{k(\varphi)}{1+e^{-bs_b}}-\frac{k(\varphi)-4}{2}\right)\frac{p_0}{2} \tag{7}$$

Assuming: $A=e^{-bs_a}$ (obviously, $A>1$) and $s_p=-15\ s_a$, then

$$p_{(s_b)}=\left(\frac{k(\varphi)}{1+A^{-15}}-\frac{k(\varphi)-4}{2}\right)\frac{p_0}{2} \tag{8}$$

where the value of A^{-15} approaches zero, accordingly:

$$p_{(s_b)} = \frac{k(\varphi)+4}{4} p_0 = p_{(\to+\infty)} \tag{9}$$

Rearrange equation (9) to give expressions for $k(\varphi)$ below.

$$k(\varphi) = \frac{4k_p}{k_0} - 4 \tag{10}$$

From equation (6), the expression for *A* can be obtained as

$$A = \frac{k_p - k_a}{k_p - 2k_0 + k_a} \tag{11}$$

Accordingly,

$$b = -\frac{\ln A}{s_a} \tag{12}$$

VALIDATION OF MODEL

In this section the comparisons are made between the predicted earth pressures from proposed model and literature data, which can be found in Yue et al. (1992).

A series of centrifuge model tests on cohesive soil has been reported by Yue et al. (1992). The soil properties used in their study are summarized in table 1. Some parameters needed for equation (2) are listed in table 2.

Table 1. Soil properties

Parameters	Γ	ρ	w	e	c_u	φ_u
	$kN \cdot m^{-3}$	$g \cdot cm^{-3}$	%		kPa	°
Value	18.7	1.91	16.8	0.663	38.2	24

Table 2. Parameters of experiment

Parameters	N*	k_0	k_a	k_p	b	$k(\varphi)$
Value	80.14	0.593	0.422	2.371	19/*h*	11.0

* Multiple of acceleration of gravity.

The test results are shown in figure 2, where the y-axis is the ratio of the lateral earth pressure (*Ex*) at the arbitrary displacement to the limit earth pressure (E_u), and x-axis is the displacement. These measured data obviously demonstrate that the earth pressure varies with the displacement of retaining structures.

The measured lateral earth pressures of points P15, P16, and P17 in model test M8 were chosen to compare with the predicted values from proposed model. The heights of points P15, P16, and P17 are 9 cm, 10.5 cm, and 12.0 cm, respectively. The comparison between the results of model tests and the predicted values from proposed model is presented in Figure 3. The figure shows that the proposed model provides a good prediction of lateral earth pressure at relatively small displacement. At relatively large displacement, the proposed model generally underestimates the measured values. The measured values appear to become almost constant with the increase of displacement. This is because the displacement exceeds the limit displacement. Therefore, the proposed model is considered good for relatively small displacement.

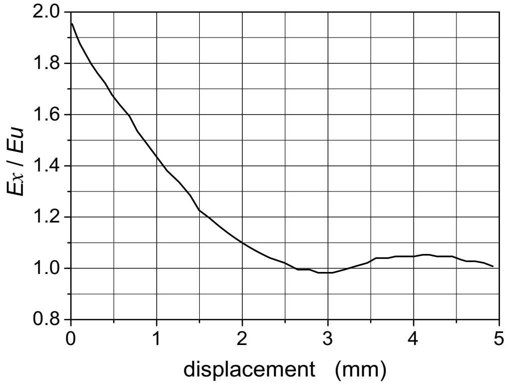

Figure 2. Relationship between earth pressure and displacement

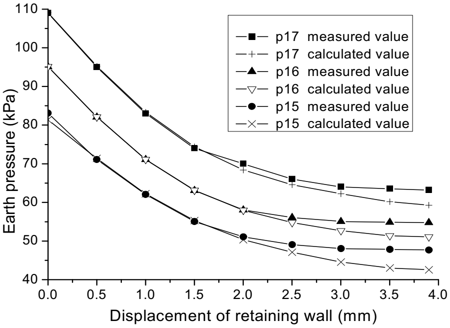

Figure 3. Comparison between measured and calculated values of earth pressure at different displacements

CONCLUSIONS

Based on above discussions, the following conclusions can be drawn.

The displacement of soil has a significant effect on earth pressures acting on the retaining structures. The real earth pressure ranges between the at-rest earth pressure and limit earth pressure.

The commonly observed earth pressure-displacement relationship can be reasonably described by a mathematical model.

The proposed model gives a good prediction of earth pressure for relatively small displacement, which is usually less than the limit displacement.

In a word, the distribution of the earth pressure has its own nature and character. The better design can be achieved in engineering practice if the nature and character of earth pressure distribution is known. It is believed that this paper sets a robust foundation for such studies.

REFERENCES

Zhou, Z.Y. 1990. Experimental investigation of active earth pressure acting on a rigid retaining wall. *Chinese Journal of Geotechnical Engineering*. 12 (2): 19-26.

Fang, Y.S. & Static. 1986. Earth pressure with wall movement. *Journal of Geotechnical and Geoenvironmental Engineering*. 112 (6): 317-333.

Terzaghi. K. 1934. Large retaining wall tests. *Engg News Record*. 11 (2): 112.

Liu, J.H. & Hou, X.Y. 1997. Handbook of excavation engineering. *Beijing*: *China Architecture & Building Press*.

Mei, G.X. & Zai, J.M. 2000. A new formula for earth pressure. *China Civil Engineering Journal*. 33 (5): 79-82.

Mei, G.X. & Zai, J.M. 2001. Earth pressure calculating method considering displacement. *Rock and Soil Mechanics*. 56(1): 83-85.

Li, H.G. 2004. Design and project cases of new type support structures. *Beijing: China Communications Press*.

Gao, J.P. & Wu, J.H. 1995. New study on the earth pressure calculation method. *Journal of Xi'an Highway University*. 15(2): 7-12.

Yue, Z.R. 1992. Centrifuge model tests on lateral pressure on walls retaining compacted clayey backfill. *Chinese Journal of Geotechnical Engineering*. 14 (6): 90-96.

Research on Deformation and Instability Characteristic of Expansive Soil Slope in Rainy Season

Bingxu Wei[1] and Jianlong Zheng[2]

[1] Teacher, Changsha University of Science & Technology School of Highway Engineering; weibingxu555@163.com; 13077346801
[2] Teacher, Changsha University of Science & Technology School of Highway Engineering

ABSTRACT: The analysis of the deformation and instability characteristic for the cutting slope in expansive soil during a rainy season by FLAC software is presented in this paper. The main conclusions are as follows: if the moisture content is increasing, Poisson ratio decreases with the increase of the depth in atmosphere influence zone, while elastic modulus, internal friction angle and cohesion increase on the contrary. However, the changing zone does not extend the atmosphere influence zone. By the moisture increment, horizontal displacement mainly concentrates on the surface because there is no constraint in horizontal direction on free face of the slope. The soil mass located at the toe of the slope reaches saturation state first, as the rainwater filtering into the slope aggregate, and further, to the toe-slope under gravity load, which on the one hand increase the soil bulk density, on the other hand reduce the soil strength after absorbing water. In addition, the shear stress is concentrated on the toe-slope. So slumps occur at the toe-slope first. When it happens, the support for upper slope decreased and the resistance of lateral swelling become weakened, which will cause sliding upwards again, finally engenders the imbricated surface shape.

INTRODUCTION

The instability and slump of expansive soil slope in the rainy season is an important engineering geology problem. Aiming at this problem, many scholars have done a lot of research. Such as Chen [1] solved unsaturated soil seepage differential equation using finite element method (FEM), and obtained humidity field and suction field, he has also done some research on the stability of slope. Fredlund [2] simulated transient seepage process using Galerkin FEM and studied the stability of the expansive soil slope. Liu[3] analyzed the stress of the instable channel slope by FEM. Qin[4] introduced the expansive force regarded as a kind of constant body force into nonlinear FEM, performed the stress and strain analysis of the instability failure mechanism of the expansive soil slope .Yao[5] performed transient seepage analysis and stability analysis of the expansive soil slope filtered with rainwater, based on quantitative description of the expansive soil fracture. However, most researches above are doing stability analyses from mineral and strength characteristics. In this paper, the theory of moisture content field was introduced into equilibrium differential equation and ideal elastic-plastic constitutive equation, and the strength field and deformation field of the expansive soil slope as well as the deformation and instability characteristic of expansive soil slope were analyzed by FLAC software .

THE ANALYSIS METHOD AND MODELING

The equilibrium differential equation of humidity field

The literature[6] gives strain components of expansive soil ε'_{ij}, caused by the increase of moisture content :

$$\varepsilon'_{ij} = \beta \Delta w \delta_{ij} \tag{1}$$

where β =isotropic linear expansion coefficient ; Δw = increment of moisture content ; δ_{ij} =Kronecker symbol; And equilibrium differential equation of humility stress field.

$$\frac{\partial \sigma_{ij}}{\partial x_j} + F_i - \frac{\partial}{\partial x_j}\left[\frac{E\beta\Delta w\delta_{ij}}{1-2\mu}\right] = 0 \tag{2}$$

where c_{ij}= stress components; x_j= coordinate in the j direction; F_i=unit body force in the i direction; E = deformation modulus; μ =Poisson ratio.
Eq.（2）is obliviously similar to the equilibrium differential equation in the theory of temperature field.

Constitutive model considered moisture_content field

According to the landslide survey, the change of moisture content in the atmosphere zone is the mainly cause of the superficial failure of the expansive soil slope. Therefore, if the soil skeleton force caused by moisture content variation is not considered, the ideal elastic-plastic constitutive model[7] can be improved as followed
The ideal elastic-plastic equation of saturated soil is given

$$d\varepsilon_{ij} = \frac{dI_1}{9K}\delta_{ij} + \frac{1}{2G}dS_{ij} + d\lambda S_{ij} \tag{3}$$

where dS_{ij} = deviator stress vector ,the elastic part is

$$d\varepsilon^e_{ij} = \frac{dI_1}{9K}\delta_{ij} + \frac{1}{2G}dS_{ij} = \frac{1-2\mu}{E}d\sigma_m\delta_{ij} + \frac{1+\mu}{E}dS_{ij} \tag{4}$$

and is related with deformation parameters E、μ, the plastics part is $d\varepsilon^p_{ij} = d\lambda S_{ij}$ and is related to flow rule, flow rule is expressed by

$$d\varepsilon_{ij}{}^{p} = d\lambda S_{ij} = d\lambda \frac{\partial f}{\partial \sigma_{ij}} \tag{5}$$

where f = yield function, according to Mohr-Coulomb criteria :

$$f = \frac{1}{3} I_1 \sin\varphi - c\cos\varphi + \sqrt{J_2}\left(\cos\theta_\sigma + \frac{\sin\theta_\sigma \sin\varphi}{\sqrt{3}}\right) = 0 \tag{6}$$

where I_1 = first invariant of stress tensor; J_2 = second invariant of deviator stress tensor; θ_σ =stress Lode angle ; c and φ = cohesion and internal friction angle. The total stress strength[8] are used in this paper, i.e., the total cohesion c_{total} ,and the total internal friction angle φ_{total} , which include contribution of suction and structure of soil to the strength, changing with the moisture content.

It is assumed that expansive soil is isotropic before and after submerged in water, the stress field and humility field is quasi coupling, substituting Eq.(1)into Eq. (3).

$$d\varepsilon_{ij} = \frac{dI_1}{9K}\delta_{ij} + \frac{1}{2G} dS_{ij} + d\lambda S_{ij} + \beta\delta_{ij}\Delta w \tag{7}$$

E、μ 、 c_{total} 、 φ_{total} in Eq.(4) and Eq.(6)are considered as the related field variable of the humility field and the stress field. If these field variables are used in conjunction with Eq.(5), Eq.(6), Eq.(7), constitutive model considering moisture content field is formed.

The governing differential equations are constitute by the Eq. (2) and the Eq.(7) with the geometric equation, compatibility equation and boundary condition. When humility field changes, the stress and strain field, and the displacement field can be got by the governing differential equations and given boundary condition.

BOUNDARY VALUE PROBLEM WITH FLAC SOFTWARE

Determination of the slope failure

The breakthrough of the plastic zone and mutation of the displacement are features of the slope destruction. Therefore, In this paper, the displacement of feature point and breakthrough or not of the plastics zone are integrated as the criterion of the slope deformation.

FLAC geometric mode

Fig.1 shows an expansive soil cutting slope of the expressway from Nanyang to Dengzhou, with a height of 14m and a gradient of 1:1.5. The slope height of calculation scope is 7m, and 5m on the left, 20m on the right. the unit weight of soil is 16kN/m^3.The calculation model is considered as plain strain problem. The boundary conditions consist of roller boundaries on the left and right sides of the model as well as fixed base. The atmosphere influence depth in Nanyang is 2m. The calculation parameters include the strength parameters C_{total}, $\phi_{total}$and the deformation parameters E、μ 、 β .

DEFORMATION PARAMETERS OF EXPANSIVE SOIL

Humility expansion coefficient

The expansion rate caused by increase of the unit moisture content can be defined as loaded expansion coefficient β , when initial moisture content and the upper load are defined. Expansive coefficient of Nanyang expansive can be got of Nanyang expansive soil can be got by adopting lateral restricted swelling experiment, given by

$$\beta = (9.3215 w_0 - 0.6344) e^{-((0.2329 e^{-21.85 w_0}) \times p)} \tag{8}$$

where w_0 =initial moisture content (%); p =upper load (Pa)

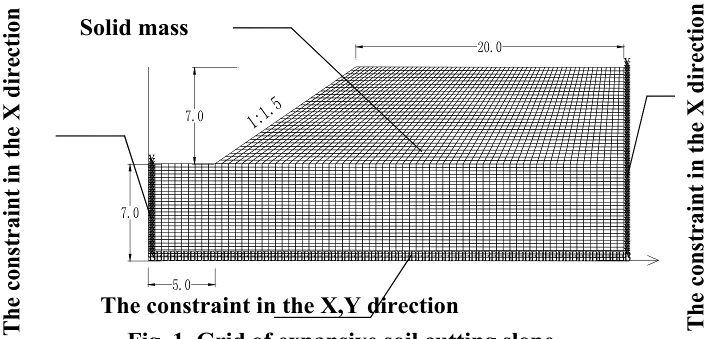

Fig. 1. Grid of expansive soil cutting slope

Model parameters for numerical analysis

The change of moisture content field in expansive soil cutting slope is resulted from rainwater infiltration, which leads to softening of the elastics modules E and Poisson ratio μ .

By triaxial test, results show that under the condition of different moisture content and volumetric stress, the deformation modulus E and Poisson ratio μ of Nanyang expansive soil can be expressed as follow:

$$\mu(p,w) = 0.002p + 0.50 - \frac{-\ 0.35}{1 + e^{(w-0.22508)/0.4231}} \tag{9}$$

where w = moisture content (%); p =upper load (Pa) $\mu =$ Poisson ratio

$$E(p,w) = (-15.206 w^2 + 4.7889 w - 0.1959) \cdot p + (-447.48 w + 121.9) \tag{10}$$

where w =moisture content (%); p =upper load (Pa); $E =$ deformation modulus(MPa)

Strength parameters of expansive soil

The results of laboratory direct shear test for Nanyang expansive soil are compared to those of in-situ direct shear test by author, considering the in-situ construction factors. Then the reduction factors between soil mass and soil block of Nanyang expansive soil are proposed, with reduction factor of internal friction angle of 1/7 and that of cohesion of 1/14. That is similar to the conclusion of the scientific project of ministry of railway(85-I-52 the basic properties of cracking soil and technical conditions used in embankment, cutting and slope engineering).

Under the condition of different moisture content w, the cohesion c and internal friction angle φ of Nanyang soil block can be expressed as the follow.

$$c_{total} = 610e^{-7.0535w} \tag{11}$$

Where $w =$ moisture content (%); $c =$ Cohesion (kPa)

$$\varphi_{total} = 424.22e^{-10.505w} \tag{12}$$

Where $w =$ moisture content (%); $\varphi =$ Internal friction angle(°)

Crack developed expansive soil in the atmosphere influence zone is proposed to adopt soil mass strength, That is to say, Eq. (11), (12) are multiplied respectively by the reduction coefficient. Soil block strength is adopted by crack -undeveloped expansive soil which lies in deep body of slope.

THE ANALYSIS OF SIMULATION RESULTS

The moisture content field distribution

The temperature module in FLAC is used to analyze the distribution of moisture content. It is assumed the natural moisture content of soil mass is 25%, and the rainwater mainly affect in the atmosphere zone, the soil on the surface reaching the saturated moisture content of 35%. When rainwater infiltrate deeply to the internal boundary of the atmosphere influence zone, that is to say, the moisture content of boundary is up to 25.5%, the seepage is over. So a moisture content field in Fig.2 is formed in the slope.

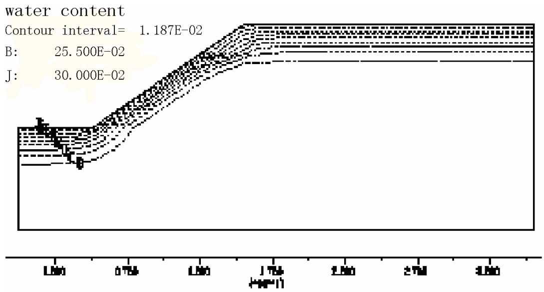

Fig. 2. Moisture Distribution in cutting slope

The distribution of the strength parameters

The strength parameter is a very important index in numerical analysis, which decides distribution and adjustment of stress for slope body, resulting in production of the various elastics-plastics zone.

However, the development of elastics-plastics zone distribution and the stress state are commonly taken as standard of instability or not of the slope.

Fig.2 shows that moisture content distribution of inner slope body is various with the depth. The Eq.(11), (12) are programmed to achieve the distribution of the strength field of slope body, which is showed in Fig.3,Fig.4.

Fig.3 shows cohesion of the expansive soil reduces from 56Kpa in the slope to 6Kpa on the surface. And Fig.4 shows friction angle of the expansive soil reduces from 21° in the slope body to 3° on the surface. According to some paper , cohesion can reaches over 200Kpa and friction angle can reaches 40°～60°,when expansive soil samples are in natural dry state. But when moisture absorption of the sample is up to the expansion limit moisture content, the shear strength decreased quickly, c ranges from 0 to1Kpa, even $c = 0$. φ ranges from 1° to 3°.

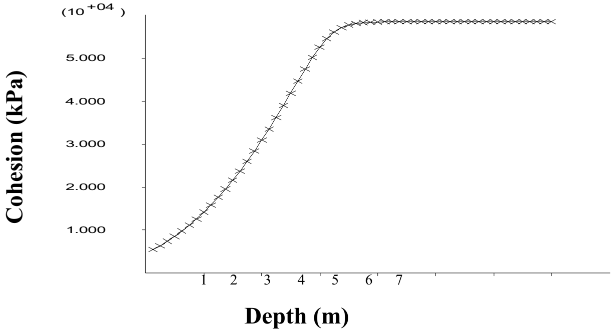

Fig. 3. Cohesion variation with the Depth

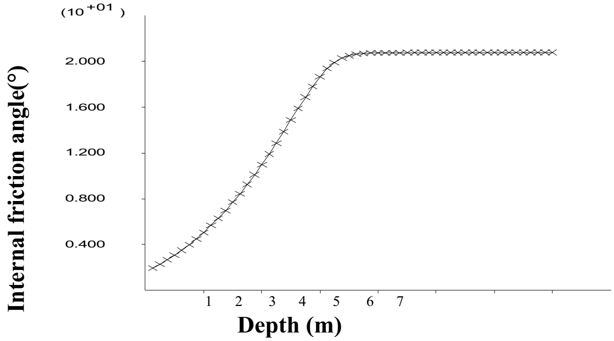

Fig. 4. Internal friction angle variation with the Depth

The distribution of the deformation parameters

The diffusion of moisture content in expansive soil is coupled with moisture absorption, absorbing moisture force and volume deformation, which results in changes of elastic modulus, Poisson's ratio and expansion coefficient. The different distribution of the deformation parameters of slope body varies with the moisture content in different zones, which is showed in Fig. 5, Fig.6, and Fig.7.

Fig.5 shows Poisson ratio decrease with increase of depth, this is because the moisture content is not influenced in a certain depth of slope body where poisson ratio does not change, when moisture absorption decreases quickly from the surface to the inner of the slope. So do Young's modules. Fig.6 shows the Young's modules increase from the surface to a certain depth of slope body, because of Young's modules of the expansive soil decreasing with increase of the moisture content, and the highest absorbing moisture content is on the surface with the lowest Young's modules, which results from the little variation of moisture content in a certain depth of slope body and the tendency to the fixed value of Young's modules.

Fig.7 shows the surface expansion coefficient which decreases with increase of the depth show a complex variety curve, which is caused by the moisture content and the stress state.

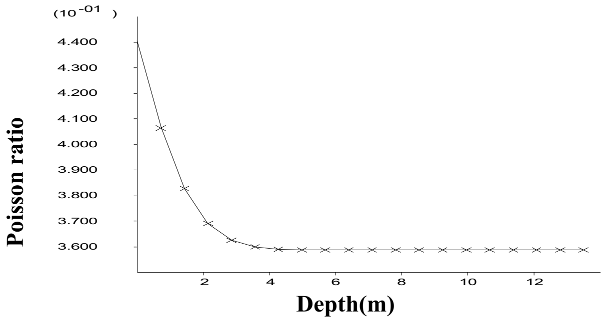

Fig.5. Poisson ratio variation with the Depth

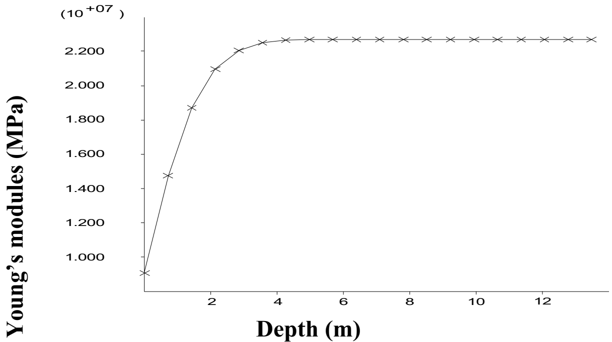

Fig. 6. Young's modules variation with the Depth

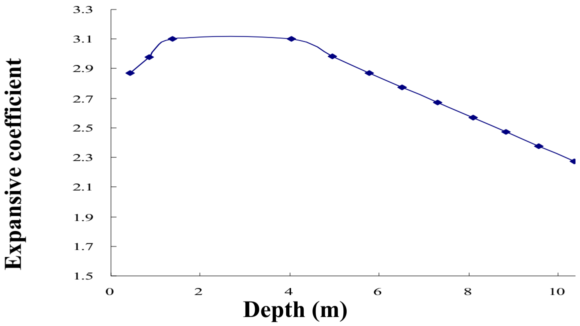

Fig. 7. Expansive coefficient variation with the depth

THE ANALYSIS OF DEFORMATION PROPERTIES

A certain degree of deformation which is the precursor of the slope destruction will cause the disintegration caving and back falling of the slope. It is important to study deformation properties and destruction mechanism, and learn the destruction law of the cutting slope, and to prevent from the deformation destruction. Fig.8-13 show deformation and destruction state of expansive soil slope in rainy season.

Velocity contour of destruction state of soil cutting slope is computed by the method of strength reduction, (Fig. (8)). Fig.(9) shows the distribution and breakthrough of plastics zone. Both figures are combined to analyze ,the results show the largest velocity value appears at the slope toe (Fig.8) which the shear yielding state lies in ,and tension yielding state (Fig.9) of the slope top is found. Therefore, when shear yielding in the slope toe and tension yielding on the top of slope are appeared, the instability of the slope is obviously. The cause of sliding surface appeared in the atmosphere influence zone is that the soil in that zone experiences alternating dry-wet cycles and own therefore, developed cracks , and under the action of rainwater infiltrating, the suction decrease, and the shear strength reduces.

The displacement contour got by the method of strength reduction is showed in Fig.10, when the slope destruction is formed. The lateral uplift displacement occurs mainly on the surface of the slope because of the increase of the humility and moisture swelling. On the other hand, the horizontal displacement is mainly concentrated on the surface and lies in the shallow layer; because there is no constraint in the horizontal direction on the slope surface. When the deformation in the destruction zone is too large, the soil mass may have progressive destruction, which is the reason that the expansive soil often has the shallow crushing and slumping.

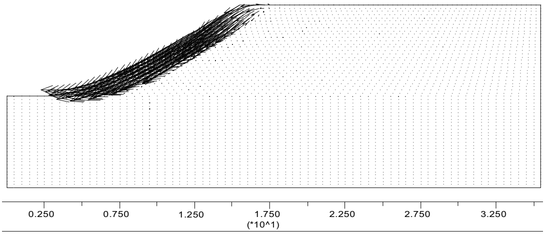

Fig.8. Velocity field of expansive soil cutting slope in the destruction state

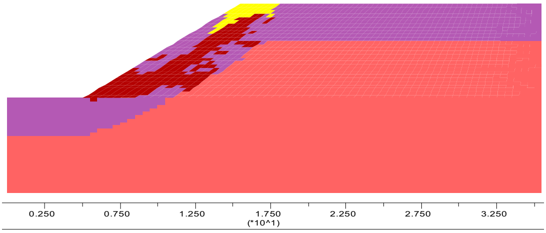

Fig.9. Plastic zone of expansive soil cutting slope in the destruction state

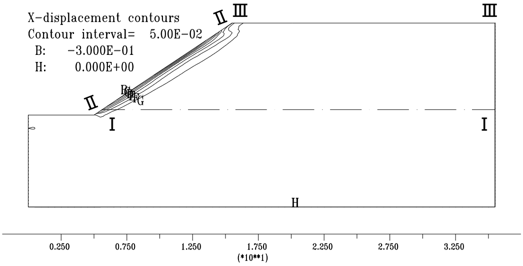

Fig.10. Displacement field of Expansion soil slope in the destruction state

Figs.11-13 show I-I section, the II-II section, the III-III section of the horizontal displacement curve of expansive soil cutting slope in Nanyang-Dengzhou expressway, where negative displacement means uplifting I-I section represents horizontal profile near the toe of the slope, II-II section represents the surface of the slope, and the III-III section represents the ground line on the top of the slope. The data in the figures display changes of the horizontal displacement in three different stages which are gravity balance stage, excavation finished stage and moisture absorbing and expansion stage. And lateral uplift displacement of three sections is formed during the excavation stage and the moisture absorbing and expansion stage. The displacement during the moisture absorbing stage is much larger than that in the excavation stage because of wet expansion effect. The uplift displacement increases quickly in the atmosphere influence zone, reaching its max at a surface zone of 2/3 length of slope. It is easy to find that the increase of moisture content is the main reason of the deformation of the slope.

CONCLUSIONS

The softening of the strength parameters and deformation parameters are resulted from hygroscopic expansion of expansive soils in the atmosphere influence zone, which leads to instability and deformation of cutting slope of expansive soils.
Lateral heave displacement of cutting slope of expansive soil is formed during the excavation stage and moisture absorbing and expansion. However, the effect of the moisture absorbing and expansion is much more than that of the excavation.

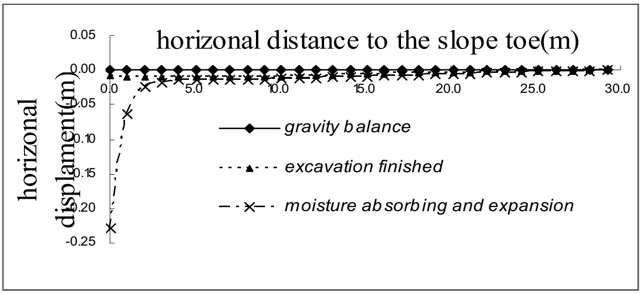

Fig.11 Horizontal Displacement of I-I Section vs. Depth

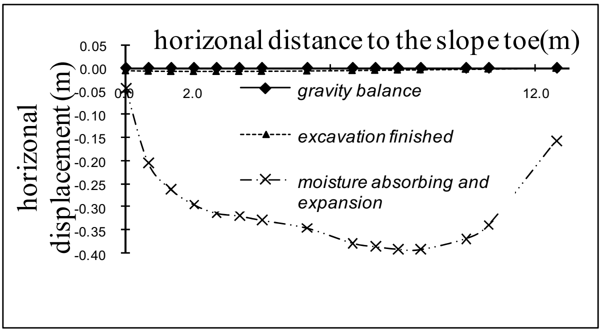

Fig.12. Horizontal Displacement of II-II Section vs. Depth

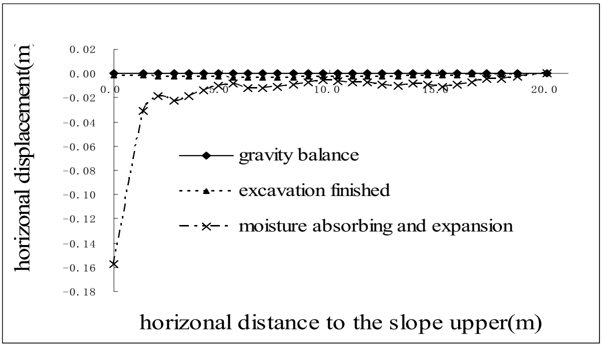

Fig.13. Horizontal displacement of III-III Section vs. Depth

REFERENCES

Chen Shouyi.(1997). "A Method of Stability Analysis Taken Effects of Infiltration and Evaporation into Consideration for Soil Slopes". *Rock and soil mechanics*. VOL.18(2):8-12

Fredlund D G, Rahardjo H(1993). " An overview of unsaturated soil behavior" . *A.Proceedings of sessions of Dallas[C].texas:[s.n.]*, 24-28.

Liu Zude, Kong Guanrui(1993); "Analysis on Canal Slope Excavated in Expansive soil by FEM" *Journal of Wuhan University of Hydraulic and Electric Engineering*. VOL.26(3):237-244

Qin Lu-sheng; ZHENG Jian-long(2001); "Analysis of surficial failure mechanism of expansive soil slopes with FEM" *China Journal of Highway and Transport*.,VOL.14(1):25-30.

Yao Hai lin; Zheng Shaohe; Chen Shouyi (2001). "Analysis on the slope stability of expansive soils considering cracks and infiltration of rain". *Chinese Jounal of Geotechnical Engineering*.VOL.(23)5:606-609.

Li kangquan, Zhou zhigang. (2006). "Numerical Investigation and Analysis for seepage field of unsaturated soil" *Journal of China & Foreign Highway*. VOL.26(3):29-30.

Yang guitong(2006). "Introduction to elasticity and plasticity" *M.Tsinghua University press*. 2006.1:67-77.

Wang Zhi-wei; Wang Geng-sun(2005). "FLAC simulation for progressive failure of fissured clay slope" *Rock and Soil Mechanics*. 26(10):1637-1640.

Dual-control Method to Determine the Allowable Filling Height of Embankment on Soft Soil Ground

Li-Min Wei[1], Qun He[2], and Bo Rao[3]

[1]Professor, School of Civil Engineering and Architecture, Central South University, Changsha City, Hunan Province, China 410075; lmwei@mail.csu.edu.cn
[2]Doctor, School of Civil Engineering and Architecture, Central South University, Changsha City, Hunan Province, China 410075; hequn@mail.csu.edu.cn
[3]Engineer,Guangdong Metallurgical and Architectural Design Institute, Guangzhou City, Guangzhou Province, China 510080; csu507@126.com

ABSTRACT: In order to plan rationally the construction process of embankment on the soft soil ground, the information construction technology to determine the allowable filling height of embankment was proposed, which is based on slope stability and allowable settlement after construction. The correlative program had been developed. The method of effective consolidation stress was adopted to analyze the stability of the embankment and the enhancement of the sheer strength of the soft ground with its consolidation process was taken into account. Method that modifies the degree of consolidation using the monitored settlement was proposed too. All these were performed to the practical case and the results show that the dual-control method proposed is effective and practicable to guild the information-construction of embankment on soft soil ground.

INTRODUCTION

In China, the method that 'thin stratum placement step by step' is used widely for construction of embankment on the soft ground. However, the stratum thickness and filling time usually determine empirically. For example, if the rate of settlement at ground surface under the midline of the embankment is no more than 1.0cm/day and the rate of horizontal displacement at the slope toe is no more than 0.5cm/day (MOC, 1997), the next stratum can be filled. For guiding the construction of embankment on soft soil ground rationally and concretely, the Dual-control Method to determine the allowable filling height was proposed in this paper.

METHOD TO DETERMINE THE ALLOWABLE FILLING HEIGHT

Calculating the Stability Factor Using Effective Consolidation Stress Method

The circular arc analysis is adopted usually to analysis the stability of the embankment in practice (Ning-Hu company, 2001). In this paper, the effective consolidation stress method was performed to analyze the stability of the embankment, in which the strength increasing of the soft ground with its consolidation was taken into account, so that the construction process simulated factually.

The main idea of the effective consolidation stress method is calculate the strength increasing caused only by compress, and that caused by shear is neglected. It's expressed

$$\Delta\tau_f = U\sigma_Z \tan\varphi_{cu} \tag{1}$$

where, $\Delta\tau_f$ is the strength increment of soft ground; U is the degree of consolidation of soil; σ_Z is additional stress in soil; φ_{cu} is angle of internal friction tested by consolidated undrained triaxial compression test.

Fig.1 illustrates an embankment on the soft ground, the subscript I indicate the ground and II for embankment. Slip circle ABC through the embankment and the ground. The soil slice at the left of B is numbered by *i* and by *j* at its right.

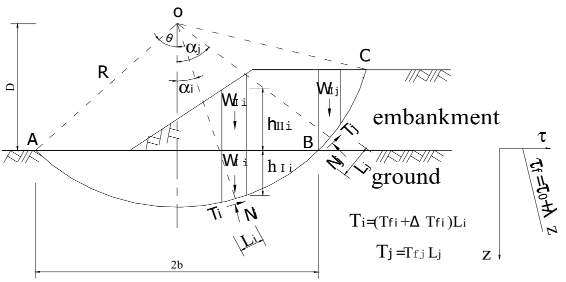

Fig. 1. Calculating sketch of the effective consolidation stress method

According to the basic principle of the effective consolidation stress method, the stability safety factor can be calculated as follow:

$$F_S = \frac{2R[(\tau_0 - \lambda D)\theta + \lambda b] + \sum_A^B U_i \sigma_{zi} l_i tg\varphi_{cu} + \sum_B^C (c_{\mathrm{II}} l_j + W_{\mathrm{IIj}} \cos\alpha_j tg\varphi_{\mathrm{II}})}{\sum_A^B (W_{\mathrm{I}} + W_{\mathrm{II}})_i \sin\alpha_i + \sum_B^C W_{\mathrm{IIj}} \sin\alpha_j)} \tag{2}$$

where, τ_0 is initial shear strength of soft clay; $\lambda$is rate of strength increasing with depth, $\lambda = (\tau_f - \tau_0)/z$; D is the height of the centre of slip circle above the ground; θ is half of the central angle of the slip arc in the ground; b is half of the width of the slip arc in the subgrade; U_i is degree of consolidation of the soil where the slice's undersurface is; σ_{zi} is additional stress on the soil slice's undersurface cause by embankment; l_j is length of arc of the soil slice's undersurface; c_{II},ϕ_{II} is cohesion and angle of internal friction of filling material respectively; α_i is the angle between the undersurface of the soil slice and the horizontal.

The Effect of Degree of Consolidation on the Filling Height

It can be seen that sliding stability factor F_S is correlation with the degree of consolidation of the ground. if the degree of consolidation is neglected, the term

$R\sum_{A}^{B} U_i \sigma_{zi} l_i tg\varphi_{cu}$ in formula (2) is zero, and W_{II} is correspond with the maximal load that fill rapidly only utilizing the natural strength (if F_S=1, the height equal the limit filling height)for the first stratum.

After the first stratum was placed for some term, the soft ground consolidation to some extent and its strength enhanced, the term of $R\sum_{A}^{B} U_i \sigma_{zi} l_i tg\varphi_{cu}$ would be add into, If the allowed F_S keep the same, the W_{II} could be established by formula (2), which was the second fill weight (filling height) that reckon the strength increasing cause by the ground consolidation under the first stage load. If regarded situation at this moment as the new initial state again, repeat above-mentioned computational processes, the limit filling height of next stratum could be established, took this situation as initial state and repeating the calculating process above, the next filling height could be established too, and the rest filling height in the different stage of construction process may be deduced by analogy. With the development of high-speed railway , the demand for settlement after construction of soft ground is stricter day by day, besides meeting the above-mentioned stabilities demand , the filling height must full the demand of settlement after construction too; For expression convenient, we defined the maximum height that meeting the demand either stability or settlement after construction as allowable filling height.

Calculating the Degree of Consolidation during the Process of Construction

From above, it is necessary that the degree of consolidation at any time during construction be confirmed at first in order to calculate the allowed filling height by taking account of the ground strength increase with degree of consolidation.

When loading in grades, the degree of consolidation of the soft ground can calculated by the theory of average degree of consolidation (Gong xiaonan, 1996) .that is as follows:

$$U_t = U_{t1}\frac{p_1}{\Sigma p} + U_{t2}\frac{p_2}{\Sigma p} + U_{t3}\frac{p_3}{\Sigma p} + \cdots \tag{3}$$

where, $\sum p$ is the sum of every grades load; U_t is the degree of consolidation for the sum of every grades load $\sum p$ at time t; U_{tn} is the degree of consolidation for the load p_n at time t; U_{tn} can be calculated by Terzaghi one-dimensional consolidation theory, according to soil layer distribution, situation of stress and the drainage condition of the ground. For the ground improved by sand well or plastics drainage board, the degree of consolidation can be calculated as follow:

$$U_{tn} = 1 - \frac{8}{\pi^2} e^{-\frac{8}{F}\frac{C_h}{d_e^2}tn} \tag{4}$$

where $F = \frac{m^2}{m^2-1}\ln(m) - \frac{3m^2-1}{4m^2}$, $m = \frac{d_e}{d_w}$

where C_h is horizontal coefficient of consolidation; d_w is diameter of sand well; d_e is effective diameter of sand well.

Because of the limitation of various kinds of consolidation theories and complexity of the geological condition of the real project, the calculated settlement is not equal to the tested settlement in situ usually. If the total settlement calculated by layer-wise summation method, the degree of consolidation defined from both above are not equal too. To future moment, the calculative degree of consolidation can get by formal (3), but the tested settlement hasn't gotten. In order to get the practice degree of consolidation in situ, it is undoubtedly effective method to modify the calculated settlement according to the test data.

Have already tested settlements S_{T1}, S_{T2}, S_{T3},…… S_{Tn} at the time t_1, t_2, t_3,…… t_n, correspondingly the calculated settlement are S_{C1}, S_{C2}, S_{C3},…… S_{Cn},which can be expressed $S_t = U_t \times S$, in which U_t can be calculated by the formula (3) and S is the total settlement. Define the ratio of tested settlement S_T to calculated settlement S_c as K_t, $K_t = S_T / S_c$ at time t, Similarly, they can calculated, namely $K_{t1}, K_{t2}, K_{t3}, \ldots\ldots, K_{tn}$.

The tested degree of consolidation at the time t_{n+1} is

$$U = \frac{S_{T(n+1)}}{S} = \frac{K_{n+1} \times S_{C(n+1)}}{S} \tag{5}$$

For the future time t_{n+1}, the settlement $S_{t\,(n+1)}$ is unable to be actually tested, K_{n+1} is unknown. Therefore, the least square method is adopted to confirm K_{n+1} according to $K_{t1}, K_{t2}, K_{t3}, \ldots\ldots, K_{tn}$.

CALCULATING PROGRAM

In order to guarantee the stability of the embankment, it is necessary that suppose several sliding surface and take that one with the minimal stability coefficient as potential slip surface to judge the stability of embankment. A program was developed based on theories above-mentioned, its flow chart was shown in Fig.2. The conditions adopted were: the minimum stability coefficient K=1.2[1] for the effective consolidation stress method and the settlement after construction $S_p \leq$20cm. By this program, the allowable filling height at any time during construction can be calculated.

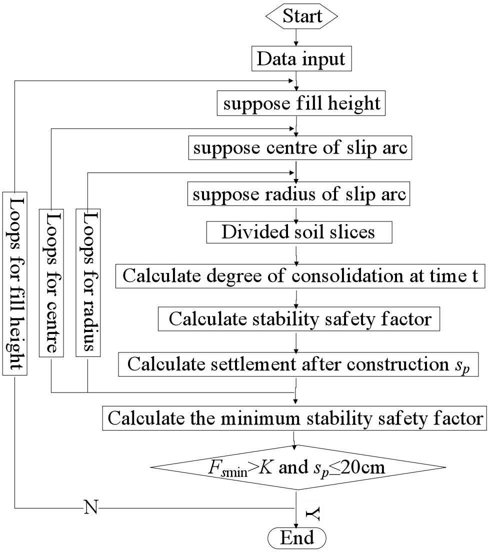

Fig. 2. Program flow chart

PRACTICAL CASE

General situation of project

Zhapu-Jiaxing-Suzhou expressway is through the north of the Hangjia lake area at and the middle of Jiaxing city, China. The tested data from section K16+250 were used to verify the theory proposed.

The designed pavement width is 28m and the slope grade of the embankment is 1:1.5, the ground improved by geotextile and Plastic drainage board in depth 20m. The benchmark term of settlement after consolidation is 20 years and the total time of construction is 3 years. The parameters used in calculate are: the ratio of effective diameter to real diameter of sand well is 27.3, the diameter of sand well is 0.05m, the effective diameter of sand well is 1.365m, the length of sand well is 21m, the average of the vertical coefficient of consolidation is $4.264\times10^{-4}\text{cm}^2/\text{s}$. The parameters of ground soil in monitored section are shown in table 1.

Table 1. Parameters of Ground Soil in Monitored Section

Number of soil	Name	Depth	Density	Specific gravity	Compression			Shear strength			
					Coefficient of compressibility	Modulus of compressibility	Coefficient of consolidation *V*/*H*	R test		Q test	
								c	φ	*c*	φ
		M	g/cm^3		MPa^{-1}	MPa	10^{-4}cm^2/s	kPa	°	kPa	°
1	**Clay**	**2.10**	**1.98**	**2.74**	**0.69**	**3.90**	**15.3/4.72**	**22**	**9.1**	**28.5**	**2.65**
2	**Silty clay**	**16.8**	**1.80**	**12.74**	**0.73**	**2.80**	**3.77** **3.94**	**15**	**11.0**	**17.8**	**3.8**
3	**Loam**	**5.30**	**2.01**	**2.72**	**0.23**	**7.16**	/	**32**	**11.3**	**45**	**10.3**
4	**Loam**	**5.00**	**1.94**	**2.72**	**0.24**	**8.03**	/	**23**	**15.3**	**31.5**	**20.5**
5	**Loam**	**7.10**	**1.99**	**2.73**	**0.34**	**4.98**	/	**42**	**15.6**	**35**	**7.6**
6	**Loam**	**3.60**	**2.01**	/	**0.14**	**11.6**	/	**20**	**26.5**	/	/
7	**Loam**	**4.80**	**1.93**	**2.72**	**0.33**	**5.67**	/	**18**	**19.6**	**18**	**19.6**

RESULT AND ANALYSIS

The allowable filling height at any time during construction can be calculated by the theory and program proposed above, which dedicated in Fig. 3. It can be seen that:

The allowable filling heights at any time during the construction increase basically with the construction, and keep approximately a fixed value after the consolidation finished.

During construction, the embankment can be filled safely only when the load-time curve lies lower than the predicted allowable filling height, and the demand of settlement after construction can be meet too at the same time.

There is a small section of construction height go beyond the allowable filling height in Fig. 3. It indicated that the calculated allowable filling height is less than the factual value, which is caused by the contribution of the geotextile to the stability of the embankment is neglected.

The calculated settlement is in accord with the tested settlement, it shows that equation (3) or (4) is feasibility for established the degree of consolidation of the soft ground that improved by plastics drainage board.

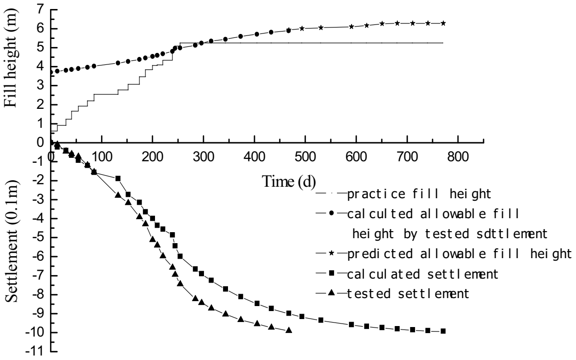

Note：when t=710d, the degree of consolidation is U= 100%

Fig. 3 Allowable filling height at any time during the construction

CONCLUSIONS

From above, the conclusion can be drawn:

The proposed method and program are convenient and swift to establish the allowable filling height, which guiding the embankment construction safely and ensuring the settlement after construction was admitted;

The proposed method to modify the calculated settlement by monitored settlement data is simple and practical, which can be used to determine the degree of consolidation more accurately.

REFERENCES

The Ministry of Communications of the People's Republic of China (MOC). (1997). "The technical specification for design and construction of highway embankment on the soft soil ground. JTJ 017-96. " *People's Transportation Press*, Beijing, China.

The Jiangsu Ning-Hu expressway Limited Company, Hohai University. (2001). "The manual for soft soil ground of the traffic and civil engineering." *People's Transportation Press*, Beijing, China.

Gong xiaonan. (1996). "Advanced soil mechanics." *Zhejiang University publishing house*, Hangzhou, China

Research on the Criterion of Instability of the High-Fill Soft Roadbed

Chun-Yuan Liu, Wen-Yi Gong, Xiao-Ying Li, and Jin-Na Shi

HeBei University of Technology，TianJin，300132

ABSTRACT: In one fleet of a freeway construction, the right side of the roadbed suddenly taken place to sideslip and collapse largely towards outside, then the left side of it began to slip and collapse too. The slumping section is 130 m, and the highest degree of collapse of the Roadbed slump is 4.3m, both the pavement of construction and the lateral reed field welling up for 1.0m, settlement crack appears in the culvert around the fleet, among which the width of largest crack is 40cm.The wall of the culvert have distorted deformation. The creeping section ranges from the freeway "K39+720" to "K39+920", within which "K39+720"—"K39+868" was treated by Plastic Drainage Board and "K39+868"—"K39+920" was treated by concrete mixed piles. Not before the fifth day did the landslip stopped.

The main content of this passage is to analyze the main factors that affect the Slope progressive failure calculating result. In use of this theory, two-dimensional progressive failure about the slope mentioned above can be calculated; and then on the results of the slope program, the security analysis on the slope combined with specific characteristics is carried. At last, design standards on security indicators of the high-fill soft soil roadbed are given.

ENGINEERING INTRODUCTION

The total length of the main road along the motorway is 63.673 miles and the joint road is 1.309 miles. The main line used six lanes freeway design standards. The design speed is 120 miles per hour, the roadbed width is 34.5m; there are 5 interchange overpasses, 8 separated overpasses, 6 flyovers, 1 extremely big bridge, 9 big bridges, 33 middle bridges, 30 small bridges, 17 channels.

The soil along the road is mainly the forth formation of the new EC Q^{4}_{mc+m}, and it is caused by marine strata. The exposed formation includes such kind of soil as clayey, clay, mud-clayey, mud-clay, silt, fine sand, and so on. Known from the investigation, the shallow groundwater level is very low. Along the whole line which the road covers, soft soil and weak soil layer is very common. As the request of construction timetable, embankments in some sections are filled with slag, gravel instead of fly-ash, lime-soil and so on. On November 18th 2007, the roadbed suddenly began to slip from the stake "K39+720" to "K39+920".

The geomorphologic configuration feature of this section belongs to Mainland accumulation of stagnant water landscape(swamp), it is low-lying and has a little ups and downs, the ground elevation is between 0.44—2.25m,. The sketch of calculating cross section is shown in figure1.

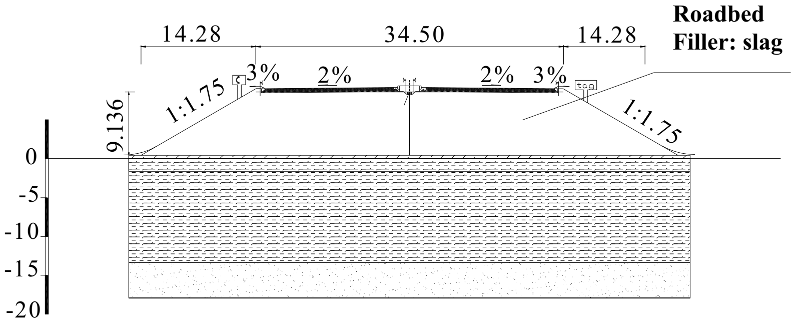

foundation handling: mixed piles

illustration:
1.each figure is scaled by M.
2. <u>proportion</u> : V:1:350; H:1:350

Figure 1 Sketch of calculating cross section Freeway: **K39+900**

The specific geology is like this: According to the results from Geological drilling, Standard penetration test, CPT experiment, and in laboratory, the formation is divided into six major layers. The parameters are in table 1 below.

Table 1 . Soil parameters

No.	**soil type**	**Thickness(m)**	**e**	I_L	**a1-2(MPa-1)**
1	Mud-clayey	3.0-9.5	0.911-1.196	0.67-1.20	0.39-0.87
2	Clayey	1.3-4.0	0.628-0.788	0.75-0.83	0.37-0.58
3	Mud-clayey	1.7-3.6	1.105-1.288	0.72-1.01	0.63
4	Fine sand	1.0-5.9	——	——	——
5	Soft soil	4.5-4.9	0.998	0.75-0.93	0.3-0.45
No	**Es(MPa)**	**c(kPa)**	**φ**	[c_0 **(MPa)**	τ_i **(MPa)**
1	3.6-5.0	3-10	5.5-7	85-110	20-25
2	4.5-5.2	13-31	8.9-32.2	140-160	35-40
3	3.1-3.5	12-24	3.0	105-110	20-25
4	22.83	0	23.0-35	180-200	40
5	4.2-6.5	28-31	4.8-14.0	140	36

ANALYSIS AND CALCULATION

The fundamental calculation principle is using the Simple Bishop Method of the limit equilibrium theory. The assumption is that when the slope is at the limit of balance, the potential slip surface is being searched, and the corresponding minimum safety factor is calculated. In the actual calculation, since the physical properties of the original design is strong, the safety factor from the calculation is higher, but the actual filler is weaker, so first we search the most dangerous slip surface in the condition of the original designed filler, and then find which section's safety factor is lowest. If the original designed filler is not stable, the actual filler must be unstable. So we points out this most dangerous section based on the original designed filler, and then check the safety factor of the actual filler. The checking profiles are these two profiles as K39+900 and K39+800 from the slump sections.

The profile of K39+900

The original design filling material was lime-soil while the actual material was 50cm' gravel cushion and 9.16m'slag. After the slump, the filler was changed to fly-ash. The thickness could be neglected when calculating. The groundwater level is -0.5m;the foundation handling is mixed piles; the piles are laid in triangular form; the diameter "d" is 0.5m;the handling depth "hv" is 8m and length "l" is 64m;the total length "lt" of the piles is 20644m;the handling width "hw" is 62.5m;the handling area is 4000 m^2 ;the pile spacing is 1.2~1.5m;the distance the of pile spacing changes gradually; the cement incorporation was 5% of reinforced soil; the water-cement ratio is 0.5.

According to the geological survey data, the actual formation is simplified, here are the original foundation parameters. Results are shown in table2.

Table 2. Embankment fill parameters

embankment fill	thickness (m)	γ (kN/m3)	cohesive force C (kPa)	internal friction angle φ
lime-soil	9.16	18.20	18.00	28.00
slag	9.16	23.00	0.00	33.50
fly-ash	9.16	15.00	15.00	23.00

Table 3.Concrete mixed pile parameter Table 4.Original foundation parameters

γ_c (kN/m3)	cohesive force c_c (kPa)	internal friction angle φ_c
Same to the soil around	80.00	20.00

No.	thickness (m)	γ (kN/m^3)	c (kPa)	φ
1	4.00	19.27	10.50	7.20
2	3.50	18.85	15.00	10.00
3	3.60	18.90	16.00	15.00
4	1.90	20.00	0.00	25.00
5	3.10	19.10	28.00	20.40

As the foundation was handled by mixed piles, so the original parameters should take a composite foundation check. Recommended by the corresponding norms, the composite foundation should be calculated like this: $c' = c\ (1-m) + c_c m$; $\varphi' = \varphi\ (1-m) + \varphi_c m$, where m is the rate of replacement, $m = \frac{l_t s_0}{h_v s}$; s_0 is the cross-sectional area of each pile; $s_0 = \pi(\frac{d}{2})^2$ .After all the parameters put into the formulas, we get the following composite foundation parameters table—table5. The calculating results are shown in the table 6.

Table 5. Composite foundation parameters

No.	**thickness (m)**	γ **(kN/m^3)**	c **(kPa)**	φ
1	4.00	19.27	19.32	8.82
2	3.50	18.65	23.25	11.27
3	0.50	18.90	24.12	15.63
4	3.10	18.90	16.00	15.00
5	1.90	20.00	0.00	25.00

Table 6. Checking results of the landslide stability for K39+900

	model	**R (m)**	**X (m)**	**Y (m)**	**H (m)**	**K**
original design	lime-soil	18.63	7.33	14.66	3.98	1.166
actual construction	Slag	18.63	7.33	14.66	3.98	1.023
refilled	fly-ash	20.42	7.33	16.49	3.93	1.199

The profile of K39+800

The embankment fill is the same to K39+900, while it's filling height is 8.36m; groundwater level is -0.5m; the foundation is handled in the way of Vertical drainage board and preloaded. The embankment fill parameter is the same to K39+900 except for the filled up; the original foundation parameters are in the table 4. the results are shown in table7. The final calculating results are shown in table 8.

Table 7. Composite foundation parameters

No.	**thickness (m)**	γ **(kN/m^3)**	c **(kPa)**	φ
1	4.00	19.27	14.70	9.36
2	3.50	18.65	21.00	14.00
3	0.50	18.90	22.40	21.00
4	3.10	18.90	16.00	15.00
5	1.90	20.00	0.00	25.00

Table8. Checking results of the landslide stability for K39+800

	model	R (m)	X (m)	Y (m)	H (m)	K
original design	lime-soil	17.37	6.69	13.38	4.00	1.110
actual construction	Slag	17.37	6.69	13.38	4.00	0.973
refilled	fly-ash	16.86	6.69	13.38	3.49	1.139

INSTABILITY CRITERION RESEARCH

From the whole line of the road, we can see qualitatively that the location of slip first occurred where the slope safety factor is lowest, then it developed to the whole section progressively. The slip plane sketch is shown in the figure 2.

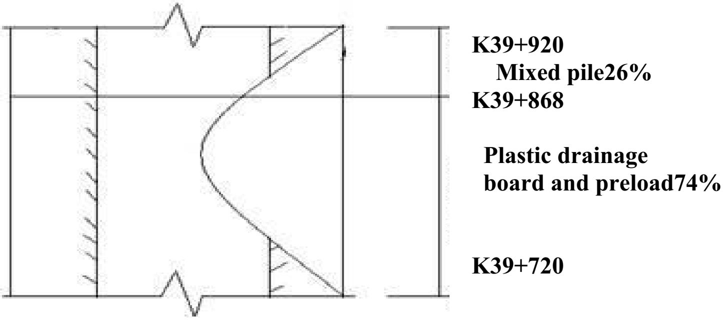

Figure2 .Slip plane sketch

We can see from the plane that the track of whole slip section is generally an arch, and the center of the slip surface should be in the section handled by drainage board. So, analyzing qualitatively, instability occurs first in the section handled by drainage board, after that, the whole section was driven to slip.

Thereby, the safety factor could be considered a criterion for embankment instability judgment. There are a lot of factors that infect the slip safety factor, such as embankment parameters, loading condition, embankment structure, construction method, conservation measures and so on. As the C and of φ of the first mud-clay layer is too small, a potential slip surface forms. Considering the C and of φ of the second mud-clay layer to become stronger, the slip surface stops to continue cutting deeper. Safety factor up to or more than 1.1 can meets the relative requirements.

CONCLUSIONS

High-fill Roadbed instability starts first from some profile where it has reached the limit state of stability, and developed gradually to the whole slip section. Thus, the slip safety factor of the profile can be considered the criterion of profile instability.

In the design, construction, and landslide control, the embankment fill properties need more attention and the performance decline of embankment fill which the construction change leads to must be combated effectively. As for the weak foundation soil, appropriate handling must be taken in order to reinforce the internal friction angle “C” and cohesive force “φ”. Composite foundation such as concrete mixed pile can be calculated according to the norms, and parameters of consolidation methods can be reinforced according to the experience and actual field situation. In this way, the safety factor of landslide stability can meet the corresponding requirements.

REFERENCES

[1] TU Bing-xiong and LIU Chun-xiao(2007). “Discussion on the analytical methods of the slope stability,” *Shanxi Architecture* 100926825 (2008) 0120092202

[2] TANG Hong-xiang and LI Xi-kui(2007). “Finite element analysis of Cosserat continuum for progressive failure and limit bearing capacity of soil foundation,” *Rock and Soil Mechanics* 1000－7598－(2007) 11－2259－06

[3] NIU Jian-dong and XU Lin-rong(2007). “Sensitivity analysis of soft Soil model’s parameters,” *J. of Plasticity Engineering* 100722012 (2007) 0420156206

[4] GE Xiao-ming and TANG Tong-zhi(2006). “A Study of Flexible Permeable Hose as a New Vertical Drainage Material Applied in Ground Treatment,” *J. of Yan Cheng Insti.of Technology* (Natural Science) 1671-5322(2006)03-0051-0.

AUTHOR INDEX

Page number refers to the first page of paper.

SUBJECT INDEX

Page number refers to the first page of paper.